DISS. ETH NO. 23785

Development of Oxide Dispersion Strengthened Titanium Aluminides for Additive Manufacturing

A thesis submitted to attain the degree of

DOCTOR OF SCIENCES of ETH ZURICH

(Dr. sc. ETH Zurich)

presented by

CHRISTOPH KENEL
MSc ETH

born on 06.08.1987
citizen of Arth SZ

accepted on the recommendation of

Prof. Dr. Konrad Wegener, examiner
Dr. Christian Leinenbach, co-examiner
Prof. Dr. Gordon Tatlock, co-examiner

2016

Acknowledgement

This thesis was written during my time at the Swiss Federal Laboratories for Materials Science and Technology (Empa) in the group Alloy Design for Advanced Processing Technologies (ADAPT) from February 2013 until August 2016 in collaboration with the Institute of Machine Tools and Manufacturing (IWF) of ETH Zurich. The work was conducted in the frame of the multinational EU FP7 research project Oxide Dispersion Strengthened Materials for the Additive Manufacture of High Temperature Components in Power Generation (OXIGEN).

I would like to thank my supervisor Prof. Dr. Konrad Wegener (IWF-ETH) for giving me the opportunity to do my PhD on this topic. His inputs and, in a positive sense, critical questions beyond the material science part of this study are highly appreciated.

I am very grateful to my supervisor at Empa, Dr. Christian Leinenbach, head of the ADAPT group, for giving me his trust and the freedom to pursue my research in a truly constructive and open-minded environment. He provided me with the necessary infrastructure, his guidance and scientific input to successfully complete this thesis.

This thesis would not have been possible in this form without contributions of many people, working at Empa and elsewhere. They provided materials, technical support, measurements, access to equipment, scientific input, pleasant and fruitful discussions and advice throughout my time at Empa. Special thanks to Toni Ivas, Adrian Lis, Nico Weyrich, Ariyan Arabi-Hashemi, Xiaoshuang Li, Georgia Dasargyri, Wookjin Lee, Hansruedi Elsener, Michael Koster, Sara Romer, Martin Sauder, Sascha Populoh, Remo Widmer, Erwin Pieper, and Barbara Zeps, as well as the past and present members of the Labs "Joining Technologies and Corrosion" and "Advanced Materials Processing". I also thank Thomas Bauer and Adriaan Spierings (Inspire AG, CH), Gordon

Tatlock, Keith Arnold and Karl Dawson (University of Liverpool, UK), Alberto Colella (Matres, Italy) and Carl Hauser and Josh Barras (TWI, UK) from the OXIGEN consortium for their support and discussions throughout our project. Finally, I express my gratitude to Daniel Grolimund, Vallerie Ann Samson, Julie Fife, Steven van Petegem and Helena van Swygenhoven from PSI for their support with the *in situ* diffraction experiments.

I would like to thank my family for their support allowing me to pursue my path in science. A special thank you to my partner Johanna Nyffeler for her advice and patience throughout these stressful years.

The research leading to these results has received funding from the European Union Seventh Framework Program [FP7/2007-2013] under grant agreement no. 310279 (OXIGEN).

Contents

1 Introduction 1

2 State of the art 5
  2.1 Constitution of titanium aluminides 5
  2.2 Microstructure formation and related properties 8
  2.3 State-of-the-art higher-order titanium aluminide alloys . . . 17
  2.4 Powder-based processing of titanium aluminides 19
  2.5 Reinforced titanium aluminides 31
  2.6 Aim of the thesis 34

3 Experimental and analytical methods 37
  3.1 Materials and consolidation methods 37
  3.2 Materials characterization 42
  3.3 Materials testing 44
  3.4 Computational thermodynamics 49

4 Microstructure formation of Ti-Al alloys at high cooling rates 51
  4.1 Experimental setup and concept 51
  4.2 Computational framework 61
  4.3 Influence of cooling rate and composition in binary Ti-Al . . 66
  4.4 Influence of the ternary alloying elements Nb and Mo 81
  4.5 Alloy design of titanium aluminides for additive manufacturing 95
  4.6 Conclusions 99

5 Microstructure and oxide particle stability in an ODS γ-TiAl alloy 101
  5.1 Alloy design and selection 101
  5.2 Processing results and discussion 107
  5.3 Summary and conclusions 124

6 Performance of ODS titanium aluminides 125
6.1 High temperature degradation behavior in air 125
6.2 Mechanical properties at low and high temperature 140
6.3 Conclusions 147

7 Selective laser melting of a β-solidifying ODS γ-TiAl alloy 149
7.1 Experimental details 149
7.2 SLM processing results 153
7.3 Summary and conclusion 169

8 Summary and Outlook 171

Abstract

Titanium aluminides gained a lot of interest over the last decades due to a potential weight reduction and increased performance of high temperature components. Further increasing their performance at high temperatures is a crucial factor to compete with the heavier Ni-base superalloys. Processing this class of structural intermetallics using additive manufacturing is also of great interest to produce novel parts with unprecedented complexity. In this work an oxide dispersion strengthened (ODS) titanium aluminide alloy is developed taking into account the non-equilibrium conditions during beam-based additive manufacturing. In order to understand the influence of cooling rate and composition on microstructure formation, rapid solidification experiments on binary Ti-Al and ternary Ti-Al-Nb and Ti-Al-Mo alloys are performed using a novel experimental liquid droplet quenching technique. In combination with *in situ* X-ray diffraction experiments at a synchrotron light source, the observed behavior of Ti-Al-(Nb, Mo) is mapped and compared to thermodynamic simulations based on the CALPHAD approach taking into account the non-equilibrium nature of the process. Based on this fundamental study, a matrix alloy is selected for production of ODS titanium aluminide by mechanical alloying. Consolidation tests using spark plasma sintering, selective laser melting and direct metal deposition show the influence of the processing route on the formed microstructure and the resulting dispersoid size. Apart from the effects of alloy composition and ODS particle addition on microstructure and processing also the influence on mechanical performance and degradation behavior is studied. Compared to the dispersoid-free alloy, the ODS variant is superior in terms of yield stress and ultimate tensile strength at 293 to 1073 K as well as more oxidation resistant. Finally it is demonstrated that complex lattice structures can be produced from the ODS alloy by selective laser melting. Additionally, the beneficial effect of adapted re-scanning strategies on the occurrence of cracking is discussed.

Zusammenfassung

Seit rund drei Jahrzehnten sind Titanaluminide sind im Fokus der Forschung, da ihr Einsatz Gewichtseinsparungen und bessere Eigenschaften in Hochtemperaturkomponenten verspricht. Eine kontinuierliche Verbesserung dieser Eigenschaften ist ein entscheidender Punkt um eine Konkurrenz zu den deutlich dichteren Ni-Basis Superlegierungen zu schaffen. Die additive Fertigung dieser Klasse von intermetallischen Strukturwerkstoffen ist zudem seit kurzem von grossem Interesse um Komponenten mit bisher unerreichter Komplexität zu produzieren. Im Rahmen dieser Arbeit wurde eine oxid-dispersionsverstärkte (ODS) TiAl Legierung entwickelt, wobei die Nichtgleichgewichtsbedingungen während der strahlbasierten additiven Fertigung miteinbezogen wurden. Eine neuartige Methode, basierend auf abgeschreckten Metalltropfen, erlaubt den Einfluss der Kühlrate als auch der Legierungszusammensetzung auf die ausgebildete Mikrostruktur in Ti-Al, Ti-Al-Nb und Ti-Al-Mo zu untersuchen. In Kombination mit *in situ* Röntgenbeugungs-Experimenten an einer Synchrotronquelle wurde das Verhalten der Ti-Al-(Nb,Mo) Systeme bestimmt und unter Berücksichtigung der Nichtgleichgewichtsbedingungen der Prozesse mit thermodynamischen Berechnungen verglichen. Basierend auf dieser Untersuchung wurde eine Zusammensetzung für die Produktion einer ODS Legierung durch mechanisches Legieren ausgewählt. Konsolidierungstests mittels Spark Plasma Sintern, Selektivem Laserschweissen und Laserauftragsschweissen zeigen den Einfluss des Prozesses auf die Mikrostrukturbildung und die resultierende Partikelgrösse. Zusätzlich wurde auch der Einfluss der Oxidpartikel auf die mechanische Festigkeit und Oxidationsbeständigkeit bestimmt. Die verstärkte Variante zeigt eine höhere Dehn- und Streck-Grenze sowie Oxidationsbeständigkeit verglichen mit der unverstärkten Variante. Am Ende der Arbeit wird die Herstellung von komplexen Gitterstrukturen mittels Selektiven Laserschweissen demonstriert. Der positive Einfluss von diversen Wiederaufschmelz-Strategien auf die Rissbildung wird ebenfalls diskutiert.

List of Abbreviations

2Theta	Diffraction angle in X-ray diffraction
ADAPT	Alloy Design for Advanced Processing Technologies
AM	Additive manufacturing
Ar 6.0	Argon gas with a purity of 99.9999%
BSE	Back scattered electrons used for imaging
CALPHAD	CAlculation of PHase Diagrams
CTE	Coefficient of thermal expansion
DMD	Direct metal deposition
EBM	Electron beam melting
EDM	Electro-discharge machining
FIB	Focussed ion beam
FWHM	Full width at half maximum
HV	Vicker's Hardness
IMC	Intermetallic matrix composite
IWF	Institute for machine tools and manufacturing
m.r.d.	Multiples of random distribution
microXRD	X-ray diffraction with a micrometer sized beam
ODS	Oxide dispersion strengthened
OX 45-3	Ti-45Al-3Nb alloy developed in OXIGEN
OX 45-3 ODS	Ti-45Al-3Nb-Y_2O_3 alloy
OXIGEN	EU FP7 project no. 310279
REE	Rare earth element effect
SEM	Scanning electron microscopy
SLM	Selective laser melting
SLS	Swiss light source at PSI
SPS	Spark plasma sintering
STEM	Scanning transmission electron microscopy
TEM	Transmission electron microscopy
Ti-48Al	Alloy consisting of 52 at.% Ti and 48 at.% Al
Ti-45Al-(0-10)Nb	Alloy range with 0 to 10 at.% Nb
TNB	Alloy family based on Ti+Al+Nb
TNM	Alloy family based on Ti+Al+Nb+Mo
TNM^+	TNM alloys further alloyed with C and Si
XRD	X-ray diffraction
YAG	Yttrium-aluminium garnet

List of Symbols

A	Area
a	Fit parameter, proportionality constant
α	α-Ti phase
$\alpha[0001]$	Direction along the [0001] axis in α
$\alpha_2(0002)$	(0002) reflection of the α_2 phase
α_2	α_2-Ti_3Al phase
$\alpha_2\{1\bar{1}00\}$	Family of $1\bar{1}00$ planes in α_2
b	Fit parameter, proportionality constant, power law exponent
B	Length of the Burgers vector
β	β-Ti phase
β_0	β_0-Ti phase
c	Speed of light in vacuum
$c(F)$	Force-dependent proportionality function
c_{1L}	First radiation constant
c_2	Second radiation constant
d	Particle diameter
d_L	Laser spot diameter
d_i	Distance to interface
E	Young’s modulus
E_a	Area energy density
E_l	Line energy density
e_m	Machine elongation
ε	Strain
ε_f	Fracture strain
e_s	Specimen elongation
E_v	Volume energy density
F	Force
F_{max}	Maximum force
f_{nc}	Non-crystalline fraction
G	Gibb’s free energy
G	Shear modulus
G_A	Gibb’s free energy of phase A
$G_{A,T}$	Gibb’s free energy of phase A at temperature T
G_B	Gibb’s free energy of phase B
$G_{B,T}$	Gibb’s free energy of phase B at temperature T

γ	γ-TiAl phase
<110]	Convention: 0 fixed, permutation for 11 allowed
γ_{m}	γ-TiAl formed by a massive transformation
γ_{seg}	γ-TiAl formed by segregation
H	Enthalpy
h	Planck constant
h_L	Hatch distance
I_{am}	Scattering intensity of the amorphous fraction
I_{bg}	Background intensity
I_c	Intensity of the crystalline fraction
I_{CCD}	Intensity measured by the CCD chip
I_{tot}	Total intensity
k	Boltzmann constant
k_p	Parabolic growth constant
L	Liquid phase
l	Inter-particle distance
L_A	Crack length per unit area
λ	Wavelength
l_c	Particle center distance
M	Convertion factor
m	Mass
m	Growth exponent
N	Number of particles
$\mathbb{N}$	Natural number
ν	Poisson's ratio
P	Laser power
P_L	Number of intersection per line length
q	Scattering vector
r	Radius
R	Radiant expsoure
R'	Radiant exposure for overlapping melt tracks
$\mathrm{R_m}$	Ultimate tensile strength
$\mathrm{R_{p0.1}}$	Yield strength at 0.1% strain
$\mathrm{R_{p0.2}}$	Yield strength at 0.2% strain
σ_{Or}	Orowan stress
T	Temperature
t	Time
t_L	Layer thickness
T_0	T_0 temperature
$\mathrm{T}_0^{\mathrm{A}\rightarrow\mathrm{B}}$	T_0 temperature of the A $\rightarrow$ B transformation
Θ	Diffraction angle
w	Dislocation dissociation width
V	Volume
v	Scan speed
v_{rescan}	Scan speed of the re-scan strategy

1 Introduction

Titanium aluminides and other structural intermetallics have gained a lot of interest over the last decades due to a potential weight reduction and increased performance of high temperature components. In the intermetallic structure combining two light elements, Ti and Al, high mechanical strength and good creep resistance is paired with a low density. Consequently, titanium aluminides can compete with established Ni-base alloys in terms of specific or density-normalized properties (Figure 1.1). These advantages are of special interest in weight-critical applications as for jet propulsion engines for military and civil applications. The aerospace industry is thus the strongest force pushing for novel alloys and commercialization due to the large market volume. Starting with GE and its GEnx engine family in the past years also Snecma and MTU recently announced to use titanium aluminides in their next engine

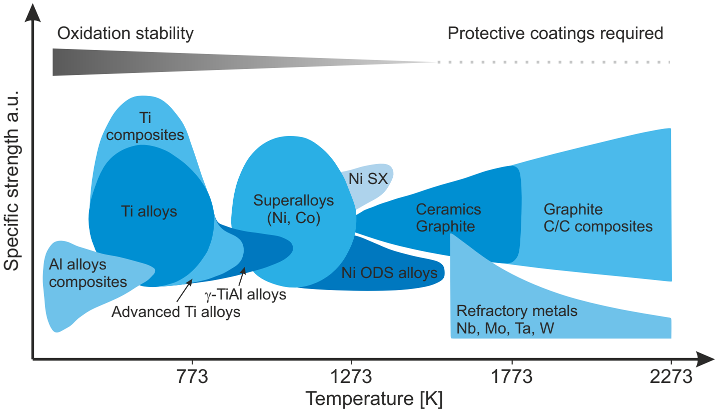

Figure 1.1: Schematic graph of the specific density and oxidation resistance of high temperature capable materials considered in weight-critical applications (Figure adapted from [1]).

generation [2, 3]. Starting from binary alloys the state-of-the art alloys are complex higher-order alloy systems with tailored properties for processing and use in critical components. While the primary alloy development was directed towards higher room temperature ductility, recent developments were driven by demands for higher strength and improved castability or formability. Modern alloys, such as the Ti-Al-Nb based TNB and Ti-Al-Nb-Mo based TNM alloy families [4–7] or the recently in jet engines applied GE alloys [2, 8] are representatives of such castable alloys. The alloys developed so far are optimized for consolidation by casting or powder metallurgical processing. These processes involve considerably low cooling rates which are typically below 100 K/s. Subsequent heat treatments may involve quenching steps with cooling rates in the order of 400 K/s by water quenching. The emerging and advancing field of additive manufacturing, however, requires alloys which are suitable for rapid solidification and subsequent cooling at small melt pool dimensions and multiple reheating and cooling cycles. While a vast body of data regarding the phase evolution during high temperature heat treatments and subsequent quenching is available, only little is known about rapid solidification at realistic cooling rates for additive manufacturing. The development of alloys specifically designed for additive manufacturing taking into account the special requirements for this processes is still an open field.

It has become clear in the recent past that additive manufacturing is not only a solid free-form production technique, it is also an enabling technology to produce novel materials which cannot be produced using conventional processing. This opens a completely new space for material scientists to create novel materials to fulfill the needs of the modern world for economically, ecologically and socially sustainable solutions of current and future technical challenges.The dynamic and fast nature of beam-based additive manufacturing allows preserving non-equilibrium phases and microstructures throughout the process. In this way time-dependent material changes can be avoided and for example heat sensitive diamonds can be preserved to form metal-diamond-composites [9]. In the case of oxide dispersion strengthened (ODS) alloys the distribution of oxide particles in the range of tens of nanometers throughout the alloy matrix needs to be preserved. Entering the liquid state, rapid growth, agglomeration and slagg-off of these particles occurs, typically limiting their processing to the solid state, for example by extrusion. Recently, additive manufacturing with its short lifetime of the melt pool and high cooling rates has been proven to be a novel processing route for Fe-based ODS alloys [10]. While ODS alloys are well known since decades for their good high temperature properties, machining of such strengthened alloys is naturally difficult. Combined with the fact that the solid state extrusion and sintering techniques can only provide a very limited degree of complexity, ODS alloys were only applied if there was no alternative. But with a technique at hand which can provide exceptionally high freedom in geometrical complexity combined with the beneficial properties of ODS alloys, this old class of alloys might be right at the threshold of revival.

Conventionally, ODS alloys are typically Fe- or Ni-based due to the widespread use of their non-strengthened variants as high temperature alloys. With structural intermetallics starting to compete with established alloys, optimizing their properties as strength retention and creep resistance at high temperature becomes an important field of research. While other intermetallic systems have been studied as ODS variants as ODS FeAl and ODS NiAl, only little is known on the effects and properties of ODS titanium aluminides. Together with the emerging processing technology this creates a novel field of research for the development of ODS titanium aluminides for and by additive manufacturing.

2 State of the art

In this chapter an insight is given into the current state of knowledge regarding titanium aluminides. First the constitution of the binary Ti-Al phase diagram and the phases of interest are discussed followed by the important phase transformations, the related microstructures and their properties. Then a section is dedicated to state-of-the-art higher-order titanium aluminides of commercial interest. Subsequently, the studies on Ti-Al alloys processed by spark plasma sintering and beam-based additive manufacturing and their behavior under rapid solidification conditions are presented. As closing part of the literature review, past studies on oxide dispersion strengthening are presented. This overview yields then the current research gaps that motivate this thesis. All compositions given in this work are in atomic percent.

2.1 Constitution of titanium aluminides

Titanium aluminides are a class of intermetallics that has been studied since several decades and a vast body of knowledge has been collected on an engineering and fundamental science level. Despite the abundance of data on alloys of Ti and Al, the binary phase diagram is debated until today. In 1978 Kaufmann and Nestor [12] published the first thermodynamic assessment combining the experimental data available at this time. From this point on the phase diagram was re-assessed every one to three years when new experimental data on phase relations, transformation temperatures and crystal structures became available. Wider attention was attracted by the assessment of Murray [13] in 1988 and the experimental phase diagram by McCullough *et al.* [14] one year later. In 1992 Kattner and Boettinger [15, 16] published a binary re-assessment and a preliminary ternary assessment on Ti-Al-Nb, as Nb was found to be of great importance in TiAl alloys. The growing interest in titanium aluminides then sparked the construction of a large thermodynamic database for light alloys in 1994 by Saunders [17]. This database is used until today but it contains inconsistencies which needed to be addressed. Ohnuma *et al.* [18] presented an updated assessment two years later. At the same time a lot of effort was undertaken by Braun and Ellner [19, 20] to study the binary phases and by Kainuma *et al.* [21] to establish the ternary phase relations. These works were the base for the re-assessment by Schuster and Palm [22] combining all experimental data and previous assessments in 2006. This data set was then used as the base for further key experiments and an improved thermodynamic description by Witusiewicz *et al.* [11] in 2008. Until today this assessment is the most accurate calculated version of the Ti-Al binary phase diagram and is used in most higher-order assessment as for the Ti-Al-Nb [23], Ti-Al-Ta [24, 25], Ti-Al-Cr [26] and recently the Ti-Al-V system [27]. The currently accepted binary phase diagram of Ti and Al shows

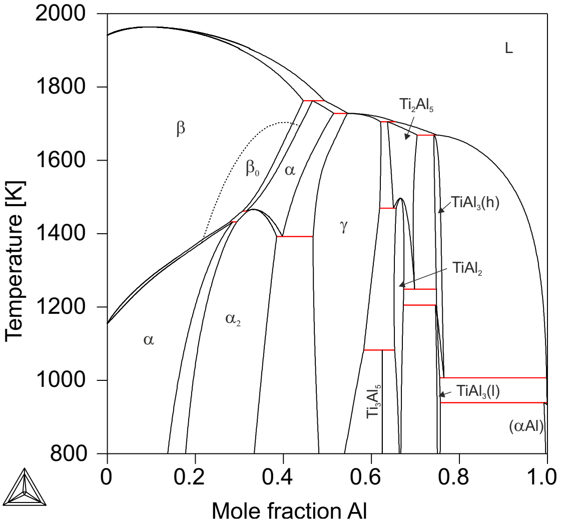

Figure 2.1: Re-calculated binary Ti-Al phase diagram according to the thermodynamic assessment by Witusiewicz *et al.* [11]. The single phase fields are indicated. For more information on phase structures see Table 2.1.

Table 2.1: Designation and crystal structure of Ti-Al phases according to Schuster and Palm [22] considered in the Ti-Al assessment of Witusiewicz *et al.* [11].

Phase designation	Pearson symbol	Space group	Prototype structure	Struktur-Bericht designation
α, α-Ti	*hP*2	$P6_3/mmc$	Mg	*A*3
β, β-Ti	*cI*2	$Im\overline{3}m$	W	*A*2
β_0	*cI*2	$Pm\overline{3}m$	CsCl	*B*2
α_2, Ti_3Al	*hP*8	$P6_3/mmc$	Ni_3Sn	$D0_{19}$
γ, TiAl	*tP*4	$P4/mmm$	AuCu	$L1_0$
Ti_3Al_5	*tP*32	$P4/mbm$	Ti_3Al_5	-
η, $TiAl_2$	*tI*24	$I4_1/amd$	$HfGa_2$	-
ζ, Ti_2Al_5	*tP*28	$P4/mmm$	Ti_2Al_5	-
ε(h), $TiAl_3$(h)	*tI*8	$I4/mmm$	$TiAl_3$(h)	$D0_{22}$
ε(l), $TiAl_3$(l)	*tI*32	$I4/mmm$	$TiAl_3$(l)	-
α-Al	*cF*4	$Fm\overline{3}m$	Cu	*A*1

several disordered, ordered and intermetallic phases (Figure 2.1 and Table 2.1). The disordered α and β Ti phases show extended solubility for Al at high temperature. Exceeding these limits, the ordered hexagonal α_2-Ti_3Al is formed from the parent disordered α-phase. Around the equiatomic composition, the γ-TiAl is observed. This phase has a $L1_0$ structure with an ordered

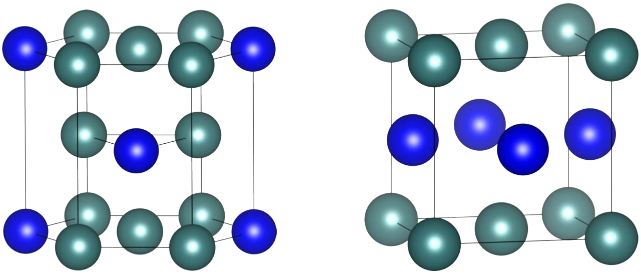
(a) (b)

Figure 2.2: Perspective view of the atomic structure of the technically important Ti-Al intermetallics a) α_2-Ti_3Al and b) γ-TiAl. Ti atoms are shown in grey, Al atoms in blue.

face-centered tetragonal lattice (see Figure 2.2). A similar crystal structure is observed in other technically important intermetallic phases as Ni_3Al providing exceptional high-temperature properties to the Ni-base super-alloys. In the Al-rich part of the phase diagram a multitude of stoichiometric line compounds and complex intermetallics is found which typically have tetragonal unit cells containing a large number of atoms (see the numbers in the Pearson symbols in Table 2.1). However, only the α_2-Ti_3Al and the γ-TiAl phase have been found to be of engineering importance, as the other binary phases are too brittle for an application in critical components [28]. Historically, starting from the conventional Ti-alloys first the super-alpha alloys containing α_2 and later the so called γ-titanium aluminide alloys based on the γ-phase were developed [29, 30]. In the compositional space of 42 to 48 at.% Al this class of structural intermetallics contains as main constituents the γ- and α_2-phases together with additional minor phases in higher order alloy systems, depending on the specific composition.

2.2 Microstructure formation and related properties

2.2.1 Phase transformations

In the compositional space of interest in titanium aluminides several phase transformations are observed. These transformations define the microstructure, the spatial arrangement of the phases, and finally the properties of the material as reviewed in detail by Appel *et al.* [31] and shortly summarized here. The three most important phase reactions are the two high temperature peritectics $L + \beta \rightarrow \alpha$ and $L + \alpha \rightarrow \gamma$ at 1764 K and 1729 K, respectively, and the eutectoid reaction $\alpha \rightarrow \alpha_2 + \gamma$ at 1392 K [11]. The first peritectic reaction divides the solidification behavior into three classes: β-solidifying, hypo-peritectic and hyper-peritectic. Consequently, three different solidification paths are observed in the compositional space of interest of 42 to 48 at.% Al: $L \rightarrow L + \beta \rightarrow \beta$, $L \rightarrow L + \beta \rightarrow L + \beta + \alpha \rightarrow \beta + \alpha$ and $L \rightarrow L + \beta \rightarrow L + \beta + \alpha \rightarrow L + \alpha \rightarrow \alpha$. All alloys form β as primary phase, but the Al-rich alloys then solidify by α compared to the Al-lean alloys which solidify by β. This differences then influence already the solidification microstructure, as the body-centered cubic β prefers the <100> directions while the hexagonal α solidifies with the [0001] direction aligned with the heat flow direction. In fully β-solidifying alloys, the α-phase is later on formed according to the Burgers relation

$$\{110\}_\beta \parallel (0001)_\alpha \text{ and } \langle 111\rangle_\beta \parallel \langle 11\bar{2}0\rangle_\alpha \tag{2.1}$$

This yields 12 different variants of α from a single parent β grain. Consequently, the β-solidifying alloys show only slight texture after solidification. Interestingly the α-phase does not nucleate at the primary β in Al-rich alloys. Although β is unambiguously the primary phase, α does not take over the orientation of the primary phase but forms according to its own preferred [0001] orientation for solidification. Instead of nucleating with the expected 12 different variants from the primary β, a strong texture along $[0001]_\alpha$ is observed after solidification [31]. The parent α decomposes into $\alpha_2 + \gamma$ at 1392 K. As the compositional space of interest is in the hyper-eutectoid region, γ is precipitated from the parent α already at higher temperature (see Figure 2.1). The crystallographic orientation of the three phases α, α_2 and γ according to the Blackburn-orientation relationship [32] is

$$(0001)_{\alpha_2} \parallel \{111\}_\gamma \text{ and } \langle 11\bar{2}0\rangle_{\alpha_2} \parallel \langle 110]_\gamma \tag{2.2}$$

The densely packed atomic layers along $(0001)_{\alpha_2}$ and $\{111\}_\gamma$ are oriented parallel and the dense atomic rows along $\langle 11\bar{2}0\rangle_{\alpha_2}$ and $\langle 110]_\gamma$ are aligned. Due to the anisotropy of the γ-phase only a restricted subset of directions in the base plane is allowed, whereas all rows on the side faces are incompatible. Based on this relationship the two phases α_2 and γ share atomically flat and perfect interfaces. With the crystallographic orientation of all phases being correlated by the Burgers and Blackburn orientation relationships, the observed microstructure and arrangement of the intermetallic phases α_2 and γ is directly correlated to the microstructure at high temperature of the disordered parent α and β. Upon decomposition of the parent α typically a lamellar structure is formed consisting of alternating oriented plates of

α_2 and γ. Depending on the texture of the parent α, the texture of these lamellar colonies is defined. In Al-lean alloys forming 12 α-variants from β the orientation of the colonies is almost random. In Al-rich alloys having a distinct texture along $[0001]_{\alpha_2}$ the lamellar structure is typically oriented perpendicular to the heat flow direction based on the Blackburn relation. Depending on the cooling rate also lamellar structures oriented parallel to the heat flow direction are observed. It could be shown that in this case the parent α was not solidified along [0001] but along $<11\overline{2}0>$ which is oriented perpendicular to the former one. Consequently, also the intermetallic phases are forming in an orientation turned by 90° to the normally observed direction under slow cooling [33]. This allows, in principle, the production of directionally solidified parts from seed crystals with an aligned intermetallic structure. It becomes clear that while the Burgers relation and the preferred solidification directions define the microstructure of the parent α and β, the Blackburn relation defines the internal structure of the lamellar colonies. Together, the microstructure formation of titanium aluminides can be understood. Close control of the solidifying phases and their orientation allows then to influence the intermetallic microstructure and the properties after solidification.

2.2.2 Microstructures

Metallic alloys are usually not directly applied in the as processed form but are heat treated to modify the microstructure, form new phases and thereby control the properties. While the microstructure obtained during the processing may affect the processability of an alloy, the suitability of an alloy for service conditions can to a certain extend be optimized by following heat treatments. For titanium aluminide alloys four different general microstructural classes are distinguished: fully lamellar, near-lamellar, duplex and near-γ [34–36]. The fully lamellar microstructure is obtained after a heat treatment in the α single phase region (T_1 in Figure 2.3). Due to the absence of additional phases strong grain growth occurs. After cooling below the eutectoid temperature the parent α decomposes into $\alpha_2 + \gamma$ yielding a coarse grained fully lamellar microstructure with colony sizes up to 1000 µm (Figure 2.4a). A heat treatment close to the α-transus temperature leaves behind γ grains in between the lamellar colonies after cooling (T_2 in Figure 2.3). This is the so-called near-lamellar microstructure (Figure 2.4b). Between the near-lamellar and duplex structure a smooth transition is observed. With decreasing heat treatment temperature to T_3 the amount of retained γ is increased leading to a duplex microstructure consisting of distributed equiaxed γ and lamellar colonies. Due to competing growth of α and γ at high temperature neither phase can coarsen substantially and typically grain sizes around 10 µm are observed (Figure 2.4c). The fourth class is formed when the alloy is heat treated below the eutectoid temperature yielding a near-γ microstructure consisting of equiaxed γ and α_2 located at the triple points (Figure 2.4d and T_4 in Figure 2.3). In titanium aluminide alloys the α-transus temperature is strongly depending on the composition (see Figure 2.1). While similar microstructures can be obtained with different alloys, the corresponding heat treatment temperatures need to be evaluated individually for every alloy. This effect needs to be taken into account when

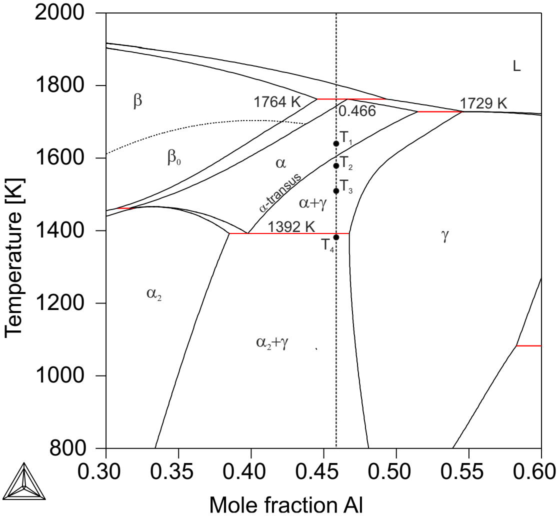

Figure 2.3: Central part of the Ti-Al phase diagram. The temperatures T_1 to T_4 to form the four main classes of microstructures according to Leyens and Peters [34] are indicated together with the α-transus temperature.

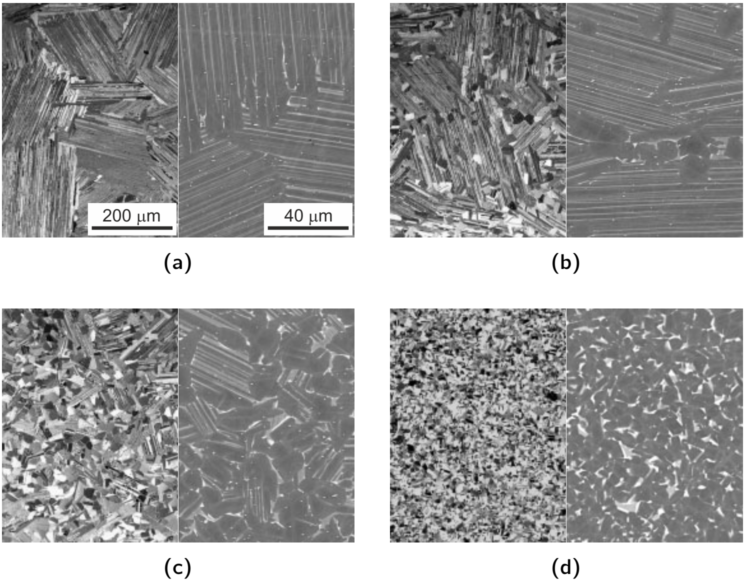

(a) (b) (c) (d)

Figure 2.4: The four general classes of microstructures observed in a TiAl alloy depending on the heat treatment: a) fully lamellar, b) near-lamellar, c) duplex and d) near-γ adapted from Leyens and Peters [34]. The left side shows an optical micrograph, the right side a micrograph from electron microscopy. The scale bars in a) apply for all micrographs.

different alloys are compared in terms of response to heat treatment but also in terms of resulting properties.

2.2.3 Brittleness and deformation mechanisms

Titanium aluminides like most intermetallics suffer from brittleness at low temperatures. The three main reasons for brittle fracture are a high yield strength compared to the cleavage stress, a low number of available slip systems and weak grain boundaries [37]. The first reason can be understood on a phenomenological base as cleavage will rule when brittle failure can occur at lower stress than plastic deformation. As the flow stress typically is reduced with increasing temperature a ductile-to-brittle transition temperature is observed. Rice and Thomson investigated the evolution of the yield point and the fracture strength and correlated the latter to the surface energy γ_s of newly formed surface by an opening crack, the shear modulus G and the Burgers vector B [38]. They found a simple rule that brittle fracture occurs if $G \cdot B/\gamma_s > 10$ and ductile behavior is expected if $G \cdot B/\gamma_s < 7.5$. Consequently, structures with high γ and low B should be preferred. Structures with reduced modulus may help in terms of ductility but typically the high stiffness of intermetallics is considered a main advantage. Based on the Von Mises criterion a material needs five independent slip systems to undergo an arbitrary deformation [38]. γ-TiAl having a tetragonal $L1_0$ structure has only three independent slip systems and thus does not fulfill this criterion [31]. Grain boundary weakening is typically not an intrinsic problem of intermetallics but caused by impurities as S, P, Sn or Sb [37]. These elements weaken the metallic bonds and lead to inter-granular fracture and low ductility. Interestingly B was found to increase grain boundary strength in many intermetallics and is thus an important doping element to retain ductility. The deformation mechanisms in γ-TiAl were investigated as early as 1974 by Shechtman *et al.* [39] in Al-rich alloys. Later on also Al-lean dual phase $\alpha_2 + \gamma$ alloys were considered [40]. Three main elements contribute to the deformation of γ: ordinary $\frac{1}{2}\langle 110]$ dislocations, dissociated $\frac{1}{2}\langle 112]$ and $\langle 011]$ super-dislocations as well as $\frac{1}{6}\langle 11\bar{2}]\{111\}$ twinning. It was observed that mainly the movement of ordinary dislocations and twinning contribute to deformation. In the case of dual phase $\alpha_2 + \gamma$ alloys the deformation at room temperature is mainly confined to the γ-phase while α_2 remains largely defect-free [41]. One of the reasons is that the α_2 preferentially deforms only by $\{1\bar{1}00\}$ prism glide of $\frac{1}{3}\langle 11\bar{2}0\rangle$ super-dislocations [42]. Consequently, the residual stresses are higher in α_2 compared to neighboring γ grains as shown by Seiler *et al.* [43]. This creates internal anisotropy and enhanced mechanical properties in $\alpha_2 + \gamma$ alloys compared to their monolithic single phase counterparts [40]. As a consequence only the γ-TiAl based alloys containing γ and α_2 in a controlled microstructure are considered for application.

2.2.4 Mechanical properties

The microstructure formation mechanisms in titanium aluminides were debated over a long time and inspired a lot of fundamental studies leading to a deeper understanding of the alloy behavior. As discussed before, a multitude of microstructures can be obtained from the very same alloy. But the determining factor for an application of titanium aluminides are the resulting properties. Already 25 years ago in 1991 Kim and Dimiduk [44] published a general comparison of alloys based on intermetallic Ti-Al with Ni-base super alloys (Table 2.2). A distinction is made between Ti_3Al-based and TiAl-based alloys. The latter is what we see as modern titanium aluminide alloys whereas the former ones are not considered as structural intermetallics. However, it is still interesting to compare the properties as modern TiAl-based alloys are typically weaker and have lower elongation to fracture at room temperature but are lighter than the Ti_3Al-based alloys and the Ni-base super alloys. At high temperature also TiAl-base alloys show large elongations up to superplasticity [45]. The properties of modern dual phase TiAl alloys are to some extent depending on the phase fractions of the γ- and α_2-phases. Both phases show an anomalous positive temperature dependence of yield stress leading to superior properties at high temperatures. The super-dislocations present in both phases have an intrinsically low mobility and in the case of γ a Kear-

Table 2.2: Comparison of mechanical properties of titanium aluminides and super alloys according to Kim [28].

Property	**Ti_3Al-base**	**TiAl-base**	**Super alloys**
Structure (main phase)	$D0_{19}$	$L1_0$	$A1$
Density (g/cm^3)	4.1-4.7	3.7-3.9	7.9-8.5
Modulus (GPa)	110-145	160-180	206
Yield strength (MPa)	700-990	350-600	800-1200
Tensile Strength (MPa)	800-1140	440-700	1250-1450
Ductility at 298 K (%)	2-10	1-4	3-25
Ductility (%; K)	10-20; 933	10-600; 1143	20-80; 1143
K_{Ic} ($MPa \cdot m^{1/2}$)	13-30	12-35	30-100

Wilsdorf-like configuration is observed. Consequently, single-crystalline γ and α_2 have their maximum yield stress around 873 K and 1173 K, respectively [46]. Thus the high temperature strength can be improved in general by increased amounts of α_2. In terms of elongation a ductile-to-brittle transition is observed for γ at 1100 K. Above this temperature the material has a ductility comparable to Ni-base alloys, below it the typically low fracture strain of intermetallic materials is observed. Kim and Dimiduk also constructed a schematic relationship between microstructure, grain size and the resulting mechanical properties (Figure 2.5). The implications of this simple figure are tremendous for the application of titanium aluminides. The alloy composition, processing technology, heat treatment and the resulting microstructure are

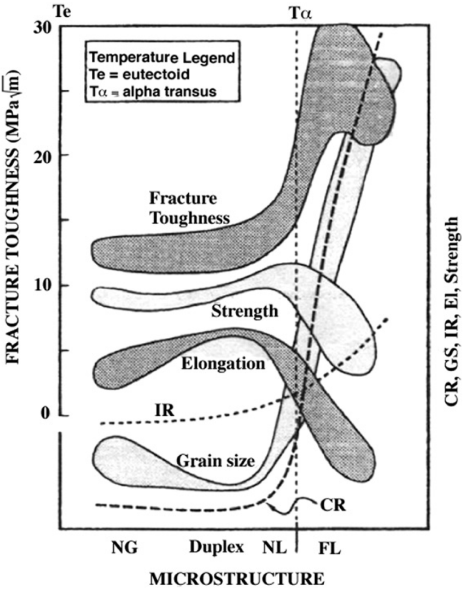

Figure 2.5: The schematic relationships between microstructures of near-gamma (NG), duplex, near-lamellar (NL) and fully lamellar (FL) Ti-Al and grain size (GS) as well as the resulting fracture toughness, tensile strength and elongation (El), impact resistance (IR), and creep resistance (CR) after Kim and Dimiduk [44].

intertwined with the mechanical properties. This makes the understanding of the effects of alloying elements in Ti-Aluminides so difficult. There is always the question how the influence of the alloying element can be separated from the microstructural changes. The duplex microstructure provides highest elongation to fracture at comparably high strength but suffers from poor creep resistance at high temperature and a low impact resistance combined with a low fracture toughness. On the other side of the spectrum lies the fully lamellar microstructure with superior creep resistance and most important a high impact resistance and a fracture toughness exceeding 20 $\mathrm{MPa \cdot m^{1/2}}$ [46]. However, this type has typically lower strength and almost no elongation to fracture. Located in between the two extremes is the near-lamellar microstructure providing typically the highest strength together with balanced properties for creep resistance and fracture toughness. It is known that within each of the microstructural classes the Hall-Petch-relation holds, predicting higher yield stress with decreasing grain size [47, 48]. A finer microstructure is thus generally correlated with higher mechanical strength [46]. The negative correlation of elongation to fracture and fracture toughness is a specialty of titanium aluminides which further complicates their use in critical applications as a more ductile material may be in fact less resistant to fracture. For generations design engineers selected the more ductile material because of its usually higher fracture toughness, but in the case of titanium aluminides a decision needs to be made: What is more important, higher fracture strain or higher fracture toughness? Depending on the application the answer may be different and consequently also the choice of alloy and heat treatment needs to be varied. In most critical applications that are depending on the observation of a crack before catastrophic failure, a high fracture toughness should always be preferred over high strength or ductility due to safety reasons. Consequently, lamellar or near-lamellar microstructures are typically applied although their strength is inferior to other microstructures.

2.3 State-of-the-art higher-order titanium aluminide alloys

The development of titanium aluminides has started decades ago and there have been several waves of research inspired by new findings finally making these materials promising candidates as structural intermetallics in critical high temperature components in aerospace engines. The different types of alloys have been classified into generations according to the time of their development and their general set of properties by Kim [28] already in 1994. The first generation of alloys were ternary Ti-Al-V alloys with occasional C additions. This alloy system is famous for the widely applied Ti-6Al-4V (Ti Grade 5), which is based on the disordered α- and β-phases. Increasing the Al content, intermetallic α_2 and γ are formed and the first alloyed γ-TiAl alloys were produced. The following 2nd and 3rd generation alloys were already higher-order alloy systems with four or more metallic elements. According to Clemens and Kestler [49] the general composition of 2nd generation alloys can be summarized as Ti-(45-48)Al-(1-3)X-(2-5)Y-(<1Z), where X = Cr, Mn, V; Y = Nb, Ta, W, Mo and Z = B, C, Si. The X-elements increase the low temperature ductility while the Y-elements enhance the static and cyclic oxidation resistance as well as high temperature strength and creep resistance [50–53]. The Z-elements are mainly added for grain refinement and thus enhance the castability of the alloys and produce precipitates for increased strength [54, 55]. Interactions between elements of the X, Y and Z group can lead to combined effects as the grain refinement with W and B additions [56, 57]. This approach is applied in the recent IRIS alloy Ti-48Al-2W-0.08B used for sintering of turbine blades with outstanding creep properties [58]. The famous GE alloy GE48-2-2 with a composition of Ti-48Al-2Cr-2Nb is a representative of a 2nd generation alloy due to its additions of Cr and Nb to enhance room temperature ductility and oxidation resistance. This alloy has recently been applied as airfoils in the last two stages of the low pressure turbine in the GEnx turbine for the Boeing 787 and 747-8 aircraft according to Weimer and Kelly [8]. The airfoils are centrifugally cast to avoid porosity [59]. However, it took GE over 20 years from patenting the alloy to the full characterization and approval for application in commercial civil jet

Table 2.3: Selected state-of-the-art titanium aluminide alloys according to Kim [28], Appel *et al.* [31] and Kothari [36].

Alloy name	Nominal composition [at.%]	Company / Institute
GE48-2-2	Ti-48Al-2Cr-2Nb	General Electric
γ-MET	Ti-46.5Al-4(Nb, Cr, Ta, B)	Plansee
47XD	Ti-47Al-2Mn-2Nb-0.8TiB_2	Martin Marietta
γ-TAB	Ti-47Al-4(Nb, Cr, Mn, Si, B)	GKSS Research Center
ABB Alloy	Ti-45Al-2W-0.5Si	ABB
TNB-V5	Ti-45Al-5Nb-0.2C-0.2B	GKSS Research Center
TNM-B1	Ti-43Al-4Nb-1Mo-0.1B	GKSS Research Center

engines [2]. So the GE alloy family remains the only titanium aluminide alloy generation that has been successfully commercialized for critical aerospace components so far. Further development towards increased strength and high-temperature capabilities led to the 3rd generation of titanium aluminide alloys with an increased Nb content up to 10 at.%. These alloys can also be further strengthened by precipitates containing the Z-elements. Especially Si has been found to enhance the creep resistance of the alloys is thus added in some modern alloys [60]. Additionally, Hf, Zr and rare earth elements have been used for alloying. These alloys are typically solidifying by the β-phase to avoid segregation and contain B as grain refiner [61]. Well known members of these advanced alloys are the TNB (TiAl+Nb) alloys, developed in Germany and Austria [4, 5] and the TNM (TiAl+Nb+Mo) alloys, published by Clemens *et al.* [6, 7] in 2008. However, this new generation of alloys has not been exploited in engineering so far, according to Clemens and Mayer [35]. TNM alloys show increased deformability and thus offer the possibility to use conventional hot forming techniques to produce turbine blades. Such blades shall be used in the future for the engines of the A320neo family produced by MTU Aero Engines in Germany [3]. Beside casting and hot forming also powder metallurgical processing can be applied for TNM alloys [62]. However, the alloying elements Nb and Mo are expensive and thus limit the application of this alloys to less cost-critical areas. In order to reduce material cost, Liu *et al.* developed Ti-Al-Fe-Mo alloys where Nb is replaced by the potent and cheap β-stabilizing element Fe [63]. Following the naming tradition researchers meanwhile claim to develop 4th generation alloys as for example Ti-45Al-5Nb-2Cr-1Mo-0.5(B,C)-0.2Si by Szkliniarz and Szkliniarz [64]. Taking a closer look at the alloy composition this is a TNM alloy (TiAl+Nb+Mo) alloyed with Cr, C, and Si. While the intention of the authors is clear, increasing plasticity by Cr, deformability by increased β-content by Mo and increased creep strength by C and Si, their results show poor creep resistance at high temperature. This is an effect of excessive amounts of β-phase stabilized by the combined effects of Nb, Mo and Cr. Such interfering effects of alloying elements make alloy development in titanium aluminides a complicated task that can only be accomplished with deep understanding of the involved phase relations. Kastenhuber *et al.* have recently shown that C and Si alloyed TNM^+ alloys with proper β content can have indeed better properties than their parent TNM variants [65]. A selection of state of the art alloys according to Kim [28] and Appel *et al.* [31] which have gained wider interest among the scientific community are summarized in Table 2.3. Although probably hundreds of alloys have been experimentally produced over the last decades, only a few alloys were considered as promising for further research, patenting and possible applications. It is worth noting that a large part of the research over the last decade was driven by large aero engine manufacturers. Thus a lot of research results may have never been published and experimental alloys may be in use for special applications without the general scientific community knowing about. The fact that structural intermetallics are of general interest by defense industry for light weight high temperature applications may further contribute to extended research behind closed doors.

2.4 Powder-based processing of titanium aluminides

Titanium aluminides have been studied in the past using different processing routes as for example casting, sintering, extrusion, forging and also laser and electron beam based additive manufacturing. Today, casting is the state-of-the-art process to produce turbine blades for aero-engines [2, 8]. But powder-based processes have the potential to eliminate inherent problems of castings like macro-segregation, locally different mechanical properties, expensive homogenization heat treatments and limited part size [66]. In this work spark plasma sintering is applied as a solid state sintering technique and serves as a reference to compare the bulk material to additively manufactured parts. The state-of-the-art for titanium aluminides consolidated applying these two powder-based processing routes is discussed in more detail in the following sections. Additionally, an overview over the current knowledge on the rapid solidification behavior is given.

2.4.1 Spark plasma sintering

Spark plasma sintering (SPS) is increasingly applied for material consolidation since 1994. It offers the possibility to consolidate almost every material to full density and has been used for the production of bulk metallic, intermetallic, ceramic and composite materials [67]. The process involves the sintering of powdered material in a die under simultaneous application of pressure and electrical current. Typically graphite dies are used and pressure is applied uni-axially together with a pulsed current mode. Due to the Joule heating effect the material and the die are heated to a dwell temperature controlled by pyrometers or thermocouples. Characteristics for the SPS process are the high heating rate up to 1000 K/min, the applied pressure and the effects of the current. The heating rate influences mainly grain size while higher pressure increases density. The effect of current is strongly depending on the material and its conductivity, sensitivity to electromigration and the eventual creation of local plasma between powder particles.

Titanium aluminides consolidated by SPS have been studied mainly in the last 15 years. Early works were focused on binary Al-rich Ti-(47-49.8)Al alloys. It was observed that sintering already starts as low as 925 K but maximum density is obtained at 1473 K [68]. The mechanical properties of the material were promising, as a compressive strength of 1963 MPa was observed in Ti-47Al sintered at 1173 K [69]. Xiao *et al.* [70] reported 1990 MPa compressive strength in the same alloy sintered at 1373 K. Compared to casting, the

SPS process typically retains finer microstructures with superior mechanical properties. Calderon *et al.* [71] studied Ti-Al-X, X = Cr, Mn, Fe, alloys produced by mechanical alloying and sintered at 1373 K. Nanocrystalline Ti-48Al-2Cr with a compressive strength of 3500 MPa was obtained. In the same alloy sintered at 1323 K Sun *et al.* [72] reported a bending strength above 1 GPa. In order to replace the expensive atomized elemental Ti and Al powders, Sun *et al.* [73] also studied powder production from cheap sponge Ti and chip Al. The consolidated Ti-46Al-2Cr material achieved a bending strength of 1051 MPa. With progressing alloy development also complex alloy systems were consolidated. The needed powders were typically not produced by mechanical alloying anymore but by atomizing of pre-alloyed material. Ti-46Al-9Nb, a member of the TNB alloy family, was consolidated from pre-alloyed powder at 1548 to 1573 K yielding duplex and coarsened fully lamellar microstructures, respectively [74]. The material was inhomogeneous and retaining the duplex structure was difficult due to a narrow optimum sintering temperature field. A minimum creep rate of $5{\cdot}10^{-8}$ s^{-1} at 973 K and 300 MPa was reported. The microstructural control was improved by the application of higher-order alloys as Ti-44Al-2Nb-2Cr-1B [75]. The material sintered at 1498 K had a yield stress of 710 MPa, a tensile strength of 890 MPa combined with an elongation of 1.91 %. Despite its promising strength and microstructure it had poor creep resistance with a minimum creep rate of $2.37{\cdot}10^{-7}$ s^{-1} at 973 K and 300 MPa due to an increased content of β. A slightly lower creep rate of $1{\cdot}10^{-7}$ s^{-1} was reported for the same alloy with similar microstructure at the same temperature and stress by Couret *et al.* [76]. In the same work spark plasma sintered fully lamellar Ti-47Al-2Cr-2Nb achieved a creep rate $1{\cdot}10^{-8}$ s^{-1}. Lu *et al.* [77] studied Ti-45Al-8.5Nb-0.2W-0.2B-0.1Y, in principle a high-Nb TNB variant alloyed with W and Y, and obtained maximum density above 1273 K and fully lamellar material at 1473 K. Depending on the microstructure an ultimate tensile strength of 1024 MPa and 964 MPa is reported for duplex and lamellar microstructures, respectively. While most studies focused on the achieved density at various consolidation temperatures, the resulting microstructures and properties, the detailed SPS consolidation mechanism was in fact unknown. Jabbar *et al.* [78] studied in detail the densification during SPS of a Ti-47Al-1W-1Re-0.2Si alloy. At 1173 K particle deformation leads to a compaction and full density is achieved at 1448 K where recrystallization starts. In contrary to the name of the process, no indications for the formation of local plasma and overheating were observed. Today more complicated shapes like turbine blade preforms can be produced using SPS [58]. Voisin *et al.* consolidated Ti-48Al-2W-0.08B at 1633 K. The obtained near-lamellar material achieved a yield stress of 496 MPa, an ultimate tensile strength of 646 MPa combined with an extremely low creep rate of $3.7 \cdot 10^{-9}$ s^{-1} at 973 K and 300 MPa. The reference material in this study, Ti-48Al-2Cr-2Nb (GE48-2-2), achieved a creep rate of $1.1 \cdot 10^{-8}$ s^{-1} and $1.4 \cdot 10^{-7}$ s^{-1} at 973 K and 300 MPa in sintered and cast form, respectively. The processing by SPS already improved the creep properties of this alloy making SPS an interesting alternative also for established alloys.

2.4.2 Rapid solidification and cooling behavior

From a materials point of view additive manufacturing is the repeated cyclic fast melting and the following rapid solidification and cooling. Under such conditions the alloy behavior deviates from the equilibrium state and special experimental techniques are required to study it. Two classes of techniques are typically applied to reach such conditions, the nucleation controlled and the growth controlled methods [79]. An example of the former one is atomization where nucleants are separated into singled droplets. Nucleant-free droplets can then experience undercooling and severe non-equilibrium solidification. A similar effect is observed in levitated and undercooled melts in a nucleant-free environment. In the latter class melt spinning and surface melting are considered. Here the nucleation is temporally isolated as the solidification front lags behind the thermal front and a region of undercooled liquid develops. In this zone the phase selection is driven by thermodynamic stability and kinetic factors and may deviate significantly from the equilibrium phase diagram. Knowledge on alloy behavior under these non-equilibrium conditions is thus crucial to understand and predict phase selection and microstructure formation in additively manufactured material.

Titanium aluminides have been studied over the past 30 years using various techniques. Atomized Ti-50Al was studied by Graves *et al.* [80] and Valencia *et al.* [81]. Their studies where motivated by the uncertainties regarding the true nature of the binary Ti-Al phase diagram, but they already observed a strong dependence of the solidification path on the cooling rate and direct $\alpha \rightarrow \alpha_2$ ordering in the absence of nucleation sites. Hall and Huang [82] applied melt spinning to Ti-(46-70)Al and observed the formation of equiaxed α_2 in Ti-46Al while a lamellar microstructure was found in Ti-48Al. Valencia *et al.* [83] used levitation and supercooling to clarify the solidification paths in Ti-(45,50,55)Al. They observed that β is kinetically preferred over α and γ at large undercooling. In order to understand the deviation from equilibrium they constructed phase selection hierarchy maps based on T_0 temperatures estimated from the available phase diagram at that time [14]. Using the same experimental technique, Anderson *et al.* [84, 85] later confirmed the formation of primary β in Ti-(<51)Al at all undercoolings and for Ti-(51-54)Al if the undercooling exceeds 100 K. Wang *et al.* [86] observed increased hardness with increased cooling rate in melt spun Ti-48Al. This effect was attributed to a structural refinement.

Liu *et al.* [87, 88] used laser surface remelting on Ti-53Al and observed a change in solidification path from primary α to primary γ with increasing solidification velocity. Beside the binary Ti-Al also ternary and higher-order alloys have been studied using rapid solidification techniques. Venketaraman *et al.* [89] observed better ductility and hardness in Ti-Al-Cu(-Nb) due to the structural refinement. Nb as a slow diffusing element was found to suppress diffusion-related transformations. The enhanced ductility was attributed to the presence of β_0-phase. Vujic *et al.* [90] used a hammer and anvil solidification technique to quench ternary Ti-(50-60)Al-(1-4)(V, Cr, Fe, Co, Ni, Ge) alloys. The rapid solidification shifted the TiAl phase field from 49-56 to 55-62 at.%. The alloying elements modified the tetragonal unit cell of γ and increased ductility by the activation of twinning. Ti-48Al-5B and Ti-48Al-0.5Er were prepared by Schwartz *et al.* [91] using splat quenching. The focus of the study was the feasibility to obtain small dispersed oxides and borides. While successful in the particle formation, the dispersion was not homogeneous.

McKamey *et al.* [92] used melt spun Ti-48Al-0.5Ni to produce powder for subsequent hot isostatic pressing and obtained a tensile strength of 506 MPa. The low ductility was explained by Fe and Mo contamination. Levitated and undercooled Ti-47Al-2(Fe, Cr, Mn) was studied by Wettlaufer and Laakmann [93]. The different alloying elements lead to similar behavior. Undercoolings up to 285 K could be obtained while β-solidification was observed when 100 to 150 K were exceeded. The measured solidification front velocity reached 9 to 10 $m \cdot s^{-1}$ for all alloys. Singh and Banerjee [94] used arc melting on water-cooled Cu blocks to solidify Ti-(44-50)Al-(2-6)Mo. The slow diffusing Mo strongly segregated to β and locally stabilized the β_0-phase. Shuleshova *et al.* [95] applied levitation and undercooling combined with in situ X-ray diffraction to study solidification in Ti-(45-50)Al-(5-10)Nb. In these alloys primary β prevailed at all undercoolings. At 300 K undercooling a growth velocity of up to 20 $m \cdot s^{-1}$ was measured. Later the same group studied a larger set of alloys in the Ti-Al-Nb system to clarify the solidification path [96]. Liu *et al.* [97, 98] studied the influence of Y additions in melt spun Ti-46Al-2Cr-2Nb-(0-2)Y. It was found that the rapid solidification increased the solubility of Y and its addition refined the microstructure and promoted the formation of massively transformed γ. While α_2 is the main phase up to 1 at.% Y, β_0 becomes the major phase above 1.5 at.% Y.

Compared to the rather limited set of studies where the material is rapidly solidified, studies involving rapid cooling in the solid state are reported frequently. Due to the high reactivity, experiments involving the liquid phase require sophisticated setups while annealing and water quenching can be done using standard laboratory equipment. For binary Ti-Al most studies involve annealing in the single phase α phase field and quenching to room temperature. Wang and Vasudevan [99] observed a high α_2 content in Ti-43Al. Massive γ_m was observed above 46.54 at.% Al. They found that the massive reaction $\alpha \rightarrow \gamma_m$ is stopped, as soon as the $\alpha \rightarrow \alpha_2$ ordering takes place. Jones and Kaufman [100] determined schematic continuous cooling diagrams based on quenching experiments in Ti-(40-50)Al. They confirmed the dominance of direct ordering of α in Al-lean Ti-Al alloys. Yamabe *et al.* [101] experimentally measured the T_0 temperatures for the $\alpha \rightarrow \alpha_2$ transformation in Ti-(40-45)Al.

They observed a decrease of T_0 with increasing Al content. For Ti-45Al they measured T_0 between 1303 and 1333 K. The α-phase is also able to form twins upon quenching, as observed by Wang *et al.* [102]. If lamellar colonies are formed, they have then distinct orientation relationships to the parent α along the twin directions [103]. Veeraraghavan and Vasudevan [104] focused on the formation temperature of massive γ_m in Ti-47.5Al by a combination of resistivity and temperature measurements. With increased cooling rate the start temperature of the transformation was decreased. At 18.3 $K \cdot s^{-1}$ the start temperature for γ_m was 1313 K, the finish temperature was 1133 K. The observed finish temperature lies more than 450 K lower than the equilibrium formation temperature for γ (compare Figure 2.3). Applying a thermodynamic description for the formation of γ_m, the same group found that the growth is governed by interfacial rather than by volume diffusion [105]. With this knowledge the nucleation was studied in more detail. It was revealed that γ_m nucleates on the grain faces rather than edges or corners of one grain and grows into the opposite grain with an incoherent interface [103]. This was later confirmed in Ti-46.8Al-1.7Cr-1.8Nb by Dey *et al.* [106]. The γ_m nucleates from the parent α according to the Blackburn orientation relationship. Subsequently growth takes place into the adjacent grain by the formation of twin-related γ-variants. Nuclei which are misoriented remain dormant and do not grow [107]. Beside the formation mechanism of γ_m also other alloying effects were studied. Xia *et al.* [108] observed that higher Al content increases the amount of γ_m in quenched Ti-48Al-2Cr compared to Ti-46Al-2Cr-2Nb. The massive transformation only occurs at high cooling rate, but the amount of γ_m is reduced again for very high cooling rates as the $\alpha \rightarrow \alpha_2$ reaction prevails. Prasad *et al.* [109] observed the same effect in quenched Ti-45Al-2Nb-0.4Mn and Ti-45Al-2Nb-2Mn. Alloying with Mn increased the critical temperature as well as the amount of γ_m in the microstructure. By comparing Ti-45Al and Ti-45Al-2Nb-(0-2)Mn it was concluded that the addition of Nb reduces the amount of γ_m at high cooling rates [110]. The influence of impurity O was studied by Huang *et al.* [111] in Ti-46Al-8Nb with 500 and 1500 ppm O. The massive transformation was suppressed by the presence of 1500 ppm O, a strong α stabilizing element.

Furthermore, the segregation of O to grain boundaries retained some α at the grain boundaries. The modeling of the formation of γ_m was recently performed by Singer *et al.* [112] using phase-field models and by Gamsjäger *et al.* [113] combining density-functional theory, thermodynamic and kinetic models.

Beside the formation of γ_m which was studied extensively also the influence of alloying elements on other microstructural features was investigated. Yang *et al.* [114] obtained a larger degree of microstructural refinement with increasing cooling rate in Ti-46Al-2Cr-2Nb. That this refinement leads to enhanced mechanical properties was shown by Seo *et al.* [115] in Ti-(45,47)Al-2Nb-2Mn-0.8 vol.% TiB_2. The addition of B in this alloy was found to increase microstructural stability at 1073 to 1173 K. B was later found to increase the critical cooling rate to obtain a certain microstructural feature in general and to promote the formation of lamellar structures by Jiang *et al.* [54]. The influence of Nb and Mo on the stability of β_0 was studied by Stark *et al.* [116] for Ti-45Al-10Nb and Ti-45Al-7.5Nb-1Mo-0.1B. In the ternary alloy β_0 transforms to a metastable ω"-phase by a simple reaction involving rearrangement only over short distances. In the Mo containing alloy this transformation was not observed and it was concluded that even small amounts of Mo stabilize β_0 against transformation.

It can be summarized that the knowledge on rapid solidification is mainly concentrated on the binary Ti-Al system or selected higher-order alloys. On the other hand a vast body of knowledge is available on the alloy behavior and influence of alloying elements on the behavior in solid state quenched binary and higher-order alloys. Only limited knowledge exists about the rapid solidification processing behavior of titanium aluminides. For decades all the development effort was put into enhanced castability and deformability of titanium aluminides, leaving the rapid solidification behavior of titanium aluminides an essentially open field. While solid state transformations occurring under water quenching conditions from the high temperature phases are well understood and today also can be modeled using thermodynamic data, rapid solidification and subsequent cooling was only reported scarcely. Furthermore, the applied experimental techniques as melt spinning and splat quenching lead to cooling rates up to 10^6 K·s^{-1}, which is about two orders of magnitude higher than reported for titanium alloys in beam-based additive manufacturing by Ahsan *et al.* [117].

2.4.3 Additive manufacturing of titanium aluminides

Beam-based additive manufacturing (AM) of metallic powders by local melting to produce complex 3D objects can be divided into two main groups, powder-bed and blown-powder based methods. Examples of these approaches are Selective Laser Melting (SLM) and Direct Metal Deposition (DMD), respectively. The main features of the SLM process are the deposition of a thin powder layer from a feedstock over the complete build platform, selectively melting the powder by a scanned laser beam in a defined manner and deposition of the next layer. Finally, the produced part needs to be freed of the non-molten powder and be separated from its build plate. Figure 2.6 schematically shows the SLM process. Detailed solutions as the powder coating device and feedstock positions vary depending on the machine

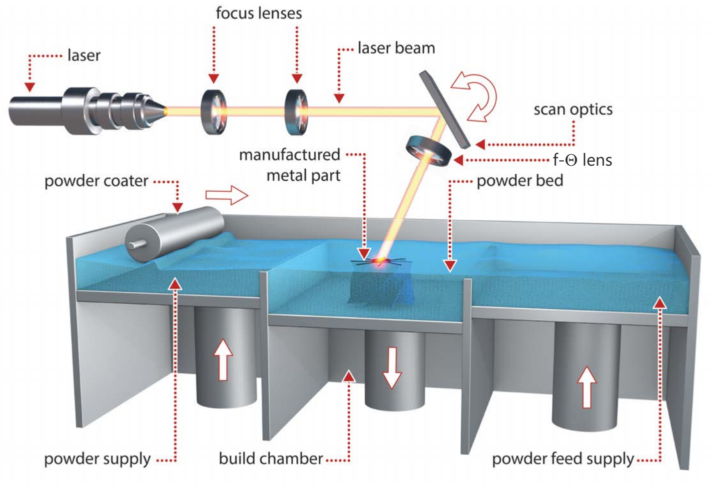
focus lenses
laser
laser beam
scan optics
f-Θ lens
manufactured metal part
powder coater
powder bed
powder supply
build chamber
powder feed supply

Figure 2.6: Schematic depiction of the SLM process adapted from Empa [118].

manufacturer. The DMD process essentially consists of a deposition head including the laser beam in the center and co-axially arranged nozzles for the powder supply (Figure 2.7). Purging, carrier and shielding gas is used to avoid clogging of the laser guide, to transport the powder and to provide an inert environment, respectively. Attaching this build head to a multiple axis robot stage allows then to move along the trajectories defined by the desired part geometry. The continuous deposition of material along the defined path finally forms the 3D object. After processing the part needs cleaning of attached powder particles and eventually separation from its base structure. DMD can be applied to curved substrates or pre-existing structures with a complex shape while deposition in SLM is possible only on a substrate parallel to the powder-bed surface

In the past several attempts have been reported for additive manufacturing of titanium aluminides that are summarized in this chapter. Additive manu-

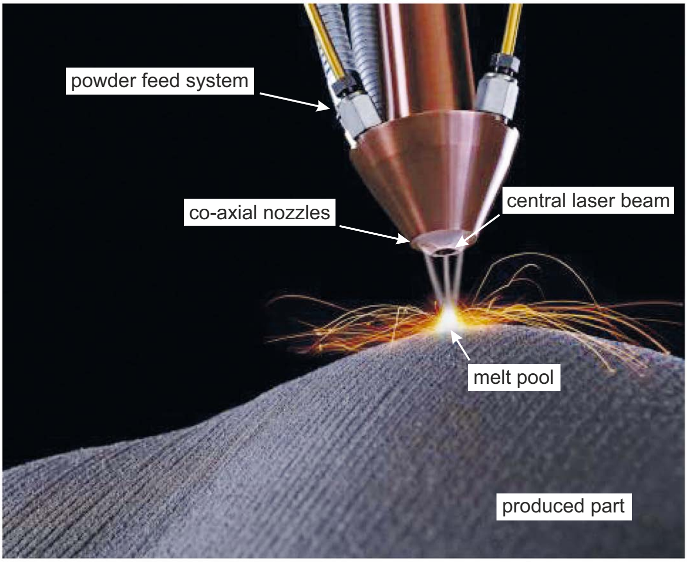

Figure 2.7: DMD processing of a complex shaped object adapted from Empa [118].

facturing of titanium aluminide alloys is still at its infancy for several reasons. First, the titanium aluminides are inherently brittle at low temperature due to the intermetallic structure which ensures the promising properties at elevated temperatures. But at lower temperatures the ductility of these materials is strongly reduced rendering them susceptible for severe cracking during processing due to thermal stresses. Second, many alloys tend to exhibit strong segregation already in cast form, an effect which will be probably further increased with higher cooling rates. In AM this phenomenon is the cause of hot-cracking, when the remaining liquid phase cannot sustain the thermal stresses imposed on the solidifying material. Furthermore, titanium aluminides undergo several solid state phase transformations upon solidification and cooling. These transformations may be altered or completely suppressed at the typical cooling rates of laser based additive manufacturing techniques and metastable phase relations may be developed (see Section 2.4.2). In 1991 to 1992 Abboud and West [119, 120] studied surface alloyed layers with compositions of Ti-(17-36)Al and Ti-43Al up to Ti-80Al. Due to uncertainties regarding the true nature of the binary Ti-Al phase diagram at this time, their study contributed mainly to the understanding of the phase relations. The comparison of the hardness of the laser alloyed material with cast and quenched material showed drastic differences in the properties which today can be attributed to the non-equilibrium conditions. With the availability of various AM technologies, they have been applied also for TiAl alloys. Nowadays usually excessive preheating is applied to achieve crack-free TiAl components. The earliest method applied for TiAl material was blown powder-based DMD promising potential applications for blade tips to replace conventional welding [121]. Srivastava *et al.* [122] deposited Ti-48Al-2Mn-2Nb and observed a fine lamellar structure. The observed γ had different composition, depending on its formation path directly from the melt or upon decomposition of the parent α. It was clearly shown that the obtained microstructure depends on the processing parameters and the following heat treatment [123]. Moll and McTiernan [66] used the similar alloy Ti-47Al-2Cr-2Nb and obtained fully lamellar microstructures with comparable properties to cast material. Zhang *et al.* [124] applied the methodology to

Ti-48Al-2Nb-0.4Ta and Ti-48Al-2Cr-2Nb and obtained microstructures rich in α_2. After heat treatment at 1173 K fine lamellar structures are observed. Liu and DuPont [125] reported preheating temperatures of 723 to 737 K to obtain crack-free deposits using laser metal deposition of Ti-48Al-2Cr-2Nb. It was clearly shown that although higher energy inputs during processing reduce the cracking frequency, this effect is limited and external preheating was needed. Beside DMD also powder-bed based methods, namely SLM and selective electron beam melting (EBM), have been applied. Inherently, EBM is applied more frequently, as processing is normally performed under vacuum and preheating-capabilities are state-of-the-art for EBM machines. Preheating in SLM conducted in an inert gas atmosphere with typically finer powder is inherently more difficult. Vilaro *et al.* [126] have reported successful processing trials of Ti-47Al-2Cr-2Nb using selective laser melting and laser metal deposition using preheated substrates to slow down cooling speed and enhance the ductility of the alloys. The exact preheating temperature was not specified. In 2010, Murr *et al.* [127] used Ti-47Al-2Cr-2Nb for EBM and obtained a fine duplex structure. Franzen *et al.* [128] reported crack-free deposits of Ti-48Al-2Cr-2Nb with a preheating temperature of 1323 K. Biamino *et al.* [129] used the same alloy and obtained a duplex structure after heat treatment. Schwerdtfeger and Körner [130] recently reported preheating temperatures of 1203 K to 1223 K for the same alloy . It was observed that higher cooling rates increase the amount of α_2. Biamino *et al.* [131] reported the successful consolidation of Ti-48Al-2Nb-0.7Cr-0.3Si and the formation of fully lamellar microstructures after heat treatment. The same research group also used TNMB1 for processing trials in collaboration with GEAvio and AvioAero for the production of TiAl turbine blades [132]. Tang *et al.* [133] used an Al-lean Ti-45Al-7Nb-0.3W alloy at high energy inputs to avoid cracking. Beside the work of Vilaro *et al.* [126] on SLM processed Ti-47Al-2Cr-2Nb only a few studies have been published. Recently Löber *et al.* [134] processed the TNM-B1 alloy (Ti-44Al-4Nb-1Mo-0.1B) by SLM. The processing temperature remains unmentioned. A study of SLM of Ti-44.8Al-6Nb-1Mo-0.1B (TNM family) at elevated temperatures up to 1273 K was published by Gussone *et al.* [135]. Due to the high preheating temperature and energy input by the laser beam excessive Al-losses up to 8 at.% are reported which alter the alloy behavior, microstructure and finally also the mechanical properties. Beside the powder-based AM techniques also wire-based methods have been developed. As sourcing of TiAl alloys is inherently challenging as bulk or powder, producing TiAl wires is prohibitively expensive and difficult. Consequently, Ma *et al.* [136] used *in situ* alloying of pure Ti and Al feed wires in gas tungsten arc welding. Depending on the mixing ratio and final composition, different microstructures are obtained. This method is interesting for larger structures and due to the use of relatively cheap and easily available starting materials.

From the summarized work it is evident that the 2nd generation alloys, such as the Ti-48Al-2Cr-2Nb (GE 48-2-2), are mainly applied for processing trials by DMD and EBM. Only recently the 3rd generation TNM alloys are applied for SLM and EBM. Published results so far are mainly focused on processing parameters and obtained microstructures. But the influence of alloy composition and alloying elements on the rapid solidification behavior and on additive manufacturing processability is still an open field. Interestingly, the texture of the produced components was not evaluated in any of the cited studies. The inherent anisotropy of the intermetallic phases and their distinct crystallographic alignment make it a necessity to know the texture in the as processed state (see Section 2.2.1). After initial deposition and solidification, the material is later partially remelted upon deposition of subsequent layers. The newly solidifying material grows from an already textured seed layer from the previous layer. Additionally, the already deposited material is subjected to fast annealing cycles upon heat extraction from the solidifying top layer. It remains an open question at this point what texture is formed after additive manufacturing and how the alloy composition influences it.

2.5 Reinforced titanium aluminides

Although GE48-2-2 (Table 2.3) is the best known representative of the titanium aluminide alloys which was successfully applied based on its set of properties, attempts have been made to further enhance the mechanical properties and oxidation resistance. While for the 3rd generation of titanium aluminides mainly high alloying levels are employed which typically enhance density, the production of composite material offers the possibility to combine low-density high-strength ceramic material with the intermetallic alloys to produce intermetallic-matrix-composites (IMC) with superior properties at high temperatures. In the past IMCs based on TiAl have been developed using fibers and particles which are shortly summarized in the following sections.

2.5.1 Intermetallic-Matrix-Composites based on TiAl alloys

Composite materials based on a TiAl matrix have been considered since the development of the first TiAl alloys for high temperature applications. In order to enhance the strength at high temperature, mainly fiber-reinforced composites have been studied, as reviewed by Froes *et al.* [137]. The factors determining the suitability of a strengthening phase are the similarity of the coefficient of thermal expansion (CTE) to reduce stresses, chemical compatibility, a low density, a high modulus of elasticity to ensure load transfer, high strength at high temperature and good oxidation resistance. The incorporation of fibers also increases toughness by crack deflection, fiber pull-out and interface separation retarding crack growth. Regarding the CTE, the oxides Al_2O_3, Y_2O_3 and ZrO_2 are similar to the TiAl matrix while SiC and Si_3N_4 have significantly smaller CTEs [138]. Interestingly, Ti_3Al + Nb/SiC and TiAl/SiC are the most studied TiAl-based systems [139]. This can be explained by the availability of fiber material and the superior strength of SiC fibers. Chemical compatibility with the matrix is essentially stability against the aggressive TiAl melt. Only a handful of materials is more stable than the reaction products of Ti and Al with O and N. Minimal reactivity is observed for rare earth oxides of group III of the periodic system of elements and Al with the M_2O_3 stoichiometry [140]. Additionally, TiB_2, CaO and Ti_5Si_3 are sufficiently stable. However, there is no material that is fully stable against a TiAl melt in terms of zero dissolution and contamination of the material. Thermodynamic studies on ZrO_2 in contact to TiAl show partial dissolution of the oxide [141]. However, the solubility limits for TiO_2 and Al_2O_3 are not exceeded. Consequently, the matrix is doped with the constituents of the strengthening phase. An effect to be considered in interpretation of data from reinforced TiAl alloys.

2.5.2 Dispersion strengthened titanium aluminides

Compared to continuous fibers, strengthening by particles has several advantages. First and most important, particles are typically much cheaper than long fibers. Second, the chemical and mechanical compatibility is less important as the occurring thermal stresses are randomly distributed and the volume fraction of dispersoids is typically below 10 vol.% [140]. Additions of oxide particles to intermetallics has been proposed early on for the FeAl, NiAl and TiAl systems [142]. The ODS NiAl and FeAl systems have been studied in detail using Y_2O_3 as dispersed phase [143, 144]. ODS TiAl has advantages over ODS NiAl in terms of compatibility with the strengthening particles and a higher melting point of the matrix [140]. But TiAl alloys are very sensitive to contamination in production and consequently, are considered as too difficult and are thus not produced.

For titanium aluminides, the best established dispersed strengthening phases are titanium carbides and borides which either form *in situ* or are added as particles to the melt [145, 146]. Gerling *et al.* [45] reported a significant increase in strength of the alloys up to 1073 K by such boride additions. The abundantly used carbides present in the TNB and TNM^+ alloy families have very similar effects but recent studies by Wang *et al.* [147] show limited stability at high temperatures exceeding 1073 K. Other approaches also use alloying with Fe to stabilize additional phases as strengthening dispersoids [148] or the addition of ductile Nb particles to enhance toughness [149]. Also TiC has been used to produce Ti-48Al-2Cr-2Nb/TiC composites using DMD [125]. While carbides and borides are well established, little information is available about oxide dispersion strengthened titanium aluminides. Early attempts using B and Er additions were published in 1991 by Schwartz *et al.* [91]. They reported the existence of Er containing oxides with diameters below 50 nm. Suryanarayana and Froes [150] later reviewed the addition of Er and Gd to a $\alpha_2+\beta$ Ti-25Al-10Nb-3V-1Mo alloy to form the corresponding oxides as fine particles. A uniform particle dispersion could not be obtained. However, the reported results indicate enhanced hardness without excessive embrittlement of the alloys. Later studies by Trivedi *et al.* [151] used Y additions in GE48-2-2 to form an ODS material by mechanical alloying and hipping. The fine oxide particles that formed with a uniform dispersion during processing were identified as $Al_2Y_4O_9$. In the studied alloy the particles restricted grain growth up to 1423 K. These results indicate superior properties of ODS titanium aluminides compared to their non-strengthened parent alloy regarding low and high temperature strength without losses in fracture toughness and ductility. Recently, the fabrication of *in situ* $TiAl/Al_2O_3$ composites was reported [152, 153]. The resulting strengthening effects could be attributed to the presence of the oxide particles and the reduced grain size. It is evident that although it is known that ODS TiAl has the potential to provide superior properties compared to established ODS intermetallics, only a few studies have been published.

2.6 Aim of the thesis

The literature review presented in the previous sections clearly shows the existence of several research gaps that need to be addressed for the development of ODS titanium aluminides for additive manufacturing. These gaps are defined and shortly discussed in the following sections.

- **Rapid solidification behavior of Ti-Al between 10^2 and 10^4 $K{\cdot}s^{-1}$** A novel experimental technique with adjustable cooling rate in the typical range between 10^2 and 10^4 $K{\cdot}s^{-1}$ observed for beam-based additive manufacturing needs to be developed. The technique needs to be independent from the availability of material from commercial suppliers and be suitable for testing of highly reactive material. Assisting simulations based on computational thermodynamics to evaluate the alloy behavior under non-equilibrium conditions can save experimental effort and allow to predict alloy behavior. The comparison of computational and experimental results yields then the accuracy and predictability of the simulation model.

- **Influence of alloying elements on rapid solidification behavior** The effects of alloying elements on the rapid solidification behavior in the important range of cooling rates for additive manufacturing are a crucial point. An experimental base is needed to understand alloy behavior and to allow the development and selection of TiAl alloys for additive manufacturing. Being the most important alloying elements in modern TiAl alloys, the influence of Nb and Mo on microstructure formation and phase stability is not sufficiently well known at the moment. Applying the novel framework consisting of an experimental rapid solidification technique and adapted computational thermodynamics the influence of Nb and Mo is studied.

- **Alloy selection for additive manufacturing** While a vast body of knowledge has been generated on the castability of titanium aluminides and the findings have been applied in alloys of the latest generations (TNB and TNM families), alloy development towards a higher processability using additive manufacturing is an open field. Based on the findings in binary and ternary TiAl alloys, this research gap will be addressed and the influence of alloy composition on the processed material will be discussed.

- **ODS titanium aluminides produced using powder-based processing** The combination of ODS TiAl alloy powder production and laser-based processing to produce ODS titanium aluminides is a novel approach to obtain such material. The combination of premixed powder to form a complex 3D object out of ODS material using additive manufacturing offers great potential for the application of new ODS materials. This approach has not been reported for ODS TiAl. The suitability of TiAl alloys for this processing route will be studied and the influence of the consolidation technique on the resulting oxide dispersion will be addressed.

- **Microstructure and texture of laser-processed titanium aluminides** A solidification sequence leading to a textured solid body will typically develop an intermetallic structure which is also anisotropic. Finally, the properties of a part, built by additive manufacturing, will depend on the texture developing during solidification and solid state phase transformations. Both are typically depending on the alloy composition. In this work, processing trials on different TiAl alloys will be compared in terms of microstructure, texture evolution and elemental distribution to study the influence of alloy choice and its implications for the incorporation of oxide particles to produce ODS titanium aluminides.

- **Performance of ODS titanium aluminides at elevated temperature** The ODS titanium aluminides are foreseen to extend the range of operating temperatures of titanium based alloys towards higher temperatures. To demonstrate a beneficial effect, ODS TiAl needs to maintain a high flow stress and tensile strength up to high temperature ideally combined with superior creep properties. It is expected that oxide dispersoids influence both properties. Due to the absence of ODS titanium aluminides so far, data regarding the long term stability against air and the mechanical properties at high temperatures are not available and will be part of this work.

- **Complex structures from ODS TiAl by selective laser melting** Finally, the possibilities to produce complex shaped lattice structures from ODS TiAl by SLM will be exploited as an outlook for future studies. In a first step a parameter screening will be applied to identify a potential processing window. Layer and bulk deposition will be applied to study the integrity of the consolidated material. As TiAl alloys typically suffer from cracking due to residual stresses upon cooling, the effects of re-scanning of individual layers on the material integrity will be studied. The application of such a strategy has not been reported for SLM of TiAl and will be assessed in this work.

3 Experimental and analytical methods

In this chapter the standard experimental and analytical methods applied in this work are presented. Novel methods developed within this work are presented in the individual chapters dedicated to the results of this work. Here, first the materials and consolidation methods are discussed, followed by materials characterization and testing. At the end of the chapter the applied computational thermodynamic method is briefly explained.

3.1 Materials and consolidation methods

3.1.1 Materials

In this work two sources of material are used, pure elements in bulk form and titanium aluminide alloy powders. The pure elements (Al 99.999 %, Ti 99.98 %, Nb 99.95 % and Mo 99.95 %) are supplied by Alfa Aesar, USA, as slugs or wires and are used for the production of experimental alloys by arc melting. The titanium aluminide alloy powders are produced and supplied by

Table 3.1: Titanium aluminide alloy batches studied in this work.

Batch No.	Nominal composition [at.% / mol.%]	Particle size [µm]	Lot No.
P-1	Ti-45Al-3Nb	45-106	OX-LMD-3A01-01
P-2	Ti-48Al-2Cr-2Nb	45-106	-
P-3	Ti-45Al-3Nb-<0.2Y_2O_3	10-45	OX -SLM-3A03-01
P-4	Ti-50Al	46-106	g-TiAl OX-LMD-3B01
P-5	Ti-45Al-3Nb-<0.2Y_2O_3	10-45	OX-SLM-3C01-01
P-6	Ti-45Al-3Nb-<0.2Y_2O_3	46-106	OX-SLM-3C01-01
P-7	Ti-45Al-3Nb	15-45	OX-SLM-3B01-01
P-8	Ti-45Al-3Nb-<0.2Y_2O_3	10-45	OX-SLM-3C01-01

MBN Nanomaterialia, Italy, in the frame of the OXIGEN project according to the specifications derived from this work. High-energy ball milling is applied to produce the intermetallic alloy from the elemental Al, Ti and Nb stock powders. In the case of ODS variants, yttria is added as a nanopowder directly in the milling process. Heat treatments in between milling steps or at the end of the process ensure the formation of the intermetallic compounds and homogenize the elemental distribution. Detailed processing parameters as milling time, energy and processing atmosphere are proprietary knowledge of MBN Nanomaterialia. The powder batches delivered in the course of OXIGEN are shown in Table 3.1. They are numbered chronologically as received over the course of the project. The batch P-1 was a first trial of MBN to produce an alloyed titanium aluminide. Analysis revealed a strong deviation from the nominal composition and high O content. Thus this batch was only used for first SPS trials but later abandoned. Batch P-2, gas-atomized GE48-2-2, was sourced from LPW Technology Ltd., UK, to study the influence of alloy composition on processability and microstructure formation in laser metal deposition. A small amount (2 g) was delivered to Empa for phase analysis. The first batch close to the specified nominal composition and containing the ODS particles, P-3, was used for phase analysis, SLM trials and SPS consolidation. Batch P-4 was an attempt at producing pre-alloyed Ti-50Al as a precursor for further alloying by high-energy ball milling and heat treatments at MBN. An amount of 25 g was delivered to Empa for phase analysis. The batches P-5 and P-6 were produced for processing trials and were delivered to TWI, UK, for DMD processing trials. Processed specimens were then delivered to Empa for analysis together with small powder samples (2 g each). The final batches P-7 and P-8 were specifically produced for Empa from the same parent batch. After milling to obtain the specified alloy, the nonODS powder batch P-7 was retrieved. The remaining powder was then milled with the yttria nanopowder to obtain the ODS variant. This powder was then sieved into two fractions, the finer one for Empa and SPS testing (P-8), the coarser fraction was delivered to TWI, UK, for DMD processing trials. These batches P-7 and P-8 were then used for mechanical testing of SPS material to study the influence of the ODS addition on mechanical properties.

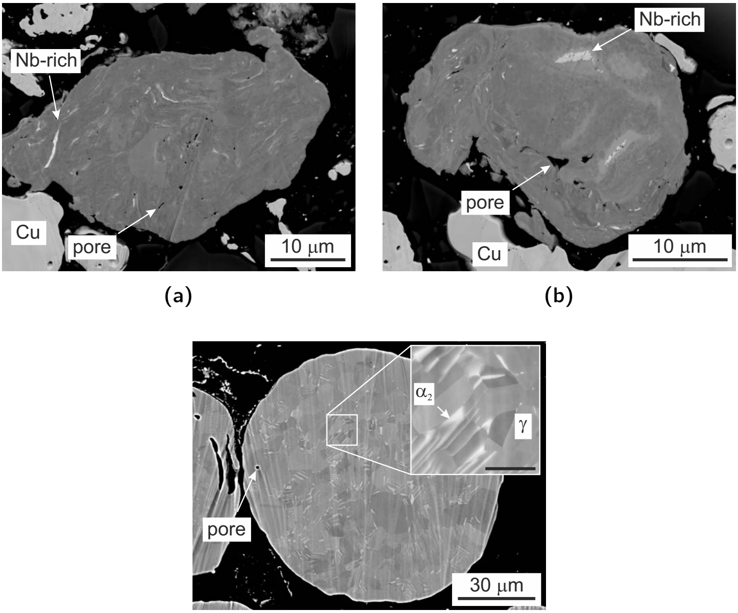

(a)

(b)

(c)

Figure 3.1: BSE SEM micrographs of a) Ti-45Al-3Nb (P-7), b) Ti-45Al-3Nb-<0.2Y_2O_3 (P-8) and c) GE48-2-2 (P-2) (inset: Scale bar is 5 µm). The bright Cu particles in a) and b) are part of the used embedding material.

The HEBM milled powders have a globular but irregular shape and a fine structure of typically sub-micrometer thin Nb-rich flakes is visible (Fig. 3.1a and 3.1b). Internal porosity is also observed. In order to reduce production costs, the producer tries to reduce milling time. While for conventional powder metallurgy, for example extrusion, a very homogeneous mixture of the elemental constituents is needed, AM leads to a local homogenization in the liquid state. Thus a certain degree of inhomogeneity or residual elemental material can be tolerated. For comparative DMD processing trials, a gas-atomized Ti-48Al-2Cr-2Nb (GE48-2-2) powder with a particle size of 46-106 µm was sourced from LPW Technology, UK. This powder is spherical with little internal porosity and has a fine microstructure consisting of equiaxed γ and $\alpha_2 + \gamma$ lamellae (Fig. 3.1c). The microstructure indicates post-atomization heat treatment. In the atomized state a dendritic microstructure with segregation of Al would be expected based on the previous results.

3.1.2 Arc melting

The master alloys for further analysis and additional experiments were produced by non-consumable tungsten electrode arc melting in water cooled Cu crucibles in 500 mbar Ar 6.0 atmosphere, purified by an OXISORB cartridge (Messer, Switzerland). The pure elements were weighted according to their content in a desired alloy composition on a precision balance (ALJ 120-4, Kern & Sohn, Germany, ± 0.1 mg). Every alloy was re-melted eight times combined with specimen flipping to ensure good sample homogeneity. After arc melting the weight of the produced alloy was determined again to calculate the weight loss. All alloys used for further studies had losses below 0.3% with typical losses below 0.1%. This ensures that the produced alloys are very close to their nominal composition. Alloys with losses exceeding 0.3% or showing chemical inhomogeneity in the form of un-melted material after fracturing the produced button were discarded. Alloy buttons with sufficiently small losses were crushed in a WC mortar (Durit, Germany) to yield smaller parts for further melting experiments and analysis without introducing contamination from metallic tools.

3.1.3 Spark plasma sintering

Solid state sintering was performed by SPS on a HP D 10 commercial setup (FCT Systeme GmbH, Germany) in cylindrical graphite dies lined with graphite sheets. For consolidation trials and the production of oxidation test specimens dies with an inner diameter of 20 mm were used. For the production of tensile test specimens from SPS material, a die with an inner diameter of 50 mm was applied to maximize specimen number and length. Sintering was performed at a pressure of 50 MPa under vacuum in pulsed current mode with 12 pulses of 3 ms followed by a waiting time of 6 ms with zero current. The heating rate was 100 K/min up to the maximum temperature of 1598 K with a 2 min holding stage before cooling. The heating parameters were adapted from Molénat *et al.* [75]. After cool down the sintered specimen was removed from the die and the reaction zone between the graphite sheets and the alloy was removed by grinding to yield a contamination-free bulk alloy for further specimen production and analysis.

3.1.4 Selective laser melting and laser metal deposition

SLM trials were performed at Inspire AG, Switzerland, on a Concept M2 (Concept Laser GmbH, Germany) equipped with a Nd:YAG laser (1064 nm) operated in continuous mode with a maximum power output of 200 W and a spot size of ∼100 µm. The powder layer thickness was 50 µm in accordance with the maximum powder particle diameter of 45 µm of the used batch P-3. Base plates were machined from ASTM Grade 2 Ti material and ground co-planar to ensure a homogeneous powder thickness. In order to reduce the amount of powder needed for processing, build plate reductions were used to restrict the build space to 150 x 130 mm^2. The parameters scanning speed, laser power and hatch distance were varied in screening experiments to determine processing windows and parameter influence on microstructure and part integrity (see Chapter 7). Ar 4.8 was used as processing gas and the oxygen content was controlled to be below 0.1% throughout the process. After running the test program the excess powder was removed from the build and feeder platforms and sieved to remove coarse debris particles. DMD was performed by the project partner TWI, UK, on a Trumpf DMD system (Trumpf Laser GmbH, Germany) equipped with a CO_2 laser and a coaxial powder delivery head. Ar was used as transport and shielding gas during processing. The processing parameters scanning speed, laser powder, hatch distance and processing atmosphere were varied during trials. Base plates were machined from Ti Grade 2 material. Preheating was achieved by induction heating of the base plate to the desired temperature. After processing the parts were freed of excess powder, marked and selected ones shipped to Empa for further analysis together with the used parameter sets.

3.2 Materials characterization

3.2.1 Metallography and microscopy

It is a well known phenomenon, that different titanium aluminides need different polishing procedures to produce artifact-free surfaces for examination. In the past various recipes have been proposed that claim to produce the best finish [154]. In this work a general recipe was used based on little grinding, diamond suspension polishing and a chemo-mechanical final polishing step. For the microstructural analysis the specimens were embedded into cold-setting epoxy resin (EpoxyCure2, Buehler, Germany) and ground with P240 SiC grinding paper. After flattening, they were polished using diamond suspensions from 9 over 3 to 1 µm (MetaDi, Buehler). The 6 µm diamond polishing led typically to a worse result and was omitted. The final polished specimens were prepared using a 20 nm silica solution (MasterMet 2, Buehler) with H_2O_2 addition. The last step was repeated until optical microscopy under polarized light showed no more deformation marks or blurred grain boundaries. In order to achieve this state, final polishing times between 15 and 60 min were needed. To remove the remaining surface deformation layer present after the final polishing step, Ar ion beam polishing was applied on selected specimens using a Hitachi IM4000 ion beam polisher at 4 kV acceleration voltage and an incident beam angle of 80° to the surface normal direction. It has to be noted that excessive Ar milling can lead to pore-like artifacts in titanium aluminides. Especially, metastable supersaturated solutions of α_2 are prone to formation of a speckle pattern probably originating from Ar incorporation or local alloy decomposition by ion irradiation.

After surface preparation, the specimens were investigated using an Axiobserver microscope (Zeiss, Germany) under polarized light and by SEM using a Hitachi S3700N (Hitachi, Japan) equipped with secondary electron (SE), back-scattered electron (BSE) and energy-dispersive X-ray spectroscopy (EDX) detectors (EDAX, USA) for general imaging and a Hitachi S4800 and a FEI XL30 ESEM (FEI, USA) for high resolution imaging and particle measurements in SLM and DMD processed specimens.

Solid state SPS sintered material was analyzed using transmission electron microscopy (TEM) and scanning transmission electron microscopy (STEM) on an aberration-corrected JEOL 2100FCs S/TEM operating at 200 kV (K. Dawson, University of Liverpool). The electron-transparent lamellae were prepared using a FEI Helios 600i dual beam focused ion beam (FIB) instrument. Specimens were prepared by lift out method and low energy (2kV) polishing was applied as a final step. The size of the lamellar colonies and γ-TiAl grains in SPS sintered and heat treated material was determined using the line intersection method on 2560x1920 pixel BSE SEM micrographs recorded at 2000x magnification along a rectangular line grid. The fraction of lamellar colonies was determined by their area fraction on the same micrographs. The size distribution of the ODS particles in SPS material was measured on 1024x1024 pixel bright-field STEM micrographs at 20'000x magnification using the maximum particle diameter (n_{SPS}=1718). The fewer and larger ODS particles after SLM and DMD processing were measured on a series of high-resolution SEM micrographs at up to 4096x3200 pixels and 32'000x magnification (n_{SLM}=386 and n_{DMD}=391). Particle densities were estimated from the same micrographs assuming particle detection in a 2D plane yielding the area number density N/A with N the number of particles and A the area. The volume particle density is then calculated as

$$\frac{N}{V} = \left(\frac{N}{A}\right)^{\frac{3}{2}} \tag{3.1}$$

with V being the volume. The mean particle center distance l_c is then estimated as

$$l_c = \left(\frac{3 \cdot V}{4 \cdot \pi \cdot N}\right)^{\frac{1}{3}} \tag{3.2}$$

assuming a spherical volume element centered at the particle position. Using the median size of the particles d_{median} the inter-particle distance l can be calculated simply as

$$l = l_c - d_{median} \tag{3.3}$$

For TEM lamellae with a certain thickness, the particle volume density is clearly overestimated by Equation 3.1. However, the error of this estimation can be neglected in this case where the order-of-magnitude differences in between the different consolidation methods are of interest.

3.2.2 X-ray diffraction

X-ray diffraction (XRD) and XRD pole figure measurements were performed with Cu K_α radiation using a Bruker D8 DISCOVER (Bruker, Germany) equipped with a LynxEye 1D detector. Measurement conditions were 40 kV and 40 mA with a step size of 0.02°± 0.0001° (2Θ). XRD pole figure data was corrected for defocusing effects and normalized to yield multiples of random distribution (m.r.d.) using the MULTEX software package of Bruker. Additional pinhole snouts were used to restrict the beam diameter to the area of the specimens. Specimens were mounted free-standing, embedded into epoxy or as complete test builds on base plates from AM trials. The epoxy resin used for embedding was found to contribute only to an amorphous background without distinct peaks. Consequently, the epoxy system does not interfere with the measurements and can be used for small specimens and polished cross sections. The obtained signal can then be corrected for the contribution of the embedding material yielding the XRD spectrum of the specimen of interest.

3.3 Materials testing

3.3.1 Hardness testing

Vickers hardness was measured using a Fischerscope HM2000 (Fischer, Germany) on polished specimens prepared for microscopic investigation. The indentation with the Vickers diamond tip was performed with a maximum load of 400 mN and load increase time of 20 s. For bulk material a 5 by 5 array of indentations with a spacing larger than 50 µm was measured to ensure statistical relevance of the data. Based on indentation depth and load, the indentation hardness in Vickers (HV) is directly calculated by the machine software taking into account corrections for the tip shape and the testing machine. The machine is calibrated using standards to ensure data repeatability and create the necessary correction functions. The typical indentation diameter is in the order of 10 µm. In coarser microstructures this can lead to large variations as different phases with differing mechanical properties are probed. Consequently, the spread of the data set is a qualitative measure for microstructural homogeneity and phase size.

3.3.2 *In situ* mechanical testing

In situ mechanical testing in the range of 293 K to 1073 K was performed with a tensile/compression module developed by Kammrath & Weiss, Germany (F_{max}=± 5 kN). The setup is vacuum-compatible and can be mounted in electron microscopes or vacuum chambers for experiments at elevated temperatures up to 1073 K. In this work, all room temperature tests were performed in air, while the experiments with $T > 273$ K were conducted at $2 \cdot 10^{-5}$ mbar in a vacuum setup. The specimen geometry is a flat dog bone shape with a nominal gauge length of 10 mm, 3 mm width and a thickness of 1 mm (Figure 3.2). Specimens were produced from bulk material by electro-discharge machining (EDM) and ground to P600 using SiC grinding paper. Grinding was performed parallel to the testing direction to avoid stress concentration at surface flaws. Prior to testing all specimens were heat treated at 1123 K for 12 h in vacuum. It was observed that this heat treatment is best applied prior to EDM to avoid distortion and cracking of thin walls during cutting due to residual stresses from SPS. Tests at room temperature are performed with

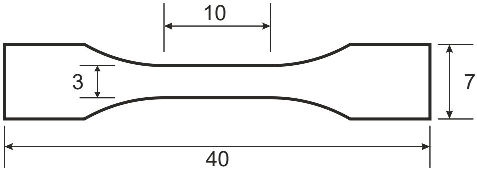

Figure 3.2: Specimen geometry for *in situ* tensile testing. All dimensions are given in mm.

an extensometer attached to the specimen (EXA10-1x, Sandner, Germany, ±0.1 µm) while the load is measured by a load cell (±0.5 N). For tests at elevated temperature a ceramic heating element covered with a W plate is mounted directly to the specimen with W springs. Temperature is measured by a thermocouple in the W plate close to the specimens lower interface. Based on this signal the temperature is actively controlled ± 1 K. Prior to testing the setup is heated with 40 $K \cdot min^{-1}$ from room temperature to the test temperature to allow thermal equilibration of the specimen. The thermal expansion and developing compressive stress is compensated using the load control mode of the module maintaining an effective load of 0±5 N during heating. After reaching the target temperature and a dwell time of 2 min the specimen is loaded in tensile mode until fracture. After fracture the heater is shut off and the setup is allowed to cool in vacuum to below 473 K before Ar 6.0 is introduced to allow for faster convective cooling to room temperature. Due to geometric restrictions the extensometer cannot be mounted for the high-temperature experiments. Consequently, only the machine elongation and load are measured for these experiments. Assuming that the machine stiffness is independent of the testing temperature and if the same specimen geometry is applied, the machine elongation e_m and specimen elongation e_s are correlated by

$$e_s = c(F) \cdot e_m \tag{3.4}$$

where c is a function of the applied load F. The constant c(F) is determined based on the room temperature experiments where both e_m and e_s are simultaneously measured. For the experiments at elevated temperature the effective strain ε is then calculated using Equation 3.4 and

$$\varepsilon = e_s / 100\ \mu m \tag{3.5}$$

based on the gauge length of 10 mm of the extensometer. This procedure allows to estimate the fracture strain ε_f and characteristic yield values for different temperatures. The rupture strength is directly obtained from the specimen geometry and the measured load and has the same precision as for the room temperature experiments. As ε_f of titanium aluminides is typically one order of magnitude lower than in conventional Ti alloys, the usually applied yield stress $R_{p0.2}$ at 0.2% plastic strain may be effectively larger than the actual rupture strength R_m. Consequently, the yield stress at 0.1% plastic strain, $R_{p0.1}$, is additionally used in this work.

3.3.3 Heat treatments

Short term and high temperature heat treatments of SPS, SLM and DMD processed specimens were conducted in an induction furnace (in-house developed at Empa, Switzerland) under 5 mbar of Ar 6.0 to avoid excessive elemental losses due to evaporation. Specimens larger than 10 mm were placed on an alumina substrate and directly heated in the induction coil. Smaller specimens cannot be heated efficiently by the current setup and were placed in a crucible made from vitreous carbon, an extremely inert and thermal shock resistant form of ceramic carbon related to graphite. Due to its electrical conductivity, the entire crucible and the specimen are heated. The specimen temperature is directly measured by a ratio pyrometer (QKTR 1085-1, ±1 K, Maurer, Switzerland). After reaching the desired dwell time, the specimen was allowed to cool naturally to room temperature. Heat treatments below 1273 K and exceeding 30 min dwell time were performed in fully metal-lined high vacuum furnaces (Cambridge, UK and Schmetz, Germany) at pressures below 10^{-5} mbar. The temperature was controlled by calibrated thermocouples placed next to the specimen. After reaching the end of the dwell time the heating system is shut off and the complete setup is allowed to naturally cool to 537 K where the furnace is actively cooled by the introduction of circulated Ar 6.0 passed over water-cooled heat exchangers.

3.3.4 Oxidation testing

The degradation behavior of consolidated TiAl alloys was measured at 923 K and 1073 K in static laboratory air. The tests were performed in an air furnace equipped with $MoSi_2$ heating elements (Nabertherm, Switzerland). Temperature was measured by a K-type thermocouple (Labfacility Ltd, UK, ±2.5 K) placed directly beneath the alumina test containers. The setup consists of an alumina crucible (Almath Crucibles Ltd, UK) with the specimen suspended by Pt-Rh wire from an alumina bar (Figure 3.3). This ensures access of air to all surfaces of the specimen while the specimen is irradiated from all directions by the surrounding alumina crucible separating it from the hot heating filaments. Additionally, all potential debris from oxide spallation is collected in the crucible and can be analyzed. All ceramic parts were fired at 1473 K for 2 h in air to remove residual moisture and binder from production. Specimen geometry were maximum 10 x 10 x 1 mm^3 platelets ground to P1200 using SiC grinding paper. Prior to testing the specimen size is measured with calipers (Mitutoyo CD-15DC, ± 0.01 mm) and the weight is determined on a precision balance (ALJ 120-4, Kern & Sohn, Germany, ± 0.1 mg). The furnace is started 48 h before specimen introduction to allow for thermal equilibration of all components. The alumina crucibles serving as main containers are fired for 24 h at the testing temperature to remove moisture or organic contamination. They are allowed to cool for 30 min before inserting the suspended metallic platelets for testing and placed directly in the continuously running furnace. The insertion time is taken as the start of the oxidation experiment. After the desired oxidation time the complete setup is removed from the furnace and allowed to cool for 30 min. Then the weight

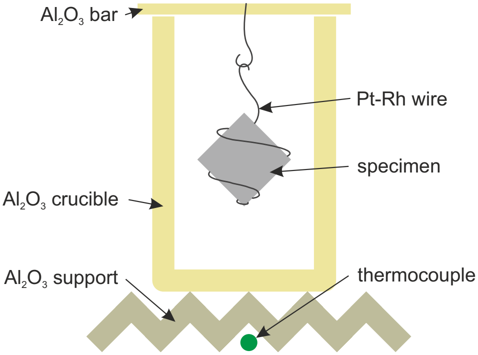

Figure 3.3: Schematic cross section of the experimental setup for oxidation testing of plate-shaped specimens in static air in a laboratory furnace.

of the specimen is determined again to obtain the total weight gain. The weight gain per unit surface area is then calculated as $\Delta m/A$. Gaussian error propagation is applied to estimate the errors introduced by the uncertainties of specimen size and weight. These errors are later shown as error bars with the data points.

3.4 Computational thermodynamics

The presented results have been obtained using the CALculation of PHAse Diagrams (CALPHAD) approach. The methodology of CALPHAD is based on available experimental data on phase equilibria and thermochemical and thermophysical measurements. The thermodynamic properties are then modeled using mathematical models for the Gibb's energy. The philosophy of CALPHAD is a consistent description of the experimental phase equilibria and thermodynamical properties using the determined models and associated parameters. However, these models are based on real experimental data. Additionally CALPHAD allows predictions of higher order systems which cannot be directly evaluated but can be simulated with a combination of sub-systems. The evaluated models and parameters for the Gibb's energy of every element and phase present in a system are stored in a database and allow re-calculation of the phase diagrams and properties using specific software packages [155]. Today a set of commercial databases are available for different applications. In this work the Thermo-Calc 3.0.1, 4.1 and 2015a software packages have been used [156]. For the titanium aluminides published models and parameters have been used for the Ti-Al [11], Ti-Al-Nb [23] and Ti-Al-Mo [17] systems. The latest assessment of the Ti-Al-Nb system by Liu *et al.* [157] was not considered as calculated metastable phase diagrams show nonphysical metastable phase boundaries and an unreasonable stability of the ordered α_2-phase at high Al contents. The available Ti-Al-Mo phase diagrams are still subject to discussions and while the equilibrium solidification sequence involving the liquid, α and β phases is well described, the solid state phase transformations and especially the transformation temperatures were found to be poorly predicted [158]. Currently, no fully consistent thermodynamic assessment of the Ti-Al-Mo system is available that is optimized for the full compositional range and agrees well with the published experimental results. For restricted compositional spaces and close to extensively studied alloy compositions, updated assessments and modified interaction parameters are available [159, 160]. However, these do not allow calculations in a wide compositional range as studied in this work. Consequently, the Ti-Al-Mo assessment of Saunders [17] is used in this work.

4 Microstructure formation of Ti-Al alloys under non-equilibrium conditions at high cooling rates

In this chapter the microstructure formation of Ti-Al alloys under conditions observed in AM is discussed. This extensive work is the foundation for alloy development and selection for later ODS particle addition and AM processing. First, the novel experimental setups are presented that are specifically designed for the non-equilibrium conditions of interest. Next, the computational framework to simulate solidification paths and phase evolution taking into account rapid cooling and the resulting reduced diffusion of elemental species is introduced. These experimental and computational techniques are applied for the binary Ti-Al and ternary Ti-Al-Nb and Ti-Al-Mo systems. The results on the parent Ti-Al system give insight in the fundamentals of microstructure formation. The ternary systems show the influence of the alloying elements Nb and Mo. This chapter is published in [161–164].

4.1 Experimental setup and concept

4.1.1 *Ex situ* rapid solidification

The *ex situ* rapid solidification experiments are performed by re-melting and rapid cooling of small samples (2 mg to 250 mg) of the master alloys under similar conditions as the initial alloy production (see Section 3.1.2). Figure 4.1 shows a schematic drawing for the rapid solidification experiment. The electric arc is ignited directly above the pre-alloyed material and hold for approximately 1 s to fully melt the specimen. Then the arc is immediately moved laterally at maximum distance from the specimen and allowed to cease to prevent overheating the specimen and alter the formed microstructure or reduce the cooling rate. Due to the high heat extraction rate of the water cooled Cu crucible, the near-spherical, liquid specimen is rapidly solidified and subsequently cooled to room temperature.

The cooling rate as a function of the specimen radius is estimated by finite element modeling using Abaqus/CAE 6.13-2 (3DS Simulia) with a 160'000 element hexahedral (DC3D8) mesh. The minimal mesh size is 1/50th of the specimen diameter. The specimen is approximated as a truncated sphere with a radius r and a height of $1.8 \cdot r$ (see Figure 4.2a). The geometry is chosen based on measurements from real specimens. The water cooled Cu crucible is modeled only in the surrounding space as a simplified cylindrical Cu part (see Figure 4.2b). The contact area in the simulation is assumed perfectly flat and horizontal. An ideal contact is realized between the specimen and the Cu crucible through model partition. In the areas of the Cu part close to the contact zone with the specimen the same fine mesh as in the specimen is used in order to compute small time steps with high thermal gradients. Substrate areas in far distance from the specimen are meshed with larger sized elements to reduce computational cost (see Figure 4.2b). The temperature of the Cu substrate is set to T = 293 K on the lower surface and the circumferential plane. The model includes conductive heat transfer between the specimen and the Cu substrate as well as surface radiation from the specimen to the

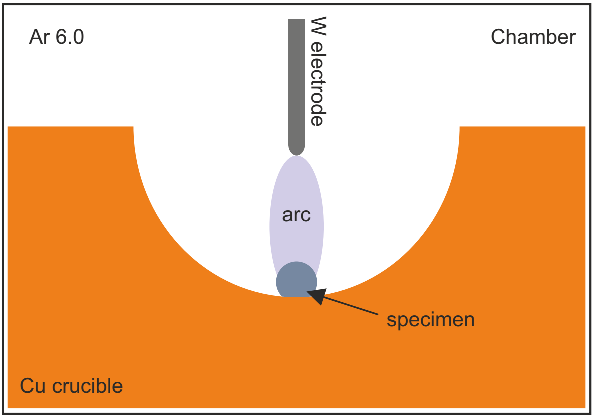

Figure 4.1: Geometrical situation for *ex situ* rapid solidification. The arc is ignited between the specimen and the tungsten electrode, while the water cooled Cu crucible acts as a heat sink.

ambient surrounding. For Ti-Al published data of a Ti-45.5Al-8Nb alloy is used due to the large range in temperature and the completeness of the set of thermophysical properties [165]. For pure Cu, a linear extrapolated thermal conductivity between 398 $W \cdot m^{-1} \cdot K^{-1}$ at T = 298 K and 357 $W \cdot m^{-1} \cdot K^{-1}$ at T = 1000 K, respectively, is used for the simulation [166]. During arc melting the water cooled Cu crucibles do not melt and thermophysical data for high temperatures or the liquid state is not needed.

A transient analysis of the temperature change with an initial temperature of the liquid alloy droplet of 2000 K is performed to extract the cooling curves at various positions of the specimen and to calculate the corresponding characteristic cooling rates $\left|\frac{\Delta T}{\Delta t}\right|_{T=1273K}$ at T = 1273 K. This temperature is below the eutectoid temperature (T = 1392 K) according to the binary Ti-Al phase diagram and is in the $\alpha_2 + \gamma$ two phase field (Figure 2.3). The initial temperature for transient heat transfer analysis is set based on pyrometer temperature measurements of the melt during arc melting of the master alloys. The results indicate that increased convection in the melt and very effective heat removal by the Cu crucibles avoids overheating the melt above 2000 K. Small specimens with low contact area and restricted convection may achieve

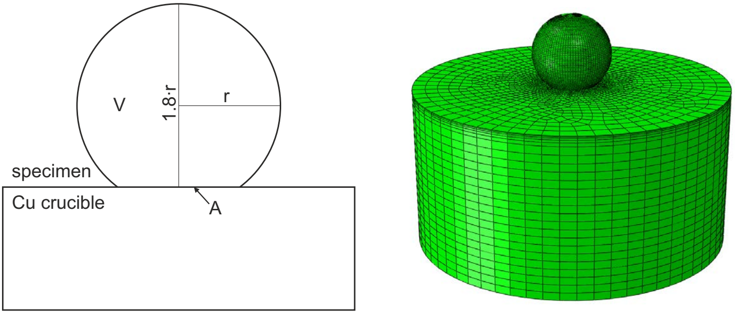

(a) (b)

Figure 4.2: a) geometry of the specimen used for finite element simulations and b) the meshed part with a fine mesh in the specimen and in the Cu substrate close to the contact area.

higher temperatures. The temperature changes for the center and top point of the sphere are extracted from the finite element simulation and used for further analysis (Figure 4.3). The characteristic cooling rate

$$\left|\frac{\Delta T}{\Delta t}\right|_{T=1273K} = \frac{1}{2} \cdot \left(\left|\frac{\Delta T}{\Delta t}\right|_{T=1273K,top} + \left|\frac{\Delta T}{\Delta t}\right|_{T=1273K,center} \right) \tag{4.1}$$

is defined as the mean slope $\left|\frac{\Delta T}{\Delta t}\right|$ at a temperature of T = 1273 K for the top and center position of the spherical specimen. Subsequent microstructural analysis is conducted in this region of the specimen. Based on the finite element simulations a function correlating the specimen radius r and the characteristic cooling rate $\left|\frac{\Delta T}{\Delta t}\right|_{T=1273K}$ is derived according to

$$\left|\frac{\Delta T}{\Delta t}\right|_{T=1273K} = a \cdot r^b \tag{4.2}$$

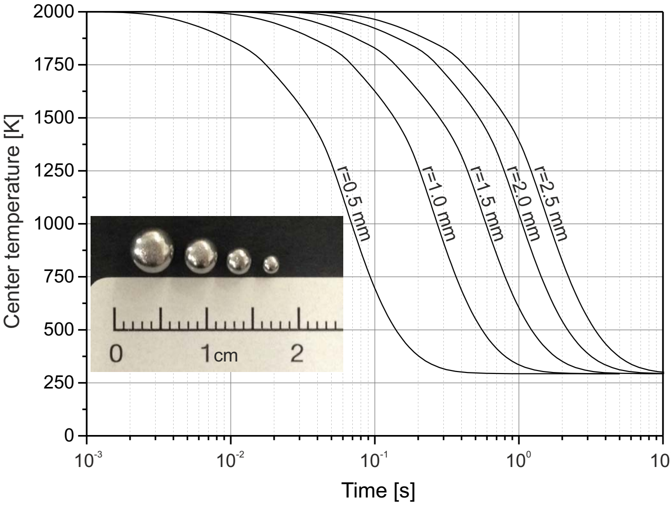

Figure 4.3: Simulated temperature change at the specimen center upon rapid solidification for different radii according to Figure 4.2a. Changes in the slope of the curves are caused by the enthalpy of fusion upon solidification and dependence of the thermophysical properties on temperature. Inset: Specimens for rapid solidification with r = 2.5, 2, 1.5 and 1 mm.

The exponent b of the power law curve can be determined by a dimensional analysis. Based on the dependency of the cooling rate on the contact area A, specimen volume V and the distance to the interface to the Cu crucible d_i (see Figure 4.2a). As $\frac{\Delta T}{\Delta t} \sim \frac{A}{d_i \cdot V}$; and $A \sim r^2$, $V \sim r^3$ and $d_i \sim r$; it follows that $\frac{\Delta T}{\Delta t} \sim r^{-2}$. The results of the simulations show that this idealized analysis is a valid assumption as the calculated values only slightly differ from the idealized curve based on

$$\left|\frac{\Delta T}{\Delta t}\right|_{T=1273K} = a \cdot r^{-2} \tag{4.3}$$

as can be seen in Figure 4.4. Thus, the entire curve can be described using a single material parameter $a = 4354 \pm 7 \cdot 10^{-6}$ K·m^2·s^{-1} in a range of $0.5 \leq r \leq 2.5$ mm. The upper and lower boundaries correspond to the cooling rates at the top and center position of the specimen, respectively.

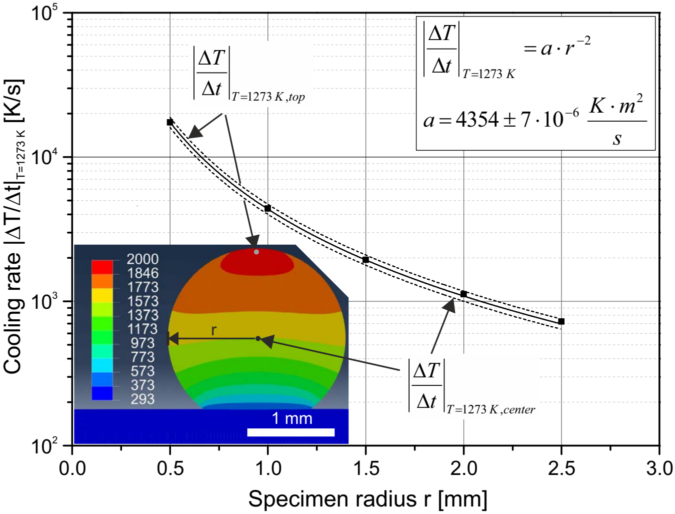

Figure 4.4: The characteristic cooling rate $\left|\frac{\Delta T}{\Delta t}\right|_{T=1273K}$ (solid) and the cooling rates at the top and center positions (dashed) versus the specimen radius r; the inset shows the temperature distribution during rapid cooling of a specimen, characteristic positions are indicated.

Considering the low bandwidth between both boundaries the upper hemisphere of the spherical specimens can be assumed to have similar thermal histories irrespective on the exact location.

The finite element simulations are verified by high-speed camera measurements using a Motion Xtra HG-100K high-speed camera (maximum frame rate 100 kHz) operated at a reduced acquisition rate of 500 Hz and 200 µs dwell time. Considering a changing surface emissivity as a function of the temperature, the solidification front propagation can be monitored [93, 167]. The measurements showed comparable solidus surface propagation in comparison with the simulation with a solidus temperature of 1773 K (see Figure 4.5). Due to geometrical restrictions of the arc furnace, the high-speed camera frames are taken from an inclined angle with respect to the upper substrate surface, which leads to a tilted view on the specimens (see Figure 4.2a). Based on these measurements, the calculated cooling rates are assumed to be representative for the studied specimens.

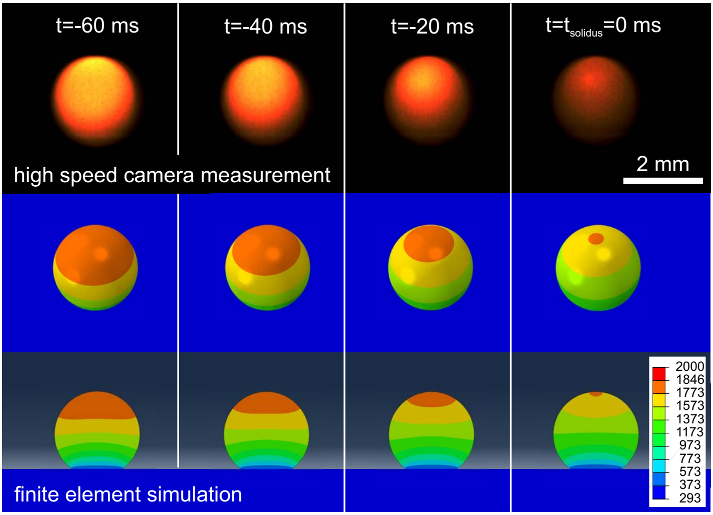

Figure 4.5: Comparison of high-speed camera frames (top) and finite element simulations with inclined view (middle) and in cross-section (bottom) for a rapidly solidified Ti-44Al specimen at the same point in time.

4.1.2 *In situ* microXRD

The specimens for the *in situ* experiments are produced from the master alloys using arc melting of 2 mg of material and subsequent rapid solidification. The material is prepared by cleaving fracture to avoid contamination. Using this process, near-spherical specimens with a diameter of 1 mm are obtained. As shown in Figure 4.4, a characteristic cooling rate of $1.7 \cdot 10^{4}$ K·s^{-1} is imposed on so-produced specimens during arc melting and subsequent solidification. For the *in situ* heating and cooling experiments, the near-spherical alloy specimens are heated using a laser-based heating system incorporating two diode lasers, providing a maximum power of 150 W each (Figure 4.6a). The lasers operate at a wavelength of 980 nm with a rectangular spot size of 0.2 x 1 mm (height x width) and a beam inclination angle of 20° to the horizontal [168]. Water cooled beam dumps ensure safe operation if no specimen is in the beam path or if it is lost during the experiment. The complete setup has translational axes in three dimensions to heat different locations or follow sample movements. Subsequently *in situ* rapid solidification is ensured by fast heat extraction into the Cu support structure (Figure 4.6b). The excellent thermal conductivity

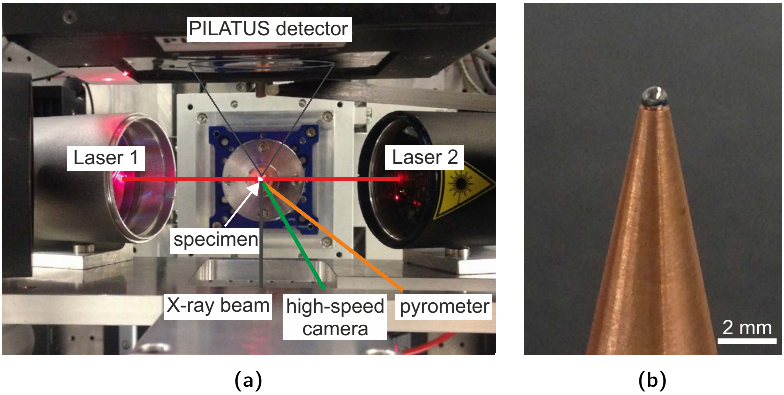

Figure 4.6: Experimental setup for in situ microXRD combined with high-speed camera imaging and laser-based heating. (a) top view of the experimental setup at the microXAS beamline, (b) Cu specimen holder and specimen.

of Cu allows rapid quenching of the liquid specimen and dissipation of the thermal energy throughout the support structure. The temperature of the Cu part close to the contact zone remains below its melting point, and thus no contamination or reaction with the specimen is observed during the few seconds of the experiment. While the upper part of the specimen reaches the liquid state, the contact zone to the Cu structure remains solid and acts as a base, separating the liquid alloy from the Cu structure. It ensures conditions similar to beam-based additive manufacturing where the newly formed liquid is in contact with previously deposited material of usually the same composition. This is an important difference of the presented approach to other rapid solidification techniques; for example, in melt spinning, the liquid is brought in direct contact with the Cu, quenched and solidified.

The surface temperature of the specimen is monitored for process control using the built-in pyrometer from the laser system. The pyrometer detection spot size is in the order of 1 mm and thus reflects an average surface temperature on the specimen. In order to avoid excessive specimen oxidation, Ar 4.8 shielding gas is applied using a laminar flow shielding gas nozzle

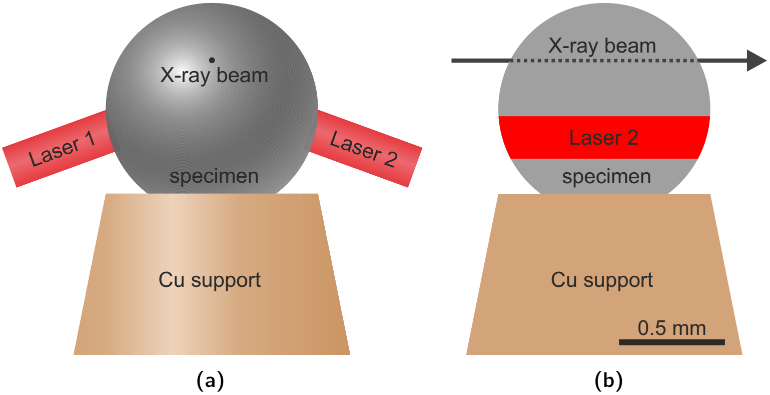

Figure 4.7: Measurement geometry for *in situ* microXRD combined with laser heating. Schematic view (a) parallel and (b) perpendicular to the incoming X-ray beam. The scale bar in (b) applies for both figures.

positioned above the specimen. This provides a flowing vertical column of Ar, separating the specimen from the oxygen containing atmosphere. The use of a laminar flow nozzle eliminates the need of a specially designed chamber with windows that are both X-ray and near-infrared transparent. A window-less setup provides high intensities of the incoming and diffracted X-ray beams and consequently allows short dwell times and high temporal resolution. During the complete heating and cooling cycle, *in situ* microXRD (micro referring to the beam size) is performed in transmission mode using a focused X-ray beam with a diameter of 20 μm at 17.3 keV. After passing the specimen, diffracted intensities are recorded on a PILATUS 100K detector operated at 100 Hz frame rate [169] at the microXAS beamline of the Swiss Light Source (SLS). The beam is positioned in the upper hemisphere of the specimen (Figure 4.7). At this location above the cross-over point of the lasers, the melt is stable over a longer time as solidification proceeds upwards due to unidirectional heat flow. Additionally, the interaction path length is shorter to reduce intensity loss of transmitted beams. Pure Ti and Al foils and 1 mm spheres are used for calibration of the beam energy, position and specimen-detector distance. Data calibration and azimuthal integration of the 2D diffraction patterns are performed using the XRDUA v6.5.3.2 software package [170]. Every 2D pattern is integrated and background subtracted in a range of 14 nm^{-1} $< q <$ 70 nm^{-1}; $q = \frac{4\pi \sin \Theta}{\lambda}$, λ the wavelength and Θ the scattering angle. Integrated peak intensities, peak positions and full-width-at-half-maximum (FWHM) values are evaluated by fitting selected peaks for every time step. In order to separate the signal originating from the liquid phase and the systematic background, the background determined at 7300 ms is used, as the specimen is fully solidified at this point. The systematic background generated by the beam optics and the setup is assumed to remain unchanged over the experiment due to high beam stability provided by the SLS.

Knowing the full measured signal I_{tot}, the systematic background I_{bg} at 7300 ms and the signal originating from crystalline phases I_{c}, the remaining amorphous signal I_{am} can be extracted according to $I_{\mathrm{tot}} = I_{\mathrm{bg}} + I_{\mathrm{c}} + I_{\mathrm{am}}$. It should be noted that the signal I_{am} contains contributions not only from the liquid phase but also from every component in the system providing time-depended diffuse scattering over the experiment. Having the separated signals, the non-crystalline fraction f_{nc} is calculated at every time step using the separated integrated total peak area I_{c} and the remaining amorphous signal I_{am} according to

$$f_{\mathrm{nc}} = \frac{I_{\mathrm{am}}}{I_{\mathrm{am}} + I_{\mathrm{c}}} \tag{4.4}$$

Additionally, high-speed camera imaging using a Motion Xtra HG-100K camera (maximum frame rate 100 kHz) operated at a reduced acquisition rate of 500 Hz and 200 µs dwell time is applied for direct visual experimental control and is also used to estimate the local temperature evolution in the vicinity of the X-ray beam position. While pyrometers are typically restricted to a narrow wavelength window and provide only an integrated temperature value over the full spot size, CCD chips can provide local temperature estimations [171]. In order to estimate the local temperature using the signal recorded by the CCD chip of the high-speed camera, offline calibration measurements using the very same acquisition settings and optics are performed on a specially designed Ti block containing deep cavities, which approximates the emission characteristics of a black body (emissivity $\varepsilon \approx 1$). The block is inductively heated in a high vacuum chamber while the temperature is controlled using a ratio pyrometer (QKTR 1085-1, Maurer, ±1 K). The intensity measured by the CCD chip on the surface and in the cavity takes into account the deviation of the surface from an ideal black body behavior ($\varepsilon < 1$). The transmissivity of the chamber windows is also considered using comparative measurements with and without the window in the optical path. The complex full radiometric model proposed by Sentenac *et al.* [171] requires 9 parameters, which are largely unknown here. Consequently, the obtained calibration curve is fitted based on Planck's law using a simplified model according to

$$I_{\mathrm{CCD}} = \frac{a \cdot c_{1L}}{\exp\left(\frac{c_2}{b \cdot T}\right) - 1} \tag{4.5}$$

where I_{CCD} is the intensity on the CCD chip, $c_{1L} = 2hc^2$ is the first radiation constant with h being the Planck constant and c being the speed of light in vacuum, $c_2 = \frac{hc}{k}$ is the second radiation constant with k being the Boltzmann constant, T is the temperature and $a = 7.95 \cdot 10^{22}\ \mathrm{W}^{-1} \cdot \mathrm{m}^{-2}$ and $b = 7.32 \cdot 10^{-7}$ m are the fitted parameters. Using this model and the optimized parameters, the local temperature evolution in the vicinity of the material exposed to X-rays can be estimated based on the high-speed imaging data. As it is apparent from Equation 4.5, the response of the CCD chip is approaching its lower sensitivity limit or minimum measurable temperature in an asymptotic manner. Consequently, the error of the temperature estimation based on one intensity unit ($0 \leq I_{\mathrm{CCD}} \leq 255$, $I_{\mathrm{CCD}} \in \mathbb{N}$) is close to 100 K at 1150 K. At high temperatures $T > 1300$ K this error is below 20 K and further decreasing with increasing temperature. Based on the residuals from the interpolation using Equation 4.5, the error between measured calibration and calculated temperature is also on the order of 20 K above 1300 K.

4.2 Computational framework

The applied CALPHAD method is based on thermodynamic properties that are modeled using mathematical models for the Gibb's energy. Using energy minimization the stable or equilibrium state is calculated. Combining the Gibb's energies of a variety of phases containing different elemental species the complex multi-dimensional phase diagrams for metals, ceramics and chemical compounds can be calculated. Although of great importance, equilibrium phase diagrams represent only an extreme case which is more often than not not representing the reality. Complete equilibration at every temperature requires infinite time scales which are in direct contradiction to the highly dynamic nature of beam-based additive manufacturing. At this time scales diffusion is limited, phase formation can be suppressed and locally changed phase relations may apply due to segregation. In this work, non-equilibrium phase relations are calculated using the available thermodynamic assessments for the equilibrium state. On the opposite side of time scale to full equilibration we find the assumption of composition-invariance. If time becomes sufficiently short, no diffusion is possible. This case, also being an extreme one, may not fully represent the reality as well. But in between the two extremes, equilibrium and composition-invariance, the true nature of our system will be found. While conventional heat treatments or casting will be close to equilibrium, beam-based AM at high scanning speeds will be found closer to the composition-invariant side. Comparing both gives thus a good indication on the behavior of a system under highly dynamic, non-equilibrium conditions of beam-based AM. Classically, Scheil-Gulliver simulations are applied to understand solidification with limited diffusion. In this work, the T_0 concept is applied to calculate phase selection hierarchy maps that will be discussed in the following sections.

4.2.1 The T_0 concept

Under equilibrium conditions, an alloy will transform from a single phase into a dual phase structure if the total energy of the system can be reduced by the formation of a second phase. Geometrically, this is equivalent to finding the

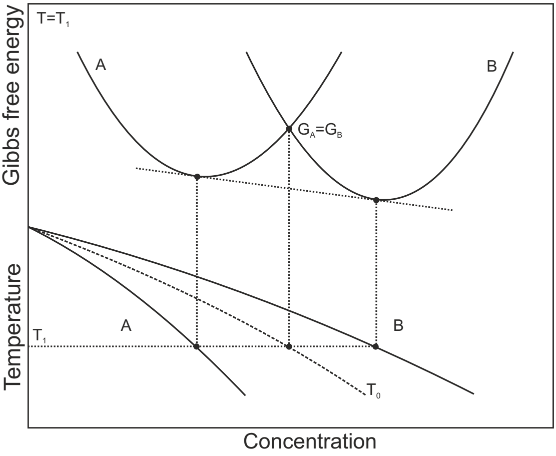

Figure 4.8: The relation of the Gibbs free energy, the equilibrium phase diagram and the T_0 temperature. Without diffusion the phases do not form in their equilibrium composition but are expected below T_0 without compositional changes.

common tangent of the Gibbs energies of two competing phases (Figure 4.8). Both phases will have their individual equilibrium composition. Consequently, the formation of a second phase involves diffusion over larger distances. If time is not sufficient for diffusion, a potential phase transformation is composition-invariant. The parent phase and the newly formed one have the same composition, but different crystal structure. Energy minimization is thus only possible by selecting the phase with the lowest Gibbs energy at a certain composition. Geometrically, this point is the cross-over point of the Gibbs energies of the phases involved. The temperature of this change in preferred phase selection is called T_0. This temperature is composition dependent and exists for every phase transformation in the system.

The so called T_0 temperature is the temperature at which the Gibbs free energies of the two phases are equal with the same composition (Figure 4.8). Under equilibrium conditions, the energy is minimized by the formation of two phases with a different composition. However, at rapid cooling conditions diffusion is strongly reduced, which imparts the formation of the equilibrium phases. The formation of the low-temperature phase A is expected as soon as $T < T_0^{A \to B}$, where $G_A < G_B$. Consequently, the formed phases are metastable as the energy of the intersection point of the Gibbs free energy curves where $G_A = G_B$ is always larger than the energy of the points lying on the common tangent line. In other words, the phases are supersaturated above their equilibrium limit of solubility. This metastable state is inherently less stable than the equilibrium and if the temperature allows sufficiently fast diffusion of the elemental species, the supersaturated phases will decompose into their equilibrium counterparts. This can happen by simple changes in composition or by precipitation of the equilibrium phases from the metastable matrix.

4.2.2 Phase selection hierarchy maps

Combining the different T_0 temperatures, phase selection hierarchy maps can be constructed. These maps allow to predict transformation sequences based on thermodynamical information and correlate it with the observed behavior under non-equilibrium conditions. In order to create a phase selection map, all relevant phase transformations and compositions must be considered. Consequently, a number of T_0 temperatures needs to be calculated. In the most general form these can be expressed as $T_{0,x_1...x_{n-1}}^{i \rightarrow j}$ with i and j the high and low temperature phases, respectively, and $x_1...x_{n-1}$ the elemental molar fraction of a n-component system. Consequently, for every phase transformation of interest a composition-dependent T_0 temperature curve is created. The overlay of these curves creates then the phase selection hierarchy map. Crossing a line in such a diagram is equivalent to switching the Gibbs energy and thus phase stability between two phases (Figure 4.8). Considering several phase transformations simultaneously, a sequence in Gibbs energy and stability is created. The phase with the lowest energy is the most stable one.

It is noteworthy to point out, that phase stability is not equivalent to the existence of a phase. Reaching T_0 a phase A is not formed, as the driving force ΔG

$$\Delta G = G_{A,T_0} - G_{A,T} \tag{4.6}$$

becomes only positive when $T < T_0$. Then the system can nucleate and grow the more stable phase A. The T_0 only defines the highest temperature where the phase A is stable against phase B.

Solidification in the presence of seeding crystals, as it is observed in beam-based AM, has no nucleation barrier to overcome. In the tail of a moving melt pool a region of undercooled liquid may develop [79]. But suppressing completely the formation of the solid phase and retaining the liquid for extended time scales in the presence of seeds is not possible. In the solid state, however, phase formation can be completely suppressed if the driving force is not high enough for nucleation and growth of the stable phase. Metastable states are then preserved. In the case of TiAl alloys, the formation the γ phase from its parent α phase is known to be depending on the cooling rate and composition (see Chapter 2.4.2). Exceeding a critical cooling rate at low Al contents, its formation can be completely suppressed. Although the formation of γ can occur in a composition-invariant or so-called massive manner, as covered by the phase selection hierarchy maps, it may not be observed at small driving forces. This correlation allows to predict the effect of alloying elements on this driving force and ultimately tendency for phase formation using the data contained in the T_0 temperature curves.

The driving force for the massive $\alpha \rightarrow \gamma_m$ transformation can be estimated using the expression [105, 172]

$$\Delta G^{\alpha\rightarrow\gamma_m} \cong \Delta H^{\alpha\rightarrow\gamma_m}\left(\frac{\Delta T}{T_0^{\alpha\rightarrow\gamma}}\right) \tag{4.7}$$

where $\Delta T = T_0^{\alpha\rightarrow\gamma} - T_{\mathrm{start}}$ with T_{start} being the temperature when the $\alpha \rightarrow \gamma_m$ transformation takes place, $T_0^{\alpha\rightarrow\gamma}$ being the corresponding T_0 temperature, $\Delta G^{\alpha\rightarrow\gamma_m}$ being the driving force and $\Delta H^{\alpha\rightarrow\gamma_m}$ the enthalpy of the massive transformation. The competing tendency for massive γ_m-formation from the parent α-phase instead of full $\alpha \rightarrow \alpha_2$ ordering for a certain alloy composition is estimated based on the difference of the relevant T_0 temperatures for both transformations. It is assumed that the alloys undergo an $\alpha \rightarrow \alpha_2$ ordering transformation when $T \leq T_0^{\alpha\rightarrow\alpha_2}$ preventing any formation of γ_m at lower temperatures. Consequently, the composition dependent driving force for the massive $\alpha \rightarrow \gamma_m$ transformation reaches its maximum value for a large potential undercooling in alloys where $T_0^{\alpha\rightarrow\gamma} >> T_0^{\alpha\rightarrow\alpha_2}$. Equation 4.7 can thus be rewritten as

$$\Delta G^{\alpha\rightarrow\gamma_m} \cong \Delta H^{\alpha\rightarrow\gamma_m}\left(\frac{T_0^{\alpha\rightarrow\gamma} - T_0^{\alpha\rightarrow\alpha_2}}{T_0^{\alpha\rightarrow\gamma}}\right) \tag{4.8}$$

with

$$\left(\frac{T_0^{\alpha\rightarrow\gamma} - T_0^{\alpha\rightarrow\alpha_2}}{T_0^{\alpha\rightarrow\gamma}}\right) = \left(\frac{\Delta T}{T_0^{\alpha\rightarrow\gamma}}\right)_{\mathrm{max}} \tag{4.9}$$

where $T_0^{\alpha\rightarrow\gamma}$ and $T_0^{\alpha\rightarrow\alpha_2}$ are the calculated T_0 temperatures for the $\alpha \rightarrow \gamma$ and $\alpha \rightarrow \alpha_2$ transformations, respectively.

As discussed earlier, the Ti-Al-Mo system is still debated (see Chapter 3.4). Thus the complete phase selection hierarchy maps are only calculated for the well described Ti-Al and Ti-Al-Nb systems. For the Ti-Al-Mo system the phase selection hierarchy map is constructed only for L → α and L → β solidification and the following $\beta \rightarrow \alpha$ transformation in the compositional range of Ti-(43-50)Al-(0-2)Mo.

4.3 Influence of cooling rate and composition in binary Ti-Al

4.3.1 *Ex situ* rapid solidification

The microstructure and the phase evolution during rapid solidification of binary Ti-(44-48)Al (at.%) alloys at defined cooling rates between $6 \cdot 10^2$ and $1.5 \cdot 10^4$ $K \cdot s^{-1}$ is systematically studied. For this, the developed methodology which combines *ex situ* rapid solidification experiments of small alloy samples with finite element simulations of the temperature evolution in the samples and thermodynamic simulations using the CALPHAD method is applied. The resulting microstructures of the different alloys show a strong dependency on the Al content. According to the equilibrium phase diagram, all alloys have an α_2 + γ microstructure with varying amounts of α_2 and γ. Thermodynamic calculations and previous studies confirm that the Al-lean alloys (< 44.5 at.% Al) show full solidification via the bcc β-Ti phase while high Al containing alloys undergo a high-temperature peritectic reaction involving the bcc β-Ti, the hcp α-Ti and the liquid phase [35]. At all studied cooling rates, Ti-Al alloys with Al $\leq$ 45 at.% formed a coarse-grained α/α_2 microstructure (Figure 4.9a and 4.9b). A slight Ti enrichment of the primary bcc β-Ti dendrite cores is observed. The presence of the Ti_3Al α_2-phase is confirmed by XRD measurements while TiAl γ-phase is not found (see Figure 4.10). The Ti-48Al alloy formed a fine dendritic microstructure, consisting of lamellar α_2 + γ dendrites and inter-dendritic γ-phase (Figure 4.9e and 4.9f). In the inter-dendritic area Al contents of up to 55 at.% are detected, indicating pronounced Al segregation in the liquid phase. The α_2- and γ-phases are confirmed by XRD. A strong texture of the formed phases can explain the absence of peaks that are expected based on the powder diffraction spectra of the phases. Such texture is expected as heat is extracted uni-directionally into the Cu crucible. Consequently the solidification front proceeds from the contact zone towards the top of the sphere (see Figure 4.5). Furthermore, the amount of material interacting with the X-ray beam is limited as well as the number of grains in the specimen itself. This effect is especially strong in the coarse-grained Ti-44Al specimens as there are only a few grains in the cross section plane (see Figure 4.9a and 7). But the effect is also observed for Ti-46Al and Ti-48Al where the $\alpha_2(20\bar{2}0)$ (Ti-46Al) and $\alpha_2(20\bar{2}1)$ peaks (Ti-48Al) are not observed. Also, the comparably high intensity of the $\gamma(113)$ and $\gamma(311)$ peaks of γ in Ti-48Al at high 2Θ angles indicates a strong texture. For solidification via the α-phase a texture along $\alpha[0002]$ has been observed [35]. The generally low intensity of the overlapping $\alpha_2(0002)/\gamma(111)$ peaks also indicates a texture along this direction in the Ti-(> 45)Al alloys.

The alloys containing $45 < \text{Al} < 48$ at.% formed a mixed microstructure showing features of the Al-rich and Al-lean alloys (Figure 4.9c and 4.9d). A large part of the microstructure consists of coarse α/α_2 grains. In addition, a fine dendritic structure is visible that is probably formed due to local Al enrichment above the peritectic. In the inter-dendritic areas γ is found. In the surrounding of the fine dendritic structure, lamellar $\alpha_2 + \gamma$ colonies are observed. Both α_2 and γ are confirmed by XRD in these alloys. The Ti-46Al alloy showed a coarse-grained α/α_2 microstructure at cooling rates exceeding 8000 $\text{K}\cdot\text{s}^{-1}$ (see inset Figure 4.9c). In general, a clear shift of the α/α_2-forming alloys towards higher Al contents is obvious.

According to the different observed microstructures, all specimens are classified as "coarse-grained α/α_2", "mixed" or "dendritic". Based on this classification, a map showing the observed microstructures as a function of the cooling rate and the Al fraction is constructed (see Figure 4.11). Due to the rapid cooling conditions and reduced time for diffusion, the solidification and diffusion-less phase transformations occur below the corresponding T_0 temperature. In this case ordering from the disordered β- and α- phases to the intermetallic α_2- and γ-phases is expected to be dependent on alloy composition and the phases involved [83] (see Figure 4.12).

The extension of the α/α_2-forming alloys towards higher Al contents may be due to a shift of the equilibrium peritectic temperature of 1764 K to lower temperatures due to the high cooling rates. This leads to a suppression of the hcp α-Ti phase and prolonged growth of the β-Ti phase with a higher Al content than predicted by the equilibrium CALPHAD calculations. Consequently, full

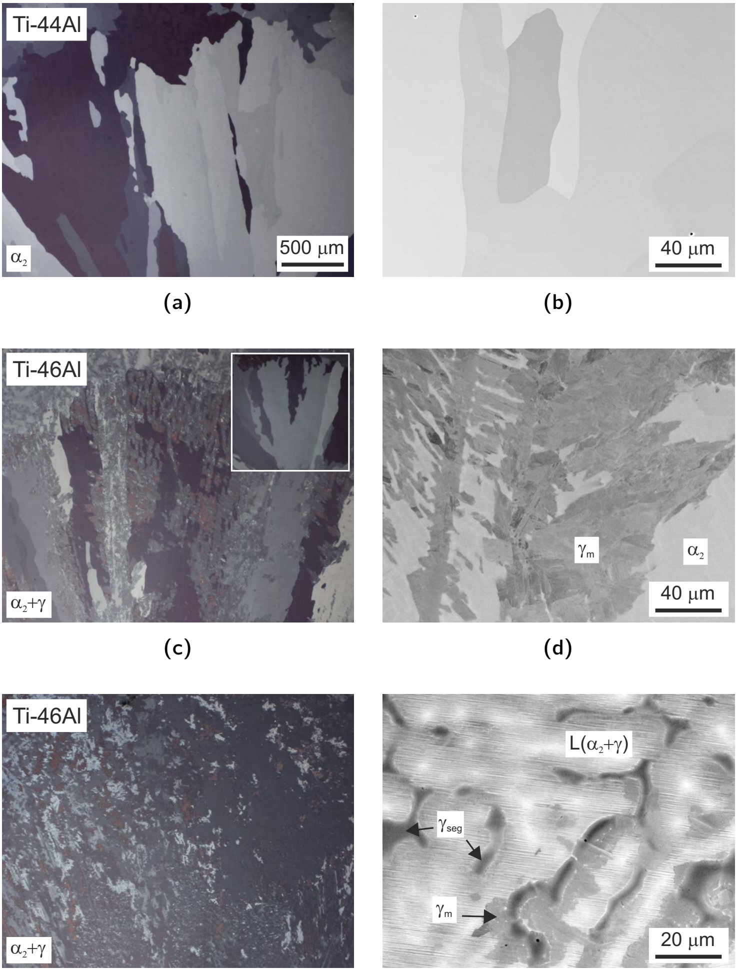
Ti-44Al
α2
500 μm
40 μm
Ti-46Al
α2+γ
γm
α2
40 μm
Ti-46Al
α2+γ
L(α2+γ)
γseg
γm
20 μm

(a) (b)

(c) (d)

(e) (f)

Figure 4.9: Microstructures in OM (a, c, e) and SEM (b, d, f) of rapidly solidified (10^3 K·s^{-1}) (a, b) "coarse-grained α/α_2" Ti-44Al, (c, d) "mixed" Ti-46Al (inset: solidified at $8 \cdot 10^3$ K·s^{-1}) and (e, f) "dendritic" Ti-48Al. The scale bar in (a) applies for (a, c, e) including the inset. The confirmed phases from XRD are indicated in (a, c, e).

solidification through the β-phase would occur, followed by the β → α and α → α_2 phase transformations, similar to the β-solidifying Ti-44Al alloy. The phase selection hierarchy map also indicates a strong tendency to form a β-phase at Al < 46 at.% (see Figure 4.12).

The T_0 temperatures for the α → γ and the α → α_2 phase transformations show different trends for increasing Al amounts (see Figure 4.12). While $T_0^{\alpha\rightarrow\gamma}$ increases with increasing Al contents, $T_0^{\alpha\rightarrow\alpha_2}$ decreases. Thus Al-rich alloys often show massive α → γ transformations, while Al-lean alloys will more likely undergo an α → α_2 ordering reaction. This behavior is already well known from powder atomization, levitated melts and solid state quenching experiments from the single phase α-region (see Chapter 2.4.2). Under rapid solidification conditions, the low Al containing alloys show no pronounced Al segregation and undergo preferentially the α → α_2 ordering reaction. However,

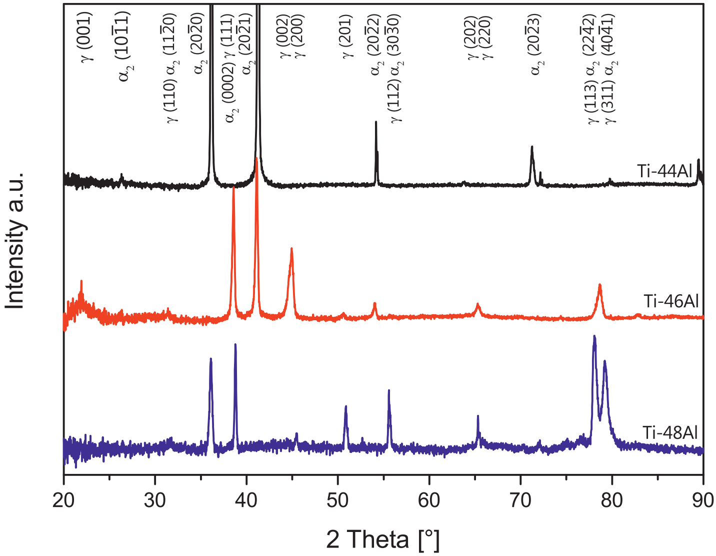

Figure 4.10: XRD spectra of Ti-44Al, Ti-46Al and Ti-48Al solidified at $6{\cdot}10^2$ K·s^{-1}. The characteristic peak positions of the α_2 Ti_3Al-phase and γ TiAl-phase are indicated.

the calculated $T_0^{\alpha\to\alpha_2}$ is around 200 K lower than the $T_0^{\alpha\to\gamma}$ for a Ti-44Al alloy. Consequently, an $\alpha \to \gamma$ transformation would be expected rather than $\alpha \to \alpha_2$ ordering. The observed ordering may be explained by a neglected energy contribution for the nucleation of the intermetallic phases from the parent α-phase as it was proposed earlier for solid state quenching for Ti-(< 46)Al where no massive γ-phase was found [99]. In this study a complete transformation to α/α_2 is only observed in alloys with $T_0^{L\to\beta} \geq T_0^{L\to\alpha}$. In the case of Ti-46Al cooling rates exceeding 8000 K·s^{-1} may favor the formation and growth of β-phase over the α-phase. Previous studies showed the kinetic preference of β over α at large undercooling in levitated melts [83, 84]. As a result, the alloy is expected to follow the phase transformation path of Al-lean alloys and to transform into α/α_2. The phase selection hierarchy map also shows a $T_0^{\beta\to\alpha_2} > T_0^{\alpha\to\gamma}$ for Al $\leq$ 46 at.% (see Figure 4.12). Based

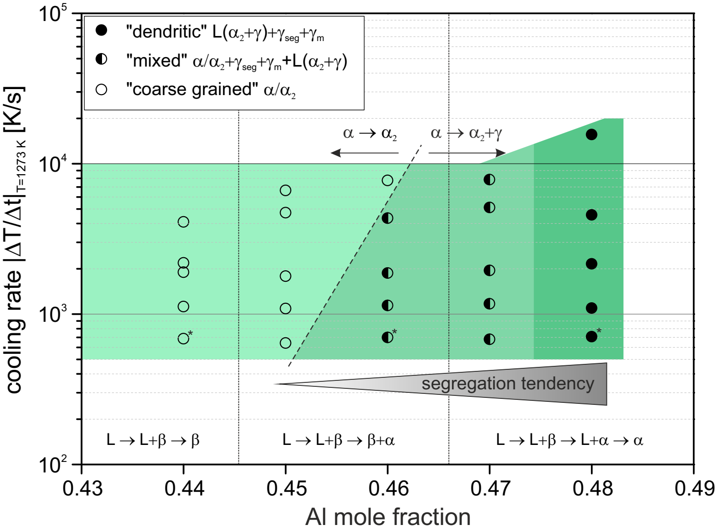

Figure 4.11: Microstructures in Ti-(44-48)Al (at.%) as a function of the cooling rate and Al content. CALPHAD solidification paths are indicated and separated by short-dashed lines. Specimens studied by XRD are indicated (*). The compositional spaces where a similar microstructure is observed are shown tentatively with a common shading to guide the reader's eye.

solely on thermodynamics, a β-solidifying alloy undergoing the β → α phase transformation and having some remaining β-phase when reaching $T_0^{\beta\rightarrow\alpha_2}$ may undergo a local β → α_2 phase transformation providing nucleation sites for a following α → α_2 ordering. Together with the proposed nucleation barrier for the α → γ transformation, this thermodynamic consideration may also explain the tendency of Al-lean alloys for complete α/α_2 ordering.

The microstructure formation of the "mixed" and "dendritic" alloys can also be explained based on the T_0 temperatures. According to the Ti-Al phase diagram (see Figure 2.3), the Ti-48Al alloy finally solidifies by α-formation from an Al-enriched liquid phase. Additionally, segregation can further increase the Al content of the remaining liquid up to 55 at.%. Thus, γ-TiAl can form directly either from the remaining melt or by α → γ transformation of the high-Al containing α-phase with a high corresponding $T_0^{\alpha\rightarrow\gamma}$ during cooling.

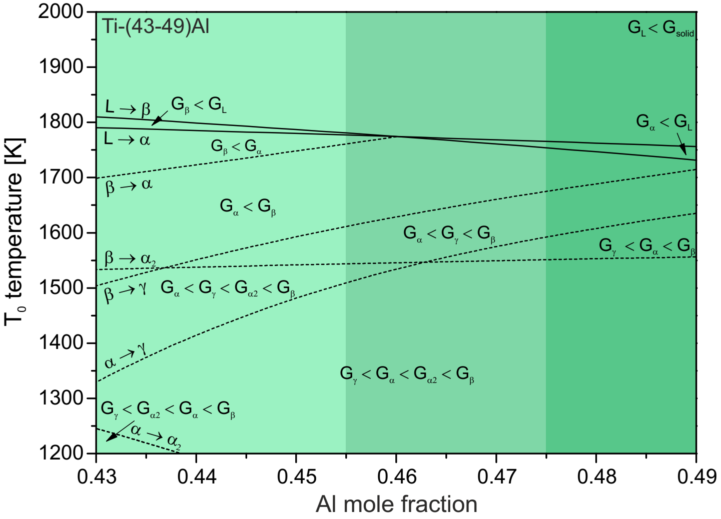

Figure 4.12: Phase selection hierarchy map assuming composition-invariant transformations for binary Ti-(43-49)Al. The corresponding phase transformations are indicated as well as the relative order of the underlying Gibbs energies (G) of the phases involved. The green shaded areas correspond to the shading applied in Figure 4.11.

In the present study the lamellar $\alpha_2 + \gamma$ colonies are observed at cooling rates up to $1.5 \cdot 10^4$ K·s^{-1} in Ti-48Al. The formation of such lamellae at high cooling rates was also observed in melt-spun Ti-48Al [81, 82] and supercooled levitated Ti-50Al [83–85]. A possible explanation is the strong segregation of Al in the liquid phase upon solidification, leading to a direct formation of the γ-phase from the melt in parallel to the $\alpha \rightarrow \gamma$ transformation. The segregation tendency increases with increasing Al amount, as indicated in Figure 4.11. The locally formed γ-phase can act as a seeding crystal for the $\alpha \rightarrow \alpha_2 + \gamma$ transformation of the adjacent α-dendrites, starting from the inter-dendritic space and proceeding towards the dendrite core [81]. As a result, the final microstructure consists of lamellar $\alpha_2 + \gamma$ dendrites and inter-dendritic γ-phase. The "mixed" microstructures of the 46-47 at.% Al alloys can be explained by their solidification path and locally different compositions. Consequently, the T_0-temperatures vary and lead to locally different phase transformations. Furthermore, $T_0^{L\rightarrow\beta}$ and $T_0^{L\rightarrow\alpha}$ are very close and $T_0^{\alpha\rightarrow\gamma} >> T_0^{\alpha\rightarrow\alpha_2}$. Based on the resulting microstructure, a significant amount of β-phase is expected to form during solidification. At lower temperature the $\alpha \rightarrow \alpha_2$ ordering reaction leads then to the coarse α/α_2 structure (see Figures 4.9c and 4.9d). Elemental segregation of Al during solidification may lead to locally higher Al contents and promote a partial $\alpha \rightarrow \gamma$ transformation. In the alloys with $45 < \text{Al} < 48$ at.%, lamellar colonies are observed in the neighborhood of locally formed γ-phase as well. However, the seeding effect, described for Ti-48Al, is not strong enough to completely transform this microstructure into the equilibrium structure of lamellar $\alpha_2 + \gamma$.

The solidification sequence of Ti-Al alloys can be influenced by different degrees of undercooling [83]. While the phase selection in Al-rich alloys shows a high sensitivity on the degree of undercooling, alloys with Al < 50 at.% Al show primary β-phase formation up to a undercooling of 262 K. Recorded high speed imaging data obtained from the experiments in this work indicates a stable temperature of the liquid before and no recalescence events after solidification for the upper hemisphere of the specimens. Additionally, the measured velocity of the solidification front in the experiments is typically two orders of magnitude slower, than published data on dendrite growth velocities in Ti-Al-Nb alloys undercooled by 75 K [95]. Although a significant undercooling is achieved for a short time at the interface to the cooled Cu substrate at the beginning of solidification, the lower thermal conductivity of already solidified material effectively isolates the remaining liquid from excessive heat extraction as indicated by finite element modeling. Finally this effect allows to control the cooling rate in the upper hemisphere in a moderate range of $6 \cdot 10^2$ to $1.5 \cdot 10^4$ $K \cdot s^{-1}$ by varying the specimen size. Based on the phase selection hierarchy map (see Figure 4.12) it can be concluded, that a moderate undercooling has no effect on phase selection upon solidification in Ti-Al alloys with Al < 46 at.% due to a higher thermodynamic stability and kinetic preference of the β-phase. Alloys with 45 < Al < 48 at.% are expected to form either primary α or β depending on the degree of undercooling. A similar effect has been shown for Ti-50Al at undercoolings exceeding 85 K, where metastable primary β was formed instead of stable α [83]. With lower Al-contents, primary β is formed under equilibrium conditions (see Figure 2.3). Under non-equilibrium conditions primary α is expected to form at moderate undercoolings (see Figure 4.12). For Ti-48Al the calculated equilibrium liquidus and T_0 temperature for α-solidification differ by 17 K. This result is in good agreement with the observed microstructure in rapidly solidified Ti-48Al showing orthogonal dendrites, which are typically assigned to primary β-solidification, at low cooling rates and hexagonal dendrites, associated with primary α-formation, at high cooling rates. Based on all these results, the achieved undercooling in the performed experiments is estimated to be in a range of 10 to 75 K.

The formation of a single phase supersaturated α/α_2 structure is considered detrimental for processing because of a high probability of thermal cracking due to a low fracture toughness. To overcome this behavior, increased processing temperatures can be applied to accelerate diffusion as well as to decelerate the cooling rate. If crack-free processing is achieved, such alloys still need post-processing heat treatments to form the desired set of phases. Based on the present data, suitable alloys for AM with reduced segregation and out-of-process $\alpha_2 + \gamma$ structure are foreseen in the range of Ti-(46-47)Al for binary alloys or in higher order alloys with similar behavior. The Al content in this range is high enough to prevent full solidification via the β-phase and complete α/α_2 ordering but does not promote the formation of a highly Al-enriched liquid phase leading to strong segregation. However, specific applications, as ODS alloys, may require Al-leaner or Al-richer alloys based on their individual properties. In such cases the presented data and predictions allow to identify possible problems during processing in an early stage and to choose strategies to overcome the limitations of such TiAl alloys for AM. In summary, it was shown that:

- systematic rapid solidification studies with varying cooling rates can be realized by a combination of experiments with heat transfer analysis based on finite element simulations;
- at the studied cooling rates, the resulting microstructure of binary Ti-Al alloys is strongly dependent on the Al content. At $\text{Al} \leq 45$ at.% the alloys undergo $\alpha \rightarrow \alpha_2$ ordering, while intermediate alloys with $45 < \text{Al} < 48$ at.% show a mixed microstructure consisting of coarse α/α_2 grains, local γ-phase and lamellar $\alpha_2 + \gamma$. The Al-rich Ti-48Al alloy exhibits a dendritic microstructure consisting of lamellar $\alpha_2 + \gamma$ dendrites and inter-dendritic γ-phase.
- at cooling rates between $6 \cdot 10^2$ and $1.5 \cdot 10^4$ $\text{K} \cdot \text{s}^{-1}$ the microstructure and phase transformation behavior of Ti-(44-48)Al alloys can be predicted and explained based on thermodynamic considerations considering reduced diffusion, extensions of single phase fields and undercooling effects, summarized in the phase selection hierarchy map.

4.3.2 *In situ* microXRD during laser melting of Ti-48Al

The previously discussed *ex situ* rapid solidification experiments give valuable information on the formed microstructures and phases, but they are providing no direct data on the involved phase transformations starting with solidification. Although dendrite orientations, formed phases and obtained microstructures can be used to discuss possible transformation paths, these findings remain essentially estimates. Undoubtedly, the solidification pathway directly influences the observed microstructure at low temperature. While Al-lean alloys solidify by β, Al-rich TiAl alloys have a complex solidification

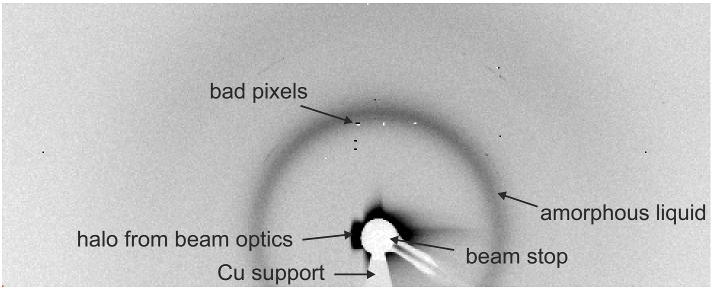

(a)

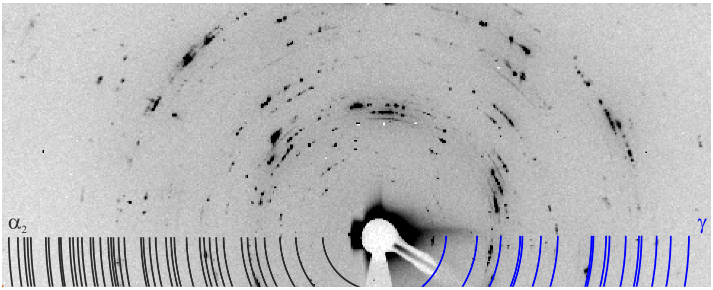

(b)

Figure 4.13: Raw 2D diffraction data obtained a) during the liquid state and b) after solidification and cooling of Ti-48Al. The theoretical positions for α_2 Ti_3Al (black) and γ TiAl (blue) are indicated.

behavior due to presence of two high temperature peritectic reactions (see Figure 2.3). Computational thermodynamics taking into account non-equilibrium conditions upon high cooling rates indicate a strong preference of Al-rich TiAl alloys to form directly primary α instead of the equilibrium primary β (see Figure 4.12). In order to validate these calculations, *in situ* rapid solidification experiments are conducted on a Ti-48Al model alloy. *In situ* XRD experiments on TiAl alloys until now were performed using levitated undercooled liquids [25, 96, 173] or laser-welding setups [174] to study phase transformation

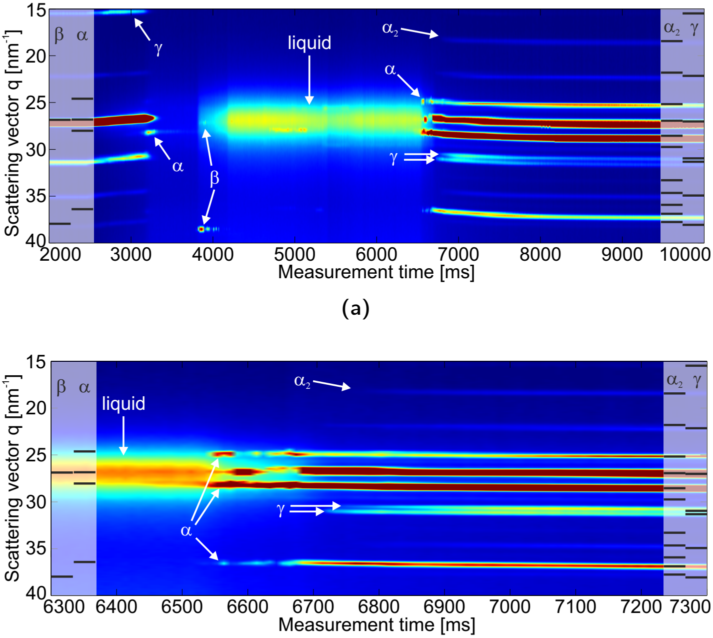

(a)

(b)

Figure 4.14: Intensity map of the scattering vector q versus time showing the phase evolution in Ti-48Al during a) complete melting cycle and b) close view on rapid solidification and cooling within 1 s. Theoretical peak positions for α, β, α_2 and γ are indicated by dashes (-). The temporal resolution is 10 ms; the graphs are composed of azimuthally integrated, background subtracted and laterally stacked diffraction spectra.

and solidification. For solid state transformations and phase evolution in multi-component alloys, *in situ* phase identification at high temperature is increasingly applied [7, 175–178]. However, none of this studies was focused in the solidification step at high cooling rates exceeding 10^3 K·s^{-1}.

The Ti-48Al specimen is heated for 4 s to achieve full melting. Continuous microXRD measurements show the formation of a liquid phase and transformation to the intermetallic α_2 Ti_3Al and γ TiAl phases after cooling (see Figure 4.13). Figure 4.14 shows the azimuthally integrated time-resolved diffraction data in the range $15 < q < 40$ nm^{-1}. Upon heating, the peak positions are shifted to lower q-values due to thermal lattice expansion (see Figure 4.14a). The intermetallic structure consisting of a high fraction of γ-phase transforms first into the disordered α-Ti structure and then transforms into the high temperature β-Ti phase. At this stage, a liquid phase is already present as indicated by the increasing broad intensity between $25 < q < 30$ nm^{-1}. While fading out, the signal of the β-phase becomes intermittent which can be explained by crystallite movement in the liquid phase. After a stable liquid state is reached for longer than 1 s, the lasers are shut off and the specimen solidifies quickly, undergoing a multitude of phase transformations within a short time (see Figure 4.14b). After the liquid state, the α-phase appears at 6650 ms before the intermetallic γ-phase is formed at 6700 ms and $\alpha \rightarrow \alpha_2$ ordering takes place at 6800 ms. A high acquisition rate is thus mandatory to observe and closely follow the solidification, transformation and ordering phenomena which take place within 150 ms. A detailed analysis of the peak evolution and non-crystalline fraction shows the coexistence of the liquid phase and theα-phase upon solidification (see Figure 4.15a). After the liquid state a fast increase of the α-peaks and decrease of the non-crystalline fraction is observed. Based on high-speed camera data, a recalescence event takes place, increasing temperature again and leading to a small plateau in the peak intensity. Due to the rapid formation of the α-phase a significant amount of latent heat is released, shortly increasing temperature and slowing down further solidification visible as the plateau in peak intensity and amorphous fraction. After the α-phase forms, the γ-phase appears quickly, within 10 to 20 ms. Simultaneously, the non-crystalline fraction decreases further. The

α and γ-phases coexist for 90 ms before α orders to the intermetallic α_2 phase. Upon further cooling, the peak intensities asymptotically approach their final values. This indicates a further relaxation of the alloy towards a state closer to the thermodynamic equilibrium.

The peak evolution versus time shown in Figure 4.15a indicates that the observed γ-phase forms from a highly Al-enriched liquid phase due to segregation. However, the surface temperature corrected data in Figure 4.15b could suggest that the observed diffraction signals are coming from γ which is formed from a parent α-phase based on the low formation temperature. If significant fractions of γ are formed rapidly by transformation from the parent α, a reduction of diffracted intensities originating from α is expected. However, the intensities of the α-phase shown in Figure 4.15 do not seem to be affected by the first formation of γ, which strengthens the proposed formation of γ directly from the liquid. This is also in agreement with the data on the non-crystalline fraction. It rapidly drops and reaches a plateau of 0.7 upon the formation of α. With decreasing temperature, the amount is reduced to 0.2 when γ is observed. The discrepancy between the data in Figure 4.15a and 4.15b on the formation of γ can be explained by an inhomogeneous lateral temperature distribution upon solidification. While the surface zone, where the temperature is calculated from the high speed camera data, is cooled below the solidus temperature and consists mostly of the α-phase, the inner core is still above the solidus temperature. This leads to a lower measured temperature on the surface than in the actual volume where γ is formed. Consequently, the formation temperature of γ from the liquid phase is underestimated based on the calculated temperature in Figure 4.15b. After complete solidification, rapid quenching takes place with solid state cooling rates similar to the rest of the upper hemisphere, which was confirmed for the *ex situ* experiments (Section 4.1.1). After solidification of α and the segregation-stabilized γ_{seg}, the α-phase starts to decompose first into $\alpha + \gamma$ and then into $\alpha_2 + \gamma$ upon further cooling. This is evident from the continuously increasing intensity of the γ peaks after their sudden appearance (see Figure 4.15a). Furthermore, this implies growth of the previously formed γ_{seg} phase into the adjacent α-dendrites; this is an effect that was observed in

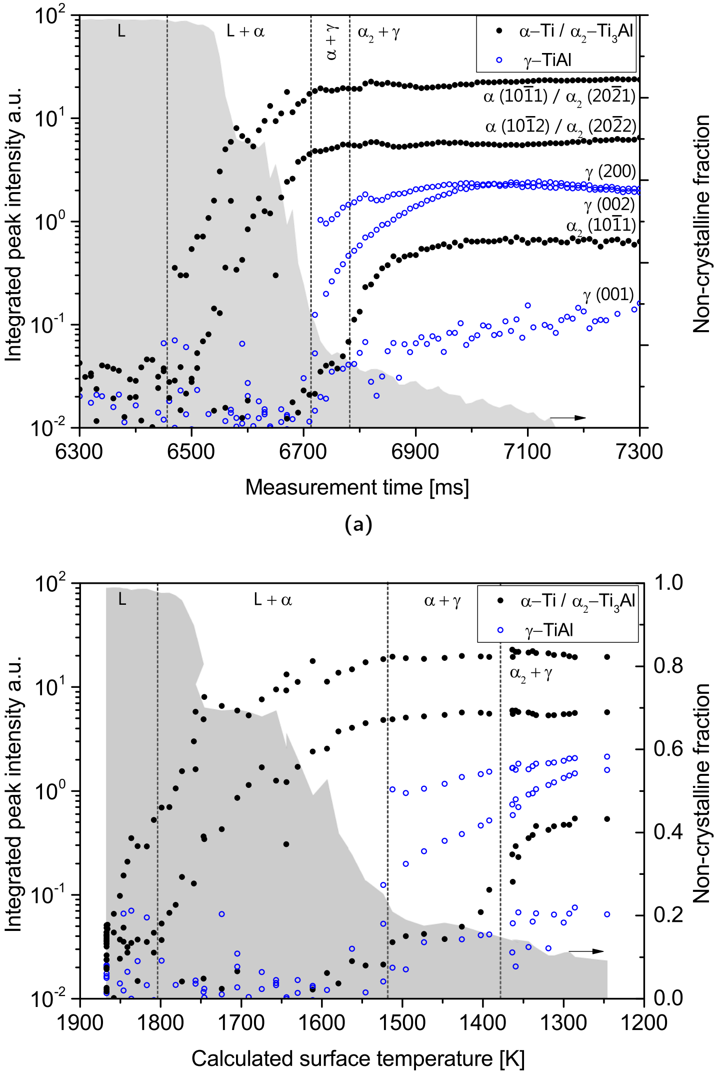

(a)

(b)

Figure 4.15: a) Integrated peak intensity and non-crystalline fraction versus time for Ti-48Al. Solidification of the α-phase (●), subsequent γ-formation (○) and α → α_2 ordering are clearly visible. Miller indices of overlapping α and α_2 peaks are shown separately (/). b) Integrated peak intensity and non-crystalline fraction versus calculated surface temperature based on high-speed camera measurements. Miller indices are omitted for clarity.

the *ex situ* experiments and which seems to be corroborated. The temperature-corrected data based on high-speed imaging is in good agreement with the established phase diagram data for Ti-Al alloys (see Figure 2.3) and previous *ex situ* results on rapidly solidified Ti-48Al (see Chapter 4.3.1). Under near-equilibrium conditions Ti-48Al shows the primary formation of the β-phase before undergoing a peritectic reaction involving the liquid, β and α-phases. In the presented measurements, no primary β could be identified in the range of $15 < q < 70$ nm^{-1}. This is in agreement with calculations based on the CALPHAD approach that takes into account non-equilibrium conditions. These calculations predict a thermodynamic preference of the α-phase over the β-phase in Al-rich alloys upon rapid solidification (see Figure 4.12). Based on the presented results, the non-equilibrium solidification and transformation of Ti-48Al follows: $L \rightarrow L + \alpha \rightarrow \alpha + \gamma_{seg} \rightarrow \alpha + \gamma + \gamma_{seg} \rightarrow \alpha_2 + \gamma + \gamma_{seg}$ under rapid solidification conditions with $1.25 \cdot 10^3$ K·s^{-1} cooling rate. In beam-based AM processed material of similar behavior a fine dendritic structure consisting of $\alpha_2 + \gamma + \gamma_{seg}$ is expected. This was indeed shown by Vilaro *et al.* [126] for laser-processed Ti-47Al-2Cr-2Nb.

To summarize, the combination of *in situ* microXRD, high-speed imaging and laser-based heating is a unique opportunity to study rapid solidification processes under conditions similar to beam-based additive manufacturing. The results in a binary Ti-48Al alloy clearly show the solidification and phase transformation sequence upon rapid solidification conditions and the deviations from equilibrium behavior. The presented experimental setup reproduces the conditions present during additive manufacturing with regards to high cooling rates, a stable liquid phase on an already solidified base and the small liquid volume formed. The possibility to estimate local temperatures and directly correlate them to diffraction signals gives deeper insights into the processes observed under non-equilibrium conditions and reliable cooling rate measurements.

4.4 Influence of the ternary alloying elements Nb and Mo

The results on the different alloy systems and individual alloys are presented in this section separately taking into account the different characteristics of microstructure formation. The technically important Ti-Al-Nb system is discussed first, followed by the Ti-Al-Mo system. Both sections are structured similarly, presenting first the observed characteristic microstructures (Figures 4.16 and 4.22) and the results from XRD measurements (Figures 4.17 and 4.23). The consolidated results showing the composition of the experimental alloys, their characteristic microstructure and the calculated equilibrium solidus surface are shown (Figures 4.18 and 4.24). Thermodynamic calculations using the CALPHAD approach to study the phase transformation behavior under non-equilibrium conditions are presented as phase selection hierarchy maps (Figures 4.19 and 4.25). The compositional dependent tendency to form γ_m in Ti-Al-Nb is presented as a color intensity map of the calculated $\left(\frac{\Delta T}{T_0^{\alpha\rightarrow\gamma}}\right)_{\max}$ (Figure 4.21). Each section is concluded with a discussion of the advantages and challenges of the observed behavior with respect to additive manufacturing.

4.4.1 Ti-Al-Nb

Ti-45Al-(3-8)Nb

The microstructure of the rapidly solidified Al-lean Ti-45Al-(3-8)Nb alloys is in all cases coarse grained α/α_2 phase (Figure 4.16a, 4.16b). XRD measurements confirm the presence of α_2 while no γ is observed (Figure 4.17). In these β-solidifying alloys the segregation tendency is low for Al. However, Nb tends to enrich together with Ti in the cores of the former β-phase dendrites and is visible as a network of slightly brighter regions throughout the alloy. This effect is typically enhanced with increasing Nb contents and consequently a stronger enrichment of Nb in the primary β-phase. In the microstructure-composition map for a cooling rate of $4.5\cdot10^3$ $\text{K}\cdot\text{s}^{-1}$ the Ti-45Al-(3-8)Nb alloys are classified as purely α/α_2 forming alloys (see Figure 4.18). Depending on the Nb content a minute fraction of β/β_0-phase, locally stabilized by the slight

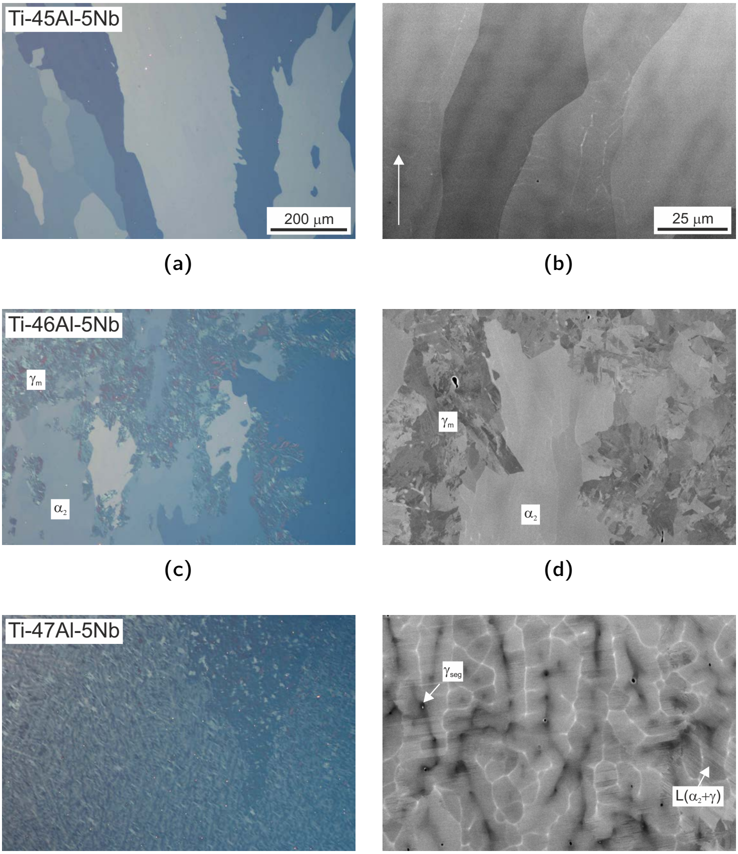
Ti-45Al-5Nb
200 μm
25 μm
Ti-46Al-5Nb
γ_m
α_2
γ_m
α_2
Ti-47Al-5Nb
γ_{seg}
$L(\alpha_2+\gamma)$

(a) (b)

(c) (d)

(e) (f)

Figure 4.16: OM and BSE SEM micrographs of the formed microstructures in rapidly solidified (a, b) Ti-45Al-5Nb, (c, d) Ti-46Al-5Nb and (e, f) Ti-47Al-5Nb at $4.5(\pm0.2)\cdot10^3$ K·s^{-1}. The scale bars in (a) and (b) are valid for (a, c, e) and (b, d, f), respectively. The solidification direction is indicated (↑) as well as the observed phases.

enrichment of Ti and Nb, may be retained in the final microstructure. The calculated solidus surfaces overlayed on the experimental results in Figure 4.18 indicate the β-stabilizing effect of Nb additions and the accompanied extension of the L + β solidus surface towards higher Al contents with increasing Nb additions. While the binary Ti-45Al undergoes a peritectic reaction upon solidification in equilibrium conditions, the Nb containing Ti-45Al-(3-8)Nb alloys are β-solidifying alloys. For the binary Ti-45Al alloy, however, a metastable extension of the β-solidification regime due to a combination of limited diffusion conditions and kinetic aspects upon rapid cooling was proposed earlier (see Chapter 4.3.1). Thus all Ti-45Al-(3-8)Nb alloys are expected to solidify solely by the β-phase upon rapid solidification. Consequently, similar coarse grained α/α_2 microstructures are formed upon the following solid state phase transformations according to $L \rightarrow L + \beta \rightarrow \beta \rightarrow \beta + \alpha \rightarrow \alpha \rightarrow \alpha_2$. The processability of these Al-lean alloys using beam-based AM technology is expected to be similar based on the formed microstructure. However, kinetic

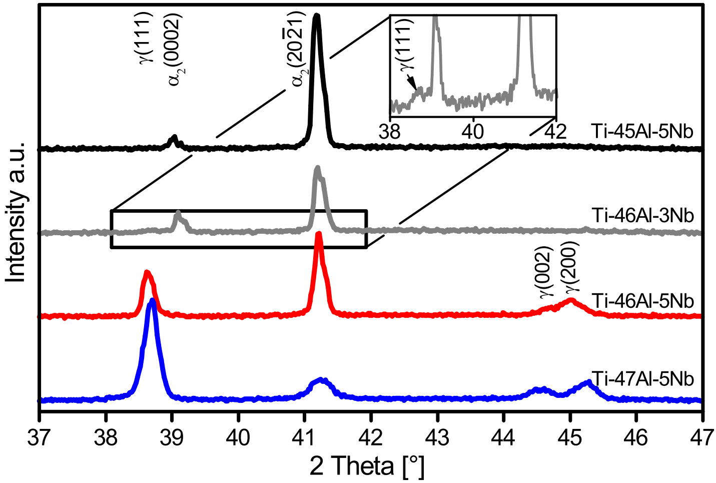

Figure 4.17: XRD spectra of Ti-46Al-3Nb and Ti-(45-47)Al-5Nb solidified at $4.5(\pm 0.2)\cdot 10^3$ $K\cdot s^{-1}$. The characteristic peaks for the γ and α_2 phases are indicated. The inset shows an enlarged section for Ti-46Al-3Nb and the position of the spurious γ(111) peak (↓).

aspects not covered by the experiments performed may additionally influence processing and following heat treatments due to the low diffusivity of Nb in the microstructure [179, 180].

Ti-46Al-(3-8)Nb

The addition of Nb changes the microstructure formation from a coarse grained α/α_2 microstructure in the Ti-46Al-3Nb alloy to a $\alpha/\alpha_2 + \gamma_m$ microstructure in Ti-46Al-(5-8)Nb. While the Nb-rich alloys show no decomposition of the α/α_2-phase into lamellar $\alpha_2 + \gamma$, local formation of γ_m is observed as visible in BSE SEM micrographs (see Figure 4.16c, 4.16d). XRD measurements also show the formation of the γ phase beside the major α_2 phase in these alloys. In the case of Ti-46Al-3Nb only a spurious shoulder is observed at

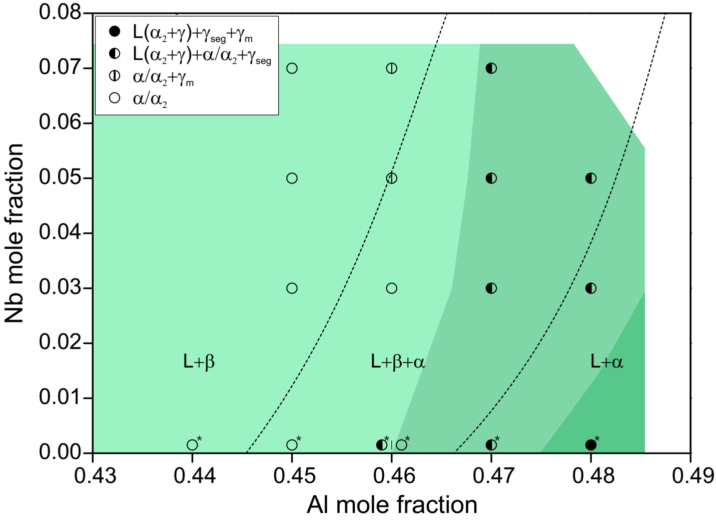

Figure 4.18: Composition-microstructure map of Ti-(44-48)Al-(0-8)Nb solidified at 4.5(±0.2)·10^3 K·s^{-1}. Data from the study of the binary system is marked (*). Overlayed is the calculated solidus surface based on a published Ti-Al-Nb assessment [23]. The compositional spaces where a similar microstructure is observed are shown tentatively with a common shading to guide the reader's eye.

the γ(111) peak position while the spectrum of Ti-46Al-5Nb clearly shows the presence of γ (see Figure 4.17). The calculated equilibrium solidus surface shows that the Nb-rich alloys are β-solidifying while the Nb-lean alloys are passing the L + β + α phase field. Based on limited diffusion considerations, the binary Ti-46Al alloy is at a composition, where the β- and α-phase directly compete based on their thermodynamic stability at the same composition (see Figure 4.12). With increasing Nb additions, this calculated point is shifted towards higher Al contents (see Figure 4.19). Combining the fact that the Nb-rich alloys are β-solidifying under equilibrium conditions and the metastable extension of β-solidification towards higher Al contents, the experimental results are in good agreement with the CALPHAD calculations regarding the solidification path. The local formation of massive γ_m in a coarse α/α_2 matrix is only observed in the Nb-rich Ti-46Al-(5-8)Nb

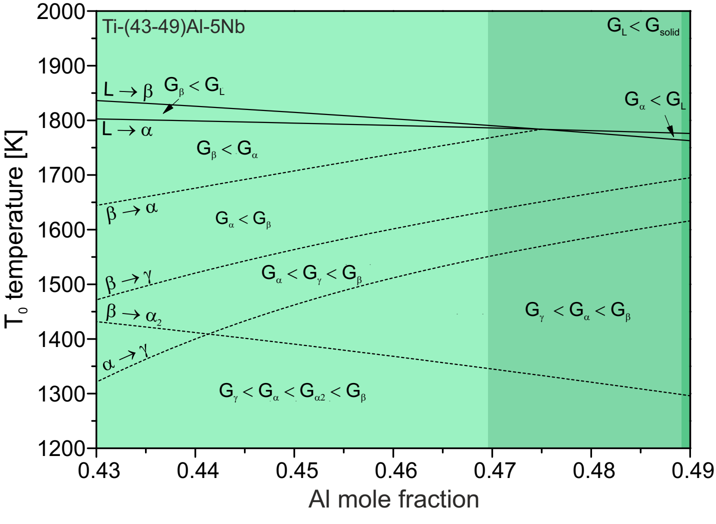

Figure 4.19: Phase selection hierarchy map assuming composition-invariant transformations for Ti-(43-49)Al-5Nb. The corresponding phase transformations are indicated as well as the relative order of the underlying Gibbs energies (G) of the phases involved. The green shaded areas correspond to the shading applied in Figure 4.18.

alloys. Comparing the phase selection hierarchy maps of binary Ti-(43-49)Al to ternary Ti-(43-49)Al-5Nb shows shifted T_0 temperature curves for the solidification as well as for solid state phase transformations (compare Figures 4.12 and 4.19). The stabilizing effect of Nb on the β-phase increases the stability range of β on the expense of the α-phase leading to a thermodynamic preference of the β-phase up to higher Al contents compared to the binary system. While $T_0^{\alpha\rightarrow\gamma}$ and $T_0^{\beta\rightarrow\gamma}$ are only slightly affected, the $T_0^{\alpha\rightarrow\alpha_2}$ and $T_0^{\beta\rightarrow\alpha_2}$ temperatures are strongly suppressed. Consequently, the temperature difference and thus also the time difference between the calculated formation of γ and the subsequent $\alpha \rightarrow \alpha_2$ ordering is enhanced by Nb additions. It is a known phenomenon in TiAl alloys that the nucleation of γ from α is suppressed at high cooling rates although $T_0^{\alpha\rightarrow\gamma} > T_0^{\alpha\rightarrow\alpha_2}$ [108]. Consequently, a certain amount of undercooling below $T_0^{\alpha\rightarrow\gamma}$ is necessary to nucleate the γ-phase. If at this point $T_0^{\alpha\rightarrow\alpha_2}$ is already reached, the alloy undergoes $\alpha \rightarrow \alpha_2$ ordering without γ-formation. The calculated $\left(\frac{\Delta T}{T_0^{\alpha\rightarrow\gamma}}\right)_{\max}$ for Ti-(43-49)Al-(0-8)Nb shows a clear effect of Nb additions for all alloys in this work (see Figure 4.21). However, the highest values of $\left(\frac{\Delta T}{T_0^{\alpha\rightarrow\gamma}}\right)_{\max}$ are reached for the simultaneously Al- and Nb-rich alloys. For the β-solidifying Ti-46Al-(0-8)Nb alloys at the studied cooling rate, $\left(\frac{\Delta T}{T_0^{\alpha\rightarrow\gamma}}\right)_{\max}$ is subcritical for Nb < 5 at.% while the obtained undercooling or time is sufficient for γ-formation if Nb≥5 at.%. As the Nb-rich Ti-46Al-(5-8)Nb alloys are near β- or fully β-solidifying, only slight Al segregation is typically observed which leads to the observed $\alpha/\alpha_2 + \gamma_m$ microstructure according to transformation scheme of $L \rightarrow L + \beta \rightarrow \beta \rightarrow \beta + \alpha \rightarrow \alpha \rightarrow \alpha + \gamma_m \rightarrow \alpha_2 + \gamma_m$. In the binary Ti-Al system the microstructure formation of Ti-46Al was found to be sensitive to the applied cooling rate in the range of 10^2 to 10^4 $K \cdot s^{-1}$ (see Chapter 4.3.1). This sensitivity is also confirmed for Ti-46Al-3Nb with a coarse α/α_2 microstructure formed at $4.4 \cdot 10^3$ $K \cdot s^{-1}$. For a reduced characteristic cooling rate of $1.9 \cdot 10^3$ $K \cdot s^{-1}$ a microstructure consisting of lamellar $\alpha_2 + \gamma$, massive γ_m as well as α/α_2 is observed. The lower cooling rate and consequently longer time available for phase transformation allows for local nucleation of the γ-phase and decomposition of the supersaturated α_2 grains. For processing using AM techniques, alloys of the Ti-46Al family show the highest sensitivity on cooling rate and composition. This may affect process stability and finally part performance due to locally different microstructures and properties depending on process fluctuations and compositional variations in commercial alloys.

Ti-(47-48)Al-(3-8)Nb

The Al-rich alloys studied in this work typically exhibit a dendritic microstructure consisting of lamellar $\alpha_2 + \gamma$, ordered α/α_2 and inter-dendritic γ_{seg}, formed directly from of the remaining Al-enriched liquid phase. The underlying coarse domains of presumably high temperature α phase are observed in OM under polarized light (see Figure 4.16e, 4.16f). The presence of a dual phase structure is confirmed by XRD. The γ is the major phase in these alloys based on relative intensities of the strongest peaks for the two phases, $\gamma(111)$ and $\alpha_2(20\bar{2}1)$, respectively (see Figure 4.17). The observed orthogonal dendrite morphology indicates β-dendrite formation from the liquid phase in the Al-rich alloys and at the studied cooling rates. This is in good agreement with both the equilibrium phase diagram and T_0 temperature calculations. The former predicts primary β-formation, while the latter shows that the β-phase is thermodynamically preferred over α in the Ti- and Nb-rich alloys up to Al contents

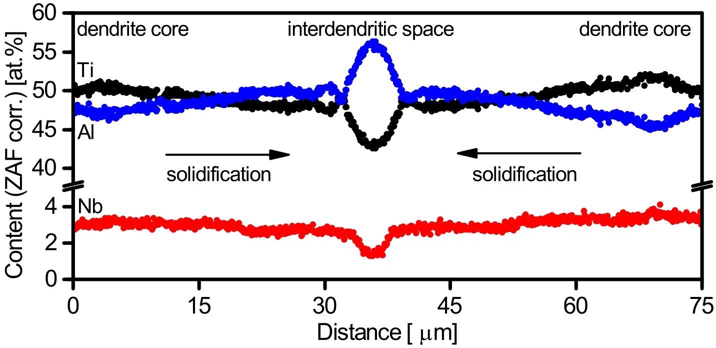

Figure 4.20: Segregation tendencies of Ti, Al and Nb in a Ti-48Al-3Nb master alloy. The scan direction is perpendicular to two adjacent dendrites. Enrichment of Ti and Nb in the dendrite core and their depletion in the inter-dendritic space is shown.

around 48 at.%. In examined specimens, the bright ribs of former β-phase in the cores of the observed dendrites are typically enriched in Ti and Nb and depleted in Al (see Figure 4.20). Consequently, the Nb content in the solid phase decreases with proceeding solidification leading finally to a Ti and Nb depleted and Al-rich liquid phase which solidifies by L → L + γ_{seg} → γ_{seg}. In this situation, a single phase selection hierarchy map based on T_0 temperature calculations assuming a homogeneous elemental distribution due to limited diffusion is no more sufficient to explain a complete solidification sequence. However, using several phase selection hierarchy maps for Nb-rich alloys (see Figure 4.19) for the beginning of solidification and for the binary Ti-Al alloys (see Figure 4.12) for the final stages, allows to predict the local changes in solidification and phase transformation behavior. The direct formation of the γ_{seg}-phase from the Al-enriched liquid phase at the final stages of solidification

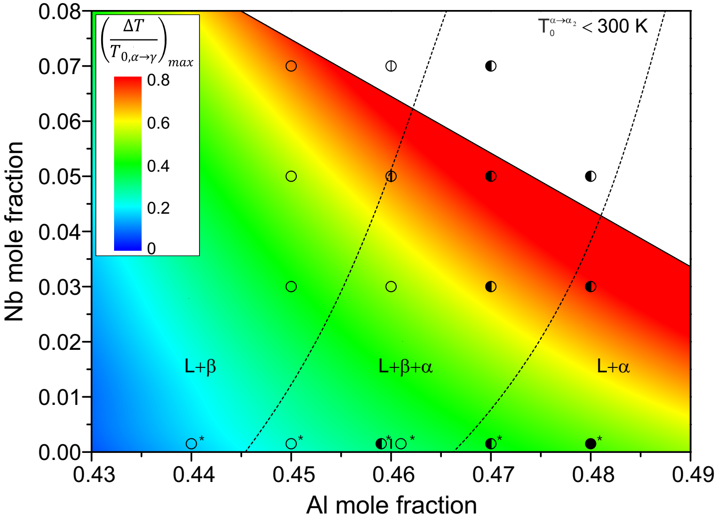

Figure 4.21: Tendency for formation of massive γ_m based on the calculated value of $\left(\frac{\Delta T}{T_0^{\alpha\to\gamma}}\right)_{\text{max}}$ for Ti-(43-49)Al-(0-8)Nb. The compositional area where $T_0^{\alpha\to\alpha_2} < 300$ K is depicted in white. Higher values (red) correspond to an increased theoretical tendency for the occurrence of the $\alpha \to \gamma_m$ transformation.

also outruns the formation of a γ_m-phase from the parent α-phase as in close distance the inter-dendritic γ_{seg}-phase provides a preferential site for further growth and decomposition of the adjacent α-dendrites into lamellar α_2 + γ. At the same time, the α-transus temperature is increasing with increasing Al content in Ti-Al alloys (see Figure 2.3). Compared to Al-lean alloys, the α-phase forms earlier in the transformation sequence at higher temperatures. Consequently, diffusion in the α-phase is faster and a state closer to equilibrium can be reached more easily as in Al-lean alloys. Additionally, the equilibrium composition for the γ-phase at a specific temperature is independent of the Al content in the dual phase region α + γ. Only its equilibrium fraction is varied. Naturally, the composition of the Al-rich Ti-Al-(Nb, Mo) alloys of interest here are closer to the ideal composition of γ. Thus, not only is diffusion facilitated by the presence of the α phase at higher temperature, the required amount of diffusion is also lower at the same time. The combination of the discussed effects explains why the Al-rich Ti-(47-48)-(3-8)Nb alloys typically show no excessive formation of γ_m even though the calculated $\left(\frac{\Delta T}{T_0^{\alpha\rightarrow\gamma}}\right)_{\mathrm{max}}$ reaches or exceeds the critical values observed in Ti-46Al-(5-8)Nb (see Figure 4.21). However, if such Al- and Nb-rich alloys are later homogenized in the α-field and subsequently quenched to low temperatures, the formation of massive γ_m is expected based on the results. Such conditions may be deliberately imposed by a heat treatment or occur naturally in a layer-wise AM process, where earlier deposited layers in a built structure are exposed to several heating and cooling cycles. The formation of predominantly lamellar microstructures in the Al-rich Ti-Al-Nb alloys at high cooling rates offers the potential to directly produce parts with a microstructure close to conventionally applied TiAl alloys. This eliminates the need for high temperature heat treatments generally applied to produce fully and near lamellar microstructures. While these heat treatment procedures are well studied in conventionally produced TiAl alloys, the possible production of hybrid components using AM techniques may restrict heat treatment temperatures. In such cases, alloys forming out-of-process lamellar microstructures may be chosen. Due to the directional solidification, the finally formed lamellar microstructure is highly textured. Depending on build direction, the final properties of a part can be adjusted and oriented in a most beneficial manner.

4.4.2 Ti-Al-Mo

For the Ti-45Al-(1-2)Mo alloys a coarse grained microstructure consisting of α/α_2 phase is observed after rapid solidification (Figure 4.22a). Additionally an increasing amount of retained high temperature β/β_0-phase is observed with increasing Mo contents in BSE SEM micrographs. EDX measurements suggest a reduced Al content of 42.5-43 at.% Al and a Mo content of 2.5-3 at.% in this phase. This is also confirmed by XRD measurements where a $\beta_0(110)$ peak is observed in Ti-45Al-2Mo (Figure 4.23). Although the additional β/β_0-phase is not observed in binary Ti-Al alloys, the similar appearance of the alloy microstructure in OM and the apparently similar mechanism of microstructure formation justify the same classification of the Al-lean Ti-Al-Mo alloys as it was proposed in Sections 4.3.1 and 4.4.1 for the Al-lean Ti-Al and Ti-Al-Nb alloys (Figure 4.24). This result is in good agreement with the calculated solidus surface for the Ti-Al-Mo alloys in this study. With an increasing Mo content, the Ti-45Al-(1-2)Mo alloys solidify solely by the β-phase under equilibrium and non-equilibrium conditions. The final coarse grained microstructure with remaining β-phase is then formed during the following solid state phase transformations according to $L \rightarrow L + \beta \rightarrow \beta \rightarrow \beta + \alpha \rightarrow \beta/\beta_0 + \alpha \rightarrow \beta/\beta_0 + \alpha/\alpha_2$. Based on phase diagram information, the β/β_0-phase is expected to be a stable phase in Mo-rich Ti-(45-47)Al-2Mo alloys, while it is only metastable in the Mo-lean Ti-(45-47)Al-1Mo alloys. This is reflected in the relative amount of retained β/β_0-phase at room temperature, which is significantly larger in the Mo-rich alloys. While the formation of a coarse grained microstructure is observed independently from the Mo content in the Ti-45Al-(1-2)Mo alloys, a compartmentalization effect of the α/α_2-phase is observed. The retained β/β_0-phase divides the coarse α/α_2-grains into smaller compartments or sub-grains that share a common crystal orientation over long distances as observed by OM under polarized light. The microstructure consisting of sub-grains, partly or fully separated by the β/β_0-phase, is expected to show enhanced ductility at elevated temperatures of these alloys. The concept of enhanced ductility by the controlled stabilization of a β-phase at elevated temperatures is successfully applied for the TNM alloys [6, 134].

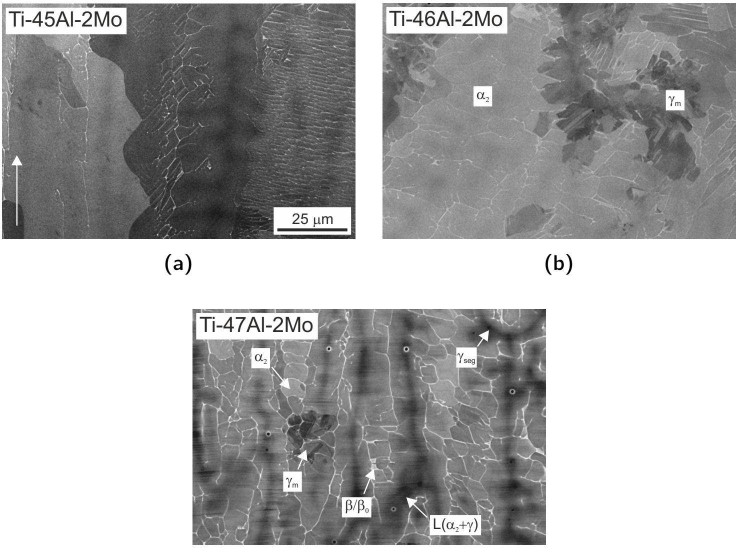

(a) **(b)**

(c)

Figure 4.22: BSE SEM micrographs of formed microstructures in rapidly solidified a) Ti-45Al-2Mo, b) Ti-46Al-2Mo and c) Ti-47Al-2Mo at $4.5(\pm0.2)\cdot10^3$ K·s^{-1}. The scale bar in a) is valid for (a-c). The solidification direction is indicated (↑).

Applying this concept in alloy development for AM may allow to dissipate thermal stresses building up during processing by plastic deformation of a ductile β-phase. In the Ti-46Al-(1-2)Mo alloys a combined microstructure consisting of coarse α/α_2-grains, retained β/β_0-phase and massively transformed γ_m is observed (Figure 4.22a). XRD measurements also confirm a small amount of γ by the presence of spurious $\gamma(002)$ and $\gamma(200)$ as well as $\gamma(111)$ in Ti-46Al-1Mo (Figure 4.23). The combination of a near β- or fully β-solidifying alloy with increased Al and Mo content leads to a stabilization of the γ-phase and consequently transformation of the parent α-phase during cooling. A similar effect is observed in Ti-Al-Nb alloys with intermediate Al and high Nb contents. Based on the observed microstructure, the phase transformation sequence is expected to follow L → L + β (→ L + β + α/ → β) → β + α → α + β/β_0 → α + γ_m + β/β_0 → α/α_2 + γ_m + β/β_0. For the Mo-rich alloy, solidification very close to or completely by the β-phase is expected (Figure 4.24). For the Mo-lean Ti-46Al-1Mo alloy the equilibrium solidification path crosses the L + β + α phase field. The observed similarity of the coarse microstructures in both the Mo-lean and -rich Ti-46Al-Mo alloys suggests a possible metastable extension of the β-solidification behavior to lower Mo-contents. The Al-rich Ti-47Al-(1-2)Mo alloys formed dendritic microstructures containing lamellar α_2 + γ colonies, α/α_2-grains, retained β/β_0-phase as well as massively transformed γ_m (Figure 4.22c). XRD measurements show a dual phase α_2 + γ structure with high γ content. Beside the retained β/β_0-phase, that is stabilized by the increased Mo content, this microstructure is comparable to the results found for binary Ti-47Al and the Al-rich Ti-Al-(3-7)Nb alloys in Sections 4.3.1 and 4.4.1. Similar to the Al-lean Ti-45Al-(1-2)Mo alloys, the retained β/β_0-phase effectively separates individual grains being transformed variants of the parent α-phase. The sepa-

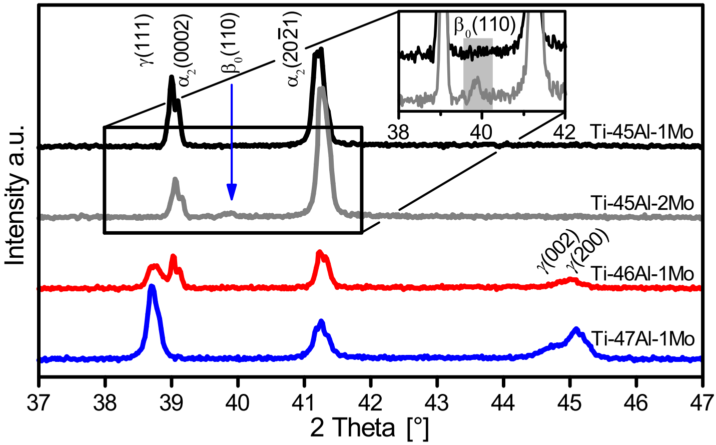

Figure 4.23: XRD spectra of Ti-(45-47)Al-1Mo and Ti-45Al-2Mo solidified at 4.5(±0.2)·10^3 K·s^{-1}. The characteristic peaks for the γ and α_2 phases are indicated. The inset shows an enlarged section for Ti-45Al-(1-2)Mo and the presence of a small fraction of β_0-phase in the material (↓)

ration effect is strong enough to allow the formation of α/α_2-grains adjacent to lamellar $\alpha_2 + \gamma$ colonies. In the grains along the inter-dendritic spaces, characterized by an Al enrichment due to segregation upon solidification, the parent α-phase decomposes into $\alpha_2 + \gamma$. The Al enrichment sufficiently stabilizes the γ-phase to allow for decomposition. In case of sufficiently strong segregation also direct formation of γ from the liquid may occur and act as a seeding site for further $\alpha \rightarrow \alpha_2 + \gamma$ decomposition. These grains are only rarely interrupted by retained β/β_0-phase and extend vertically over length scales of up to 100 μm. In the cores of the former dendrites and adjacent to the decomposed grains, the α-phase is compartmentalized by the β/β_0-phase. These isolated grains are not Al-enriched and lack the formation of any seeding γ-phase. Consequently, these grains show $\alpha \rightarrow \alpha_2$ ordering. Occasionally, the

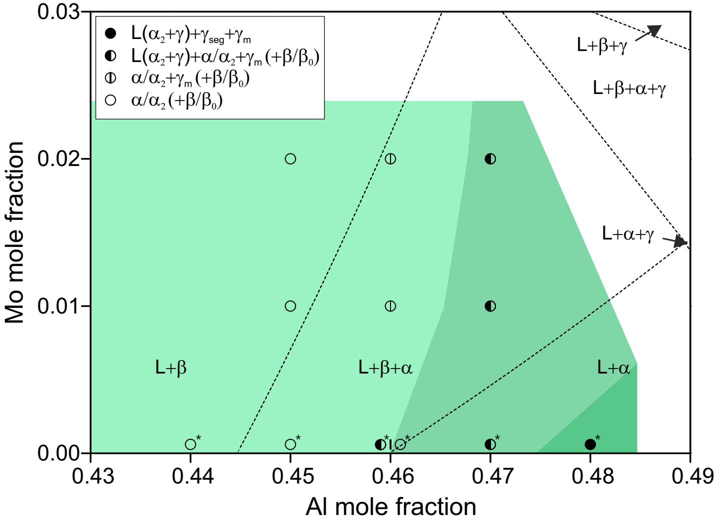

Figure 4.24: Composition-microstructure map of Ti-(44-47)Al-(0-2)Mo solidified at 4.5(±0.2)·10^3 K·s^{-1}. Data from the study of the binary system is marked (*). Overlayed is the calculated solidus surface based on a published Ti-Al-Mo assessment [17]. The compositional spaces where a similar microstructure is observed are shown tentatively with a common shading to guide the reader's eye.

formation of massive γ_m is observed. Also this reaction is efficiently stopped at the interface to the β/β_0-phase. Based on the observed microstructure and thermodynamic information, the proposed non-equilibrium solidification and phase transformation path for Al-rich Ti-47Al-(1-2)Mo alloys follows $L \rightarrow L + \beta \rightarrow L + \beta + \alpha \rightarrow \alpha + \beta/\beta_0 \rightarrow \alpha + \beta/\beta_0 + \gamma_m \rightarrow L(\alpha_2+\gamma) + \alpha/\alpha_2 + \beta/\beta_0 + \gamma_m$. In general, similar classes of alloy behavior are observed in the studied Ti-Al-Mo alloys as in the Nb-containing alloys. In the case of Mo, the alloying levels to produce a certain effect are lower, which can be attributed to its stronger β-stabilizing effect (Figures 4.18 and 4.24). Combining this effect with a low diffusivity and the tendency for enrichment in the β-dendrite cores, a fine network of β/β_0-phase can be stabilized in controlled amounts. This seems to be a promising way for future alloy development to reduce stresses in

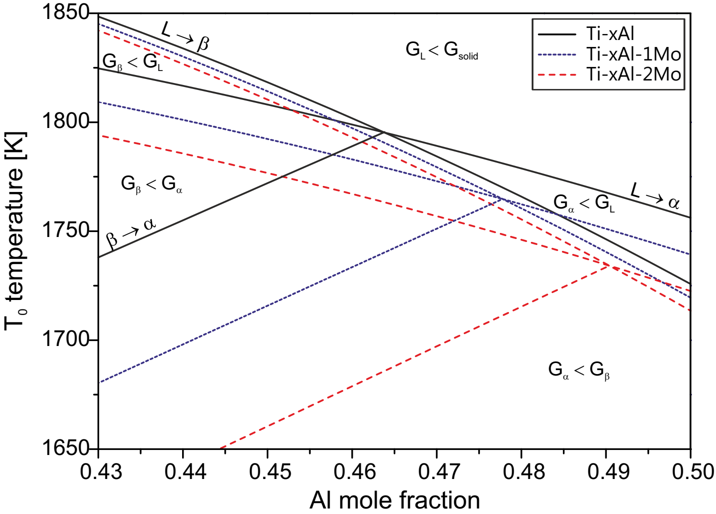

Figure 4.25: Calculated phase selection hierarchy map assuming composition-invariant transformations for solidification and the $\beta \rightarrow \alpha$ transformation for Ti-(43-50)Al-(0-2)Mo. The results for binary Ti-Al (solid), ternary Ti-Al-1Mo (short dashed, blue) and ternary Ti-Al-2Mo (long dashed, red) are shown. The corresponding phase transformations are indicated as well as the relative order of the underlying Gibbs energies (G) of the phases involved.

processing. In this respect, also other strongly β-stabilizing alloying elements as W and Ta or multi-element combinations are of interest. The TNM alloy family contains a combination of Nb and Mo to stabilize a ductile β-phase at the deformation temperature [6]. However, the alloy was developed for conditions which are close to equilibrium, namely high-temperature forging, especially when compared to the non-equilibrium conditions in AM processing. This study and earlier work clearly show that under such conditions an extension of the β-solidification regime is to be expected. Consequently, the full equilibrium stabilization of significant amounts of β-phase at elevated temperatures may lead to exceedingly high amounts of retained β-phase in AM processed alloys of this kind. This is supported by the results of Löber *et. al* [134] producing a predominantly $\beta + \alpha_2$ containing microstructure after selective laser melting of a TNMB1 alloy. The approach of combining rapid solidification experiments with computational thermodynamics clearly shows the influence of ternary additions of Nb and Mo on alloy transformation behavior in Ti-(44-48)Al-(3-8)Nb and Ti-(44-47)Al-(1-2)Mo alloys. It was shown that both elements have strong effects on the T_0 temperatures of the relevant phase transformations and solidification. This affects microstructure formation which can be roughly classified into Al-lean Nb- or Mo- alloyed alloys forming a predominantly α/α_2-containing microstructure after β-solidification, Al-rich alloys which produce a lamellar $\alpha_2 + \gamma$ microstructure containing additional phases (γ_{seg}, γ_m and β/β_0) and the intermediate Al-containing alloys which show a high sensitivity of microstructure formation on composition and cooling rate.

4.5 Alloy design of titanium aluminides for additive manufacturing

The results generated and presented in this chapter on binary Ti-Al and ternary Ti-Al-Nb and Ti-Al-Mo can directly be applied for alloy design and selection for processing involving high cooling rates. These processes are not limited to AM, but can also be welding of sintered or cast parts as well as rapid heat treatments or atomization of melts for powder production. The consolidated results are discussed in the following section with regard to alloy selection and involved considerations. The selection of a specific alloy for the production of ODS TiAl is discussed in detail in Chapter 5. The selection of a specific titanium aluminide alloy needs to take into account among others the influence of alloying elements, the processing conditions, the service conditions, specific requirements for mechanical performance and homogeneity, alloy availability and cost. It is evident, that compromises need to be accepted in many cases and focus on only one criterion may lead to scientifically interesting but technically irrelevant solutions.

4.5.1 Design rules for titanium aluminides

The influence of alloy composition and the processing conditions can be consolidated into a Schaeffler-type diagram combining the results of Ti-Al, Ti-Al-Nb and Ti-Al-Mo (Figure 4.26). In order to overlay the data, the equivalent Nb content Nb_{eq} is calculated as Nb_{eq} = [Nb] + 3.9·[Mo] according

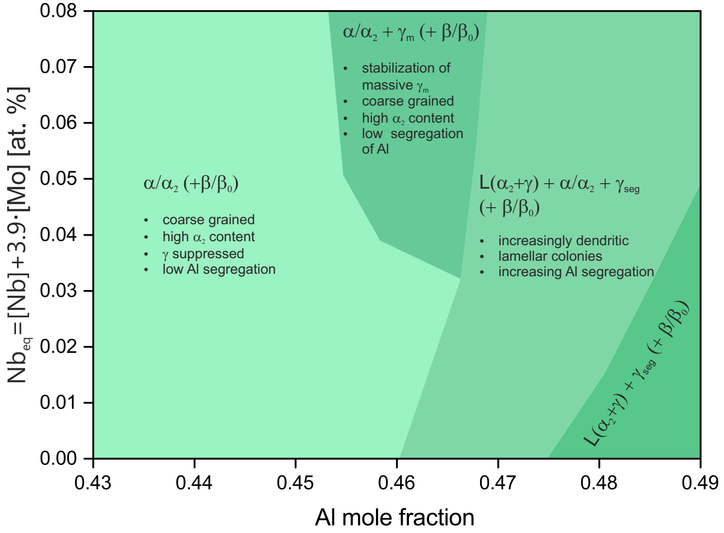
$\alpha/\alpha_2 + \gamma_m$ (+ β/β_0)
• stabilization of massive γ_m
• coarse grained
• high α_2 content
• low segregation of Al
α/α_2 (+β/β_0)
• coarse grained
• high α_2 content
• γ suppressed
• low Al segregation
L(α_2+γ) + α/α_2 + γ_{seg} (+ β/β_0)
• increasingly dendritic
• lamellar colonies
• increasing Al segregation
L(α_2+γ) + γ_{seg} (+ β/β_0)
Nb_{eq}=[Nb]+3.9·[Mo] [at. %]
0.08
0.07
0.06
0.05
0.04
0.03
0.02
0.01
0.00
0.43
0.44
0.45
0.46
0.47
0.48
0.49
Al mole fraction

Figure 4.26: Schaeffler-type diagram combining the results of the influence of composition in Ti-Al-(Nb, Mo) on microstructure formation at cooling rates of $4.5 \cdot 10^3$ K·s^{-1}.

to Clemens and Mayer [35]. The pre-factor for Mo corresponds to the much higher potency of Mo with regard to stabilization of the β-phase. Four distinct areas can be distinguished based on the consolidated data. First and most importantly, the region of Al-lean alloys where the formation of γ is suppressed and a microstructure rich in α_2 is obtained. Depending on the content of slow diffusion Nb or Mo additionally retained β/β_0 is observed. This effect increases with increasing alloying levels. A second region is observed at intermediate Al levels and high values of Nb_{eq}. In this region the thermodynamic stability of γ is sufficient to avoid complete suppression. Consequently, the microstructure additionally contains significant amounts of massively transformed γ_m compared to the Al-leaner or lower alloyed alloys. Compared to the remaining areas, the first two show very low segregation of Al and no formation of a low melting inter-dendritic liquid phase. The third area shows Al-segregation and has an increasingly dendritic microstructure. However, still a high fraction of α_2 is present combined with β/β_0 stabilized by segregated Nb or Mo. Alloys in the last area show pronounced segregation and formation of inter-dendritic γ in a mostly fine lamellar microstructure.

Using this diagram, the behavior of binary and ternary TiAl alloys in the studied compositional range can be predicted. For higher-order alloys, as for example TNM alloys, the drawn conclusions are an extrapolation from the ternary sub-systems. However, data obtained by SLM on this alloys show high contents of β/β_0 and α_2 after processing [134, 135]. The former is caused by the strong stabilization of β by the low Al content and slow diffusing Nb and Mo, the latter is a consequence of suppressed formation of γ upon cooling. Both effects are predicted by the obtained data. Also the behavior of the Ti-48Al-2Cr-2Nb alloy family are well predicted. It can be concluded that although not directly experimentally measured, the behavior of a wide range of TiAl alloys can be predicted. This renders Figure 4.26 in the most important tool for a first selection of TiAl alloys taking into account composition and processing conditions.

Although crucial for part production, compatibility with the processing conditions is irrelevant for the alloy when subjected to service conditions later on. There the mechanical performance and degradation behavior of the alloys is decisive. Higher strength is typically achieved with high alloying levels of Nb in Al-lean alloys to stabilize a high amount of α_2 in a stable microstructure. Good oxidation resistance is typically achieved in either Al-rich alloys or in highly Nb-alloyed Al-lean alloys. Chemical homogeneity is obtained by using β-solidifying alloys or extensively heat treating segregated Al-rich alloys. Alloy cost and availability are a question of the amounts used combined with the cost for the individual alloying elements. The alloying elements Nb, Mo and also W are becoming elements of strategic relevance with increasing cost on the world market. Alloy selection is thus a complex question that can only be answered considering the various factors. However, three exemplary cases for potential alloys are discussed here:

- **Ti-(43-45)Al-(0-8)Nb$_{\text{eq}}$** The TNB and TNM alloy families are part of this class of alloys. After AM a non-equilibrium, supersaturated α_2-rich microstructure is formed. These alloys need post-processing heat treatments to establish the desired microstructure in the final part. After heat treatment these alloys retain a high content of α_2 and have thus superior strength to Al-rich alloys. The solidification path ensures no segregation of Al and thus a very low risk of hot-cracking or segregation of added particles. However, the formation of brittle supersaturated α_2 does not attenuate the problem of cracking due to thermal stresses. Additionally, low textured material is obtained (see Chapter 5). The alloying level of Nb and Mo is depending on the required strength, oxidation resistance and amount of retained β/β_0 for enhanced high temperature ductility [6].

- **Ti-(47-48)Al-(1-8)Nb$_{\text{eq}}$** The GE alloy family with its most prominent member Ti-48Al-2Cr-2Nb is part of this category as well as the γ-TAB alloy. After AM a microstructure containing fine lamellar colonies and local α_2 is formed. This microstructure can be further stabilized or directly be applied. The amount of α_2 in equilibrium is lower in these alloys thus their strength is reduced compared to the first group. Due to the enhanced Al-content, these alloys have better oxidation resistance, which can be further increased by additions of Nb, Mo or W. Additionally, the low temperature ductility reaches maximum values around 48 at.% Al [28]. Upon solidification, strong Al-segregation is observed, rendering these alloys prone to hot-cracking. Based on the solidification path, a strongly textured component is obtained. Such behavior can be beneficial or problematic, depending if the part orientation and process control allow the alignment of this material texture to take advantage of the anisotropic properties.

- **Ti-(45.5-46.5)Al-(3-8)Nb$_{eq}$** The γ-MET alloy, produced by Plansee for powder metallurgy, is an alloy of this category. Upon AM a microstructure similar to the Al-lean alloys is expected. Beside the supersaturated α_2 matrix, γ is formed massively. Such an alloy needs heat treatment after processing to obtain the desired microstructure. An advantage over the Al-richer alloys is the formation of γ without strong accumulation of Al due to the massive, composition-invariant formation. Upon heat treatments, this reaction can also be used for alloy refinement [31]. However, the compositional space for this class is rather narrow which is problematic for AM at high energy densities and Al evaporation. Based on its composition, this alloy class combines enhanced Al-content and Nb$_{eq}$-alloying levels for good oxidation resistance and strength.

4.6 Conclusions

- A droplet-based rapid solidification technique is developed to study the influence of composition and cooling rate on microstructure formation under non-equilibrium conditions. Controlled cooling rates in the relevant range of 10^3 to 10^4 K·s^{-1} are achieved with this technique.

- A synchrotron based *in situ* microXRD setup combining phase identification and rapid solidification is presented to study the phase evolution upon rapid solidification and cooling with high spatial (20 µm) and temporal resolution (100 Hz).

- A computational framework based on T_0 temperatures is introduced allowing predictions on phase stabilities and changed solidification behavior upon rapid solidification.

- The behavior of Ti-Al alloys depends strongly on composition, whereas the cooling rate sensitivity was found to be low. Al-lean alloys form a coarse grained supersaturated α_2-rich microstructure without Al segregation. Al-rich alloys form a microstructure containing fine lamellar colonies and local α_2 with strong Al segregation and interdendritic γ. Intermediate alloys form a mixed microstructure consisting of coarse α/α_2 grains, local γ-phase and lamellar $\alpha_2 + \gamma$.

- A Schaeffler-like diagram is constructed for the alloying effects of Nb and Mo at a cooling rate of $4.5 \cdot 10^3$ K·s^{-1}. The three main classes of alloy behavior are determined based on experimental data and computational results.

- The behavior of existing TiAl alloys is discussed with regards to AM processing.

The combination of key experiments using adapted experimental techniques to reproduce the real processing conditions in terms of cooling rates and modified concepts based on the CALPHAD approach allows to study and predict alloy behavior under AM conditions. The presented data and explanations serve as a guideline to estimate the alloy behavior under AM conditions to select alloys for detailed studies and testing. Classifying alloys into various groups allows a fast decision on where to spend increased effort for accelerated alloy design, selection and finally application.

5 Microstructure and oxide particle stability in a novel ODS γ-TiAl alloy processed by spark plasma sintering and laser additive manufacturing

The development of a novel ODS β-solidifying γ-TiAl alloy for powder-based consolidation is described in this chapter. Alloy selection has been performed based on computational thermodynamics and previous experimental work (see Chapter 4) and taking into account service and processing conditions. Results from consolidation tests by SPS, SLM and DMD are compared in terms of the resulting microstructures, its evolution upon thermal annealing and size of the incorporated dispersoids. Finally, the influence of the processing energy density on dispersoid size and the processability of the alloy are discussed. The complete chapter has been submitted as a publication to *Acta Materialia* [181].

5.1 Alloy design and selection

The selection of the alloy serving as matrix for oxide particle strengthening and the second phase itself is dictated by various factors related to service conditions, processing technology and material compatibility. Naturally, a low density and high strength is desired for TiAl alloys to provide high density-normalized specific properties and save weight in structural components. Additional technical requirements in this work are high chemical homogeneity, a homogeneous distribution of the incorporated oxide particles and microstructural stability at elevated temperatures. From a processing point of view, low anisotropy in as-processed parts is desired and the compatibility of the alloy and the particles for powder-based sintering and AM technologies as SLM and DMD is required. Based on the technical requirements, specific alloy requirements can then be formulated. In modern TiAl alloys enhanced strength is achieved by the stabilization of a higher phase fraction of α_2-Ti_3Al of 20 to 30 % [6, 35]. This is typically achieved by a lower Al content of 43 to 45 at.% compared to earlier Al-rich TiAl alloys, as for example in the Ti-48Al-2Cr-2Nb alloy. Additionally, Nb is commonly added to enhance oxidation resistance and high temperature strength. Regarding the oxidation resistance, the Al content should be maximized at the same time, which is a competing requirement to β-solidification and a high fraction of α_2. So the selected alloy should contain an enhanced fraction of α_2 combined with moderate Nb additions and maximum Al content to ensure oxidation stability under operation conditions. The most beneficial properties in terms of balanced creep resistance, strength and toughness is then typically achieved with lamellar or near-lamellar microstructures consisting of alternating plates of α_2-Ti_3Al and γ-TiAl [28]. Additionally, Ti-Al alloys solidifying solely by the β-phase were found to strongly reduce texture and segregation in cast parts [35]. In the previously presented studies on rapidly solidified binary Ti-Al and ternary Ti-Al-Nb alloys it was found, that these alloys also show a beneficial behavior under non-equilibrium conditions involving high cooling rates (see Chapter 4). In Al-rich alloys strong segregation of Al was observed, forming a highly Al-enriched liquid towards the final stage of solidification, while Al-lean alloys show only slight changes in Al and Nb content throughout the metastable α_2-rich microstructure. The formation of a supersaturated metastable phase can then later be exploited to produce fine structured material by heat treatments. Based on these findings, the Ti-45Al-Nb system was chosen as a basis for the further alloy selection process.

Figure 5.1 shows a calculated isopleth along Ti-45Al-(0-10)Nb using published data. With increasing Nb additions, the alloy changes from the (quasi-)peritectic solidification type to full β-solidification. At the same time the γ-solvus temperature is slightly decreased and the $\alpha \rightarrow \alpha_2 + \gamma$ decomposition temperature is increased. The former reduces the necessary temperature for solution heat treatments in the α-phase field, while the latter defines the theoretical upper temperature limit of the fully intermetallic structure. At lower temperatures a ternary phase, τ-Ti_4NbAl_3, is predicted to be stable above 2.25 at.% Nb at 800 K. In this work, this phase is considered as an unwanted constituent. However, Nb diffusion is rather slow at low temperatures and thus its formation is expected to be suppressed also at higher Nb content. Under non-equilibrium conditions, extended β-solidification was observed in binary Ti-45Al and ternary Ti-45Al-Nb (Chapter 4). For simultaneously Al- and Nb-rich β-solidifying alloys the formation of large amounts of massively transformed γ_m was observed. Consequently, a slight stabilization of the β-phase is sufficient to ensure the desired solidification path. Based on the data in Figure 5.1, no substantial changes are achieved in the γ-solvus and $\alpha \rightarrow \alpha_2 + \gamma$ decomposition temperature beyond alloying levels of 3 at.% Nb.

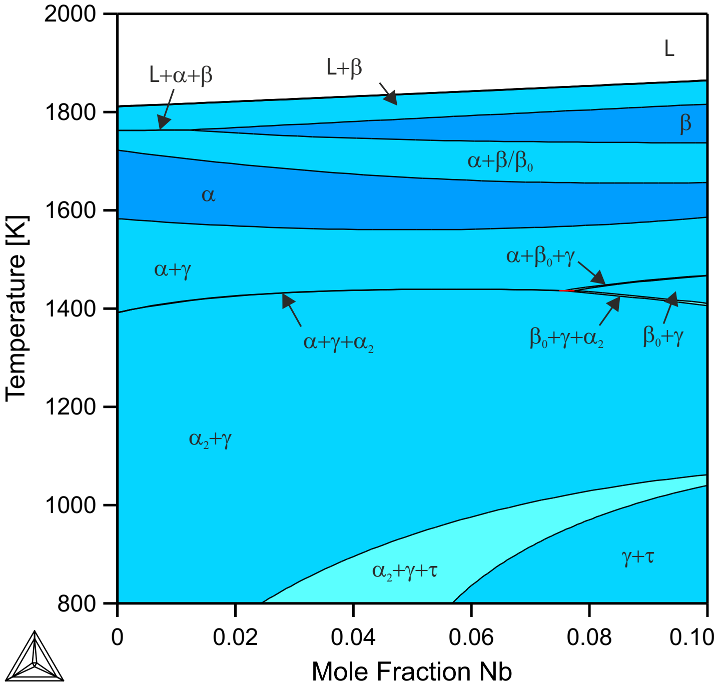

Figure 5.1: Calculated isopleth Ti-45Al-(0-10)Nb using a published assessment [23]. Solid single phase (dark), dual phase (intermediate) and triple phase fields (bright) are indicated. The liquid phase field is shown in white. The disordered α-Ti and β-Ti phases, the ordered variants α_2-Ti_3Al and β_0/B2 as well as the γ-TiAl and τ-Ti_4NbAl_3 phases are shown.

For processing of ODS alloys maintaining a homogeneous particle distribution is crucial. This problem becomes substantial, when the alloy is processed in the liquid state. ODS alloys are generally not processable by casting due to particle agglomeration and coarsening. Consequently, ODS alloys are typically processed in the solid state using powder metallurgical methods such as sintering and extrusion. In AM, the high solidification and cooling rates enable the retention of homogeneously distributed particles in Fe-base alloys [10]. It can be expected, that a strongly segregating Ti-Al alloy may also show local particle trapping in inter-dendritic spaces and agglomeration of particles in the remaining melt. Additionally, the size of the oxide particles is ideally kept in a range of 5 to 30 nm to ensure good mechanical and creep properties. This requires a short lifetime of the melt pool, which translates to a low melting range for the chosen alloy. Figure 5.2 shows the calculated solidification paths for Ti-(45-48)Al-3Nb for equilibrium and non-equilibrium Scheil-Gulliver conditions. Under equilibrium conditions, only the Ti-45Al-3Nb alloy is expected to solidify solely by the β-phase. Applying the Scheil-Gulliver model, all compositions are predicted to show substantial segregation and

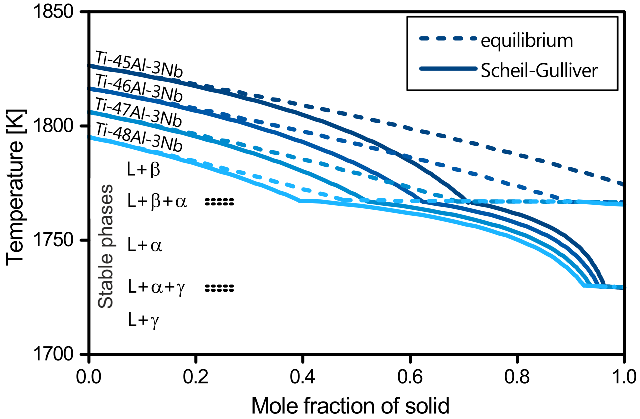

Figure 5.2: Calculated solidification path of Ti-(45-48)Al-3Nb assuming equilibrium (dashed) and non-equilibrium conditions according to the Scheil-Gulliver model (solid).

final solidification by direct formation of γ from a highly Al-enriched melt. The freezing range of the alloys is then expected to be inversely proportional to the Al content. Consequently, a high Al content would lead to lower freezing ranges. As indicated before, β-solidifying alloys were found to show low segregation under near-equilibrium conditions as well as at high cooling rates [31, 182]. Consequently, the effective solidification path follows more closely the equilibrium curve for Ti-45Al-3Nb, while it is better described by the Scheil-Gulliver model for the Al-rich Ti-48Al-3Nb. This discrepancy between the straight-forward application of a simple model and real behavior can be explained by the different diffusivities in the α and β phases. While α has a dense hexagonal close-packed structure, β is body-centered cubic with reduced packing density. Combined with the higher temperature at which β is stable, (back-)diffusion is fast enough to ensure full solidification by β, without the formation of an Al-enriched liquid. Interestingly, these differences lead to the situation, that the calculated melting range has two minima at low and high Al content. If segregation is tolerated, virtually the same melting range can be realized in the Al-rich Ti-48Al-3Nb alloy as in Ti-45Al-3Nb, if

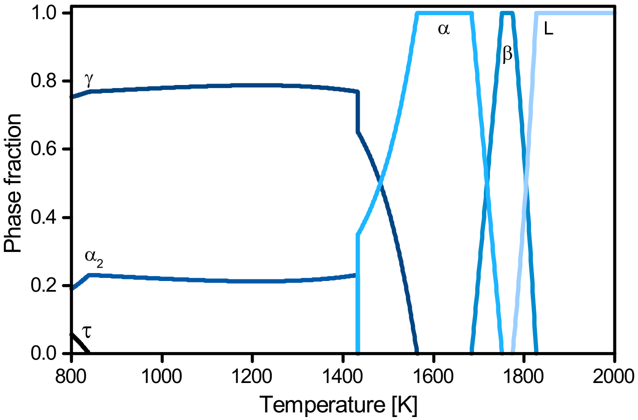

Figure 5.3: Calculated phase fractions versus temperature for Ti-45Al-3Nb using published data [23]. The stable phases and the fractions of the α, β, α_2, γ and τ phases are indicated.

the equilibrium curve is assumed for the latter and the Scheil-Gulliver curve for the former (Fig. 5.2). Based on the discussed consideration including the balanced effects of Nb addition on oxidation behavior and phase formation, high strength by enhanced levels of α_2 as well as β-solidification to minimize segregation, Ti-45Al-3Nb was selected as the base alloy for oxide particle incorporation. Figure 5.3 shows the calculated phase fractions of the stable phases versus temperature in this alloy. After solidification by β, the alloy crosses the α single phase field before forming γ and finally α_2 and γ become the stable phases. The α_2-fraction is stable above 20 % and almost independently from temperature. This ensures additional microstructural stability if components are subjected to varying temperature as both, α_2 and γ, remain stable at the same amount. At low temperatures, a small amount of $\tau$is predicted. However, its solvus temperature is lower than the operation temperature limit (923 K) and consequently no formation of τ is expected.

In conventional TiAl alloys carbides and borides are used as strengthening particles leading to enhanced mechanical properties (Chapter 2.5). Using the ODS approach, stable oxides are applied as additional phase. The particles need to be sufficiently stable in a highly aggressive Ti-Al-Nb melt to ensure the survival of particles with small size in the final part. Additionally, they need to have a high stability against coarsening upon heat treatments and long term exposure to elevated temperatures. Their melting point should be high to avoid or at least reduce melting under laser irradiation. In conventional ODS alloys as PM2000, yttria (Y_2O_3) has been proven to be compatible to Al-containing alloys and survive laser processing [10]. Elemental Y has also been used in previous studies on Y-doped Ti-48Al-2Cr-2Nb and was found to produce stable $Y_4Al_2O_9$ particles [151]. Additionally, the oxidation resistance of TiAl alloys is increased by the rare earth effect (REE) upon addition of small amounts of Y [183–187] or Hf [188, 189]. Based on its availability and stability, yttria was selected as ODS particle material and added to the base alloy by mechanical alloying to form ODS Ti-45Al-3Nb-<0.2mol.%Y_2O_3.

5.2 Processing results and discussion

In this section the results from solid and liquid state powder processing are shown. The Ti-45Al-3Nb and Ti-45Al-3Nb-<0.2Y_2O_3 intermetallic powders (hereafter named OX 45-3 and OX 45-3 ODS) used for consolidation are produced by mechanical alloying and are supplied by MBN Nanomaterialia S.p.A., Italy. Sintered material is used to study the formed microstructure and its stability upon high temperature annealing. SLM and DMD are applied to test the alloy behavior under AM processing conditions and evaluate microstructure formation, texture and the possibility to achieve a desired microstructure by thermal annealing. Additional TEM investigations provide information about the size and distribution of the oxide particles in the alloy matrix. Finally, the particle incorporation is compared for solid state SPS and liquid state additive SLM and DMD.

5.2.1 Spark plasma sintering

Solid state consolidation using SPS is successful in producing dense material from the OX 45-3 ODS powder (P-3). Figure 5.4a shows the fine grained duplex microstructure consisting of lamellar colonies and equiaxed γ and α_2 grains in the as SPS state. After the SPS consolidation, the specimen cools down with a maximum cooling rate of 9 $K \cdot s^{-1}$. Consequently, the specimen contains a high fraction of α_2 phase around 49 % and is in a metastable state. For any application, the microstructure needs to be stabilized closer to its equilibrium state. Additionally, fast non-homogeneous cooling gives rise to residual stresses in the as SPS consolidated material. To achieve the stabilization a thermal annealing at 1123 K for 12 h is performed in vacuum. Figure 5.4b shows the resulting structure with γ and α_2 fractions of around 75 % and 25 %, respectively, and a lamellar fraction of 26 %. Comparing these results to the calculated phase fractions (Fig. 5.3), the obtained state is close to equilibrium. Note that the consolidation by SPS is performed at 1598 K, which is in the α phase field for the chosen alloy. So already during consolidation, the formation of a coarse grained lamellar microstructure would

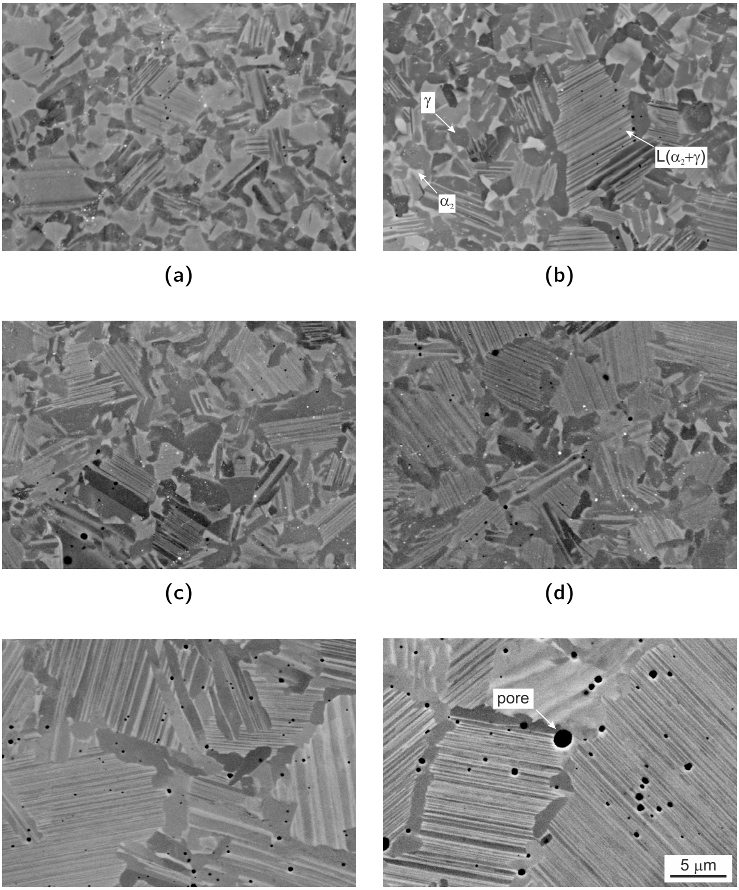

(a) (b)

(c) (d)

(e) (f)

Figure 5.4: BSE SEM micrographs of SPS (a-d) OX 45-3 ODS and (e, f) ODS-free OX 45-3 a) in the as SPS state, and after thermal annealing at (b, e) 1123 K/12 h, c) 1573 K/15 min + 1123 K/12 h and (d, f) 1673 K/15 min + 1123 K/12 h. The α_2 (bright) and γ (dark) phases are indicated as well as the lamellar colonies formed of $\alpha_2 + \gamma$. The scale bar in f) applies for all micrographs.

be expected. Conventional heat treatments to obtain lamellar microstructures for TiAl alloys typically involve a high temperature treatment in or close to the α phase field at temperatures around 1573 K to 1673 K, depending on the composition. Figures 5.4c and 5.4d show the resulting microstructures after two step thermal annealing involving a high temperature step at 1573 K or 1673 K for 15 min and the stabilization treatment described before. The two temperatures are selected based on the calculated phase fractions and are close to the lower and upper boundary of the calculated α phase field for this alloy (1563 K to 1683 K). The obtained microstructures are very similar to the one obtained by the stabilization annealing only. The measured intersection length of the equiaxed γ grains is determined as 1.4±0.8 µm for the stabilized state and 1.5±1 µm and 1.3±0.6 µm after the thermal annealing at 1573 K and 1673 K, respectively. The fraction of lamellar grains increased from 26 % to 36 % after 1573 K and to 63 % after 1673 K. Figure 5.5 shows the distribution of the measured intersection lengths of lamellar colonies after the various thermal annealings for OX 45-3 ODS. Independently from the chosen thermal annealing, the peak values are obtained around 2 µm

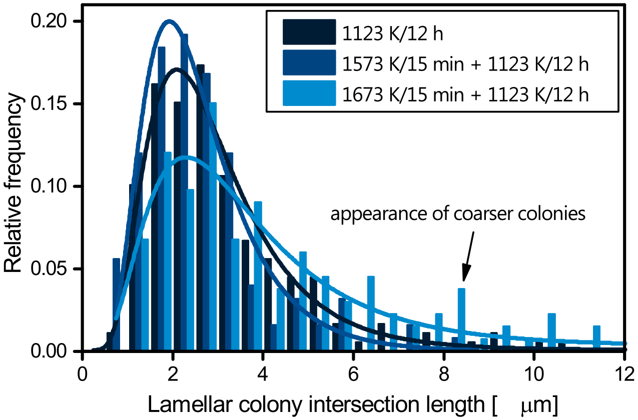

Figure 5.5: Distribution of the measured intersection length of lamellar colonies in SPS OX 45-3 ODS after different thermal annealing. Least-square-fitted log-normal distribution curves are shown overlaid.

due to the presence of very small colonies. The mean intersection lengths of lamellar colonies for thermal annealing at 1123 K for 12 h, 1573 K or 1673 K for 15 min and the stabilization treatment are 3.2±2.2 µm, 2.6±1.4 µm and 4.4±3.1 µm, respectively. After 1673 K for 15 min the fraction of larger colonies starts to increase, which is also evident from Figure 5.4d. At this temperature, the γ grains are slowly dissolving in the disordered α matrix resulting in larger lamellar colonies in the final microstructure. With increasing temperature this process is expected to occur faster as it is observed in the SPS material. Figure 5.4e shows the microstructure of the OSD-free variant OX 45-3 (P-7) after SPS and 1123 K for 12 h. Large lamellar colonies are formed with γ at the colony boundaries along with a multitude of sub-micrometer pores. After a high temperature anneal at 1673 K for 15 min and the stabilization treatment, the microstructure is further coarsened. The mean intersection length of the lamellar colonies after 1123 K for 12 h and 1673 K for 15 min plus 1123 K for 12 h are 10.9±8.9 µm and 11.0±8.2 µm, respectively. After high temperature annealing, larger pores appear in the γ-seams along the colony boundaries (Fig. 5.4f). This pore expansion is explained by a combination of high temperature, absence of strengthening particles and a high internal pressure in the pores. During SPS the pores and any contained gas are compressed with 50 MPa. This is equivalent to an overpressure of 500 bar inside the pores assuming residual gas pores with atmospheric pressure contained in the powder. As the alloy is later annealed, the high internal pressure leads to deformation of the surrounding matrix and an increased pore size. The appearance of the pores in the γ-seams further strengthens this argument, as the lamellar structure is expected to have superior creep resistance compared to the γ-phase. Additionally, dissolved gas may be liberated and further contribute to pore expansion. It has to be noted, that the observed pore size is expected to be an overestimate of the true pore size, as chemo-mechanical final polishing is applied. Thus the material is attacked and exposed pores are expected to increase in size.

The observed behavior upon consolidation and thermal annealing shows an exceptional microstructural stability of the produced SPS ODS alloy variant at high temperatures during consolidation and following thermal annealing. The increased microstructural stability of the SPS material can be directly related to the presence of the ODS particles in the alloy matrix. With the possibility to produce near-net shape turbine blades by SPS the newly developed OX 45-3 ODS alloy or similar ODS TiAl alloys have potential applications as solid state sintered component in high temperature environments in the future. Additionally, microstructural stability is a crucial factor for application of SPS consolidated alloys [58]. The introduction of dispersoids effectively limits colony coarsening and allows production of alloy with colony sizes around 5 to 10 µm promising interesting mechanical properties at high temperatures.

5.2.2 Selective laser melting

Liquid state consolidation using SLM is successful in creating test parts with high density. Figure 5.6a shows the observed microstructure in the as processed state. The major constituent is a metastable α_2 phase which forms during rapid cooling. Starting from the melt pool boundary, a grain selection process takes place producing a gradient in grain size. Subsequent laser scans partly re-melt the previously deposited material and eliminate the very coarse grains.

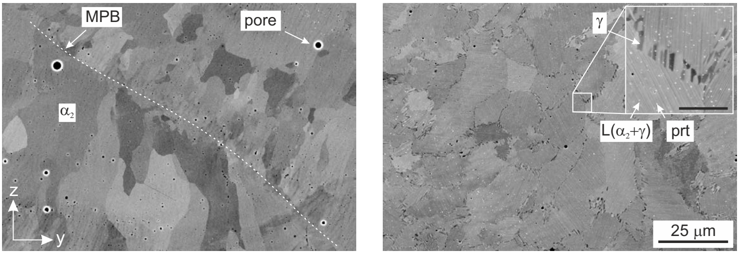

(a) **(b)**

Figure 5.6: BSE SEM micrographs of SLM processed OX 45-3 ODS (E_a=4.5 J/mm^2) in a) as processed state and b) after thermal annealing at 1123 K for 12 h (inset: scale bar = 4 µm). The observed phases, pores, melt pool boundary (MPB) and dispersoids (prt) are indicated. The scale bar in b) applies for both micrographs. The build direction (z) and the beam translation (y) are shown. The scanning direction (x) is out-of-plane.

Again, selected grains continue to grow. Consequently, the deposited material contains fine grained former melt pool boundaries and coarser bulk regions. In the material close to the former melt pool boundary a fine structure is visible originating from the primary β cells later transformed to α are visible. Residual porosity below 5 µm is also observed. Based on the spherical shape it is proposed, that these are caused by the entrapped gas from powder production or processing. Material from the same specimen is subjected to a thermal annealing at 1123 K for 12 h similar to the SPS consolidated material. Figure 5.6b shows the obtained near-lamellar microstructure consisting of lamellar $\alpha_2 + \gamma$ colonies in a size range of 5 to 30 µm and sub-micrometer γ and α_2 grains formed at the colony boundaries. These grains show an elongated shape and are oriented typically parallel with respect to each other and to one of the adjacent colonies (inset Fig. 5.6b). This bimodal lamellar structure, fine inside the colonies and coarse at the boundary, can be explained by the kinetics of the phase transformation. First, fast decomposition of the former α grains into primary $\alpha_2 + \gamma$ colonies takes place upon thermal annealing. The size and shape of the primary lamellar colonies is similar to the α_2-grains observed in the as processed material. This indicates a direct decomposition of the metastable microstructure upon thermal annealing. Later a slow decomposition of the fine structure into a coarser lamellar structure starts. This requires diffusion over greater length. At 1123 K the diffusion in TiAl alloys is expected to be rather slow based on their intermetallic ordered structure. Consequently, this second transformation is observed in its initial stage after the thermal annealing. Inside the colonies finely distributed dispersoids are visible as bright spots due to the mass contrast of the yttrium-based oxides (inset Fig. 5.6b). It needs to be pointed out, that the applied thermal annealing temperature is far below conventional heat treatment temperatures to obtain near-lamellar microstructures. In cast parts of similar composition, temperatures as high as 1653 K in the α-field are applied [31]. This is more than 500 K higher than the thermal annealing which is applied in this work. The formation of a supersaturated metastable microstructure during rapid solidification enables such low heat treatment temperatures and phase decomposition.

The obtained results clearly show that the OX 45-3 ODS alloy can be consolidated using laser processing and later be transformed into conventional microstructures by heat treatments. This opens the space to complex shaped ODS TiAl alloys for demanding applications. Detailed studies on suitable processing parameter windows and part integrity are presented in Chapter 7.

5.2.3 Laser metal deposition

Compared to the powder-bed based SLM technique, blown-powder based DMD provides higher deposition rates at higher energy densities. In this work, the applied area energy densities for DMD are a factor of 27 higher than for SLM. Figure 5.7 shows the observed microstructures for OX 45-3 ODS and GE48-2-2 in the as-processed and annealed state. The Al-rich GE48-2-2 alloy forms a dendritic microstructure consisting of lamellar $\alpha_2 + \gamma$ colonies and inter-dendritic γ phase. The Al-leaner OX 45-3 ODS forms a columnar grained structure consisting mainly of the α_2 phase with some spurious γ. The largest dispersoids are visible as white spots in the SEM micrograph. After a thermal annealing at 1123 K for 12 h both alloys start to recrystallize (Fig. 5.7c and 5.7d). While GE48-2-2 retains its fine lamellar structure with equiaxed γ, OX 45-3 ODS decomposes into small lamellar $\alpha_2 + \gamma$ colonies. Residual areas between the colonies still resemble the α_2 structure observed in the as processed state. The presence of a dual phase structure in these areas with a very fine lamellar spacing would be expected based on the results of annealed SLM-consolidated material (Fig. 5.6b). If present, the resolution of the SEM or compositional difference and thus contrast is not high enough to resolve this structure. After annealing at 1573 K for 15 min and 1123 K for 12 h, GE48-2-2 is fully recrystallized into a duplex structure with an increased amount of γ. This is in agreement with established phase diagram data on Ti-48Al-2Cr-2Nb predicting 1573 K to be in the $\alpha + \gamma$ two phase field and consistent with observations on DMD of similar alloys [126]. OX 45-3 ODS forms a fully lamellar microstructure with ragged colony boundaries, as the chosen temperature is in the α single phase field (Fig. 5.7e and 5.7f). Figure 5.8 shows XRD spectra of DMD processed OX 45-3 ODS (top) and GE48-2-2 (bottom). The ODS alloy contains a large fraction

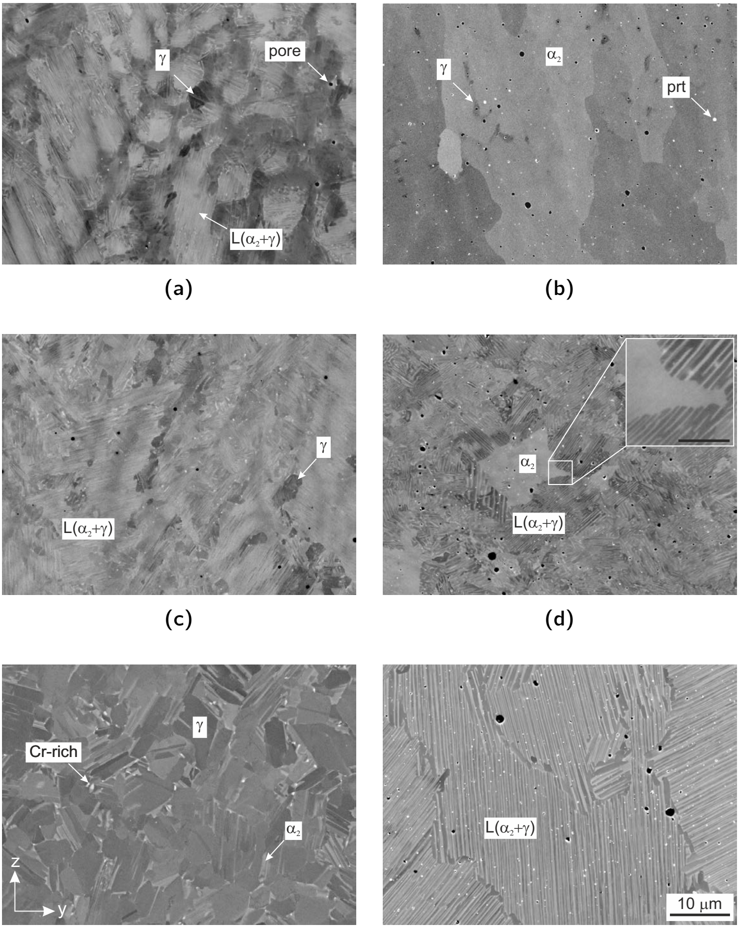

(a)

(b)

(c)

(d)

(e)

(f)

Figure 5.7: BSE SEM micrographs of DMD processed (a,c,e) GE48-2-2 (E_a=179 J/mm^2) and (b,d,f) OX 45-3 ODS (E_a=120 J/mm^2). (a,b) in the as processed state and after thermal annealing of (c,d) 1123 K/12 h and (e,f) 1573 K/15 min + 1123 K/12 h. The α_2 and γ phase, pores and dispersoids (prt) are indicated. Bright spots in e) correspond to Cr-rich areas. The scale bar in f) applies for all micrographs (inset: scale bar = 2 μm). The build direction (z) and the beam translation (y) are shown. The scanning direction (x) is out-of-plane.

of α_2 with a minor γ content. Additionally, Y_2O_3 is clearly observed which is enriched at the surface due to partial slagging-off of the oxide particles in the last deposited layer during processing. The GE48-2-2 alloy contains mainly γ together with α_2 based on the relative intensities of the $\gamma(111)$ and $\alpha_2(20\bar{2}1)$ peaks. This different behavior is explained by the dependence of the solidification path on alloy composition. OX 45-3 ODS is fully β-solidifying, while GE48-2-2 is forming primary β, undergoes a peritectic reaction and then solidifies by α under equilibrium conditions. Performed *in situ* XRD experiments on Ti-48Al at high cooling rates show that the formation of β-phase is suppressed at high cooling rates and the alloy forms primary α phase

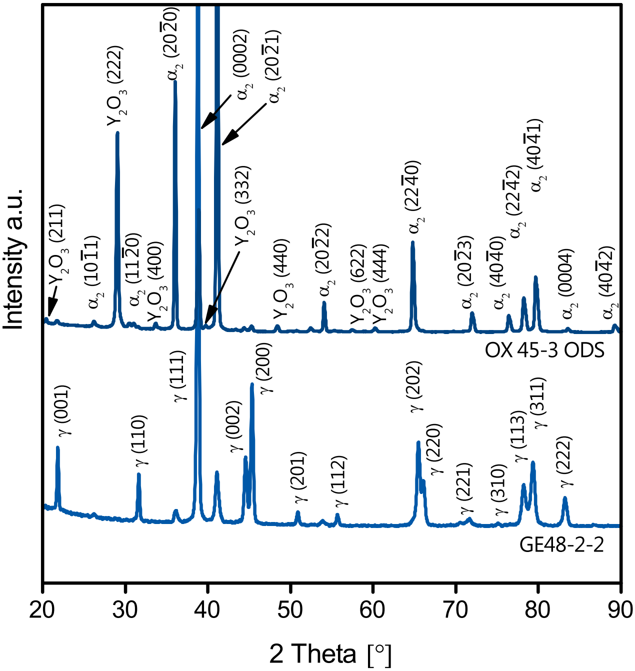

Figure 5.8: XRD spectra of DMD processed OX 45-3 ODS (top) and GE48-2-2 (bottom). Peaks of the intermetallic α_2 and γ phases and of Y_2O_3 are indicated.

(see Section 4.3.2). Additionally, it is known that Al-rich alloys typically show much stronger segregation than Al-lean alloys. Consequently, GE48-2-2 shows a fine structure dominated by the solidification of the α phase, whereas OX 45-3 ODS shows a coarse structure originating from the primary β phase. Beside the phase fractions and segregation, the texture is also strongly influenced by the alloy composition. Figure 5.9 shows XRD pole figures for DMD processed GE48-2-2 (top) and OX 45-3 ODS (bottom) for the $\gamma(111)/\alpha_2(0002)$ reflection (left) and the $\alpha_2(20\bar{2}1)$ reflection (right). For GE48-2-2 a fiber texture is observed for both reflections while OX 45-3 ODS is much less textured based on the intensity distributions. No distinct alignment

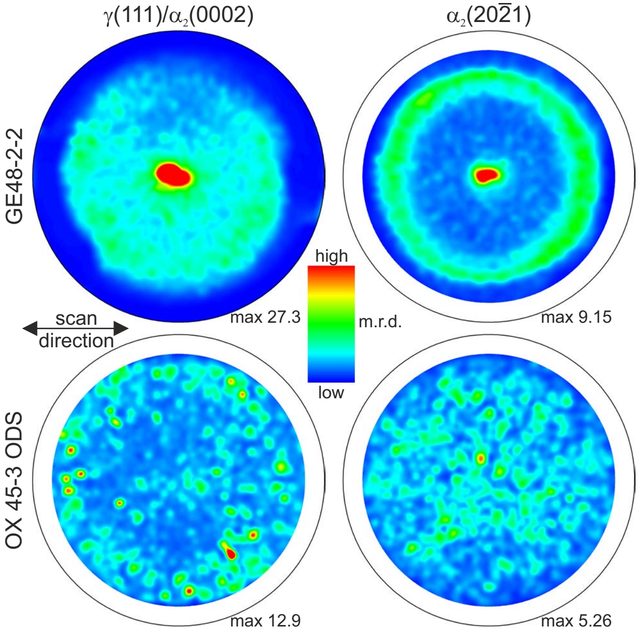

Figure 5.9: XRD pole figures of DMD processed GE48-2-2 (top) and OX 45-3 ODS (bottom) for the most intense reflections $\gamma(111)/\alpha_2(0002)$ (left) and $\alpha_2(20\bar{2}1)$ (right). The coloring corresponds to low (blue) to high (red) values of m.r.d. The laser scan direction is horizontal for all sub-figures. The surface normal is out-of-plane.

of the principal peaks of α_2 and γ is observed with the out-of-plane direction in the center of the pole figures. Based on the observed intensity distributions, $\gamma(111)/\alpha_2(0002)$ is slightly oriented towards the in-plane direction, whereas $\alpha_2(20\overline{2}1)$ is observed more frequently at lower angles to the surface normal direction. The distinct ring shape for the $\alpha_2(20\overline{2}1)$ pole figure of GE48-2-2 is formed by the other planes of the $\alpha_2\{20\overline{2}1\}$ family of planes rotated around the out-of-plane direction. The calculated ideal inter-planar angles between $\alpha_2(20\overline{2}1)$ and $\alpha_2(02\overline{2}1)$ and between $\alpha_2(20\overline{2}1)$ and $\alpha_2(20\overline{2}\overline{1})$ are 52.32° and 56.31°, respectively. These angles agree well with the observed ring shape between 50 and 70° taking into account the spread of the central peak of ±11° and ±9° parallel and perpendicular to the laser scan direction, respectively. This spread indicates a misalignment of the α_2 phase with the out-of-plane direction and is caused by slightly different crystal orientation depending on the position in the overlapping melt pools. Consequently, the ring shape of the $\alpha_2\{20\overline{2}1\}$ plane family is also spread. The different phase fractions of γ and α_2 in the two studied alloys have to be taken into account when interpreting the pole figure data for $\gamma(111)/\alpha_2(0002)$. In GE48-2-2 the resulting pole figure is dominated by the principal orientation of the γ phase as the main component. On the contrary, the pole figure of the same reflection for OX 45-3 ODS reflects the orientation of mainly $\alpha_2(0002)$, as only a minor fraction of γ is present in this alloy. The difference in data smoothness for the two alloys is explained by the different grain sizes of the formed microstructures. GE48-2-2 formed a very fine dendritic microstructure providing a multitude of different grains that simultaneously fulfill the diffraction conditions. The coarser structure in OX 45-3 ODS provides only a reduced number of grains that can contribute to diffracted intensity in a certain direction. Thus a speckle-like intensity distribution is observed in the pole figures of OX 45-3 ODS. However, these differences related to the dual phase microstructures of the alloys do not the change the fact, that the overall degree of texture after DMD processing is significantly reduced in the β-solidifying OX 45-3 ODS alloy. As observed from the orientations of the lamellar colonies after annealing, there seems to be also no preferential lamellar orientation after thermal annealing (Fig. 5.7d and 5.7f).

The results clearly show the possibility to consolidate OX 45-3 ODS using

DMD. Furthermore, the chosen β-solidifying alloy induces significantly reduced texture in as processed parts. Finally, the obtained microstructure can be transformed to a conventionally applied one by adapted thermal annealing (see Section 5.2.2). The compatibility of the developed ODS alloy with DMD opens possibilities to produce large complex shaped ODS TiAl components which cannot be efficiently produced by powder-bed based methods as SLM or have too intricate features to be just produced by solid state sintering. Furthermore, the geometrical freedom in DMD processing facilitates controlled preheating to avoid the formation of large residual stresses, part deformation and potentially cracking.

5.2.4 ODS particle incorporation

It was shown that the OX 45-3 ODS alloy can be consolidated using solid state and additive liquid state processing technologies. In ODS alloys, the size and distribution of the ODS particles is crucial for the desired properties. Based on the well-known Orowan-relation

$$\sigma_{Or} = M\frac{G \cdot B}{2(l-r)} \tag{5.1}$$

where $M = 3$ is the conversion factor between shear and normal stress, G is

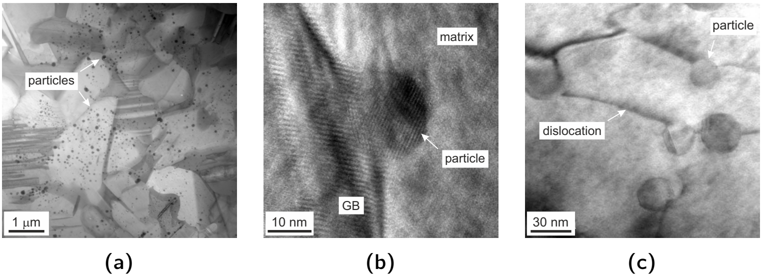

Figure 5.10: Microstructure of SPS OX 45-3 ODS stabilized at 1123 K for 12 h. a) STEM bright-field micrograph showing the distribution of fine ODS particles, b) HRTEM micrograph of an ODS particle pinning a grain boundary (GB) in the intermetallic matrix, c) TEM micrograph of ODS particles interacting with dislocations (images by K. Dawson, ULIV).

the shear modulus, B is the Burgers vector, the stress σ_{Or} is increased with smaller particle diameter r and smaller inter-particle distance l for non-cuttable particles. For dispersion strengthened ordered intermetallics more complex models are applied in order to account for detachment of the dissociated dislocations from the embedded particles [190, 191]. The optimum dispersoid diameter d is then related to the dissociation width w by $w/d \approx 0.6$. As the involved energies of the formed faults in TiAl alloys are high, the corresponding dissociation width is typically less than 8 nm [192]. Consequently, the most effective dispersoid size for enhanced creep strength in ODS TiAl alloys is around 13 nm or less. Figure 5.10a shows the distribution of fine dispersoids throughout the intermetallic matrix in SPS OX 45-3 ODS stabilized at 1123 K for 12 h. The median particle size and volume number density are determined as 29 nm and $4.4 \cdot 10^{20}$ m^{-3}. The calculated median particle interspacing is 134 nm. The dispersoids are present in the equiaxed grains as well as in the lamellar colonies. The obtained particle sizes are comparable to the particle sizes in recrystallized PM2000, an established ODS Fe-base alloy [10, 193]. Already in the stabilized state, grain boundary pinning is observed (Fig. 5.10b). The particles stop grain boundary movement and effectively retain a fine

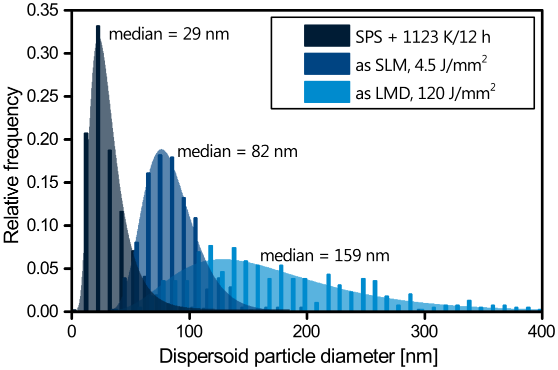

Figure 5.11: Size distribution of ODS particles in solid state SPS sintered and stabilized, SLM and DMD processed OX 45-3 ODS. Least-square-fitted log-normal distribution curves are shown overlaid as well as the corresponding median value.

microstructure and also seem to slow down the $\gamma \rightarrow \alpha$ phase transformation as discussed in Section 5.2.1. It is observed, that the particles interact with dislocations in the material (Fig. 5.10c). Dislocation pinning at the particles and bowing in between is evident. During service at elevated temperature these effects can be exploited to retain the fine grained microstructure for enhanced mechanical properties and long term stability. Figure 5.11 shows the observed particle size distributions for solid state and additive liquid state processing. Fitted log-normal distribution curves are shown overlaid. Comparing these results it is evident, that liquid state processing leads to a certain degree of particle coarsening due to the high temperature and the presence of a liquid phase allowing fast diffusion of the elements necessary for particle growth. The diffusion of Y and O is limiting the growth of pure Y_2O_3 particles. But the formation of higher-order oxides containing Ti and/or Al and having various crystal structures has been described earlier for Al-containing ODS alloys [193]. Specifically for TiAl alloys, the formation of Y-Al-O particles has been observed [151]. Consequently, the particle coarsening is not limited only by the diffusion of Y anymore and rapid growth can occur in the liquid state by incorporation of Ti and/or Al. After SPS and stabilization at 1123 K for 12 h a rather sharp size distribution with a median size of 29 nm is preserved. In SLM processed material a slightly broader distribution with a median size of 82 nm is observed. The volume number density is decreased to $7.4 \cdot 10^{18}$ m^{-3}. Consequently, the median particle interspacing is increased to 554 nm. DMD processing leads to a very broad size distribution ranging from sub-50 nm dispersoids to particles with a diameter of several hundreds of nanometers. These large particles are recognizable due to their high Y-content in BSE SEM micrographs (Figure 5.7d). In accordance with the coarsening also the volume number density is reduced to $1.1 \cdot 10^{18}$ m^{-3}. The calculated median particle interspacing becomes relatively large with 1043 nm. Comparing the different consolidation methods, reducing the energy input in the material during processing clearly reduces the preserved oxide particle size. The two applied liquid state processing technologies SLM and DMD have greatly different heat input and melt pool sizes based on their laser spot diameters and area energy densities of 100 µm and 1.3 mm, and 4.5 J/mm^2

and 120 J/mm^2, respectively. Figure 5.12 shows the correlation of oxide particle size distribution and applied area energy density. The results from solid state SPS are shown for comparison. Overlaid is a power law fit of the median particle size according to

$$d = a \cdot E_a^{\frac{1}{m}} \tag{5.2}$$

where d is the median oxide particle diameter, a is the proportionality constant, E_a is the area energy density and m is the growth exponent. Simulations on melt pool life times in SLM show an approximately linear dependence on applied area energy density [194]. This allows applying a conventional parabolic diffusion-dominated growth model with $d \sim t^{\frac{1}{m}}$ where $t \sim E_a$ is the time and linear proportional to the area energy density E_a. The data and the fitted curve indicate that the energy input would need to be decreased to very low and finally unreasonable values to obtain similar particle sizes by liquid state processing as in solid state SPS material. It also shows the limited effect of slight parameter variations in process control, as area energy input between SLM and DMD in this work differs by a factor of ~27, while the

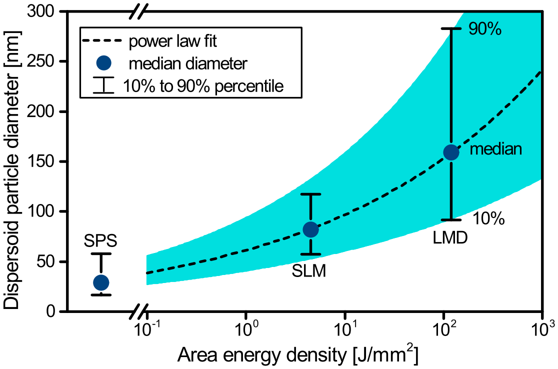

Figure 5.12: Correlation of median ODS particle diameter and area energy in laser processing. The value for SPS sintered material is shown for comparison. A power law fit and the estimated 10% to 90% percentile range are shown overlaid.

median dispersoid size is only increased by a factor of ∼2. However, if liquid state AM technologies based on very fine focused beams at low power and high scanning speeds are applied, particle sizes comparable to SPS seem to be possible. Generally, the life time of the melt pool needs to be minimized to yield the smallest particles.

5.2.5 Hardness of consolidated material

The hardness of SPS and DMD consolidated material is measured to analyze the effects of ODS incorporation and different consolidation methods on the mechanical properties (Table 5.1). Comparing the ODS-containing and ODS-free SPS consolidated alloy a beneficial effect of the yttria addition is evident. After a stabilization annealing at 1123 K for 12 h the ODS-free variant has 441±29 HV, while OX 45-3 ODS has 477±16 HV. This difference gets accentuated after high temperature annealing at 1673 K. The hardness of OX 45-3 is reduced to 409±26 HV, while it is increased in OX 45-3 ODS to 485±15 HV. DMD processed material has a high hardness in the as-processed state due to a high fraction of α_2 (Fig. 5.7 and 2.7) After thermal annealing at 1123 K for 12 h the hardness is slightly reduced to 546±38 HV but still significantly higher than for SPS material annealed similarly. After high temperature annealing at 1573 K for 15 min and 1123 K for 12 h, similar hardness values are obtained for SPS and DMD processed OX 45-3 ODS, 471±23 and 469±25 HV, respectively. The DMD processed GE48-2-2 material shows lower hardness after processing and after all thermal annealing compared to OX 45-3 ODS. The similarity of hardness of annealed SPS and DMD material has extensive implications, as the microstructure of SPS and DMD material is different. In SPS material a fine duplex microstructure is observed, while DMD produces first a columnar structure of mainly α_2 that decomposes into a near-lamellar microstructure during thermal annealing (Fig. 5.4 and 5.7). Naturally, the finer SPS structure would be expected to provide the higher hardness due to a strength increase according to a Hall-Petch relation. Such behavior is observed when comparing SPS consolidated OX 45-3 and OX 45-3 ODS. The high hardness of DMD processed material

Table 5.1: Vickers hardness (HV$\pm1\sigma$) of SPS and DMD consolidated ODS-containing OX 45-3 ODS and ODS-free OX 45-3 and DMD consolidated GE48-2-2.

Process and Material	Condition	HV$\pm1\sigma$
SPS OX 45-3	1123 K/12 h	441±29
	1673 K/15 min + 1123 K/12 h	409±26
SPS OX 45-3 ODS	as SPS	505±18
	1123 K/12 h	477±16
	1573 K/15 min + 1123 K/12 h	471±23
	1673 K/15 min + 1123 K/12 h	485±15
DMD OX 45-3 ODS	as DMD	564±61
	1123 K/12 h	546±38
	1573 K/15 min + 1123 K/12 h	469±25
DMD GE48-2-2	as DMD	512±45
	1123 K/12 h	410±19
	1573 K/15 min + 1123 K/12 h	358±15

indicates that the size of the lamellar colonies is not the factor determining increased hardness. Although the effect can be attributed to the introduction of the dispersoids, it remains unclear if it is only the presence of the particles or if the dispersoids are partly dissolved in the melt leading to a doping effect of the matrix. Given the reactivity of TiAl alloy melts and the associated problems of finding suitable ceramics for crucibles such a mechanism has to be considered.

The hardness measurements clearly show increased mechanical properties in OX 45-3 ODS by the introduction of Y-based dispersoids. These strengthening effects are also obtainable after liquid phase AM processing by DMD. This observation is a promising start for further investigations on the mechanical properties of ODS TiAl alloys at low and high temperatures.

5.3 Summary and conclusions

- SPS OX 45-3 ODS has superior microstructural stability up to 1573 K compared to the ODS-free variant. The median particle size is 29 nm at a volume number density of $4.4 \cdot 10^{20}$ m^{-3}.
- SLM produces a coarse grained α_2-rich microstructure with a median dispersoid size of 82 nm at a volume number density of $7.4 \cdot 10^{18}$ m^{-3}. Upon annealing at 1123 K for 12 h, microstructural refinement into fine lamellar material is demonstrated.
- After DMD also a coarse grained α_2-rich microstructure is formed. Fine grained material is obtained after heat treatment at 1123 K for 12 h. Coarse grained material for enhanced creep resistance is observed after a two step heat treatment at 1573 K/15 min + 1123 K/12 h. Incorporated particles have a median size of 159 nm at a number density of $1.1 \cdot 10^{18}$ m^{-3}. The as processed material shows significantly reduced texture and more evenly distributed intensity for the measured $\gamma(111)/\alpha_2(0002)$ and $\alpha_2(20\overline{2}1)$ reflections compared to DMD GE 48-2-2 alloy (Ti-48Al-2Cr-2Nb).
- Hardness measurements show superior values for SPS OX 45-3 ODS compared to its non-ODS counterpart.

From the obtained results it can be concluded that ODS TiAl alloys can be successfully produced by mechanical alloying and be consolidated by SPS, SLM and DMD. Especially the incorporation of small oxide particles using liquid state AM processing based on rapid solidification is a novel approach in TiAl alloys and was here reported for the first time according to the authors' knowledge. The compatibility of the developed Ti-45Al-3Nb ODS alloy with different processing technologies is foreseen to allow the use of solid state sintering and liquid state AM technologies to produce complex components using multi-step manufacturing taking advantage of the individual processing characteristics. The same alloy can then be used for a geometrically simple, sintered support structure with smaller oxides, combined with highly complex features produced by AM on top containing larger particles.

6 Performance of ODS titanium aluminides

After successful consolidation the degradation behavior and the mechanical properties at low and high temperature of the newly developed SPS ODS TiAl alloy described in Chapter 5 are discussed. First, the oxidation behavior in air is presented combining scale growth rates, SEM, EDX and XRD measurements on the formed scale to elucidate its structure and morphology. Additionally, the performance of the ODS TiAl alloy is compared to its ODS-free counterpart as well as commercial TNB-V5. The second section is dedicated to the mechanical performance in the range of 293 K to 1073 K. The ODS and ODS-free TiAl alloys are directly compared and the effects of the ODS addition are discussed. The experimental conditions are found in Chapter 3.3.

6.1 High temperature degradation behavior in air

6.1.1 Addition of rare earth elements

The beneficial effects upon addition of rare earth elements on oxidation resistance and the associated rare earth effect (REE) are well known and exploited in many state-of-the-art alloy systems, especially in Ni- and Fe-based alloys [195]. It was recognized early on that the REE effect also occurs if the corresponding rare earth oxide is distributed in the alloy matrix forming an ODS variant. In alumina-forming alloys, the elements Y and Hf were found to be equally effective, indicating an underlying mechanism being independent of the added element [196]. Later work, as reviewed by Pint [197], provided estimations for suitable addition levels and element combinations in alumina formers. The combination of Y with Hf or Zr provides the highest oxidation resistance, but as a single addition Y is more effective than the other elements. It was also observed that ideally Hf and Zr levels around 0.05 at.% are applied, while slightly higher Y contents in the range of 0.1 at.% provide the best results. Furthermore, the amount of Y_2O_3 to provide a slower growth rate in ODS alloys was found generally around 1 vol%. The underlying mechanism of the REE appears to be very complex, but several effects are believed to play a crucial role [197]:

- modification of the diffusion of cations and anions through the scale by segregation of the added rare earth elements
- scavenging of impurities, especially of S by Y and C by Hf, reducing scale spallation
- improved interfacial chemical bonding by rare earth elements with large cation sizes, such as Hf, Y, and Zr
- reduced interfacial void formation between the alloy and the scale.

Beside the benefits of the REE, also its limits have been exploited. The mechanical response of the substrate limits the possible improvement by the REE as stronger substrates promote spallation due to higher stresses between the alloy and its scale. The same argumentation also applies for a comparison of alloys with a higher mismatch of the coefficient of thermal expansion (CTE) between the alloy and the scale-forming oxides. While the REE can increase oxidation resistance in alumina-forming alloys by more than one order of magnitude, its effect on marginal alumina-forming alloys is much lower. TiAl alloys and other aluminides are an example of such alloys, as they tend to form mixed scales consisting of Al_2O_3 and TiO_2 instead of the desired pure alumina scale [198]. Consequently, the REE was observed to increase oxidation resistance in TiAl alloys but to much lesser extent than in Ni- and Fe-based alloys.

For TiAl alloys, the effects of Y addition on oxidation resistance have been classified as beneficial, neutral or even detrimental in the past. Taking into account the specifics of the REE, this seems obvious in the case of additions exceeding 1 at.% as over-doping leads a similar or worse oxidation resistance compared to the un-doped base alloy [197, 199]. But also for low Y levels in the alloy or applied as a coating, a beneficial [50, 183–187, 200–202] as well as a detrimental or no effect has been described [53, 200, 201, 203]. The beneficial effects described refer to reduced scale growth rates and increased scale adherence, while the observed detrimental effects are internal oxidation of Y forming locally Y_2O_3 or only limited protection due to Y depletion in the case of coatings. However, several studies focusing on a range of compositions with a rare earth level below 1 at.% confirm the existence of the REE also for TiAl alloys upon addition of Y [183–187] and Hf [188, 189]. In this work, the effect of the addition of Y_2O_3 to a TiAl alloys by means of mechanical alloying on the oxidation resistance is described.

6.1.2 Oxide scale growth

Figure 6.1 shows the weight gain per unit area for ODS-free OX 45-3, OX 45-3 ODS and TNB-V5. In order to compare the observed oxide scale growth rates of the different studied alloys, a square root growth model according to

$$\left(\frac{\Delta m}{A}\right)^2 = k_p \cdot t \tag{6.1}$$

where t is the time and k_p is the parabolic growth constant, is fitted to the data. Comparing the ODS-free and ODS-containing variant a reduced weight gain is clearly observed upon addition of the yttria. OX 45-3 ODS shows a parabolic growth of the oxide scale up to the maximum tested time of 924 h. At this point spallation is observed at the edges of the specimens. Over the complete duration of the oxidation test, the parabolic growth mode is maintained which is also seen by the data points lying on a line with a slope of 0.5 on a logarithmic scale (inset Figure 6.1). The ODS-free OX 45-3 alloy shows initially parabolic growth up to 360 h. For longer test duration accelerated growth is observed which is also evident from an increased slope on the logarithmic scale. Consequently, no fitted parabolic growth model is shown for OX 45-3. However, the data up to 360 h follows a parabolic model and is thus included in Table 6.1 for comparison. The fitted k_p value for the OX 45-3 ODS variant is about half the value of the ODS-free alloy.

Comparing the weight gain for the ODS variant to TNB-V5 a slightly better oxidation resistance is observed for the latter. The k_p values are 1.9 and $1.4 \cdot 10^{-10}$ $kg^2 \cdot m^{-4} \cdot s^{-1}$, respectively. The reference alloy TNB-V5 is also a Ti-Al-Nb based alloy with additions of B and C, containing an increased amount of Nb compared to OX 45-3 (ODS). Upon the addition of the elements Nb, C, and B, to TiAl alloys increased oxidation resistance has been observed [198]. Additionally it is well known that higher Nb levels also contribute to a higher oxidation resistance [51]. In the case of Ti-Al-Nb alloys additions exceeding 5 at.% Nb have been found to have significantly increased oxidation resistance [50]. The difference in composition thus explains the increased oxidation resistance of TNB-V5 compared to OX 45-3. It is an important observation that the addition of <0.2 mol.% Y_2O_3 leads to a similar oxidation resistance as an increased Nb alloying level by 2 at.% plus the addition of 0.2 at.% of each C and B. The k_p value for TNB-V5 determined in this work for a test

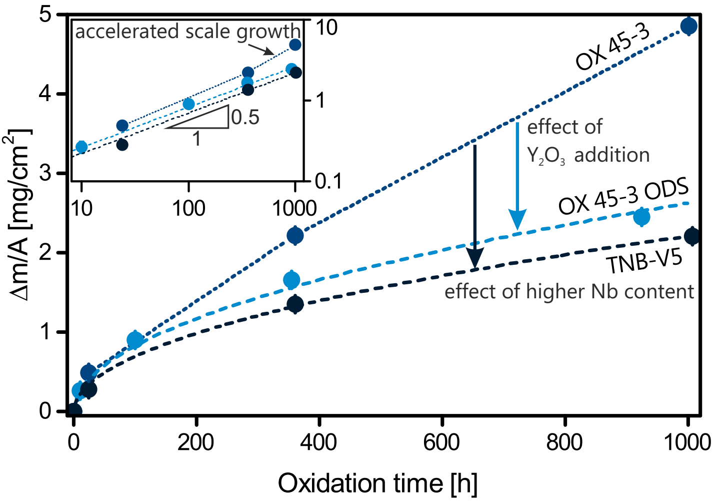

Figure 6.1: Weight gain of OX 45-3, OX 45-3 ODS and TNB-V5 at 1073 K in static laboratory air. For OX 45-3 ODS and TNB-V5 fitted parabolic curves are shown (- -). The data points for OX 45-3 have been connected to guide the reader's eye (··). Inset: data points on a log-log scale.

Table 6.1: Parabolic growth rates k_p for OX 45-3, OX 45-3 ODS and TNB-V5 at 1073 K.

Alloy	**$k_p \cdot 10^{-10}$ [$kg^2 \cdot m^{-4} \cdot s^{-1}$]**	**Time range [h]**	**Reference**
OX 45-3	3.7	$0 \leq t \leq 360$	This work
OX 45-3 ODS	1.9	$0 \leq t \leq 924$	This work
TNB-V5	1.4	$0 \leq t \leq 1001$	This work
	1.1	$0 \leq t \leq 62$	[204]

duration of 1001 h is increased by $3 \cdot 10^{-11}$ $kg^2 \cdot m^{-4} \cdot s^{-1}$ compared to the value reported by Masset and Schütze for 62 h [204] (Table 6.1). However, the weight gain at 24 h of TNB-V5 observed in this work is overestimated by the fit over the complete test duration (see inset Figure 6.1). Consequently, a lower k_p is determined for short-term testing and explains the slight difference between reported values and the ones obtained in this work.

6.1.3 Morphology and phase evolution of the formed oxide scale

The evolution of the morphology of the oxide scale on OX 45-3 ODS at 1073 K initially shows the formation of a fine grained, Al_2O_3-rich scale after 10 h (Figure 6.2a). Some coarsened oxides appear, being TiO_2 based on their composition. According to XRD, the scale after 10 h consists of TiO_2 (rutile) and α-Al_2O_3 (corundum) and trace amounts TiN and Ti_2AlN (Figure 6.3). After 100 h exposure the TiO_2 covers most of the surface with only a few spots left where the fine grained Al_2O_3-layer remains visible (Figure 6.2b). This is also represented by a strong increase in TiO_2 peak intensities in XRD. Simultaneously, the reflections of γ and α_2 start to vanish due to the formation of the oxide scale. The reflections of the TiN-phase also decrease in intensity, indicating its formation in the initial stages of oxidation and its location close to the alloy-scale interface. After 354 h of oxidation the scale surface shows mainly coarse, faceted TiO_2 crystals with a lateral size below 5 µm (Figure 6.2c). Upon exposure for 924 h no significant changes of the oxide scale surface morphology are observed (Figure 6.2d). The scale continues to increase in thickness and mass, as it is evident from Figure 6.1 but also from vanishing substrate and TiN signal intensities in XRD (Figure 6.3).

The cross-section microstructure of the formed oxide scale shows a multiphase, layered and complex structure after 354 h at 1073 K (Figure 6.4). As previously discussed, the outermost region consists out of coarse TiO_2. This is also evident from an EDX line-scan across the scale after 924 h (Figure 6.5). Below this surface layer, a region consisting of fine grained Al_2O_3 + TiO_2 is observed. Towards the base material, the Al_2O_3 disappears leaving behind a region of predominantly TiO_2. At the alloy-scale interface bulky Al_2O_3-rich phases are observed together with a thin layer enriched in Ti, Al and N. In the intermetallic base material Nb-rich phases form in the region close to the scale. Approximately 7 µm below the alloy-scale interface Ti-depletion is observed in the base material. Simultaneously, Nb is enriched in this region with its

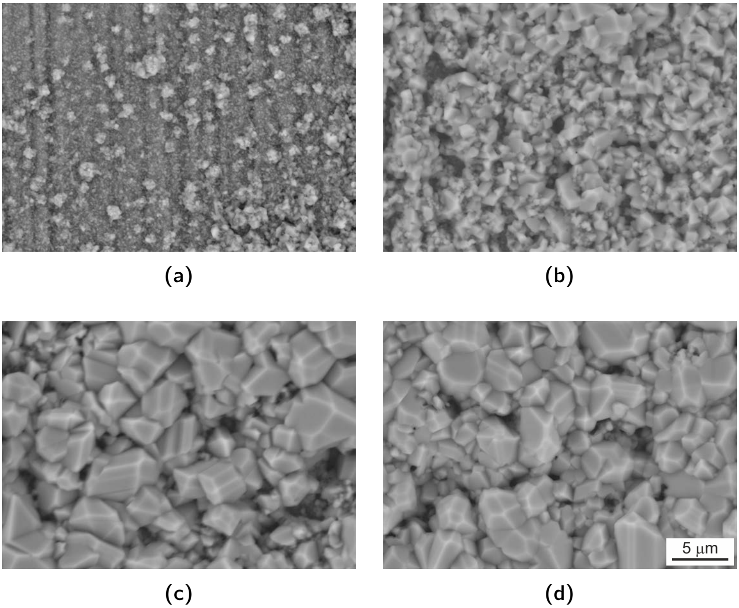

(a) (b) (c) (d)

Figure 6.2: BSE SEM top-view micrographs of OX 45-3 ODS after a) 10 h, b) 100 h, c) 354 h and d) 924 h at 1073 K in air. The scale bar in d) is valid for a-d).

maximum concentration directly below the oxide scale. Nb is also incorporated into the first TiO_2-rich zone but is absent in the outer Al_2O_3 + TiO_2 and surface TiO_2-layer. No Y-rich phases are observed, however Y is detected in small amounts in the Nb-enriched TiO_2 layer by EDX. After 924 h of exposure, small cavities are observed in the oxide scale close to the alloy-scale interface. This promotes spallation along these weak spots which is indeed observed after this exposure time.

In order to elucidate the effect of the Y_2O_3 addition in OX 45-3 ODS, the morphology evolution of the ODS-free variant OX 45-3 and TNB-V5 is studied. After 24 h exposure of OX 45-3 at 1073 K the surface is mainly covered by TiO_2 (Figure 6.6a). XRD also indicates the presence of α-Al_2O_3 as well as

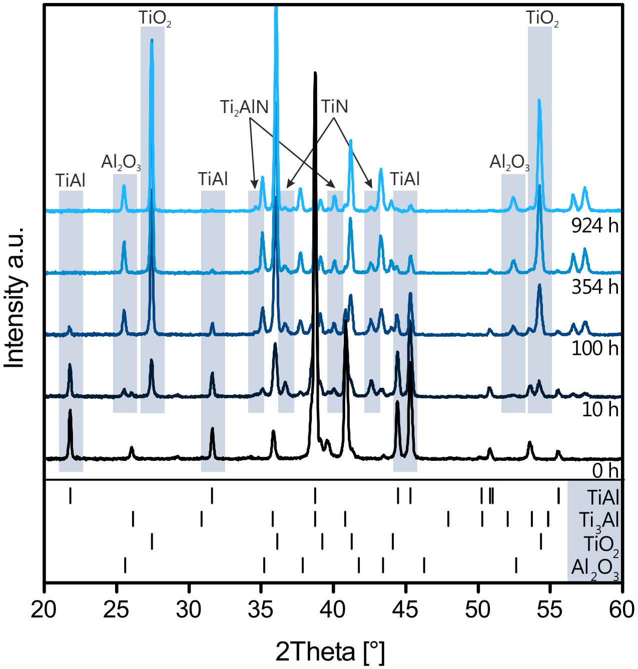

Figure 6.3: XRD spectra of oxidized OX 45-3 ODS at 1073 K. The peak positions of the major phases γ-TiAl, α_2-Ti_3Al, TiO_2 (rutile) and α-Al_2O_3 (corundum) are indicated as well as the evolution of their prominent peaks. Traces of TiN and Ti_2AlN peaks are marked with arrows (↓).

traces TiN and Ti_2AlN (Figure 6.7). After 360 h of exposure, the entire surface consists of coarse, faceted TiO_2-crystals with the larger grains exceeding a lateral size of 5 µm (Figure 6.6b). The corresponding XRD spectrum shows the presence of predominantly TiO_2 and Al_2O_3. The reflections of the alloy substrate almost completely vanished indicating a relatively thick scale at

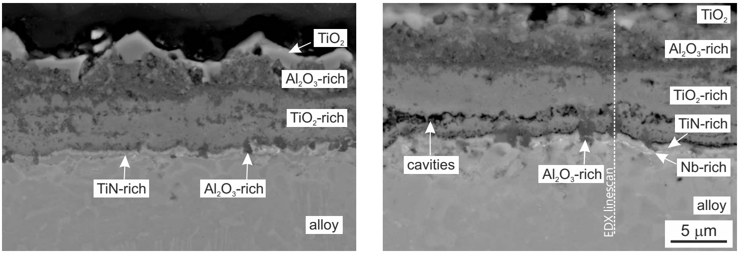
TiO2
Al2O3-rich
TiO2-rich
TiN-rich
Al2O3-rich
alloy
TiO2
Al2O3-rich
TiO2-rich
TiN-rich
cavities
Al2O3-rich
Nb-rich
EDX linescan
alloy
5 µm

(a) **(b)**

Figure 6.4: BSE SEM micrographs in cross-section of the oxide scales formed on OX 45-3 ODS after a) 354 h and b) 924 h at 1073 K in air. The different characteristic regions are indicated. The scale bar in b) is valid for a-b).

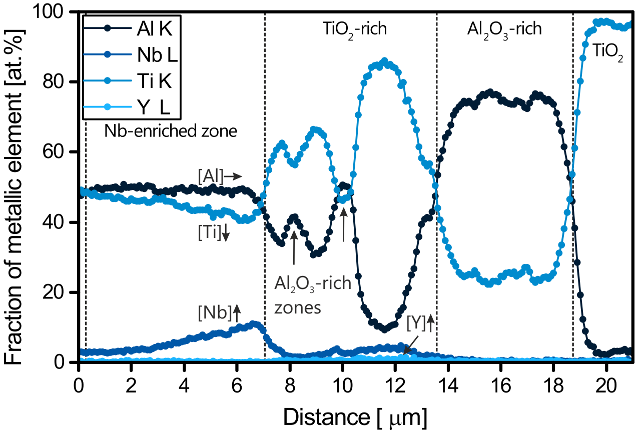

Figure 6.5: SEM EDX line-scan showing the fraction of the metallic elements Ti, Al, Nb and Y across the oxide scale in OX 45-3 ODS after exposure to air at 1073 K for 924 h (see Figure 6.4b).

this point. After 1001 h exposure, the surface structure is further coarsened. Large TiO_2-crystals form with lateral sizes exceeding 10 µm (Figure 6.6c). The XRD spectrum of the scale is dominated by TiO_2. The reflections of Al_2O_3 decrease in intensity compared to 360 h exposure, indicating fast and predominant formation of TiO_2. At this point, the substrate reflections have completely vanished. Combining these results, a thick scale consisting mainly out of TiO_2 is formed on OX 45-3 after exposure of 1001 h at 1073 K. The scale formed on the reference alloy TNB-V5 after 1001 h at 1073 K consists out of coarser, faceted TiO_2 as well as relatively fine grained regions in between them (Figure 6.6d). Comparing the morphologies of the formed scale after similar exposure time on OX 45-3, OX 45-3 ODS and TNB-V5

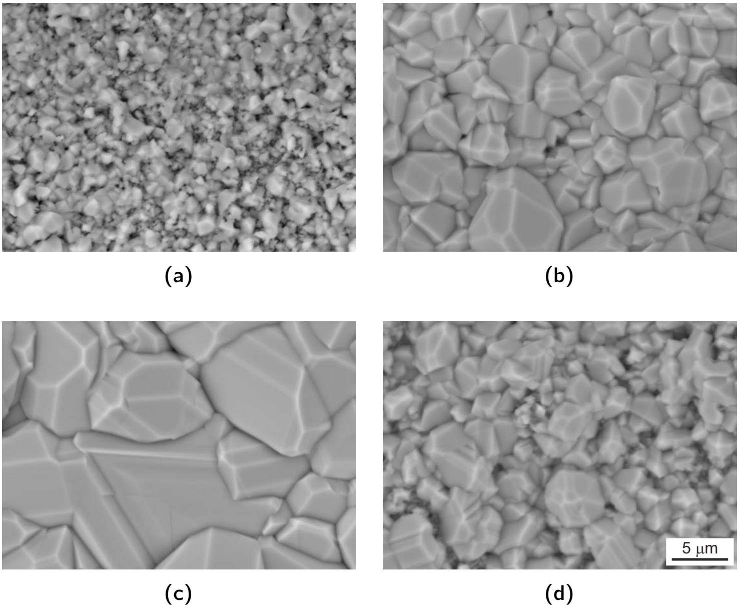

(a) (b)

(c) (d)

Figure 6.6: BSE SEM top-view micrographs of a-c) OX 45-3 and d) TNB-V5 after a) 24 h, b) 360 h, and c,d) 1001 h at 1073 K in air. The scale bar in d) is valid for a-d).

shows a very similar behavior of the latter two. Both form a scale with a bimodal grain size distribution of coarser TiO_2 and finer TiO_2 + Al_2O_3 in between. This similarity also observed in the XRD spectra after the maximum test time (Figure 6.8). While the spectra for OX 45-3 ODS and TNB-V5 are virtually the same, showing the presence of a significant fraction of Al_2O_3 beside the major TiO_2, the spectrum of OX 45-3 is dominated by the presence of TiO_2. Beside this difference, the general phase evolution appears to be similar with early formation of TiN and later formation of a predominantly TiO_2 outer scale and vanishing TiN intensities. The strongest formation of Ti_2AlN is observed in the OX 45-3 ODS variant, but this phase is also present

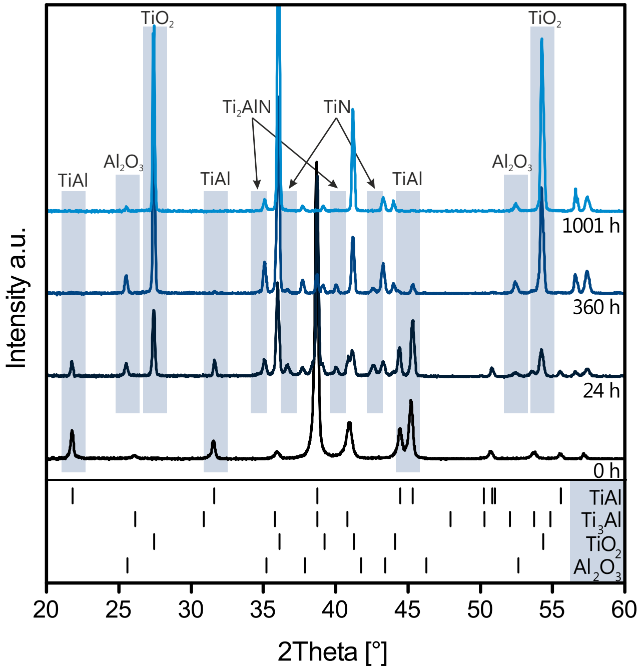

Figure 6.7: XRD spectra of oxidized OX 45-3 at 1073 K. The peak positions of the major phases γ-TiAl, α_2-Ti_3Al, TiO_2 (rutile) and α-Al_2O_3 (corundum) are indicated as well as the evolution of their prominent peaks. Trace amounts of TiN and Ti_2AlN peaks are marked with arrows (↓).

in the TNB-V5 alloy. In the OX 45-3 alloy the Ti_2AlN phase is present at earlier time, but its signal vanishes due to the overlying TiO_2. The general behavior of the three studied alloys is schematically summarized in Figure 6.9. In the initial state, the alloy has a thin native oxide layer due to the high affinity of of Ti and Al to oxygen (Fig. 6.9a). After exposure to air for up to 24 h at 1073 K the surface is covered with fine grained Al_2O_3 and TiN as well as dispersed coarser TiO_2 crystals (Fig. 6.9b). Upon prolonged exposure TiO_2 starts to overgrow the fine grained Al_2O_3-rich layer as TiO_2 provides a fast diffusion path for oxygen (Fig. 6.9c). Additionally, N diffuses

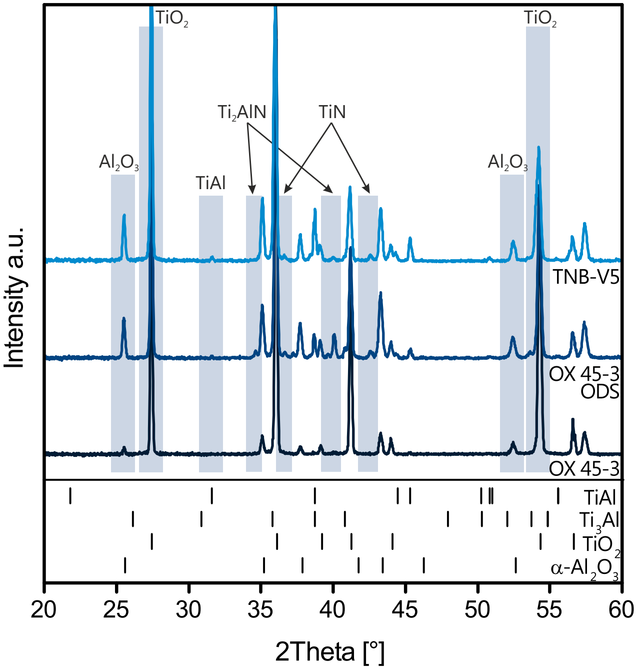

Figure 6.8: XRD spectra of OX 45-3 (bottom), OX 45-3 ODS (center) and TNB-V5 (top) oxidized at 1073 K for 1001 h, 924 h and 1001 h, respectively. The peak positions of the major phases γ-TiAl, α_2-Ti_3Al, TiO_2 (rutile) and α-Al_2O_3 (corundum) are indicated as well as the evolution of their prominent peaks. Trace amounts of TiN and Ti_2AlN peaks are marked with arrows (↓).

towards the alloy forming various nitride phases. Ti and Al diffuse into the scale forming new oxides leading to a multiphase structure. Nb as a slowly diffusing element enriches at the lower interface forming Nb-rich phases. After long term exposure the final layered oxide structure is formed with TiO_2 as the outermost layer (Fig. 6.9d). The underlying fine grained Al_2O_3-rich layer controls the diffusion of oxygen and thus scale growth. Toward the alloy-scale interface a mixed layer of Ti- and Al-oxides is formed. The interface itself consist of a mixture of nitrides, Al-oxides, and Nb-rich phases. Enhanced diffusion of N along grain boundaries favors the formation of nitrides in the sub-scale zone. Due to selective oxidation of Ti and Al these elements are depleted leaving behind a Nb-enriched zone with typically higher α_2 content due to compositional shifts towards higher Ti content.

While all three alloys show a similar scale evolution in terms of the sequence of the formed phases, their weight gains have been found to be very different,

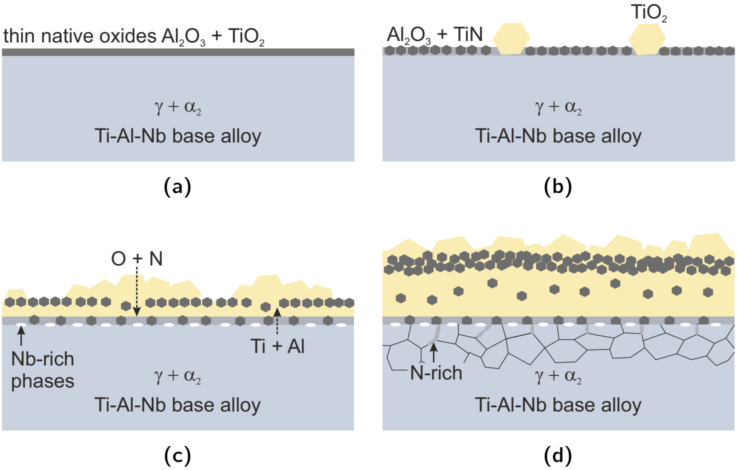
thin native oxides Al_2O_3 + TiO_2
$\gamma + \alpha_2$
Ti-Al-Nb base alloy
(a)
TiO_2
Al_2O_3 + TiN
$\gamma + \alpha_2$
Ti-Al-Nb base alloy
(b)
O + N
Ti + Al
Nb-rich phases
$\gamma + \alpha_2$
Ti-Al-Nb base alloy
(c)
N-rich
$\gamma + \alpha_2$
Ti-Al-Nb base alloy
(d)

Figure 6.9: General oxidation processes and structural evolution upon oxidation of the studied Ti-Al-Nb base alloys at 1073 K. a) native state, b) short term exposure up to 24 h, c) intermediate stage (24 h < t < 1000 h), d) final state after 1000 h.

where the ODS-containing variant and the Nb-richer TNB-V5 show similarly low growth kinetics. In the past the beneficial effect of Nb and the similar elements Mo and W have been attributed to the stabilization of Al_2O_3 forming in a sub-surface barrier layer as well as in the inner TiO_2-rich region [198]. Consequently, inward transport of oxygen along the TiO_2 is strongly reduced and higher oxidation resistance is achieved. Similar effects on the stability of Al_2O_3 have been described for Y-doped TiAl alloys [186]. Comparing the results for OX 45-3 and OX 45-3 ODS, this effect is also triggered by additions of Y_2O_3 in the form of finely distributed dispersoids. Unlike in elemental addition, the Y is concentrated in the stable dispersoids avoiding detrimental effects as formation of large internal Y_2O_3-particles, as observed by Haanappel *et al.* [53]. Although the studied alloy only contained 0.1 at.% of Y, locally accelerated degradation was observed around newly formed Y_2O_3. This effect is not observed in this work by the addition of Y in the form of a stable dispersion of Y-based oxides.

6.1.4 Size evolution of the dispersoids at high temperature

The stability of the dispersoids and their size evolution is determined for the OX 45-3 ODS variant after exposure to air at 923 K and 1073 K after 987 h and 924 h, respectively (Figure 6.10). After testing at both temperatures, the dispersoids remain stable and well distributed throughout the intermetallic matrix (Figures 6.10a and 6.10c). The particles are observed in the equiaxed region consisting of γ and α_2 as well as in the lamellar $\alpha_2 + \gamma$ colonies, where no preference for either phase is found. The dispersoids are globular and partly faceted, with diameters between sub-10 nm up to 150 nm. In both conditions a multitude of dispersoids is found on phase or grain boundaries, indicating a strong pinning effect by the dispersoids and consequently reduced grain growth due to their presence in the ODS-variant (Figures 6.10b and 6.10d). Coarser dispersoids exert a high enough pinning force to lead to locally curved grain boundaries. This clearly indicates the beneficial effects of a portion of larger particles on the microstructure stability at high temperatures. A similar effect has also been observed at short term annealing at high temperatures in

OX 45-3 ODS (Chapter 5). Upon exposure to air at 923 K and 1073 K the dispersoids show little change in their size distribution. Figure 6.11 shows the size distributions after both exposure conditions as well as the initial state in the stabilized OX 45-3 ODS alloy. After consolidation by SPS and the following stress relief and microstructural stabilization annealing at 1123 K for

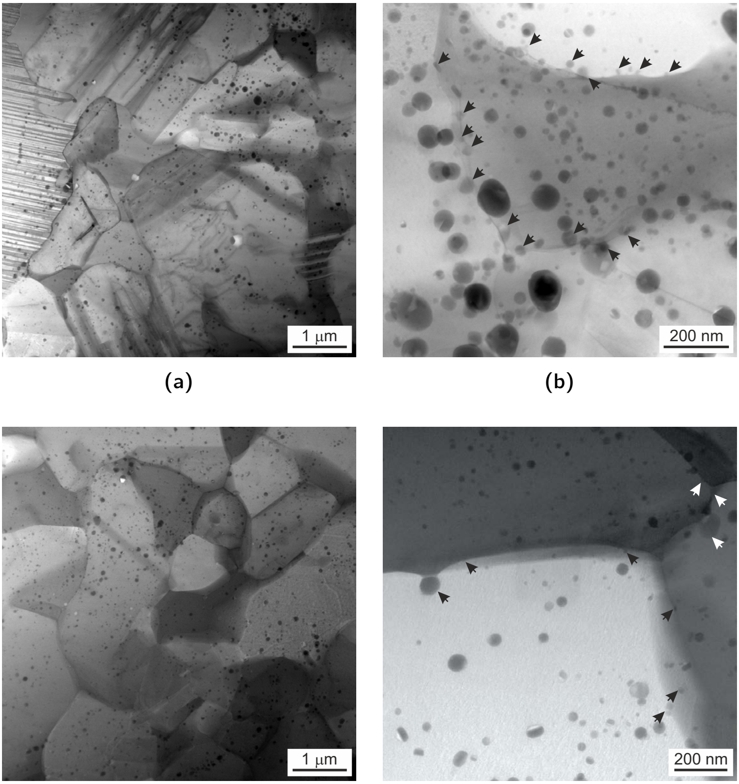

(a) (b)

(c) (d)

Figure 6.10: Bright-field STEM micrographs of the microstructure of the base alloy OX 45-3 ODS after a, b) 987 h at 923 K and c, d) 924 h at 1073 K in static laboratory air. Boundary pinning is indicated with arrows (↑). Images by K. Dawson, ULIV.

12 h, the resulting mean dispersoid diameter is 29 nm. The log-normal shape of the distribution indicates the highest fraction of particles at a slightly smaller diameter of around 23 nm. The number density of particles is $4.4 \cdot 10^{20}$ m^{-3}. Upon exposure at 923 K for 987 h the resulting size distribution is shifted to 26 nm with its maximum relative frequency in the size class of 15 to 20 nm with a particle number density of $5.3 \cdot 10^{20}$ m^{-3}. A similar oxidation time at 1073 K leads to a slight particle coarsening, shifting the size distribution to a median of 32 nm at a particle number density of $4.4 \cdot 10^{20}$ m^{-3}. While the relative frequency of the fine dispersoids is reduced, a larger amount of coarser ones appears simultaneously indicating continued growth of particles of all sizes. The appearance of a high fraction of dispersoids with sub-median size after oxidation at 923 K could be attributed to fast coarsening of very fine precipitates or re-precipitation from the matrix. In the present case the latter appears to be the case, as the fraction of small dispersoids after consolidation appears not to be high enough to explain such behavior. The increased number density also suggests the formation of new particles. But it has also to be noted that the measurement of particles below 5 nm is difficult based on their

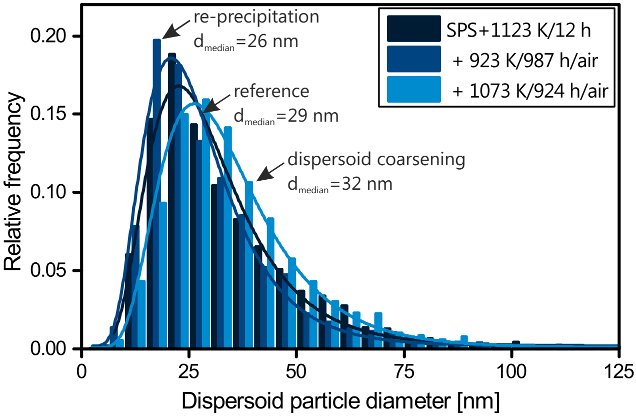

Figure 6.11: Size distribution of ODS particles in solid state SPS sintered and stabilized material after exposure for 987 h at 923 K and 924 h at 1073 K. Least-square-fitted log-normal distribution curves are shown overlaid.

low contrast to the surrounding matrix. The re-precipitation mechanism can be understood taking into account the production route of the alloy. Upon HEBM the added Y_2O_3 is finely dispersed and potentially partially dissolved into the matrix alloy. After precipitation and growth upon SPS consolidation and annealing, the formed particles are in a metastable equilibrium with the matrix, based on the relative stabilities of the phases involved. It was shown in the past that even in equilibrium a portion of the initially added dispersoid material remains in solution [141]. This leads to a doping of the TiAl alloy matrix with Y and O in the case of Y_2O_3 addition. Upon long-term oxidation at moderate temperature, the formation of new particles appears to be faster than the growth of the existing ones, leading to a effective shift of the total size distribution towards smaller diameters. At higher temperature this effect is not observed. Additional effects may be chemistry changes of the particles formed. Changing from a Y-rich to a Y-lean phase, new particles can be formed by incorporation of the abundant Ti and Al as well as O. To unambiguously determine such an effect a large amount of measurements on the formed particles is needed to ensure statistical meaning which is not the goal of the presented study. However, this remains an important topic for future studies of this class of intermetallics. Apart from the discussion about the underlying cause of the observed shifts in the particle size distribution by a few nanometers, it can be clearly stated that the particles in OX 45-3 ODS exhibit a low coarsening tendency and are stable at 1073 K for 1000 h.

6.2 Mechanical properties at low and high temperature

The addition of ODS particles has a clear influence on the tensile properties of ternary Ti-45Al-3Nb at room temperature. Figure 6.12 shows the tensile stress-strain curves for OX 45-3 and OX 45-3 ODS tested until fracture. The ODS variant has a higher yield point $Rp_{0.1}$ (+34 %) and higher ultimate strength R_m (+14 %) but lower total fracture strain ε_f (-17 %) compared to the ODS-free variant. The Young's modulus of both variants is close to 170 GPa based on the linear elastic part of the stress-strain curve. Both variants show only small scatter between the individual specimens, selected randomly from different regions in the consolidated billet. This indicates good microstructural homogeneity throughout the SPS consolidated material. The mechanical performance of OX 45-3 ODS remains superior to the ODS-free variant at all tested temperatures up to 1073 K. Figure 6.13 shows the evolution of $Rp_{0.1}$, R_m and ε_f for both variants. The $Rp_{0.1}$ of OX 45-3 ODS is slightly reduced at elevated temperature compared to its maximum value at room temperature. After the initial reduction to 729±22 MPa at 873 K it increases again to 742±6 MPa at 973 K and 745±14 MPa at 1073 K. The R_m shows a similar behavior and decreases from 293 K to 873 K. This value remains stable up to 973 K before raising again reaching 855±3 MPa which matches its R_m at room temperature. The elongation to fracture shows an similar behavior to R_m. The very similar evolution of R_m and ε_f indicates a critical strain based failure mechanism leading to premature fracture and lower R_m at intermediate temperatures. This is also evident from the increased standard deviation of R_m at 973 K, which is caused by a strong scattering of the obtained values for four specimens. This high standard deviation is unusual for this alloy comparing all the other data. Detailed analysis shows

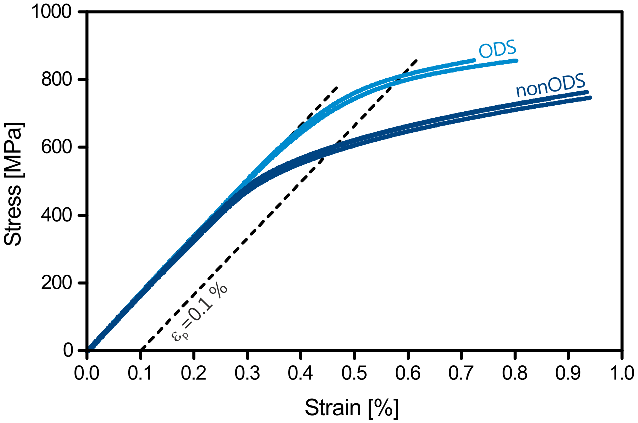

Figure 6.12: Tensile stress-strain curves for SPS OX 45-3 (nonODS, n=3) and OX 45-3 ODS (ODS, n=2) at room temperature. The yield point $Rp_{0.1}$ defined at a plastic strain of 0.1 % is indicated.

that the measured values of R_m at 973 K are 747 MPa, 755 MPa, 775 MPa and 856 MPa. At the same time the $Rp_{0.1}$ value shows only little scattering. The maximum strain at fracture is 0.77 % for 856 MPa while the minimum observed strain is 0.61 % for 755 MPa. In the ODS-free variant OX 45-3 the $Rp_{0.1}$ first increases from 593±10 MPa to 617±11 MPa at 873 K before it strongly decreases to 521±8 MPa at 973 K and increases again to 601±42 MPa at 1073 K. The R_m and ε_f show a similar evolution which is inverse to the trends of the $Rp_{0.1}$. First, both values decrease up to 873 K. At 973 K the R_m recovers to 734±22 MPa while ε_f reaches its maximum of 1.08±0.14 %. At 1073 K both values decrease again to 689±9 MPa and 0.71±0.06 %, respectively.

To understand the differences in mechanical performance and the cause of failure, the fracture surfaces are examined by SEM. Figure 6.14 shows the characteristic features observed in OX 45-3 ODS after fracture at 293 K to 1073 K. The insets show the region of the crack origin as identified by the typical star-like crack pattern forming around it. Three main failure modes are observed: trans-lamellar (TL), inter-granular (IG) and feathery trans-lamellar (FTL) fracture. The trans-lamellar modes are observed in the lamellar colonies of $\alpha_2 + \gamma$. The TL mode shows a very ragged crack

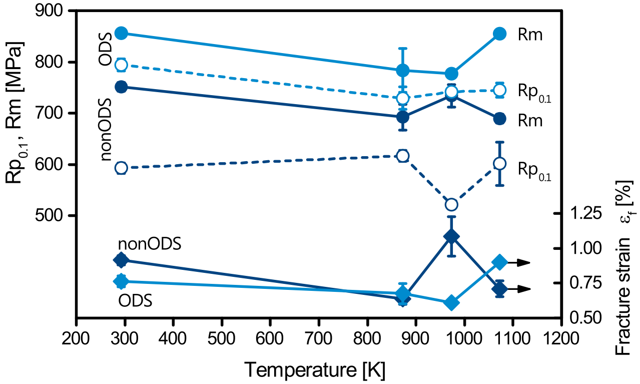

Figure 6.13: Mechanical performance of nonODS OX 45-3 and OX 45-3 ODS from 293 to 1073 K.

surface following the lamellar interfaces before crossing individual lamellae. The FTL mode crosses several lamellae without directional change along the interfaces. The IG mode is observed in the equiaxed region following the grain boundaries of the γ phase. It is evident from the micrographs that OX 45-3 ODS shows a very similar fracture mode at all temperatures. The origin of the crack is related to a cleavage fracture of the intermetallic matrix. Based on the size of these cleaved regions it is believed that is related to the lamellar colonies in the material. No mass contrast between the crack origin

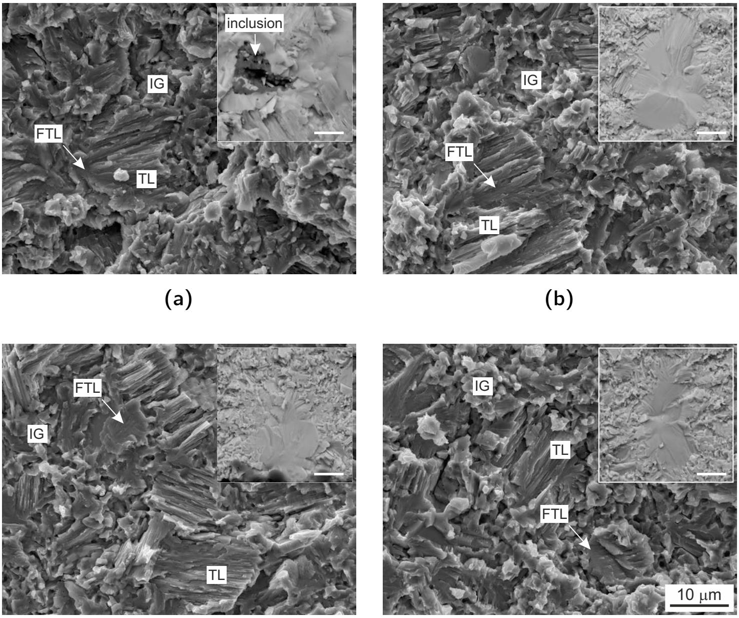

(a) (b)

(c) (d)

Figure 6.14: SE SEM micrographs of the fracture surface of OX 45-3 ODS tensile tested at a) 293 K, b) 873 K, c) 973 K and d) 1073 K in vacuum. Insets: BSE SEM micrographs of the origin of fracture. The characteristic fracture modes trans-lamellar (TL), feathery trans-lamellar (FTL), inter-lamellar (IL) and inter-granular (IG) are indicated. The scale bar in d) applies for a-d). Insets: scale bar = 10 μm.

and the surrounding matrix is observed, indicating intrinsic crack initiation in the microstructure. At room temperature a small inclusion is observed close to the cleaved region. Although probably responsible for ultimate fracture its influence on the mechanical performance appears to be minimal based on the superior strength of the material. Figure 6.15 shows the fracture surfaces of OX 45-3 after testing at 293 K to 1073 K. The same three fracture modes as in the ODS-variant are observed plus the additional inter-lamellar (IL) mode. The IL mode is observed in the lamellar colonies and separates the individual lamellae leading to large planar features. At 293 K the predominant

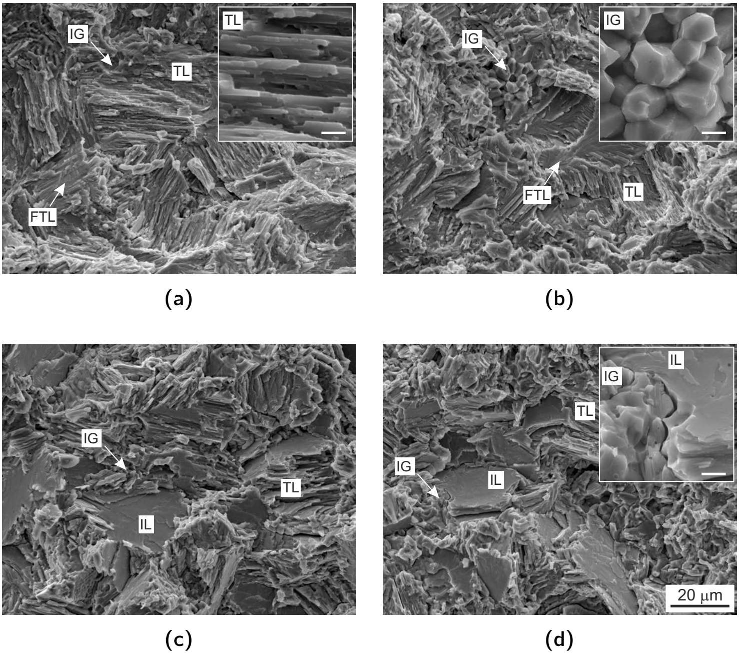

(a) **(b)**

(c) **(d)**

Figure 6.15: SE SEM micrographs of the fracture surface of OX 45-3 tensile tested at a) 293 K, b) 873 K, c) 973 K and d) 1073 K in vacuum. The characteristic fracture modes trans-lamellar (TL), feathery trans-lamellar (FTL), inter-lamellar (IL) and inter-granular (IG) are indicated. The scale bar in d) applies for a-d). Inset a): scale bar = 1 µm, insets b, d): scale bar = 2µm.

fracture mode is the TL mode (Figure 6.15a). The IG and FTL modes are also observed in the γ-rich regions and across lamellae, respectively. At 873 K the FTL mode appears on larger areas while the equiaxed γ shows very distinct inter-granular fracture with no apparent ductility (Figure 6.15b). At 973 K the IL mode is observed, thereby completely changing the appearance of the fracture surfaces. At the same time the FTL mode vanishes (Figure 6.15c). The fracture surface at 1073 K is similar to the one observed at 973 K showing TL, IG and FTL modes (Figure 6.15d). The inset shows also separation cracks forming in between the IG and IL zones in the equiaxed γ and lamellar colonies. The change in fracture mode between 873 K and 973 K is accompanied with a strong increase in ductility and reduced yield strength (Figure 6.12). This indicates that the IL mode is actually a ductile fracture mode compared to the brittle IG and TL modes. The replacement of the FTL mode by the IL mode could indicate that also the FTL mode is a ductile fracture mode. However, based on the macroscopic ductility this cannot be confirmed due to its limited occurrence within the fracture surface. Also the ODS-variant shows an increased ductility at high temperature with abundance of the FTL mode (Figure 6.14d). This indicates that indeed the FTL mode is a sign of ductility in the lamellar colonies and can explain the increased strain at fracture. Furthermore, the IL and FTL mode appear to be strongly related with the direction of the crack growth changing from trans-lamellar at low temperature to inter-lamellar in the IL mode at high temperature in the ODS-free variant while the predominant direction remains trans-lamellar in the ODS-variant. Consequently, the IL mode is not observed there.

The significant increase in yield point of the ODS-variant can be attributed to the addition of dispersoids. However, the underlying mechanism for the higher yield point is not only depending on the presence of the dispersoids and their interaction with dislocations. A second and very important contribution is from the microstructure itself. The ODS-variant has a fine microstructure with equiaxed γ between small lamellar colonies forming a duplex to near-lamellar alloy. The ODS-free alloy has less γ surrounding larger lamellar colonies and is thus closer to a near-lamellar alloy (see Figure 5.4). It is well known that in TiAl alloys all constituents, equiaxed γ, lamellar colonies and the lamellar structure itself follow a Hall-Petch relationship with increased strength with reduced feature size [48]. Duplex microstructures combining lamellar colonies and a significant fraction of equiaxed γ have typically already high strength, but are inferior to near-lamellar microstructures providing the highest strength in TiAl alloys [44]. Taking into account these findings, the microstructure of the ODS-free variant should actually provide the higher strength than the structure richer in equiaxed γ found in the ODS-variant based on its general microstructure. A refinement effect upon ODS addition of each microstructural feature can however lead to significantly enhanced strength as the Hall-Petch constants of TiAl alloys for lamellar microstructures have been found to be unusually high up to 5 $\mathrm{MPa \cdot m^{1/2}}$ compared to common metals with values close to or below unity [48]. Separation of the individual effects however remains difficult as microstructure, properties and alloy composition are intertwined in TiAl alloys. At elevated temperature the abnormal mechanical behavior of the intermetallic phases contributes to the strength retention. The single-crystalline γ and α_2 show an abnormal strength increase with increasing temperature with their maximum yield stress around 873 K and 1173 K, respectively [46]. In technical alloys this leads to a ductile-to-brittle transition around 923 K to 1073 K, as γ starts to soften. This is in agreement with the observations in the ODS-free OX 45-3 alloy. The addition of dispersoids suppresses the softening reaction found in OX 45-3 which is a clear benefit for the ODS variant providing stable yield stress for all tested temperatures. The softening is probably caused by increased mobility of previously dissociated and locked super-dislocations recombining due to thermal activation [46]. While the dissociating contribution disappears, the dispersoids remain stable and continue to hinder dislocation movement. Consequently, superior yield stress is maintained to higher temperature in ODS TiAl alloys.

6.3 Conclusions

- The addition of Y_2O_3 increases the oxidation resistance of mechanically alloyed Ti-45Al-3Nb at 1073 K by a factor of two compared to the ODS-free variant.
- Upon oxidation at a complex oxide scale is formed. XRD shows the presence of TiO_2, Al_2O_3 and TiN and Ti_2AlN nitride phases, where TiO_2 forms the outermost layer. All alloys form protective Al_2O_3 as part of their oxide scales.
- The Y-based dispersoids remain stable at 923 K and 1073 K up to 1000 h with minimal changes in median size from 29 nm in the initial state to 26 nm at 923 K and 32 nm at 1073 K, respectively. Increased number densities from 4.4 to $5.3{\cdot}10^{20}$ m^{-3} indicate precipitation of new particles at 923 K.
- At room temperature, SPS OX 45-3 ODS has a 34% higher yield point, 14% higher ultimate tensile strength at a reduction in fracture strain of 17% compared to SPS OX 45-3. The ODS variant retains its superior yield point and ultimate strength up to 1073 K.
- The fracture surfaces of OX 45-3 show increased tendency for inter-lamellar failure at high temperatures. OX 45-3 ODS shows similar fracture surfaces from 293 K to 1073 K with preferred trans-lamellar fracture.

The achieved oxidation behavior is comparable to a commercial TNB-V5 alloy richer in Nb and additionally alloyed with C and B. The addition of <0.2 mol.% Y_2O_3 provides similar resistance as the effects of additional 2 at.% Nb and 0.2 at.% C and B each. The addition of dispersed Y_2O_3 opens a new possibility to further enhance the oxidation resistance of TiAl alloys alloyed already to their maximum allowable contents of Nb or other elements as W and Mo based on the desired set of phases. Based on the presented results, the addition of ODS particles is considered a promising way to further enhance the properties of TiAl alloys in the future.

7 Selective laser melting of a β-solidifying ODS γ-TiAl alloy

In this Chapter the SLM processing of ODS Ti-45Al-3Nb-<0.2Y_2O_3 (OX 45-3 ODS, P-3) is discussed. First, the experimental details are presented followed by the results and discussion of the obtained data. The process development is started from single lines and layers and later continued to multi-layer SLM to massive blocks and complex 3D lattices. The focus lies on the formation of stable melt pools and the occurrence of cracks due to thermal stresses. The dependencies of cracking on energy input, scanning strategy and part geometry are discussed before the chapter is concluded. The experimental part of this work has been performed in the frame of a Master Thesis at ETH and Empa (G. Dasargyri, January - July 2015) with all SLM tests being performed at Inspire, St. Gallen. The major findings are summarized here and additional analysis on cracking frequencies has been performed.

7.1 Experimental details

7.1.1 Single line deposition

As a first step towards SLM of ODS TiAl, single line deposition on commercially pure Ti (ASTM grade 2) is performed. Based on these experiments, the melt pool stability and size is obtained as function of laser power and scanning speed. The powder layer thickness and the laser spot diameter are kept constant at 80 µm and 100 µm, respectively. The powder layer thickness is chosen to be representative for later SLM processing at a nominal layer thickness of 50 µm. Assuming a height reduction of 35 % due to consolidation upon melting, the thickness of the powder layer deposited onto a previously melted area is around 80 µm for nominal 50 µm layers. The laser power is varied from 50 to 200 W in steps of 50 W, the scanning speed is varied from 25 to 400 mm·s^{-1} in steps of 25 mm·s^{-1}. At 200 W the slowest scanning speed is omitted, while for 50, 100 and 150 W an additional data point at 12.5 $\mathrm{mm \cdot s^{-1}}$ is generated. In order to get preliminary data on the formation of layers, the hatch distance is reduced from 1 mm to 0.075 mm (1 mm, 0.25 mm, 0.1 mm, 0.075 mm). The lines formed at 1 mm hatch distance are analyzed to obtain the melt pool width at surface level. Eight measurements at different locations along the melt lines are used to calculate the mean width and the standard deviation. The effect of laser re-scanning on the surface condition is analyzed on selected layers with 0.1 mm hatch distance.

7.1.2 Laser re-melting of sintered ODS TiAl

While single layer deposition is a fast method to obtain initial melt pool stability data, the resulting material is a changed alloy due to dilution with the base plate material. Consequently, the microstructural evolution is changed. Additionally, the reflectivity of the ground base-plate may affect laser-material interaction and the effective energy input. In order to obtain data on the true alloy composition, selective laser re-melting using the SLM equipment is applied to bulk OX 45-3 ODS produced by SPS sintering (see Chapter 3.1.3). A total of 16 melt lines are produced where the laser power is varied from 50 to 200 W in steps of 50 W and the scanning speed is 50, 100, 200 and 400 $\mathrm{mm \cdot s^{-1}}$. Top view and cross section micrographs are analyzed to obtain the melt pool width and depth. The cracking frequency in the irradiated area is evaluated using the line intersection method yielding the number of cracks per unit length.

7.1.3 Multi-layer deposition and 3D lattices

With the obtained data from single line deposition and laser remelting, processing parameters for multi-layer deposition are identified. Deposits consisting of 7 layers are produced with various parameters with laser powers of 50, 100 and 150 W and scanning speeds from 50 to 400 $\mathrm{mm \cdot s^{-1}}$. The hatch distance is chosen based on the mean melt pool width obtained from the single line deposits to ensure an overlap of 50 % between individual melt lines. The powder layer thickness is 50 µm. A unidirectional cross-hatch melting strategy is chosen. Re-scanning is performed using two main strategies, re-melting with the same parameters as for deposition and remelting with doubled scanning speed and consequently reduced input energy density. The re-melting direction is parallel to the deposition melt lines. Additionally, re-melting tests are performed with changed re-scanning direction (45° and 90°) with respect to the initial deposition direction as well as with multiple re-scans with reduced energy density. Examination of the surface by SEM is performed to study the influence of the processing parameters on the formation of cracks in the alloys. Using the line intersection method, the crack length per unit area L_A can be calculated using [205]

$$L_A = \left(\frac{\pi}{2}\right) \cdot P_L \tag{7.1}$$

where P_L is the number of intersections per test line length. The unit of L_A is $\mathrm{mm{\cdot}mm^{-2}}$ which can be reduced to $\mathrm{mm^{-1}}$, the unit of P_L.

SLM processing of massive blocks and 3D lattices is performed using laser powers from 50 to 150 W and scanning speeds from 50 to 1000 $\mathrm{mm{\cdot}s^{-1}}$. The hatch distance is adapted accordingly to ensure an overlap of 50 %. The powder layer thickness is 50 µm. Re-scanning is applied on selected specimens with 90° orientation difference to the deposition step. The lattice geometry is a body-centered cubic structure consisting exclusively of trusses oriented with 45° to the unit cell. This allows to build them without any support. The integrity of bulk and lattice structures is later analyzed based on the crack length per unit area and cracking frequencies along the trusses, respectively.

7.1.4 Energy density considerations

When it comes to quantify energy inputs in AM, usually the line, area and volume energy densities E_l, E_a and E_v, respectively, are defined as

$$E_l = \frac{P}{v},\ E_a = \frac{P}{v \cdot h_L},\ E_v = \frac{P}{v \cdot h_L \cdot t_L} \tag{7.2}$$

where P is the laser power, v is the scanning speed, h_L is the hatch distance and t_L is the powder layer thickness. These quantities allow a comparison of processing parameter combinations and their influence on the observed properties. The characteristics of the laser, such as the energy profile and shape, are neglected in Equation 7.2. The circular shape of a typical laser beam cross-section is taken into account in the radiant exposure R, defined as

$$R = \frac{4 \cdot P}{\pi \cdot v \cdot d_L} \tag{7.3}$$

with d_L the diameter of the laser focus spot. In the case of overlapping melt tracks, the effective radiant exposure R' can then be expressed as

$$R' = R \cdot \frac{d_L}{h_L} = \frac{4 \cdot P}{\pi \cdot v \cdot h_L} \tag{7.4}$$

7.2 SLM processing results

7.2.1 Single line deposition

The deposition of single lines is performed to study melt pool formation, stability and width. Figure 7.1 shows the observed resulting characteristic morphologies of the formed melt pools. Three major classes are distinguished, the smooth melt pool, occurrence of splattering and the formation of strongly elongated melt pools with a rough surface. Using this classification, the observed morphologies are combined in a parameter-morphology map (Figure 7.2). Splattering is caused by droplet ejection from the melt pool due

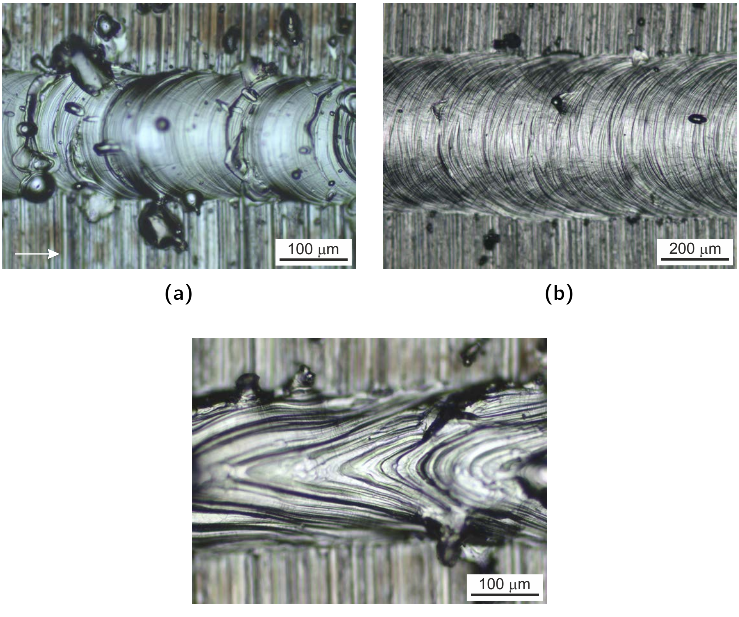

(a)

(b)

(c)

Figure 7.1: Appearance of melt lines showing a) splattering, b) smooth and c) elongated behavior for single line SLM deposition of ODS TiAl.The scan direction is indicated by a white arrow (→) and applies for all micrographs.

to increased recoil pressures upon material evaporation [206]. Smooth melt pool formation is observed for laser powers of 100 to 200 W at low scanning speeds. At high scanning speeds the formed melt pools become strongly elongated with a rough surface. Based on the obtained results, the studied TiAl alloy needs rather high energy inputs to produce smooth melt lines. An observation already made by Löber *et al.* [134]. The mean line width of the produced melt pools naturally increases with increasing power and decreasing scanning speed (Figure 7.3a). At a power level of 50 W the width is only slightly increasing with reduced scanning speed. At high scanning speeds, the melt pool width approaches the laser diameter (100 μm). Laser powers of 100 W and higher show good energy absorption with a strong increase in melt pool width at low scanning speeds. This effect can be attributed to the formation of a metal-vapor filled keyhole and increased energy absorption as the beam penetrates deep into the material reducing reflection losses from the surface. Comparing the radiant exposure to the obtained line width shows a common behavior of 100, 150 and 200 W (Figure 7.3b). This allows to predict the line width based on the calculated radiant exposure for arbitrary

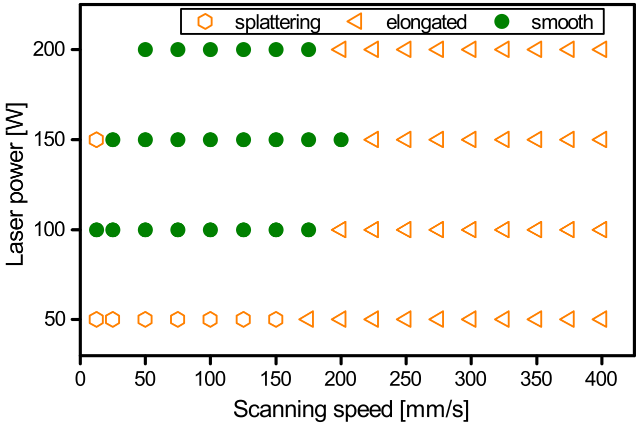

Figure 7.2: Parameter-morphology map for single line SLM processing of ODS TiAl showing the characteristic morphologies of splattering, strongly elongated and smooth melt pools.

parameter combinations at these power levels. The linewidth and the hatch distance define the overlapping of adjacent scans forming the individual layers and are thus important parameters. The inefficient energy absorption at 50 W is also evident here and is observed as a saturation of linewidth for high radiant

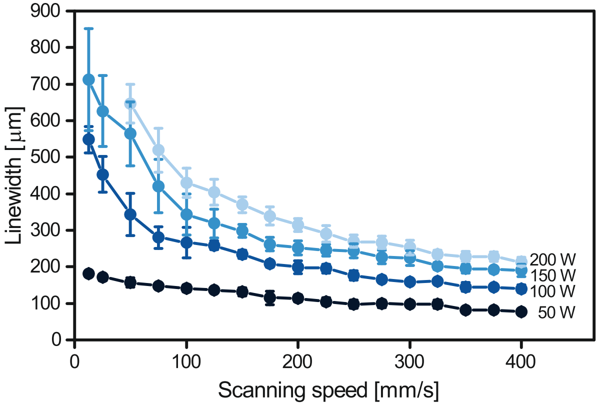

(a)

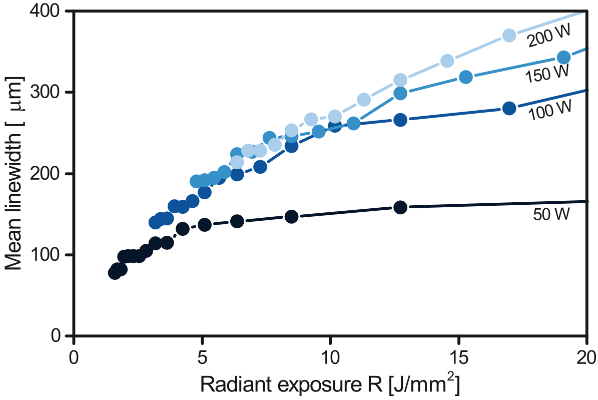

(b)

Figure 7.3: Linewidth of single line SLM deposition of ODS TiAl as a function of a) the scanning speed and b) the radiant exposure for 50 to 200 W and 12.5 to 400 mm·s^{-1}

exposures. It can be summarized that a stable SLM processing window is expected for laser powers in the range of 100 to 200 W and relatively low scanning speeds for the ODS TiAl alloy. The resulting radiant exposures are relatively high compared to SLM processing of conventional materials.

7.2.2 Laser re-melting of sintered ODS TiAl

Having established the stability range for a single powder layer, the interaction of the laser beam with SPS sintered OX 45-3 ODS and the formation of melt pools and their shape is studied. Figure 7.4 shows the observed microstructure after laser re-melting with a laser power in the range of 5o to 200 W at a scan speed of 100 $mm \cdot s^{-1}$. At 50 W a small and shallow melt pool is formed which increases in width and depth at 100 W. At 150 W the elongated melt pool shape indicates the formation of a keyhole and consequently a deep penetration of the laser into the material. This effect is further increased at 200 W where also large porosity in the 100 micron range is observed. This is believed to be caused by trapping metal vapor upon collapse of the keyhole upon cooling. Figure 7.5a shows the observed width and depth of the formed melt pools as a function of the scanning speed. The width of the melt lines is in close agreement with the observations on the single layer tests. This indicates a major influence from the alloy itself and a reduced influence of the presence of the powder and the base plate. This can be understood taking into account the shape of the HEBM powder particles. The powder surface is rough and supports diffuse scattering of the incoming laser beam. It is thus expected that the laser beam interacts only with the powder particles present on top of the powder layer and does not propagate deep into the powder layer by multiple scattering. Apparently, a ground surface of sintered ODS TiAl alloy shows a very similar absorption behavior. This is further strengthened by resulting width and depth compared to the radiant exposure (Figure 7.5b). Again a common behavior is found for the laser tracks with a power level equivalent or exceeding 100 W. The shape of the melt pools can be evaluated using the depth to half-width ratio r (Figure 7.6a). This allows a fast classification of the obtained shapes. At $r<1$ a shallow melt pool is formed. At $r=1$, a half-spherical melt pool is expected. At $r>1.73$ the depth of a melt pool exceeds its total width. This is considered as the threshold to deep welding and the formation of a keyhole. In the range of $1<r<1.73$ melt pool shapes suitable for a sufficient re-melting depth without excessive formation of porosity due to collapsing keyholes are expected. At a power of 50 W only shallow melt pools are observed. For 100 W all obtained ratios are in the range of 1 to 1.73, where the higher energy densities saturate at the upper boundary. For 150 W the higher radiant exposures lead to the formation of exceedingly deep melt pools, which is also observed for all scanning speeds

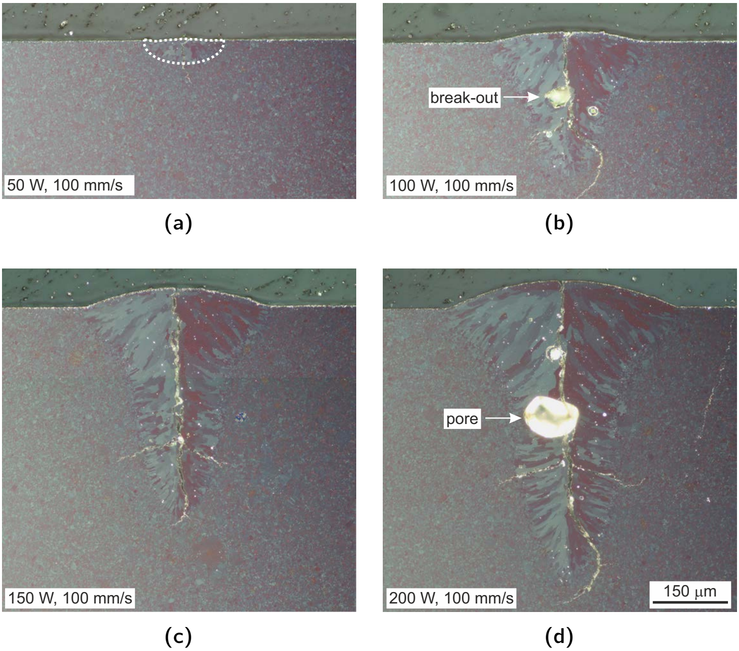

(a) (b)

(c) (d)

Figure 7.4: Cross-section of melt pools created in SPS OX 45-3 ODS by laser re-melting with a) 50 W, b) 100 W, c) 150 W and d) 200 W at a scan speed of 100 mm·s^{-1}. The melt pool at 50 W is outlined in white for better visibility. The scale bar in d) applies for all micrographs.

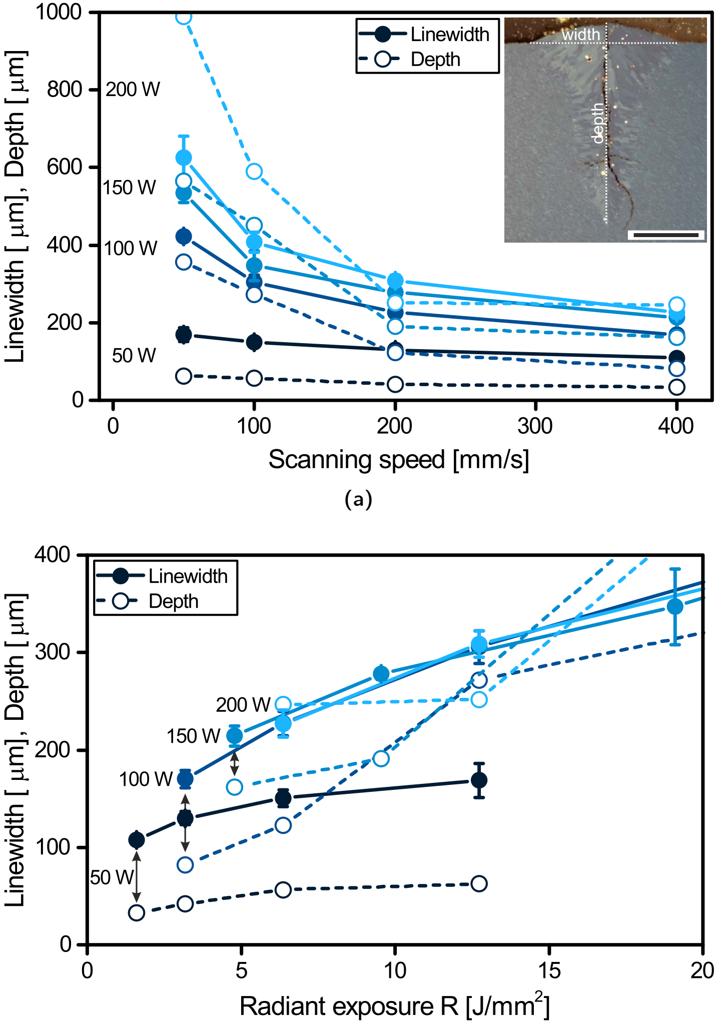

(a)

(b)

Figure 7.5: Linewidth of SLM re-melted sintered ODS TiAl as a function of a) scanning speed (inset: cross-section of a melt pool in the deep welding regime, scale bar = 200 µm) and b) radiant exposure for 50 to 200 W deposition.

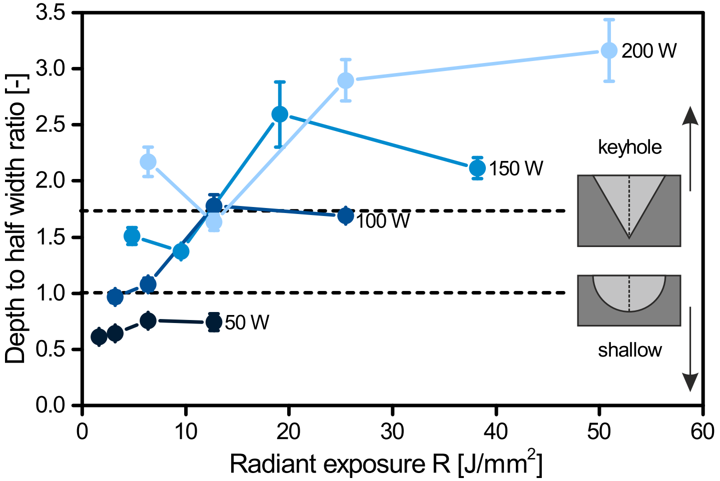

(a)

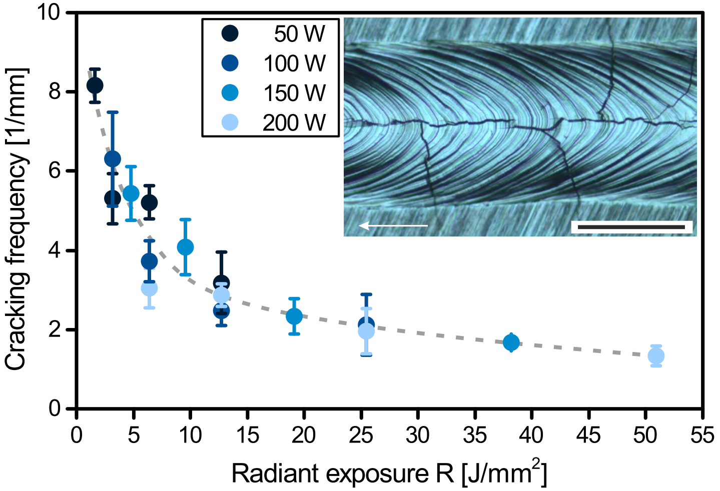

(b)

Figure 7.6: a) the melt pool depth-to-half-width ratio and b) the cracking frequency perpendicular to the scanning direction as a function of the radiant exposure for SLM re-melted ODS TiAl (inset: top-view micrograph showing the crack pattern, scale bar = 200 µm). The ideal melt pool shapes for $r = 1$ and $r = 1.73$ are shown in a).

at 200 W. The observed cracking pattern of the melt lines shows typically a central crack parallel to the scanning direction as well as multiple cracks propagating perpendicular through the melt pool into the surrounding material. The latter are used to study the influence of the radiant exposure on cracking frequency (Figure 7.6b). A common behavior is observed showing reduced cracking frequencies with increased energy input. Such behavior has also been reported by Liu and DuPont on DMD Ti-48Al-2Cr-2Nb [125]. With an increasing energy input and melt pool size the cooling rate is reduced and consequently the temperature remains for a longer period of time above the ductile-to-brittle transition of TiAl alloys. The plastic deformation leads then to stress relief during processing.

7.2.3 Influence of re-scanning and its orientation

The clear effect of the energy input onto cracking frequencies can only be exploited in a narrow parameter range. Excessively high laser powers and low scanning speeds reduce cracking frequency but at the same time are clearly in the regime of deep welding, leading to additional porosity (see Fig. 7.4). Instead of depositing the entire energy in one scan, re-scanning allows to deposit high total radiant exposures using processing parameters in the

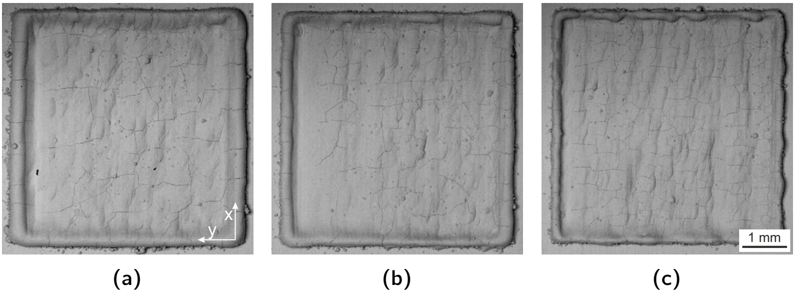

Figure 7.7: Low resolution BSE SEM micrographs of 7 layer structures deposited with 100 W and a) 100 mm·s^{-1}, b) 200 mm·s^{-1} and c) 400 mm·s^{-1}. The scale bar is valid for a-c). The scan direction (x) and the beam translation (y) are indicated.

parameter window determined earlier. Figure 7.7 shows top-view micrographs of 7 layer deposits processed with increasing scanning speed from 100 over 200 to 400 mm·s^{-1}. The observed crack length per unit area is 2.38±0.18, 2.76±0.20 and 4.51±0.25 mm·mm^{-2}, respectively. The behavior observed on single re-molten lines is directly reproduced in SLM deposited material. Comparing the radiant exposure of single scanned (scan speed=v) to re-scanned layers with the same deposition conditions and one re-scan using the same parameters ($v_{\text{rescan}} = v$) and such with doubled scanning speed ($v_{\text{rescan}} = 2 \cdot v$), the common behavior of reduced cracking frequency with increased energy input is reproduced (Figure 7.8).

Upon close examination of the data, two areas are distinguished. Starting from a highly cracked single scanned layer, also the re-scanned layers show large crack lengths. If the initial deposition step provides sufficiently low cracking, re-scanning increases the integrity of the layers. This clearly shows the possibility to increase part integrity by repeated scanning parallel to the deposition direction. The observed crack pattern is related to the scan direction and is predominantly oriented perpendicular to it with connecting

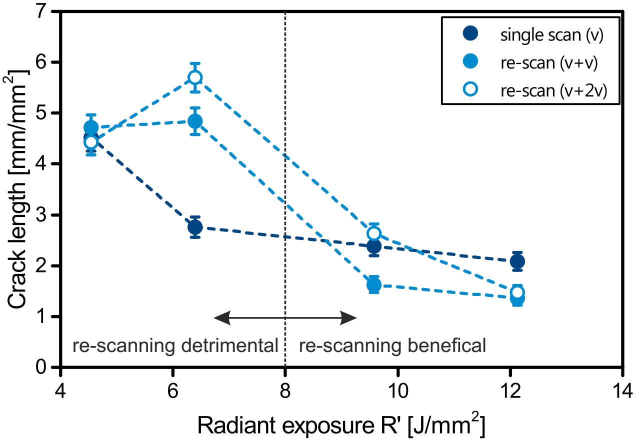

Figure 7.8: The crack length per unit area as a function of radiant exposure of 7 layer SLM deposits.

cracks in between. Re-scans parallel to the initial deposition scan can thus cross many cracks per scan line. Figure 7.9 shows 7 layer deposits produced with the same laser parameters, but with different re-scan orientations. For the parallel or 0° re-scans, the cracking pattern is oriented perpendicular to the scan tracks (Fig. 7.9a). Using a cross-hatch re-scan strategy with 90° rotation between deposition and every rescan, the cracks are predominantly formed vertically on Figure 7.9b. A rotation of 45° produces a diagonal crack pattern (Fig. 7.9c). The obtained data clearly shows the relation between scanning and crack orientation. The obtained crack lengths per unit area are 1.84±0.16, 1.67±0.15 and 1.97±0.16 mm·mm^{-2} for 0°, 90° and 45° re-scans, respectively. The lowest crack length is observed with a 90° rotation re-scan strategy. Figure 7.10 shows the cross-sections of 7 layer deposits. Single scan deposited material shows cracks propagating from the interface towards the substrate completely through the material to the top surface (Fig. 7.10a). The large crack width illustrates the high strain imposed on the material finally leading to fracture. Re-scanning with the same parameter as well as with reduced radiant exposure at doubled scan speed for deposition in every layer also leads to continuous cracks (Fig. 7.10b and 7.10c). Upon re-scanning

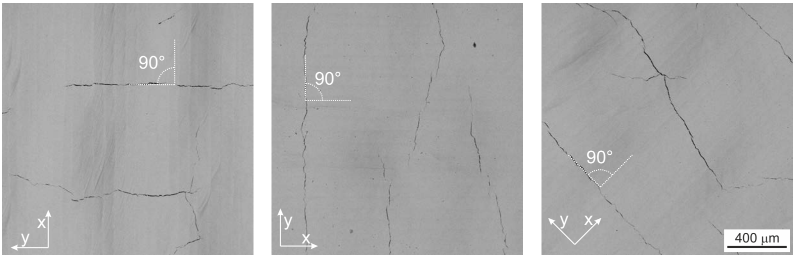

(a) **(b)** **(c)**

Figure 7.9: BSE SEM micrographs of 7 layer structures deposited with 100 W and 100 mm·s^{-1}, re-scanned with 200 mm·s^{-1}, 400 mm·s^{-1} and 400 mm·s^{-1} with a) 0°, b) 90° and c) 45° rotation in between every scan. The scanning direction (x) and the beam translation (y) of the last scan are indicated. The build direction is out-of-plane. The scale bar is valid for a-c).

with 200 W and 800 mm·s^{-1} arrested cracks are observed below the surface leading to a low cracking frequency of the surface (Fig. 7.10d). Multiple

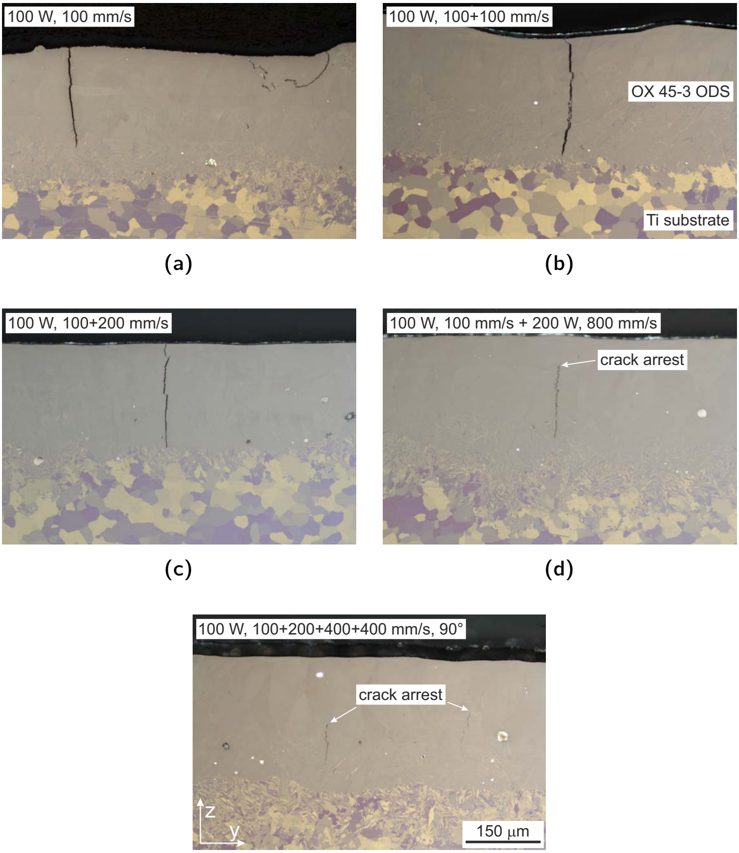
100 W, 100 mm/s
100 W, 100+100 mm/s
OX 45-3 ODS
Ti substrate
100 W, 100+200 mm/s
100 W, 100 mm/s + 200 W, 800 mm/s
crack arrest
100 W, 100+200+400+400 mm/s, 90°
crack arrest
z
y
150 μm

(a) (b) (c) (d) (e)

Figure 7.10: Polarized light optical micrographs of cross-sectioned 7 layer SLM deposits produced with a laser power of 100 W and a) 100 mm·s^{-1}, b) 100+100 mm·s^{-1}, c) 100+200 mm·s^{-1}, d) 100 mm·s^{-1} + 200 W, 800 mm·s^{-1} and e) 100+200+400+400 mm·s^{-1}, rotated by 90° in every layer. The scale bar in e) applies for all micrographs. The build direction (z) is indicated.

re-scans at reduced exposure with a 90° rotation between every re-scan as well as in consecutive layers lead to a dense top part of the deposit with arrested cracks close to the Ti substrate (Fig. 7.10e). Figure 7.11 shows the observed normalized crack length per unit area for non-rescanned, 0° rescanned and 90° rescanned layers with an initial deposition with 100 W and 100 mm·s^{-1}. The crack length is significantly reduced by 0° re-scanning by 28 to 32 %. The 90° rescan strategy is superior for all cases and reduced crack length by 30 to 47 % compared to the non-rescanned deposit. Although the effectiveness of the re-scan strategy is depending on the chosen parameters, re-scanning along the formed cracks seems to be beneficial compared to a strategy where the cracks are crossed. It is hypothesized that stress concentration is severe on a freshly solidified melt pool bridging the underlying crack and will again lead to local fracture. This is illustrated by the continuous cracks through the complete deposit in Figures 7.10b and 7.10c. However, the results clearly show reduced cracking frequencies upon re-scanning. This indicates that the amount of cracks is reduced by closing part of the cracks, while others are still able to propagate to the surface. Based on the promising results, re-scanning is an option to be considered for processing of TiAl alloys in addition to external pre-heating to reduce the cracking of consolidated material.

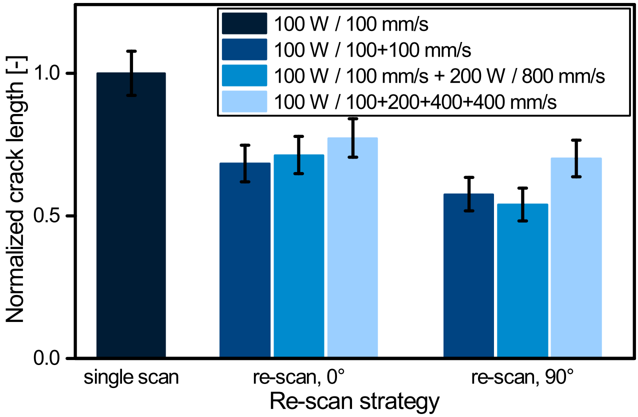

Figure 7.11: Effect of the re-scanning strategy and its direction on normalized crack length in 7 layer SLM deposits of ODS TiAl.

7.2.4 Bulk and lattice deposition

Based on the performed experiments on single line deposition, laser remelting and re-scanning, a suitable process window is identified at radiant exposures of less than 20 J·mm^{-2}. The laser power needs to be kept below 200 W due to formation of very deep melt pools and porosity. Taking into account the powder layer thickness of 50 µm, the re-melting depth does not need to exceed 250 µm or 4 solid layers. Consequently, the line width is also ideally kept below 300 µm based in the depth to half-width ratio. In order to reduce the cracking of deposited material, re-scanning should be applied with a 90° rotation. Figure 7.12 shows the observed crack length on 5x5x5 mm blocks depending on radiant exposure for single scanned and re-scanned blocks. Re-scans are performed with multiples of the deposition scan speed *v*. In the single scanned case, the lowest crack lengths are observed for intermediate radiant exposures between 8 and 10 J·mm^{-2}. The lowest crack lengths are obtained for re-scanned blocks with multiple re-scanning being superior to single time re-

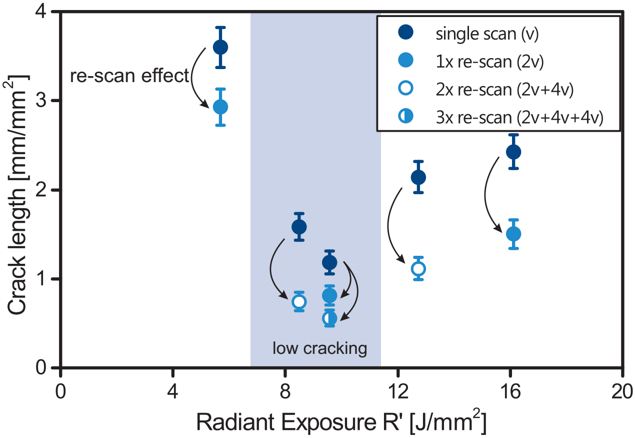

Figure 7.12: The observed crack length as a function of radiant exposure for single scanned and re-scanned massive blocks. The radiant exposure of the first scan is used for plotting. One to three re-scans are performed with multiples of the scan speed *v* used for deposition and with 90° rotation. The parameter window of lowest cracking is shown shaded.

scanned blocks. Re-scanning is also effective at radiant exposures smaller than 8 or larger than 10 J·mm^{-2} reducing the crack length significantly. However, the achieved crack length remains larger than for intermediate exposures. The beneficial effect of re-scanning for small radiant exposures is in contrast to the tests on 7 layer deposits, where re-scans at low radiant exposure are not effective. Based on the beneficial effect observed by a 90° rotation in the 7 layer deposits, all re-scans for the blocks are performed in the rotated fashion. It is believed that this explains the efficiency at low radiant exposures. Figure 7.13 shows the observed cracking frequencies measured along the trusses of 3D lattice structures. No clear dependency on the energy input is observed. Cracking frequencies below 0.5 mm^{-1} are observed for single-scanned as well as re-scanned lattices at low and high radiant exposure. The lowest cracking frequencies are observed for single-scanned lattices with radiant exposures from 6 to 10 J·mm^{-2}. Generally, cracking frequencies are substantially lower than in massive blocks. This can be understood based on the thermal history and geometry of the 3D lattice structures. Their open, powder-filled structure is thermally better isolated than fully consolidated bulk blocks. Consequently, the lattice structure experiences a lower cooling rate and thus less cracking.

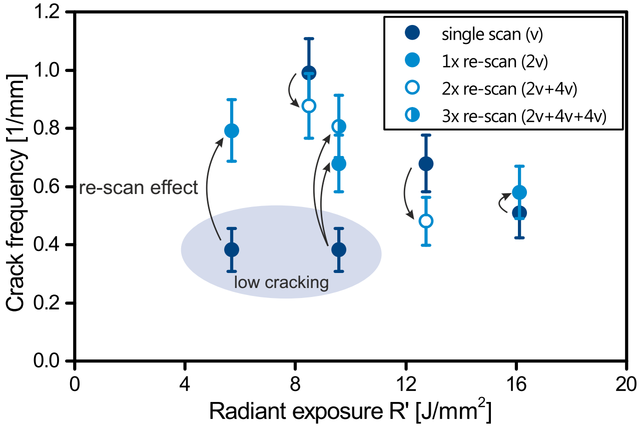

Figure 7.13: Cracking frequencies of 3D lattice structures produced with single scanned and re-scanned deposition strategies.

The body-centered cubic unit cell consists entirely of overhanging trusses that have reduced heat transport towards the base plate. A second effect is the reduced stress in a compliant structure. While massive blocks are stiff, a 3D lattice has higher compliance depending on its structure. The chosen structure provides no solid elements parallel to the build plane and has thus reduced stiffness in the x-y direction. Consequently, global stresses over the complete part are expected to be reduced leading to less cracking. Figure 7.14 shows two lattices produced from the very same source file with 150 W having cracking frequencies of 0.99 ± 0.11 mm^{-1} and 0.38 ± 0.07 mm^{-1} for 150 mm·s^{-1} and 300 mm·s^{-1}. The retention of the fine lattice structures is improved for lower energy input while the truss diameter is increased for higher energy input in accordance with a larger melt pool size. Figure 7.15 shows detailed views of the lattice produced with 150 W and 150 mm·s^{-1}. A side view shows the exposed nodes and the bcc lattice geometry (Fig. 7.15a). Numerous cracks along the build direction are visible. Opened cracks show preferential cracking close to the nodes where the individual trusses intersect (Fig. 7.15b). At this location local stress concentration is severe due to the sharp contact line between trusses in the bcc structure. The crack propagates through both trusses until reaching the top surface of the part

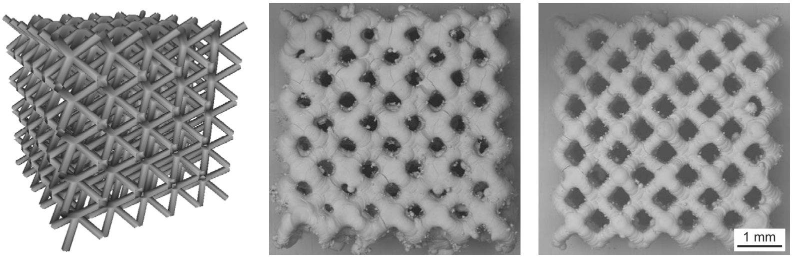

(a) **(b)** **(c)**

Figure 7.14: The source stl file of the 5x5x5 body-centered cubic lattice structure (a) and BSE SEM micrographs of the produced lattices with a laser power of 150 W and a scanning speed of b) 150 mm·s^{-1} and c) 300 mm·s^{-1}. The build direction is out-of-plane. The scale bar is valid for b-c).

(Fig. 7.15c). Detailed analysis of the fracture surface shows trans-granular failure indicating fracture at low temperatures in the intermetallic state of the alloy. Based on phase diagram information, α_2 with low ductility is only present at temperatures below the eutectoid reaction at 1373 K for the binary Ti-Al system. It is thus concluded that cracking occurs in the fully solid and intermetallic state and is caused by residual stresses in the part.

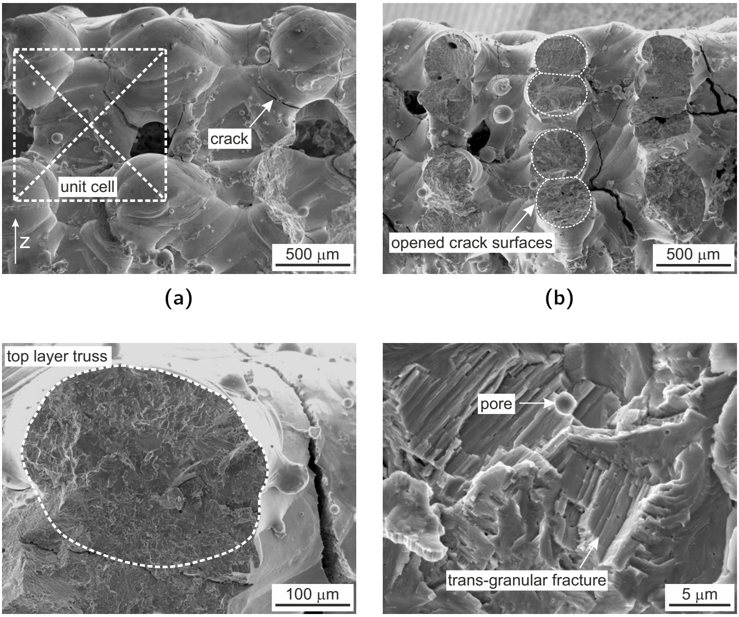
unit cell
crack
z
500 µm
opened crack surfaces
500 µm
top layer truss
100 µm
pore
trans-granular fracture
5 µm

(a) (b)

(c) (d)

Figure 7.15: SEM micrographs of the bcc lattice produced with 150 W and 150 mm·s^{-1}, a) side view showing the bcc unit cell and exposed nodes, b) side view after opening the existing cracks exposing the fracture surfaces, c) detailed view of a top level truss and d) the truss fracture surface. The build direction (z) is indicated.

7.3 Summary and conclusion

To summarize this Chapter, it is shown that

- formation of smooth melt pools is observed in single line deposition for laser powers of 100 to 200 W at low scanning speeds. Processing energies exceeding 150 W lead to deep weld pools and increased porosity.
- cracking frequency is directly related to the radiant exposure upon laser melting of massive parts. Re-scanning with a rotation of 90° is superior to parallel re-scanning and reduces cracking by up to a factor of ~2.
- complex 3D lattice structures can be produced from an ODS TiAl alloy by SLM. Their cracking frequency is independent of radiant exposure which is explained by their compliant structure and reduced cooling rate due to overhanging features.

It can be concluded that the studied OX 45-3 ODS alloy can be consolidated into complex shapes by SLM. The resulting cracking frequency can be greatly affected by adapted parameters and re-scanning strategies, which shows the potential of this approach. Despite the achieved improvement, it was not possible to produce crack-free specimens on the commercial machine used for this study. The studied alloy is thus not suitable for SLM processing without any pre-heating. Alloy adaptions towards higher ductility or extensive preheating and consequently stress-relief at high temperature during processing are possible solutions to be exploited in the future. This work is a contribution towards combining the beneficial material properties of advanced TiAl alloys with the geometrical complexity and freedom of AM to produce light-weight high-temperature resistant structures for demanding applications.

8 Summary and Outlook

In the frame of this thesis the complete alloy development sequence has been performed, starting from basic studies and computational alloy design, continued with processing trials and a characterization of the obtained properties. Finally the AM of complex structures of the novel class of ODS TiAl alloys has been demonstrated. Additionally, novel experimental methods have been developed, specifically designed to study alloy behavior under non-equilibrium conditions as observed in beam-based AM. These methods are universally applicable to any material and provide a great base for further studies.

The summarized results of this work are:

- **The rapid solidification behavior of Ti-Al between 10^2 and 10^4 K·s^{-1}** To study the alloy behavior in the relevant range of cooling rates *ex* and *in situ* methods have been successfully developed. A combination of arc melting of small specimens producing spherical specimens with finite element modeling and high-speed imaging allows to study the influence of cooling rate and composition on microstructure formation. Extending this approach to a setup combining laser melting and quenching on Cu of similar specimens at a synchrotron beamline allows the real-time *in situ* study of the solidification and phase transformation sequence. Both methodologies have been applied to binary Ti-(44-48)Al. In the *ex situ* experiments three different microstructural types have been observed: the coarse-grained α/α_2 in Ti$\leq$46Al, the mixed α/α_2 + γ_{seg} + γ_m + L(α_2 + γ) in Ti-(46-47)Al and the dendritic L(α_2 + γ) + γ_{seg} + γ_m in Ti-48Al. The microstructural type is depending on the alloy composition and the solidification sequence. However, the observed behavior deviates from the expected alloy behavior under near-equilibrium conditions. The deviations are explained by a computational framework based on the CALPHAD approach taking into account the non-equilibrium conditions of rapid solidification. The developed approach relies on the composition dependence of the relevant T_0 temperatures. Finally, phase selection hierarchy maps were calculated accurately predicting the observed alloy behavior. The predicted change in primary phase formation in Al-rich Ti-48Al was confirmed by combined *in situ* microXRD and high-speed imaging, validating the novel approach. Based on the T_0-approach novel alloys can be designed for AM taking into account the processing characteristics involving high cooling rates.

- **The influence of alloying elements on rapid solidification behavior** The influence of the important alloying elements Nb and Mo has been studied applying the previously developed *ex situ* methodology combined with calculated phase selection hierarchy maps. Experimental microstructure-composition maps at $4.5(\pm 0.2)\cdot 10^3$ $K\cdot s^{-1}$ show the increased occurrence of the coarse-grained α/α_2 type in the range of Ti-(45-47)Al-(0-7)Nb and Ti-(45-47)Al-(0-2)Mo due to a stabilization of the β-phase by Nb and Mo. It was shown that both elements have strong effects on the T_0 temperatures of the relevant phase transformations and solidification. Additionally, a sub-type of the coarse-grained α/α_2 microstructural type has been observed for intermediate Al and high Nb or Mo levels. This sub-type was found to be stabilized by the combination of β-solidification without significant Al-segregation and of a high driving force to massively transform the parent α-phase into γ_m. The driving force was estimated based on the T_0 approach. This demonstrates the versatility of this approach that can be applied not only for non-equilibrium solidification but also for composition-invariant solid state phase transformations.

- **Alloy selection for additive manufacturing** The results of the fundamental study on the microstructure formation in binary Ti-Al and ternary Ti-Al-Nb and Ti-Al-Mo have been used to compile a general picture of the influence of composition on alloy behavior. The influence of Nb and Mo has been combined in the spirit of a Schaeffler-like diagram using the equivalent Nb content Nb_{eq}. Based on this information three general classes of TiAl alloys are defined: The Al-lean, β-solidifying Ti-(43-45)Al-(0-8)Nb_{eq} alloys, the Al-rich, quasi-peritectic Ti-(47-48)Al-(1-8)Nb_{eq} alloys and the Ti-(45.5-46.5)Al-(3-8)Nb_{eq} alloys combining enhanced Al-content and Nb_{eq}-alloying levels for good oxidation resistance and strength. The expected behavior of the individual classes and the individual advantages and disadvantages for AM processing have been discussed. This provides a guideline to alloy selection and development specifically for AM.

- **ODS titanium aluminides produced using powder-based processing** The developed ODS TiAl alloy has been successfully produced by mechanical alloying and been consolidated using SPS. The addition of dispersoids in SPS material leads to superior microstructural stability at temperatures as high as 1673 K. While the fraction of lamellar colonies is increasing with increasing temperature, their size does not change substantially. This allows to retain fine grained material after high temperature heat treatments or during service at elevated temperatures. Additionally, the microstructure is refined in the SPS process upon dispersoid addition. The ODS-free variant was found to form a considerable coarser microstructure involving porosity. In the ODS-variant TEM analysis shows the presence of dispersoids at grain boundaries leading to a pinning effect. It was also observed that the particles interact with the dislocations in the material. Hardness measurements show superior properties of the ODS-variant. After the post-SPS stabilization 441±29 HV and 477±16 HV were measured for the ODS-free and ODS variant, respectively. After high temperature annealing at 1673 K for 15 min the ODS-free variant shows a loss in strength with 409±26 HV while the ODS variant shows a slight hardness increase to 485±15 HV. This demonstrates the potential application of ODS TiAl alloys for high temperature service providing good mechanical performance and microstructural stability.

- **Microstructure and texture of laser-processed titanium aluminides** In agreement with the previous results of this work, the α/α_2 microstructural type was observed in the β-solidifying OX 45-3 ODS after SLM and LMD. After both processes are columnar structure of α/α_2 is observed with a multitude of dispersed particles. No segregation of Al was observed, validating the chosen alloy design strategy to avoid an inhomogeneous particle distribution. The non-equilibrium α/α_2 microstructure was successfully transformed to conventional near-lamellar microstructures by adapted heat treatments. The texture of the deposited material was analyzed for LMD deposited material comparing OX 45-3 ODS to the commercial GE 48-2-2 alloy. A significantly reduced texture was observed for the developed ODS alloy in terms of maximum m.r.d. as well as in the spatial orientation of the phases. The GE 48-2-2 alloy formed a distinct fiber texture with a strong out-of-plane component while the OX 45-3 ODS provides a speckled but more evenly distributed texture. This can be attributed to the different solidification paths of the two alloys. The reduced texture of OX 45-3 ODS renders the alloy less susceptible for changed building directions and local heat flow direction in a part. Consequently, reduced anisotropy can be achieved after processing. It was observed, that the achieved size distribution of dispersoids depends on the processing energies. In solid state SPS the smallest particle distribution is achieved. After SLM and LMD particle coarsening is observed. The differences are explained based on the processing energies and consequently the lifetime of the melt pool.

- **Performance of ODS titanium aluminides at elevated temperature** The performance of SPS OX 45-3 ODS and the ODS-free OX 45-3 has been analyzed in terms of the oxidation resistance and the mechanical properties. The addition of Y-based dispersoids reduces the parabolic growth rate by a factor 2 upon oxidation in air at 1073 K. The ODS-variant achieves a similarly low growth rate as the commercial TNB-V5 alloy, despite the lower alloying levels in OX 45-3 ODS. In both alloys the sub-surface barrier layer consisting of Al_2O_3 is stabilized based on XRD measurements. Consequently, a similar scale morphology is observed for OX 45-3 ODS and TNB-V5 while the ODS-free variant shows a significantly coarser scale. Upon exposure to air at 1073 K for 924 h as well as 923 K for 987 h the dispersoids in the material remain stable. For the ODS-variant superior yield stress and ultimate tensile strength was observed compared to the non-ODS counterpart in the range of 293 K to 1073 K. At room temperature an R_m and $Rp_{0.1}$ of 856±0.1 MPa and 794±12 MPa and 751±8 MPa and 593±10 MPa are achieved for the ODS and ODS-free variant, respectively. At elevated temperature OX 45-3 ODS shows a stable $Rp_{0.1}$ while the ODS-free variant softens at 973 K before recovering at 1073 K. The fracture surfaces at different temperature also shows very similar behavior of OX 45-3 ODS at all tested temperatures while a change in fracture mode is observed in the ODS-free variant at the softening temperature of 973 K. The low sensitivity of the mechanical properties depending on temperature combined with superior yield and ultimate strength are a clear advantage for the ODS TiAl alloy. Superior oxidation resistance can be combined with high strength in low alloyed TiAl alloys by Y_2O_3 addition.

- **Complex structures from ODS TiAl by selective laser melting** Finally, the processing of complex 3D geometries from ODS TiAl by SLM was demonstrated. Stable melt pool formation was observed in single line deposition at laser powers of 100 to 150 W at low scanning speeds. The observed cracking frequency of processed blocks and lattices was correlated with the processing parameters and the resulting cumulative radiant exposure. Higher energy input leads to reduced cracking in solid blocks. Additionally, re-scanning was studied to increase the cumulative radiant exposure while keeping or decreasing the energy input of the individual scans. Re-scanning in an orientation of 90° to the deposition scan was found to be superior to 0° or 45° re-scanning and could decrease the cracking frequency by up to a factor of 2. In lattice structures the compliance and the intrinsically lower cooling rates attenuate the cracking problem. Additionally, no clear influence of energy input on cracking frequency was observed, allowing to select processing parameters for optimal feature retention. This study provides a first insight into the influence of part design and processing strategy on integrity of ODS TiAl alloys.

In the future, TiAl alloys will be increasingly applied in weight-critical applications as aerospace industry. With the great success of the introduction of GE48-2-2 as cast blades in the GEnx engine, TiAl alloys will be already state-of-the-art materials for the next turbine engine generation currently being developed by Snecma, GE, MTU, Pratt & Whitney and Rolls Royce. With this in mind, AM of these materials is increasingly studied for production but also repair. This thesis provides the methodology to examine the influence of the alloy composition on its behavior under the non-equilibrium processing conditions. The important alloying systems Ti-Al-Nb and Ti-Al-Mo being the parent ternaries of most TiAl alloys considered for or in operation have been studied providing guidance for alloy selection and design. In order to achieve the best combination of properties, state-of-the-art TiAl alloys contain typically more than four elements including additions of B and C for precipitation hardening. The promising ODS approach can be extended to such complex alloys to ideally further increase the specific strength of TiAl material rendering it even more competitive to Ni-base alloys. Such alloys can be studied, developed and tested using the methods provided in this thesis.

TiAl alloys are processed using very high preheating temperatures to avoid cracking. Such approaches need specific equipment and in many cases will probably not evolve beyond the proof of concept in the lab. This explains the success of EBM for TiAl due to the inherent preheating capability of the method and the low material contamination in vacuum processing. Laser-based AM methods however operate typically in a shielding gas atmosphere and usually rely on either inductive or resistive heating, if present at all. At high temperatures the confinement of the hot shielding gas and contamination of the build material become increasingly problematic. Consequently, any reduction in the necessary preheating temperature to achieve high integrity

TiAl parts, such as re-scanning or alloy composition, favors the laser-based methods. This work provides the base for process and alloy development towards optimized materials for AM. In the future this approach can be extended to more complex alloy systems, with or without ODS addition, to achieve higher high-temperature ductility and lower stresses by stabilization of additional or modified phases. The application of such novel alloys for AM requires complete certification involving high temperature degradation in various atmospheres, static mechanical properties in the relevant temperature range, fatigue testing to establish the Wöhler curves at various loading conditions, creep and relaxation testing, and the influence of potential anisotropy as well as different heat treatment states.

Beyond the development of TiAl alloys, the novel experimental and computational approaches can be applied to other important alloy systems. For example the behavior of γ'-hardening Ni-base super alloys is a matter of great problems for AM as the precipitation upon solidification and during the intrinsic heat treatment affects the processability. Additionally, this class of alloys has been optimized for different processing routes in the past by alloying to form highly complex multi-component systems. The understanding of the non-equilibrium behavior of these alloys is crucial for future alloy development and successful AM.

Bibliography

[1] A. Jones, Historical Perspective - ODS Alloy Development, 2010.

[2] P. Bartolotta, J. Barret, T. Kelly, R. Smashey, The use of cast Ti-48Al-2Cr-Nb in jet engines, JOM 49 (1997) 48–76.

[3] M. A. E. GmbH, Titanium aluminide - MTU Aero Engines develops new turbine blade material, 2015.

[4] R. Gerling, A. Bartels, H. Clemens, H. Kestler, F.-P. Schimansky, Structural characterization and tensile properties of a high niobium containing gamma TiAl sheet obtained by powder metallurgical processing, Interm 12 (2004) 275–280.

[5] R. Gerling, F. Schimansky, A. Stark, A. Bartels, H. Kestler, L. Cha, C. Scheu, H. Clemens, Microstructure and mechanical properties of Ti-45Al-5Nb+(0–0.5C) sheets, Intermetallics 16 (2008) 689–697.

[6] H. Clemens, W. Wallgram, S. Kremmer, V. Güther, A. Otto, A. Bartels, Design of novel β-solidifying TiAl alloys with adjustable β/B2-phase fraction and excellent hot-workability, Advanced Engineering Materials 10 (2008) 707–713.

[7] H. Clemens, H. Chladil, W. Wallgram, G. Zickler, R. Gerling, K.-D. Liss, S. Kremmer, V. Güther, W. Smarsly, In and ex situ investigations of the β-phase in a Nb and Mo containing γ-TiAl based alloy, Intermetallics 16 (2008) 827–833.

[8] M. Weimer, T. Kelly, Gamma TiAl Applications at GE Aviation, in: Structural Aluminides for Elevated Temperatures, 2008.

[9] A. Spierings, C. Leinenbach, C. Kenel, C. Wegener, Processing of metal-diamond-composites using selective laser melting, Rapid Prototyping Journal 21 (2015) 130–136.

[10] T. Boegelein, S. N. Dryepondt, A. Pandey, K. Dawson, G. J. Tatlock, Mechanical response and deformation mechanisms of ferritic oxide dispersion strengthened steel structures produced by selective laser melting, Acta Materialia 87 (2015) 201–215.

[11] V. T. Witusiewicz, A. A. Bondar, U. Hecht, S. Rex, T. Y. Velikanova, The Al-B-Nb-Ti system III. Thermodynamic re-evaluation of the constituent binary system Al-Ti, Journal of Alloys and Compounds 465 (2008) 64–77.

[12] L. Kaufman, H. Nesor, Coupled phase diagrams and thermochemical data for transition metal binary systems — V, Calphad 2 (1978) 325–348.

[13] J. L. Murray, Calculation of the titanium-aluminum phase diagram, Metallurgical Transactions A 19 (1988) 243–247.

[14] C. McCullough, J. Valencia, C. Levi, R. Mehrabian, Phase equilibria and solidification in Ti-Al alloys, Acta Metallurgica 37 (1989) 1321–1336.

[15] U. R. Kattner, J.-C. Lin, Y. A. Chang, Thermodynamic assessment and calculation of the Ti-Al system, Metallurgical Transactions 23A (1992) 2081–2090.

[16] U. R. Kattner, W. J. Boettinger, Thermodynamic calculation of the ternary Ti-Al-Nb system, Materials Science & Engineering: A 152 (1992) 9–17.

[17] N. Saunders, in: I. Ansara (Ed.), COST 507, thermochemical database for light elements., European Comission, 1994.

[18] I. Ohnuma, Y. Fujita, H. Mitsui, K. Ishikawa, R. Kainuma, K. Ishida, Phase equlibria in the Ti-Al binary system, Acta Materialia 48 (2000) 3113–3123.

[19] J. Braun, M. Ellner, X-ray high-temperature in situ investigation of the aluminide $TiAl_2$ ($HfGa_2$ type), Journal of Alloys and Compounds 309 (2000) 118–122.

[20] J. Braun, M. Ellner, Phase equilibria investigations on the aluminum-rich part of the binary system Ti-Al, Metallurgical and Materials Transactions A 32 (2001) 1037–1047.

[21] R. Kainuma, Y. Fujita, H. Mitsui, I. Ohnuma, K. Ishida, Phase equilibria among α (hcp), β (bcc) and γ (L10) phases in Ti-Al base ternary alloys, Intermet 8 (2000) 855–867.

[22] J. C. Schuster, M. Palm, Reassessment of the binary Aluminum-Titanium phase diagram, Journal of Phase Equilibria and Diffusion 27 (2006) 255–277.

[23] V. T. Witusiewicz, A. A. Bondar, U. Hecht, T. Y. Velikanova, The Al-B-Nb-Ti system IV. Experimental study and thermodynamic re-evaluation of the binary Al-Nb and ternary Al-Nb-Ti systems, Journal of Alloys and Compounds 472 (2009) 133–161.

[24] V. T. Witusiewicz, A. A. Bondar, U. Hecht, V. M. Voblikov, O. S. Fomichov, V. M. Petyukh, S. Rex, Experimental study and thermodynamic modelling of the ternary Al–Ta–Ti system, Intermetallics 19 (2011) 234–259.

[25] O. Shuleshova, D. Holland-Moritz, A. Voss, W. Löser, In situ observations of solidification in Ti–Al–Ta alloys by synchrotron radiation, Intermetallics 19 (2011) 688–692.

[26] V. T. Witusiewicz, A. A. Bondar, U. Hecht, T. Y. Velikanova, Thermodynamic re-modelling of the ternary Al–Cr–Ti system with refined Al–Cr description, Journal of Alloys and Compounds 644 (2015) 939–958.

[27] B. Lindahl, M. Selleby, [P24] A thermodynamic assessment of the Al-Ti-V system, Calphad 51 (2015) 379–380.

[28] Y.-W. Kim, Ordered intermetallic alloys, Part III: Gamma titanium aluminides, JOM 46 (1994) 30–39.

[29] S. Naka, Advanced titanium-based alloys, Solid State & Materials Science 1 (1996) 333–339.

[30] F. Froes, C. Suryanarayana, D. Eliezer, Review Synthesis, properties and applications of titanium aluminides, Journal of Materials Science 27 (1992) 5113–5140.

[31] F. Appel, J. D. H. Paul, M. Oehring (Eds.), Gamma Titanium Aluminide Alloys, Wiley-VCH, 2011.

[32] M. J. Blackburn, Some aspects of phase transfromations in titanium alloys, in: R. I. J. E. Promisel (Ed.), The Science, Technology and Application of Titanium, Pergamon, 1970, pp. 633–643.

[33] M. DeGraef, N. Biery, L. Rishel, T. M. Pollock, A. Cramb, On the relation between cooling rate and solidification microstructure in as-cast titanium aluminides, Gamma titanium aluminides (1999) 247–254.

[34] C. Leyens, M. Peters (Eds.), Titanium and Titanium Alloys, Wiley-VCH, 2003.

[35] H. Clemens, S. Mayer, Design, Processing, Microstructure, Properties, and Applications of Advanced Intermetallic TiAl Alloys, Advanced Engineering Materials 15 (2013) 191–215.

[36] K. Kothari, R. Radhakrishnan, N. M. Wereley, Advances in gamma titanium aluminides and their manufacturing techniques, Progress in Aerospace Sciences 55 (2012) 1–16.

[37] A. I. Taub, R. L. Fleischer, Intermetallic compounds for high-temperature structural use, Science (New York, N.Y.) 243 (1989) 616–621.

[38] R. V. Mises, Mechanik der plastischen Formänderung von Kristallen, ZAMM - Journal of Applied Mathematics and Mechanics / Zeitschrift für Angewandte Mathematik und Mechanik 8 (1928) 161–185.

[39] D. Shechtman, M. J. Blackburn, H. A. Lipsitt, The plastic deformation of TiAl, Metallurgical Transactions 5 (1974) 1373–1381.

[40] F. Appel, R. Wagner, Microstructure and deformation of two-phase γ-titanium aluminides, Materials Science and Engineering 22 (1998) 187–268.

[41] J. B. Singh, G. Molénat, M. Sundararaman, S. Banerjee, G. Saada, P. Veyssière, A. Couret, The activation and the spreading of deformation in a fully lamellar Ti–47 at.% Al–1 at.% Cr–0.2 at.% Si Alloy, Philosophical Magazine 86 (2006) 2429–2450.

[42] A. Godfrey, D. Hu, M. H. Loretto, The role of the $\alpha 2$ phase in the transmission of slip in lamellar TiAl-based alloys, Philosophical Magazine A 77 (1998) 287–297.

[43] W. Seiler, G. Hoël, M. Thomas, V. Ji, XRD stress analysis in a –TiAl based intermetallic multicrystal, Materials Science Forum 490-491 (2005) 684–689.

[44] Y.-W. Kim, D. M. Dimiduk, Progress in the understanding of gamma titanium aluminides, JOM 43 (1991) 40–47.

[45] R. Gerling, H. Clemens, F. P. Schimansky, Powder Metallurgical Processing of Intermetallic Gamma Titanium Alumindes, Advanced Engineering Materials 6 (2004) 23–38.

[46] S. Djanarthany, J.-C. Viala, J. Bouix, An overview of monolithic titanium aluminides based on Ti_3Al and TiAl, Materials Chemistry and Physics 72 (2001) 301–319.

[47] E. O. Hall, The Deformation and Ageing of Mild Steel: III Discussion of Results, Proceedings of the Physical Society. Section B 64 (1951) 747.

[48] D. M. Dimiduk, P. M. Hazzledine, T. A. Parthasarathy, M. G. Mendiratta, S. Seshagiri, The role of grain size and selected microstructural parameters in strengthening fully lamellar TiAl alloys, Metallurgical and Materials Transactions A 29 (1998) 37–47.

[49] H. Clemens, H. Kestler, Processing and applications of intermetallic γ-TiAl-based alloys, Advanced Engineering Materials 2 (2000) 551–570.

[50] J. W. Fergus, Review of the effect of alloy composition on the growth rates of scales formed during oxidation of gamma titanium aluminide alloys, Materials Science and Engineering: A 338 (2002) 108–125.

[51] D. W. McKee, S. C. Huang, The oxidation behaviour of gamma-titanium alumindes alloys under thermal cycling conditions, Corrosion Science 33 (1992) 1899–1914.

[52] V. A. C. Haanappel, J. D. Sunderkötter, M. F. Stroosnijder, The isothermal and cyclic high temperature oxidation behaviour of Ti-48Al-2Mn-2Nb compared with Ti-48Al-2Cr-2Nb and Ti-48Al-2Cr, Intermetallics 7 (1999) 529–541.

[53] V. A. C. Haanappel, H. Clemens, M. F. Stroosnijder, The high temperature oxidation behaviour of high and low alloyed TiAl-based intermetallics, Intermetallics 10 (2002) 293–305.

[54] Z. G. Jiang, B. Chen, K. Liu, Y. Y. Li, Effects of boron on phase transformation of high Nb containing TiAl-based alloy, Intermetallics 15 (2007) 738–743.

[55] Z. Chen, X. Su, Z. Xiang, Z. Nie, Microstructure and Phase Transformation of a Niobium-rich TiAl-based Alloy Containing Boron and Carbon, J. Mater. Sci. Technol. 28 (2012) 453–460.

[56] R. V. Ramanujan, P. J. Maziasz, C. T. Liu, The thermal stability of the microstructure of γ-based titanium alumindes, Acta materialia 44 (1996) 2611–2642.

[57] D. Zhang, E.Arzt, H. Clemens, Characterization of controlled microstructures in a γ-TiAl(Cr, Mo, Si, B) alloy, Intermetallics 7 (1999) 1081–1087.

[58] T. Voisin, J.-P. Monchoux, L. Durand, N. Karnatak, M. Thomas, A. Couret, An Innovative Way to Produce γ-TiAl Blades: Spark Plasma Sintering, Advanced Engineering Materials 17 (2015) 1408–1413.

[59] J. Aguilar, A. Schievenbusch, O. Kättliz, Investment casting technology for production of TiAl low pressure turbine blades - Process engineering and parameter analysis, Intermetallics 19 (2011) 757–761.

[60] V. Recina, D. Lundström, B. Karlsson, Tensile, Creep, and Low-Cycle Fatigue Behavior of a Cast γ-TiAl-Based Alloy for Gas Turbine Applications, Metallurgical and Materials Transactions A 33 (2002) 2869–2881.

[61] R. Imayev, V. Imayev, M. Oehring, F. Appel, Alloy design concepts for refined gamma titanium aluminide based alloys, Intermetallics 15 (2007) 451–460.

[62] M. Schloffer, F. Iqbal, H. Gabrisch, E. Schwaighofer, F.-P. Schimansky, S. Mayer, A. Stark, T. Lippmann, M. Göken, F. Pyczak, H. Clemens, Microstructure development and hardness of a powder metallurgical multi phase γ-TiAl based alloy, Intermetallics 22 (2012) 231–240.

[63] B. Liu, Y. Liu, C. Qiu, C. Zhou, J. Li, H. Li, Y. He, Design of low-cost titanium aluminide intermetallics, Journal of Alloys and Compounds 640 (2015) 298–304.

[64] A. Szkliniarz, W. Szkliniarz, Microstructure and Properties of a New Generation of TiAl Based Alloys, Solid State Phenomena 229 (2015) 125–130.

[65] M. Kastenhuber, B. Rashkova, H. Clemens, S. Mayer, Enhancement of creep properties and microstructural stability of intermetallic β-solidifying γ-TiAl based alloys, Intermetallics 63 (2015) 19–26.

[66] J. H. Moll, B. J. McTiernan, PM TiAl alloys: the sky's the limit, Metal Powder Report 55 (2000) 18–22.

[67] Z. A. Munir, U. Anselmi-Tamburini, M. Ohyanagi, The effect of electric field and pressure on the synthesis and consolidation of materials: A review of the spark plasma sintering method, Journal of Materials Science 41 (2006) 763–777.

[68] B. Mei, Y. Miyamoto, Preparation of Ti-Al intermetallic compounds by spark plasma sintering, Metallurgical and Materials Transactions A 32 (2001) 843–847.

[69] Y. Y. Chen, H. B. Yu, D. L. Zhang, L. H. Chai, Effect of spark plasma sintering temperature on microstructure and mechanical properties of an ultrafine grained TiAl intermetallic alloy, Materials Science and Engineering: A 525 (2009) 166–173.

[70] S.-L. Xiao, J. Tian, L.-J. Xu, Y.-Y. Chen, H.-B. Yu, J.-C. Han, Microstructures and mechanical properties of TiAl alloy prepared by spark plasma sintering, Transactions of Nonferrous Metals Society of China 19 (2009) 1423–1427.

[71] H. Calderon, V. Garibay-Febles, M. Umemoto, M. Yamaguchi, Mechanical properties of nanocrystalline Ti-Al-X alloys, Materials Science and Engineering A 329-331 (2002) 196–205.

[72] Z. Sun, H. Hashimoto, Fabrication of TiAl alloys by MA-PDS process and the mechanical properties, Intermetallics 11 (2003) 825–834.

[73] Z. M. Sun, Q. Wang, H. Hashimoto, S. Tada, T. Abe, Synthesis and consolidation of TiAl by MA–PDS process from sponge-Ti and chip-Al, Intermetallics 11 (2003) 63–69.

[74] H. Jabbar, J.-P. Monchoux, F. Houdellier, M. Dollé, F.-P. Schimansky, F. Pyczak, M. Thomas, A. Couret, Microstructure and mechanical properties of high niobium containing TiAl alloys elaborated by spark plasma sintering, Intermetallics 18 (2010) 2312–2321.

[75] G. Molénat, M. Thomas, J. Galy, A. Couret, Application of Spark Plasma Sintering to Titanium Aluminide Alloys, Advanced engineering materials 9 (2007) 667–669.

[76] A. Couret, G. Molénat, J. Galy, M. Thomas, Microstructures and mechanical properties of TiAl alloys consolidated by spark plasma sintering, Intermetallics 16 (2008) 1134–1141.

[77] X. Lu, X. B. He, B. Zhang, L. Zhang, X. H. Qu, Z. X. Guo, Microstructure and mechanical properties of a spark plasma sintered Ti-45Al-8.5Nb-0.2W-0.2B-0.1Y alloy, Intermetallics 17 (2009) 840–846.

[78] H. Jabbar, A. Couret, L. Durand, J.-P. Monchoux, Identification of microstructural mechanisms during densification of a TiAl alloy by spark plasma sintering, Journal of Alloys and Compounds 509 (2011) 9826–9835.

[79] J. Perepezko, Nucleation-controlled reactions and metastable structures, Progress in Materials Science 49 (2004) 263–284.

[80] J. Graves, J. Perepezko, C. Ward, F. Froes, Microstructural development in rapidly solidified tial, Scripta Metallurgica 21 (1987) 567–572.

[81] J. Valencia, C. McCullough, C. Levi, R. Mehrabian, Microstructure evolution during conventional and rapid solidification of a Ti-50at%Al alloy, Scripta Metallurgica 21 (1987) 1341–1346.

[82] E. L. Hall, S.-C. Huang, Microstructures of rapidly-solidified binary TiAl alloys, Acta metall. mater. 38 (1990) 539–549.

[83] J. Valencia, C. McCullough, C. Levi, R. Mehrabian, Solidification microstructure of supercooled Ti-Al alloys containing intermetallic phases, Acta Metallurgica 37 (1989) 2517–2530.

[84] C. D. Anderson, W. H. Hofmeister, R. J. Bayuzick, Solidification kinetics and metastable phase formation in binary Ti-Al, Metallurgical Transactions A 23 (1992) 2699–2714.

[85] C. Anderson, W. Hofmeister, R. Bayuzick, Phase Stability in Binary Ti-Al, MRS Proceedings 186 (1990).

[86] H.-W. Wang, D.-D. Zhu, C.-M. Zou, Z.-J. Wei, Microstructure and nanohardness of Ti-48%Al alloy prepared by rapid solidification under different cooling rates, Transactions of Nonferrous Metals Society of China 21 (2011) s328–s332.

[87] Y. Liu, F. Lan, G. Yang, Y. Zhou, Microstructural evolution of rapidly solidified Ti–Al peritectic alloy, Journal of Crystal Growth 271 (2004) 313–318.

[88] Y. Liu, Y. Han, G. Yang, Y. Zhou, Primary cellular/dendritic spacing selection in rapidly solidified peritectic alloy, Materials Letters 59 (2005) 2915–2919.

[89] G. Venketaraman, A. G. Jackson, K. R. Teal, F. H. Froes, The Influence of Nb Addition on Structure and Properties of Rapidly Solidified Intermetallics, Materials Science and Engineering 98 (1988) 257–263.

[90] D. Vujic, Z. Li, S. H. Whang, Effect of rapid solidification and alloying addition on lattice distortion and atomic ordering in $L1_0$ TiAl alloys and their ternary alloys, Metallurgical Transactions A 19 (1988) 2445–2455.

[91] Schwartz, D.S, P. Fraundorf, S. Sastry, TEM study of B- and Er-containing dispersoids in rapidly solidified dispersion-strengthened titanium aluminde alloys, Ultramicroscopy 37 (1991) 310–317.

[92] C. McKamey, S. Whang, C. Liu, Microstructural characterization of a γ-TiAl-Ni alloy produced by rapid solidification techniques, Scripta Metallurgica et Materialia 32 (1995) 383–388.

[93] M. Wettlaufer, J. Laakmann, Solidification front velocity of ternary titanium-aluminides, Materials Research Society symposia proceedings 398 (1996) 69–74.

[94] A. Singh, D. Banerjee, Transformations in $\alpha_2 + \gamma$ Titanium Aluminide Alloys Containing Molybdenum: Part I. Solidification Behavior, Metallurgical and Materials Transactions A 28 (1997) 1735–1743.

[95] O. Shuleshova, T. Woodcock, H. Lindenkreuz, R. Hermann, W. Loser, B. Buchner, Metastable phase formation in Ti–Al–Nb undercooled melts, Acta Materialia 55 (2007) 681–689.

[96] O. Shuleshova, D. Holland-Moritz, W. Löser, A. Voss, H. Hartmann, U. Hecht, V. T. Witusiewicz, D. M. Herlach, B. Büchner, In situ observations of solidification processes in γ-TiAl alloys by synchrotron radiation, Acta Materialia 58 (2010) 2408–2418.

[97] Z. Liu, L. Chai, Y. Chen, Effect of cooling rate and Y element on the microstructure of rapidly solidified TiAl alloys, Journal of Alloys and Compounds 504S (2010) S491–S495.

[98] Z. Liu, L. Chai, Y. Chen, F. Kong, H. Davies, I. Figueroa, Microstructure evolution in rapidly solidified Y added TiAl ribbons, Intermetallics 19 (2011) 160–164.

[99] P. Wang, V.K.Vasudevan, Composition dependence of the massive transformation from α to γ in quenched TiAl alloys, Scripta Metallurgica et Materialia 27 (1992) 89–94.

[100] S. A. Jones, M. J. Kaufman, Phase equilibria and transformations in intermediate Titanium-Aluminium alloys, Acta metall. mater. 41 (1993) 387–398.

[101] Y. Yamabe, M. Takeyama, M. Kikuchi, Determination of α (A3) to α_2 (D019) transition temperatures in Ti-(40-45)at % Al alloys, Scripta Metallurgica et Materialia 30 (1994) 553–557.

[102] P. Wang, D. Veeraraghavan, V. K. Vasudevan, Observation of twins in the α_2 phase in a quenched Ti-46.54 at.% Al alloy, Scripta Materialia 34 (1996) 1601–1607.

[103] D. Veeraraghavan, P. Wang, V. K. Vasudevan, Nucleation kinetics of the α to γ massive transformation in a Ti-47.5 at.% Al alloy, Acta Materialia 51 (2003) 1721–1741.

[104] D. Veeraraghavan, V. K. Vasudevan, Phase transformations in two-phase TiAl/Ti,Al alloys during continuous heating and cooling, studied by electrical resistivity measurements, Materials Science and Engineering A192/193 (1995) 950–956.

[105] D. Veeraraghavan, P. Wang, V. Vasudevan, Kinetics and thermodynamics of the $\alpha \rightarrow \gamma_m$ massive transformation in a Ti–47.5 at.% Al alloy, Acta Materialia 47 (1999) 3313–3330.

[106] S. R. Dey, E. Bouzy, A. Hazotte, EBSD characterisation of massive g nucleation and growth in a TiAl-based alloy, Intermetallics 14 (2006) 444–449.

[107] S. R. Dey, A. Hazotte, E. Bouzy, Crystallography and phase transformation mechanisms in TiAl-based alloys – A synthesis, Intermetallics 17 (2009) 1052–1064.

[108] Q. Xia, J. N. Wang, J. Yang, Y. Wang, On the massive transformation in TiAl-based alloys, Intermetallics 9 (2001) 361–367.

[109] U. Prasad, Q. Xu, M. C. Chaturvedi, Effect of cooling rate and manganese concentration on phase transformation in Ti-45 at.% Al based alloys, Materials Science & Engineering A 329-331 (2002) 906–913.

[110] U. Prasad, M. C. Chaturvedi, Influence of alloying elements on the kinetics of massive transformation in gamma titanium aluminides, Metallurgical and Materials Transactions A 34 (2003) 2053–2066.

[111] A. Huang, M. H. Loretto, D. Hu, K. Liu, X. Wu, The role of oxygen content and cooling rate on transformations in TiAl-based alloys, Intermetallics 14 (2006) 838–847.

[112] H. Singer, I. Singer, A. Jacot, Phase-field simulations of $\alpha \rightarrow \gamma$ precipitations and transition to massive transformation in the Ti–Al alloy, Acta Materialia 57 (2009) 116–124.

[113] E. Gamsjäger, Y. Liua, M. Rester, P. Puschnig, C. Draxl, H. Clemens, G. Dehm, F. D. Fischer, Diffusive and massive phase transformations in Ti-Al-Nb alloys - Modelling and experiments, Intermetallics 38 (2013) 126–138.

[114] J. Yang, J. N. Wang, Q. Xia, Y. Wang, Effect of cooling rate on the grain refinement of TiAl-based alloys by rapid heat treatment, Materials Letters 46 (2000) 193–197.

[115] D. Y. Seo, L. Zhao, J. Beddoes, Microstructural evolution during heat treatments in Ti-45 and 47Al-2Nb-2Mn+0.8vol.%TiB_2 XD alloys, Materials Science and Engineering A 329-331 (2002) 130–140.

[116] A. Stark, M. Oehring, F. Pyczak, A. Schreyer, In Situ Observation of Various Phase Transformation Paths in Nb-Rich TiAl Alloys during Quenching with Different Rates, Advanced Engineering Materials 13 (2011) 700–704.

[117] M. Ahsan, A. Pinkerton, R. Moat, J. Shackleton, A comparative study of laser direct metal deposition characteristics using gas and plasma-atomized Ti-6al-4v powders, Materials Science and Engineering A 528 (2011) 7648–7657.

[118] R. Klose, Additive Manufacturing: 4th industrial revolution, Empa Quarterly 51 (2016) 8–17.

[119] J. H. Abboud, D. R. F. West, Martensite formation in Ti–Allayers produced by laser surface alloying, Materials Science and Technology 7 (1991) 827–834.

[120] J. H. Abboud, D. R. F. West, Microstructures of titanium-aluminides produced by laser surface alloying, Journal of Materials Science 27 (1992) 4201–4207.

[121] M. H. Loretto, D. Horspool, R. Botten, D. Hu, Y. G. Li, D. Srivastava, R. Sharman, X. Wu, Controlling the properties of some ordered Ti-based alloys, Materials Science & Engineering A 329-331 (2002) 1–6.

[122] D. Srivastava, D. Hu, I. T. H. Chang, M. H. Loretto, The influence of thermal processing route on the microstructure of some TiAl-based alloys, Intermetallics 7 (1999) 1107–1112.

[123] D. Srivastava, I. T. H. Chang, M. H. Loretto, The effect of process parameters and heat treatment on the microstructure of direct laser fabricated TiAl alloy samples, Intermetallics 9 (2001) 1003–1013.

[124] X. D. Zhang, C. Brice, D. W. Mahaffey, H. Zang, K. Schwendner, D. J. Evans, H. L. Fraser, Characterization of laser-deposited TiAl alloys, Scripta Materialia 44 (2001) 2419–2424.

[125] W. Liu, J. Dupont, Fabrication of Carbide-Particle-Reinforced Titanium Aluminide-Matrix Composites by Laser-Engineered Net Shaping, Metallurgical and Materials Transactions A 35 (2004) 1133–1140.

[126] T. Vilaro, V. Kottman-Rexerodt, M. Thomas, C. Colin, P.Bertrand, L.Thivillon, S. Abed, V. Ji, P. Aubry, P. Peyre, T. Malot, Direct fabrication of a Ti-47Al-2Cr-2Nb alloy by selective laser melting and direct metal deposition processes, Advanced Materials Research 89-91 (2010) 586–591.

[127] L. Murr, S. Gaytan, A. Ceylan, E. Martinez, J. Martinez, Characterization of titanium aluminide alloy components fabricated by additive manufacturing using electron beam melting, Acta materialia 58 (2010) 1887–1894.

[128] S. Franzen, B. Karlsson, R. Dehoff, U. Ackelid, O. Rios, C. Parish, W. Peters, Microstructural Properties of Gamma Titanium Aluminide Manufactured by Electron Beam Melting, in: The Minerals, Metals & Materials Society, volume 3, 2011, pp. 455–462.

[129] S. Biamino, A. Penna, U. Ackelid, S. Sabbadini, O. Tassa, P. Fino, M. Pavese, P. Gennaro, C. Badini, Electron beam melting of Ti–48Al–2Cr–2Nb alloy: Microstructure and mechanical properties investigation, Intermetallics 19 (2011) 776–781.

[130] J. Schwerdtfeger, C. Körner, Selective electron beam melting of Ti-48Al-2Nb-2Cr: Microstructure and aluminium loss, Intermetallics 49 (2014) 29–35.

[131] S. Biamino, B. Klöden, T. Weissgärber, B. Kieback, U. Ackelid, Titanium aluminides for automotive applications processed by electron beam melting, Technical Report, 2014.

[132] G. Baudana, S. Biamino, D. Ugues, M. Lombardi, P. Fino, M. Pavese, C. Badini, Titanium aluminides for aerospace and automotive applications processed by Electron Beam Melting: Contribution of Politecnico di Torino, Metal Powder Report (2016).

[133] H. Tang, G. Yang, W. Jia, W. He, S. Lu, M. Qian, Additive manufacturing of a high niobium-containing titanium aluminide alloy by selective electron beam melting, Materials Science and Engineering: A 636 (2015) 103–107.

[134] L. Löber, F. P. Schimansky, U. Kühn, F. Pyczak, J. Eckert, Selective laser melting of a beta-solidifying TNM-B1 titanium aluminide alloy, Journal of Materials Processing Technology 214 (2014) 1852–1860.

[135] J. Gussone, Y.-C. Hagedorn, H. Gherekhloo, G. Kasperovich, T. Merzouk, J. Hausmann, Microstructure of γ-titanium aluminide processed by selective laser melting at elevated temperatures, Intermetallics 66 (2015) 133–140.

[136] Y. Ma, D. Cuiuri, N. Hoye, H. Li, Z. Pan, The effect of location on the microstructure and mechanical properties of titanium aluminides produced by additive layer manufacturing using in-situ alloying and gas tungsten arc welding, Materials Science and Engineering: A 631 (2015) 230–240.

[137] F. H. Froes, C. Suryanarayana, D. Eliezer, Synthesis, properties and applications of titanium aluminides, Journal of Materials Science 27 (1992) 5113–5140.

[138] K. Kumar, G. Bao, Intermetallic-matrix composites: An Overview, Composites Science and Technology 52 (1994) 127–150.

[139] C. Ward-Close, R. Minor, P. Doorbar, Intermetallic-matrix composites - a review, Intermetallics 4 (1996) 217–229.

[140] A. V. Antonova, K. B. Povarova, A. A. Drozdov, Composite materials with an intermetallic matrix based on nickel and titanium monoaluminides hardened by oxide particles or fibers, Russian Metallurgy (Metally) 2011 (2012) 853–864.

[141] M. Grujicic, S. Arokiaraj, Chemical compatibility between zirconia dispersion and gamma titanium aluminide matrix, Calphad 17 (1993) 133–140.

[142] C. Koch, Intermetallic matrix composites prepared by mechanical alloying—a review, Materials Science and Engineering A 244 (1998) 39–48.

[143] O. A. Skachkov, K. B. Povarova, A. A. Drozdov, A. E. Morozov, S. V. Pozharov, Deformation and Heat Treatment of NiAl-Y_2O_3-Based Powder Alloys: I. Deformation and Production of Various Pressed Sections, Russian Metallurgy 3 (2013) 217–219.

[144] O. A. Skachkov, K. B. Povarova, A. A. Drozdov, A. E. Morozov, S. V. Pozharov, Deformation and Heat Treatment of NiAl-Y_2O_3-Based Powder Alloys: II. Fabrication of Parts, Russian Metallurgy 5 (2013) 354–356.

[145] S. Kampe, J. Bryant, L. Christodoulou, Creep Deformation of TiB2-Reinforced Near-γ Titanium Aluminides, Metallurgical Transactions A 22 (1991) 447–454.

[146] F. Froes, Titanium Alumindes: Science, Technology, Applications and Synthesis by Mechanical Alloying, Journal of Materials Chemistry Science and Technology 10 (1994) 251–262.

[147] L. Wang, H. Gabrisch, U. Lorenz, F.-P. Schimansky, A. Schreyer, A. Stark, F. Pyczak, Nucleation and thermal stability of carbide precipitates in high Nb containing TiAl alloys, Intermetallics 66 (2015) 111–119.

[148] G. Sauthoff, Multiphase intermetallic alloys for structural applications, Intermetallics 8 (2000) 1101–1109.

[149] W. O. Soboyejo, S. M. L. Sastry, An investigation of the effects of ductile phase reinforcement on the mechanical behavior of advanced high temperature intermetallics, Materials" Science and Engineering A 171 (1993) 95–104.

[150] C. Suryanarayana, F. Froes, Mechanical Alloying of Titanium-Base Alloys, Advanced Materials 5 (1993) 96–106.

[151] P. B. Trivedi, E. G. Baburaj, A. Genc, L. Ovecoglu, S. N. Patankar, F. H. Froes, Grain-size control in Ti-48Al-2Cr-2Nb with yttrium additions, Metallurgical and Materials Transactions A 33A (2002) 2729–2736.

[152] Z. Li, W. Gao, D. Zhang, Z. Cai, High temperature oxidation behaviour of a TiAl–Al_2O_3 intermetallic matrix composite, Corrosion Science 46 (2004) 1997–2007.

[153] K. Zhang, W. Fen, J. Zhu, H. Wu, Mechanical Properties and Microstructure of Al_2O_3/TiAl in Situ Composites Doped with Cr and V_2O_5, Science of Sintering 44 (2012) 73–80.

[154] V. Recina, J. Ahlström, B. Karlsson, Sample Preparation and Microstructural Characterization of the Gamma Titanium Aluminide Ti-48Al-2W-0.5Si, Materials Characterization 38 (1997) 287–300.

[155] H. Lukas, S. Fries, B. Sundman, Computational Thermodynamics - The Calphad Method, Cambridge University Press, 2007.

[156] J. Andersson, T. Helander, L. Höglund, P. Shi, B. Sundman, Thermo-Calc and DICTRA, Computational tools for materials science, Calphad 26 (2002) 273–312.

[157] Y. Liu, E. Gamsjäger, H. Clemens, Thermodynamic description of niobium-rich γ-TiAl alloys, International Journal of Materials Research 102 (2011) 692–696.

[158] S. Mayer, C. Sailer, T. Schmoelzer, H. Clemens, T. Lippmann, P. Staron, V. Güther, M. Takeyama, On Phase Equilibria and Phase Transformations in β/γ-TiAl Alloys – A Short Review, BHM Berg- und Hüttenmännische Monatshefte 156 (2011) 438–442.

[159] D. M. Cupid, O. Fabrichnaya, F. Ebrahimi, H. J. Seifert, Thermodynamic assessment of the Al–Mo system and of the Ti–Al–Mo System from 0 to 20at.% Ti, Intermetallics 18 (2010) 1185–1196.

[160] R. Werner, M. Schloffer, E. Schwaighofer, H. Clemens, S. Mayer, Thermodynamic calculations of phase equilibria and phase fractions of a β-solidifying TiAl alloy using the CALPHAD approach, MRS Proceedings 1516 (2013).

[161] C. Kenel, C. Leinenbach, Influence of cooling rate on microstructure formation during rapid solidification of binary TiAl alloys, Journal of Alloys and Compounds 637 (2015) 242–247.

[162] C. Kenel, P. Schloth, S. V. Petegem, J. L. Fife, D. Grolimund, A. Menzel, H. V. Swygenhoven, C. Leinenbach, In Situ Synchrotron X-Ray Diffraction and Small Angle X-Ray Scattering Studies on Rapidly Heated and Cooled Ti-Al and Al-Cu-Mg Alloys Using Laser-Based Heating, JOM 68 (2016) 978–984.

[163] C. Kenel, D. Grolimund, J. L. Fife, V. A. Samson, S. Van Petegem, H. Van Swygenhoven, C. Leinenbach, Combined in situ synchrotron micro X-ray diffraction and high-speed imaging on rapidly heated and solidified Ti–48Al under additive manufacturing conditions, Scripta Materialia 114 (2016) 117–120.

[164] C. Kenel, C. Leinenbach, Influence of Nb and Mo on microstructure formation of rapidly solidified ternary Ti-Al-(Nb, Mo) alloys, Intermetallics 69 (2016) 82–89.

[165] I. Egry, R. Brooks, D. Holland-Moritz, R. Novakovic, T. Matsushita, E. Ricci, S. Seetharaman, R. Wunderlich, D. Jarvis, Thermophysical Properties of γ -Titanium Aluminide: The European IMPRESS Project, International Journal of Thermophysics 28 (2007) 1026–1036.

[166] ASM International Handbook Committee, ASM Handbook, Volume 02 - Properties and Selection: Nonferrous Alloys and Special-Purpose Materials, ASM International, [S.l.], 1990.

[167] B. Bassler, W. Hofmeister, R. Bayuzick, R. Gorenflo, T. Bergman, L. Stockum, Observation of alloy solidification using highspeed video, Review of Scientific Instruments 63 (1992) 3466–3471.

[168] J. L. Fife, M. Rappaz, M. Pistone, T. Celcer, G. Mikuljan, M. Stampanoni, Development of a laser-based heating system for *in situ* synchrotron-based X-ray tomographic microscopy, Journal of Synchrotron Radiation 19 (2012) 352–358.

[169] P. Kraft, A. Bergamaschi, C. Broennimann, R. Dinapoli, E. F. Eikenberry, B. Henrich, I. Johnson, A. Mozzanica, C. M. Schlepütz, P. R. Willmott, B. Schmitt, Performance of single-photon-counting PILATUS detector modules, Journal of Synchrotron Radiation 16 (2009) 368–375.

[170] W. De Nolf, F. Vanmeert, K. Janssens, *XRDUA* : crystalline phase distribution maps by two-dimensional scanning and tomographic (micro) X-ray powder diffraction, Journal of Applied Crystallography 47 (2014) 1107–1117.

[171] T. Sentenac, Y. Le Maoultt, G. Rolland, M. Devy, Temperature correction of radiometric and geometric models for an uncooled CCD camera in the near infrared, IEEE Transactions on Instrumentation and Measurement 52 (2003) 46–60.

[172] J. Perepezko, T. Massalski, The β to ζ massive transformation in Ag-Al alloys, Acta Metallurgica 23 (1975) 621–631.

[173] O. Shuleshova, W. Löser, D. Holland-Moritz, D. M. Herlach, J. Eckert, Solidification and melting of high temperature materials: in situ observations by synchrotron radiation, Journal of Materials Science 47 (2012) 4497–4513.

[174] J. Liu, P. Staron, S. Riekehr, A. Stark, N. Schell, N. Huber, A. Schreyer, M. Müller, N. Kashaev, In situ study of phase transformations during laser-beam welding of a TiAl alloy for grain refinement and mechanical property optimization, Intermetallics 62 (2015) 27–35.

[175] T. Schmoelzer, S. Mayer, F. Haupt, G. A. Zickler, C. Sailer, L. Lottermoser, V. Güther, K.-D. Liss, H. Clemens, Phase transition and ordering temperatures of TiAl-Mo alloys investigated by in-situ diffraction experiments, Materials Science Forum 654-656 (2010) 456–459.

[176] S. Kabra, K. Yan, S. Mayer, T. Schmoelzer, M. Reid, R. Dippenaar, H. Clemens, K.-D. Liss, Phase transition and ordering behavior of ternary Ti–Al–Mo alloys using in-situ neutron diffraction, International Journal of Materials Research 102 (2011) 697–702.

[177] P. Beran, M. Petrenec, M. Heczko, B. Smetana, M. Žaludová, M. Šmíd, T. Kruml, L. Keller, In-situ neutron diffraction study of thermal phase stability in a γ-TiAl based alloy doped with Mo and/or C, Intermetallics 54 (2014) 28–38.

[178] A. Stark, M. Rackel, A. Tchouaha Tankoua, M. Oehring, N. Schell, L. Lottermoser, A. Schreyer, F. Pyczak, In Situ High-Energy X-ray Diffraction during Hot-Forming of a Multiphase TiAl Alloy, Metals 5 (2015) 2252–2265.

[179] J. Breuer, T. Wilger, M. Friesel, C. Herzig, Interstitial and substitutional diffusion of metallic solutes in Ti_3Al, Intermetallics 7 (1999) 381–388.

[180] Y. Mishin, C. Herzig, Diffusion in the Ti-Al system, Acta Materialia 48 (2000) 589–623.

[181] C. Kenel, K. Dawson, C. Hauser, J. Barras, G. Dasargyri, T. Bauer, A. Colella, A. Spierings, G. J. Tatlock, C. Leinenbach, K. Wegener, Microstructure and oxide particle stability in a novel ODS γ-TiAl alloy processed by spark plasma sintering and laser additive manufacturing, submitted to Acta Materialia (2016).

[182] J. Zollinger, V. Witusiewicz, A. Drevermann, D. Daloz, U. Hecht, Solidification of high Nb containing TiAl based alloys, International Journal of Cast Metals Research 22 (2009) 339–342.

[183] K. Kasahara, Y. Ikeda, T. Kimura, T. Tsujimoto, Effects of additions of Y and rare-earth metals on the cyclic oxidation of TiAl alloys, Journal of the Japan Institute of Metals (1996) 907–913.

[184] Y. Wu, S. K. Hwang, Microstructural refinement and improvement of mechanical properties and oxidation resistance in EPM TiAl-based intermetallics with yttrium addition, Acta Materialia 50 (2002) 1479–1493.

[185] Y. Wu, S. K. Hwang, S. W. Nam, N. J. Kim, The effect of yttrium addition on the oxidation resistance of EPM TiAl-based intermetallics, Scripta Materialia 48 (2003) 1655–1660.

[186] Y. Wu, K. Hagihara, Y. Umakoshi, Influence of Y-addition on the oxidation behavior of Al-rich γ-TiAl alloys, Intermetallics 12 (2004) 519–532.

[187] Y. Wu, K. Hagihara, Y. Umakoshi, Improvement of cyclic oxidation resistance of Y-containing TiAl-based alloys with equiaxial gamma microstructures, Intermetallics 13 (2005) 879–884.

[188] S. Taniguchi, T. Shibata, H. Juso, N. Katoh, Effect of Hf addition (0.24 w/o) on the oxidation behavior of TiAl at high temperatures, Oxidation of Metals 42 (1994) 205–222.

[189] S. Taniguchi, T. Shibata, Influence of additional elements on the oxidation behaviour of TiAl, Intermetallics 4 (1996) 85–S93.

[190] E. Arzt, E. Göhring, A model for dispersion strengthening of ordered intermetallics at high temperatures, Acta Materialia 46 (1998) 6575–6584.

[191] E. Arzt, Size effects in materials due to microstructural and dimensional constraints: A comparative review, Acta Materialia 46 (1998) 5611–5626.

[192] S. H. Whang, D. P. Pope, C. T. Liu, High Temperature Aluminides and Intermetallics: Proceedings of the Second International ASM Conference on High Temperature Aluminides and Intermetallics, September 16-19, 1991, San Diego, CA, USA, Elsevier, 2013.

[193] C. Capdevila, G. Pimentel, M. M. Aranda, R. Rementeria, K. Dawson, E. Urones-Garrote, G. J. Tatlock, M. K. Miller, Role of Y-Al Oxides During Extended Recovery Process of a Ferritic ODS Alloy, JOM 67 (2015) 2208–2215.

[194] Y. Li, D. Gu, Parametric analysis of thermal behavior during selective laser melting additive manufacturing of aluminum alloy powder, Materials & Design 63 (2014) 856–867.

[195] D. P. Whittle, J. Stringer, Improvements in High Temperature Oxidation Resistance by Additions of Reactive Elements or Oxide Dispersions, Philosophical Transactions of the Royal Society of London A: Mathematical, Physical and Engineering Sciences 295 (1980) 309–329.

[196] J. Stringer, Proceedings of the 2nd International symposium on High Temperature Corrosion of Advanced Materials and Coatings The reactive element effect in high-temperature corrosion, Materials Science and Engineering: A 120 (1989) 129–137.

[197] B. A. Pint, Progress in understanding the reactive element effect since the Whittle and Stringer literature review, in: Proc. John Stringer Symposium on High Temperature Corrosion, ASM International, 2003, pp. 9–19.

[198] Y. Shida, H. Anada, The effect of various ternary additives on the oxidation behavior of TiAl in high-temperature air, Oxidation of Metals 45 (1996) 197–219.

[199] T. Izumi, T. Yoshioka, S. Hayashi, T. Narita, Oxidation behavior of sulfidation processed TiAl–2 at.%X (X=Si, Mn, Ni, Ge, Y, Zr, La, and Ta) alloys at 1173 K in air, Intermetallics 13 (2005) 694–703.

[200] W. Zhang, G. Chen, Z. Sun, Oxidation of ternary Ti–18Nb–48Al and Ti–10Nb–45Al alloys, Scripta Metallurgica et Materialia 28 (1993) 563–567.

[201] A. Gil, B. Rajchel, N. Zheng, W. J. Quadakkers, H. Nickel, The influence of implanted chromium and yttrium on the oxidation behaviour of TiAl-based intermetallics, Journal of Materials Science 30 (1995) 5793–5798.

[202] J. P. Kim, H. G. Jung, K. Y. Kim, Al+Y codeposition using EB-PVD method for improvement of high-temperature oxidation resistance of TiAl, Surface and Coatings Technology 112 (1999) 91–97.

[203] M. K. Lei, X. P. Zhu, X. J. Wang, Oxidation Resistance of Ion-Implanted γ-TiAl-Base Intermetallics, Oxidation of Metals 58 (2002) 361–374.

[204] P. J. Masset, M. Schütze, Oxidation Tests with Untreated and F-Treated TNBV5 Alloys, ECS Transactions 25 (2010) 45–56.

[205] E. Underwood, The mathematical foundations of quantitative stereology, Stereology and Quantitative Metallography, ASTM STP 504 (1972).

[206] J. Kruth, L. Froyen, J. Van Vaerenbergh, P. Mercelis, M. Rombouts, B. Lauwers, Selective laser melting of iron-based powder, Journal of Materials Processing Technology 149 (2004) 616–622.

Curriculum vitae

Christoph Kenel

MSc ETH
Lagerstrasse 2a, 8570 Weinfelden, Switzerland
Phone: +41 58 765 56 54 / Mail: Christoph.Kenel@empa.ch
ResearchGate: www.researchgate.net/profile/Christoph_Kenel

Personal details

Date of birth	6th of August 1987
Place of origin	Arth SZ, Switzerland
Nationality	Swiss

Research experience

Feb 2013 – present	PhD thesis "*Development of oxide dispersion strengthened titanium aluminides for additive manufacturing*" Alloy Design and Processing Technologies, Dr. Ch. Leinenbach, Empa and Prof. K. Wegener, ETH Zürich.
Feb – Jul 2012	Master thesis "*Characterization of the deformation and failure mechanisms of high temperature brazed steel components*" Advanced Joining Technologies, Dr. Ch. Leinenbach, Empa and Prof.P. Uggowitzer, ETH Zürich
Jul – Aug 2011	Master project II "*Study of Exchange Parameters in* Cr_2O_3" Materials Theory, Prof. N. Spaldin, ETH Zürich
Feb – May 2011	Research assistant for thermal treatment and characterization of Cu-Cr thin films Laboratory for Nanometallurgy, Prof. R. Spolenak, ETH Zürich
Jan – Feb 2011	Master project I: "*Study of thermally induced decomposition in magnetron sputtered Cu-Cr thin films*" Laboratory for Nanometallurgy, Prof. R. Spolenak, ETH Zürich
Aug – Dec 2010	Industrial internship at Carbo-Link GmbH, Fehraltorf, Switzerland "*Optimization of CFRP tensile members for crane applications*"
Feb – June 2010	Bachelor thesis "*Glass-forming ability and room temperature aging in Cu-Zr-Al and Cu-Hf-Ti*" Laboratory for Metal Physics and Technology, Prof. J. Löffler, ETH Zürich
Sept – Dec 2008	Research assistant for the development and testing of heating elements for high temperature centrifuges Laboratory for Metal Physics and Technology, Prof. J. Löffler, ETH Zürich

Education

2011 – 2012	Master of Science in Materials Science and Engineering ETH Zürich, Switzerland Grade: 5.94/6, Diploma with Distinction and awarded the Willi Studer Prize
2007 – 2011	Bachelor of Science in Materials Science and Engineering ETH Zürich, Switzerland Grade: 5.33/6
2002 – 2006	Swiss Matura (qualification for university entrance), Kantonsschule Kreuzlingen, Switzerland

Awards and grants

December 2015	3rd Place Best Presentation Award at the Empa PhD Symposium 2015
June 2015	CALPHAD Poster Award for the best poster presented at the CALPHAD XLIV conference, Loano, Italy
June 2015	Larry Kaufman Scholarship for the CALPHAD XLIV conference in Loano, Italy
September 2014	Best Paper Award at the 2014 Solid Freeform Fabrication Symposium, Texas, USA
May 2013	Willi Studer Prize for the best student in the ETH Materials Science Master programme 2013
June 2006	High school diploma thesis awarded by the 'Thurgauische Naturforschende Gesellschaft' (Society of Science of the Canton of Thurgau)

Skills

Materials development and characterization

Extensive knowledge and practical experience in materials development using experimental alloy production from powder and bulk by arc and induction melting combined with computational thermodynamics based on the CALPHAD approach using Thermocalc. Experienced in materials characterization in the fields of thermal properties (DSC), electron microscopy (SEM/TEM), mechanical testing, digital image correlation and analytical methods as lab-based and *in situ* synchrotron X-ray diffraction (XRD) and X-ray spectroscopy (EDXS). Development of novel *ex situ* and *in situ* experimental setups to study materials behavior under additive manufacturing conditions involving high cooling rates.

Scientific software

Thermocalc for computational thermodynamics, XRDua for evaluation of 2D XRD patterns, Gatan Digital Micrograph for the processing of TEM micrographs, Matlab for evaluation of large datasets, Origin for scientific data plotting, ImageJ for image processing, Corel Draw for illustrations.

Languages

(Swiss) German	native language
English	fluent in spoken and written
French	good in spoken and written

List of Publications

Publications related to this thesis

C. Kenel, C. Leinenbach, Influence of cooling rate on microstructure formation during rapid solidification of binary TiAl alloys, Journal of Alloys and Compounds 637 (2015) 242-247

C. Kenel, C. Leinenbach, Influence of Nb and Mo on microstructure formation of rapidly solidified ternary Ti-Al-(Nb, Mo) alloys, Intermetallics 69 (2016) 82-89.

C. Kenel, D. Grolimund, J.L. Fife, V. Samson, S.V. Van Petegem, H.V. Van Swygenhoven, C. Leinenbach, Combined in situ synchrotron micro X-ray diffraction and high-speed imaging on rapidly heated and solidified Ti-48Al under additive manufacturing conditions, Scripta Materialia 114 (2016) 117-120.

C. Kenel, P. Schloth, S.V. Petegem, J.L. Fife, D. Grolimund, A. Menzel, H.V. Swygenhoven, C. Leinenbach, In Situ Synchrotron X-Ray Diffraction and Small Angle X-Ray Scattering Studies on Rapidly Heated and Cooled Ti-Al and Al-Cu-Mg Alloys Using Laser-Based Heating, JOM (2016) 1-7.

C. Kenel, K. Dawson, J. Barras, C. Hauser, G. Dasargyri, T. Bauer, A. Colella, A.B. Spierings, G. J. Tatlock, K. Wegener, C. Leinenbach, Microstructure and oxide particle stability in a novel ODS γ-TiAl alloy processed by spark plasma sintering and laser additive manufacturing, submitted to Acta Materialia.

C. Kenel, A. Lis, K. Dawson, A. Colella, G. Tatlock, K. Wegener, C. Leinenbach, Increased oxidation resistance and strength in Y_2O_3-containing ODS Ti-45Al-3Nb, in preparation.

C. Kenel, G. Dasargyri, T. Bauer, A.B. Spierings, K. Wegener, C. Leinenbach, Selective laser melting of an oxide dispersion strengthened TiAl alloy towards production of complex structures, in preparation.

Additional journal publications

A. Lis, C. Kenel, C. Leinenbach, Characteristics of reactive Ni_3Sn_4 formation and growth in Ni-Sn inter-layer systems, Metallurgical and Materials Transactions A 47 (2016) 2596-2608.

M. Koster, A. Lis, W.J. Lee, C. Kenel, C. Leinenbach, Influence of elastic-plastic base material properties on the fatigue and cyclic deformation behavior of brazed steel joints, International Journal of Fatigue 82 (2015) 49-59.

A.B. Spierings, C. Leinenbach, C. Kenel, K. Wegener, Processing of metal-diamond-composites using selective laser melting, Rapid Prototyping Journal 21 (2015) 130-136.

M. Koster, C. Kenel, W.J. Lee, C. Leinenbach, Digital Image Correlation for the Characterization of Fatigue Damage Evolution in Brazed Steel Joints, Procedia Materials Science 3 (2014) 1117-1122.

M. Koster, C. Kenel, A. Stutz, W.J. Lee, A. Lis, C. Affolter, C. Leinenbach, Fatigue and cyclic deformation behavior of brazed steel joints, Materials Science and Engineering A 581 (2013) 90-97.

Conference papers

C. Leinenbach, M. Koster, C. Kenel, W.J. Lee, Influence of substrate properties on fatigue performance of brazed steel joints, International Brazing and Soldering Conference, Long Beach; 04/2015.

A.B. Spierings, C. Leinenbach, C. Kenel, K. Wegener, Processing of metal-diamond-composites using selective laser melting. Annual International Solid Freeform Fabrication Symposium, Austin TX; 08/2014.

M. Koster, C. Kenel, W.J. Lee, C. Leinenbach, Digital image correlation for the characterization of fatigue damage evolution in brazed steel joints, Trondheim; 07/2014.

M. Koster, C. Kenel, A. Lis, C. Leinenbach: Integrity of brazed steel joints under quasi-static and cyclic loading, Löt 2013, Aachen; 06/2013.

M. Koster, C. Kenel, C. Leinenbach: Characterization of the fatigue behavior of brazed steel joints by digital image correlation (DIC). 13th International Conference of Fracture, Beijing; 06/2013.

Presentations and posters

C. Kenel, K. Dawson, J. Barras, C. Hauser, G. Dasargyri, T. Bauer, A. Colella, A.B. Spierings, G. J. Tatlock, K. Wegener, C. Leinenbach, Design of an ODS-TiAl alloy for additive manufacturing technologies, Material Science and Technology Conference, Salt Lake City; 10/2016.

C. Kenel, D. Grolimund, J.L. Fife, V.A. Samson, S. Van Petegem, H. Van Swygenhoven, C. Leinenbach, In situ X-ray diffraction studies on rapidly solidified alloys under additive manufacturing conditions, THERMEC conference, Graz; 05/2016.

C. Kenel, K. Wegener, C. Leinenbach, Titanium aluminide alloy development for additive manufacturing - towards tailored alloys for non-equilibrium processing, Empa PhD Symposium, Dübendorf; 12/2015.

C. Kenel, C. Leinenbach, Microstructure formation of Ti-Al-(Nb, Mo) titanium aluminides under additive manufacturing processing conditions, Euromat Conference, Warsaw; 09/2015.

C. Kenel, T. Ivas, A. Lis, C. Leinenbach, Poster entitled "CALPHAD assisted titanium aluminide alloy development for additive manufacturing", CALPHAD XLIV Conference, Loano; 06/2015.

C. Kenel, C. Leinenbach, Poster entitled "‘Systematic Ti-Al alloy development by rapid solidification for additive manufacturing", Empa PhD Symposium, St. Gallen; 10/2014.

C. Kenel, C. Leinenbach, Simulation-assisted rapid solidification of titanium aluminides for additive manufacture, Material Science and Technology Conference, Pittsburgh; 10/2014.

C. Kenel, C. Leinenbach, Poster entitled "Development of novel titanium aluminide alloys for high temperature applications", Empa PhD Symposium, Dübendorf; 10/2013.

C. Kenel, C. Leinenbach, Application of ThermoCalc and Dictra for advanced joining and interface technologies, Computational Thermodynamics and Kinetics Seminar, Genova; 06/2013.